



Fracture properties of Soft Materials : From Linear Elastic Fracture to damage at the microscopic scale

Maxime Lefranc

► To cite this version:

Maxime Lefranc. Fracture properties of Soft Materials : From Linear Elastic Fracture to damage at the microscopic scale. Mechanics of materials [physics.class-ph]. Université Paris Sud - Paris XI, 2015. English. NNT : 2015PA112028 . tel-01294017

HAL Id: tel-01294017

<https://theses.hal.science/tel-01294017>

Submitted on 26 Mar 2016

HAL is a multi-disciplinary open access archive for the deposit and dissemination of scientific research documents, whether they are published or not. The documents may come from teaching and research institutions in France or abroad, or from public or private research centers.

L'archive ouverte pluridisciplinaire **HAL**, est destinée au dépôt et à la diffusion de documents scientifiques de niveau recherche, publiés ou non, émanant des établissements d'enseignement et de recherche français ou étrangers, des laboratoires publics ou privés.

UNIVERSITÉ PARIS-SUD

ECOLE DOCTORALE 564: PHYSIQUE EN ILE DE FRANCE
LABORATOIRE GULLIVER

DISCIPLINE: MÉCANIQUE PHYSIQUE.

THÈSE DE DOCTORAT
Soutenue le 19/02/2015 par

Maxime Lefranc

**Fracture properties of soft materials:
From linear elastic fracture
to damage at the microscopic scale**

Directeur de thèse : Mme. Elisabeth Bouchaud

Directrice de recherche (CEA/ESPCI Paristech)

Composition du jury :

Président du jury : M. Emmanuel Trizac
Rapporteurs : M. Jean-Louis Barrat
M. Serge Mora
Examineurs : M. Jay Fineberg
M Francois Hild
M Peter Schall

Professeur (Paris Sud)
Professeur (UJF Grenoble)
Professeur (Université Montpellier)
Professeur (Hebrew University of Jerusalem)
Professeur (LMT Cachan)
Professeur (University of Amsterdam)

Remerciements

"Would you tell me, please, which way I ought to go from here?"

"That depends a good deal on where you want to get to."

"I don't much care where."

"Then it doesn't matter which way you go."

– *Lewis Carroll*, *Alice in Wonderland*

Avec un peu de recul et quelques mois passés depuis ma soutenance, ces quelques lignes de Lewis Carroll reflètent assez bien ce qu'il m'est arrivé de ressentir lors de ces 3 années et demi d'aventure de doctorat! L'aventure dans laquelle je m'engageais n'avait pas d'objectif clairement établi; l'idée était plus d'ouvrir de nouvelles voies et, équipé d'un frêle esquif, de prendre la mer en espérant que mon voyage m'amènerait à explorer de lointaines terres inconnues. Evidemment, une grande partie de ces 3 années a principalement consisté à humblement longer les côtes! Mais même là, on se retrouve confronté à des éléments pas toujours favorables ainsi qu'à des récifs qui n'avaient pas tous été cartographiés! Ainsi, plusieurs fois l'embarcation a semblé prendre l'eau et il fallut rentrer au port! Heureusement, au fur et à mesure des nouvelles tentatives, le radeau devenait barque, la barque devenait voilier, le voilier devenait gallion et ce qui n'était que cabotage commençait à prendre un doux parfum d'aventure.

Tout cela n'a bien sûr pas été un exercice en solitaire. Lorsqu'on aspire à se lancer dans l'inconnu, c'est que l'on a été inspiré, entouré et soutenu. Mes premiers remerciements vont ainsi à Elisabeth qui m'a donné cette inspiration, ce goût de l'aventure, m'a donné carte blanche et a en même temps su m'aider à garder le cap. Les seconds vont à Olivier, l'armateur, qui, du port, veillait sur mon périple de manière bienveillante et m'a donné les moyens de réussir. Les suivants vont à tous les ports dans lesquels je suis venu jeter l'ancre: le laboratoire SIMM à l'ESPCI, l'équipe d'Arjun Yodh à UPenn, le groupe de Peter Schall à Amsterdam. A toutes les légendes des mers dont j'ai croisé la route: François Hild, Herbert Hui, Eran Bouchbinder, Mickael Falk, Serge Mora et bien d'autres! A mes petits mousses Tarek, Marion, Durka qui à un moment où l'autre du voyage, ont été d'un soutien sans faille et m'ont aidé à aller un petit peu plus loin! A tous les thésards et camarades de galère d'EC2M, PCT, NBP et MMN! Merci à Ziane d'avoir partagé toutes ces années depuis le Master. Merci à Aurélien et à tous les membres de MMN qui ont accepté d'accueillir un squatteur d'EC2M pour les pauses petit déjeuner, café du matin, déjeuner et goûter, etc. Ca a été un plaisir de mon côté en tout cas. Merci à Vincent mon fidèle adjoint chez les syndicalistes.

Enfin, j'insistais plus tôt sur l'importance de se sentir soutenu, encouragé. Je remercie pour cela mes amis d'enfance, ma famille et plus parti-

culièrement mes parents. Pas facile pour eux d'expliquer pendant 3 ans que leur fils "essayait de casser des liquides"; je les sens plus à l'aise à présent pour narrer mes nouvelles aventures au sein de Saint-Gobain. J'espère qu'ils sont fiers de leur fils qu'ils ont élevé et aimé et qui est aujourd'hui devenu docteur. Mais, contrairement à ce que j'ai pu penser il y a 3 ans, la thèse n'est pas un aboutissement en soi. Certes, l'étudiant est devenu docteur et ingénieur mais le jeune homme est surtout devenu mari et père de famille.

Tous les jours, je me rends un peu plus compte que l'aventure scientifique est bien peu de chose à côté de celle que je souhaite continuer à vivre avec toi Marie! Merci de ton amour et de ton soutien sans faille!

Contents

1	Introduction	3
1.1	A black box named process zone	3
1.2	Exploring the process zone	7
2	Agar, a physical polymer gel.	15
2.1	Introduction	15
2.2	Biopolymer gel of Agar	17
2.2.1	Structure and conformation of agar chains in water . .	17
2.2.2	Sol-gel transition	20
2.2.3	Gel preparation	24
2.2.4	Structure of agar gels.	26
2.3	Mechanics of Agar gels	26
2.3.1	Linear elasticity of agar gels	26
2.3.2	Rate-dependent properties of agar gels	37
2.3.3	Nonlinear elasticity	42
2.4	Conclusion	50
3	Fracture of Soft Materials	53
3.1	Fracture of soft materials: a short review	54
3.1.1	Probetack or extensional experiments	59
3.1.2	A tensile test for soft materials	61
3.1.3	Fracture in Hele Shaw geometries	64
3.2	A new experiment for fracture of soft materials	67
3.2.1	Specification list for our experiment	67
3.2.2	Toward a "on-a-chip" mechanical test	69
3.3	Design of our on a chip mechanical test	81
3.3.1	Chip geometry	81
3.3.2	Chip fabrication	85
3.3.3	Experimental procedure	92
3.3.4	Some other tested geometries	104

4	Crack tip Displacement Fields	105
4.1	Introduction	106
4.2	Learning from the crack shape	108
4.2.1	Mode I Crack profiles in soft materials	108
4.2.2	Crack shape analysis	121
4.2.3	Crack opening displacement in agar gels.	132
4.3	Crack displacement fields measured with DIC	141
4.3.1	FE-DIC: a new tool in Soft Matter	143
4.3.2	Performances of FE-DIC applied to our specimen	146
4.3.3	Capturing displacement field at the crack tip.	154
4.3.4	Projecting the measured field on known displacement fields	160
4.4	Conclusion. A comparison of COD and DIC	178
5	Rate-dependency and large strains disentangled	181
5.1	Introduction.	182
5.2	Macroscopic Dissipation at the crack tip	183
5.2.1	Measuring the energy release rate without measuring forces	183
5.2.2	How can one explain $\mathcal{G}(V)$?	194
5.3	Large strains at the crack tip.	207
5.3.1	COD and DIC: interpretation of d^*	208
5.3.2	Crack tip nonlinearities in a stiffening material	214
5.4	Conclusion: disentangling dissipation and large deformations	225
6	Conclusion & Perspectives	229
6.1	Conclusion.	229
6.2	Perspectives	230

1

Introduction

Contents

1.1 A black box named process zone	3
1.2 Exploring the process zone	7

1.1 A black box named process zone

In Fracture Mechanics, Linear Elastic Fracture Mechanics (LEFM) is a common framework used for predicting if an existing crack embedded in a structure made of a given material will be stable or not when submitted to a loading. Griffith, in 1922, was the first to propose an energy-balance criterion for crack stability: a crack propagates if $\mathcal{G} \gg \mathcal{G}_c$.

Here, \mathcal{G} is the mechanical energy release rate, i.e. the elastic energy released for an elementary crack advance. It is a mechanical quantity computed in the framework of linear elasticity for a given geometry under a given loading configuration and for a given material. The delicate task consists of knowing \mathcal{G}_c . \mathcal{G}_c is the critical energy release rate. It is a material property that encompasses all the energy costs due to the surface creation caused by the crack growth. For most materials, \mathcal{G}_c often needs to be measured as models hardly give good predictions. For understanding and improving the mechanical properties of existing materials, and in the perspective of designing new materials for stringent industrial applications, this lack of knowledge and lack of predictability dramatically slows down progress in material science.

To be modeled correctly, the energy cost for surface creation should not only take into account the rupture energy of the bonds crossing the fracture plane, it should also integrate all the energy costs due to damage occurring in the crack tip vicinity. As LEFM predicts a diverging stress at the crack tip, this task is a real challenge because it deals with all the non linearities, damage and dissipative processes that occur in what is called the process zone, where linear elasticity is known to break down.

It is both experimentally and theoretically difficult to probe the material properties in such extreme conditions. One of the fundamental reasons for this difficulty is that the physics of fracture is mainly governed by the presence of defects in the material. For crystalline materials, which are ordered at the microscopic scale, defects are dislocations, and are easy to identify: these are perturbations relative to the perfectly ordered microstructure. In the case of amorphous materials like gels, silica or polymer glasses, there is disorder at microscopic scale, which makes defects hard to identify and damage in these materials much harder to model.

Some numerical studies have been performed to investigate dissipative phenomena at stake in the process zone for some amorphous materials. Rountree & al [1] and Falk [2], performed molecular dynamic simulations of cracks propagating in amorphous silica and Lennard Jones (LJ) glasses respectively: they identified two possible dissipative processes in amorphous materials. Rountree & al [1] have shown that amorphous silica breaks in a quasi-brittle way, meaning that the main crack grows by nucleating ahead of it, crack precursors that grow and coalesce (see Fig.1.1).

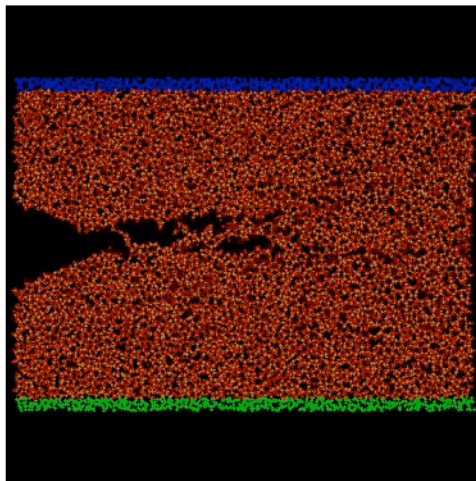


Figure 1.1: Molecular dynamic simulation of crack propagation in amorphous silica. Large stress at the crack tip are sufficient to induce crack precursors ahead of it. From [1].

Falk's crack simulation [2] deals with model LJ glasses where the interaction potential can be tuned. He is interested in the change in crack dynamics and in the non-affine displacements (the localized microstructural rearrangements) around the crack tip when tuning the width of the potential well. One of the main results is that the narrowing of the potential well results in a ductile-to-brittle transition and in a decrease of non-affine rearrangements at the mesoscopic level (see Fig.1.2).

It is no surprise that ductility goes with higher levels of non affinity. Non

affine displacements are indeed a known feature of plasticity and energy dissipation in amorphous materials [3, 4]: in the plastic regime, sheared amorphous systems are known to undergo cascades of local rearrangements, associated with quadrupolar energy fluctuations, which induce system-spanning events (shear bands for instance).

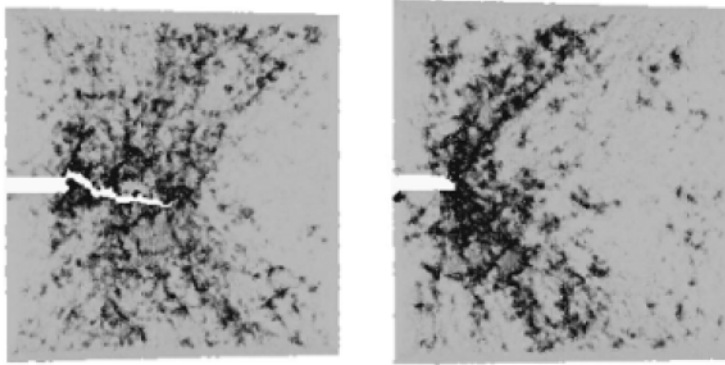


Figure 1.2: Molecular dynamics simulation of a high-deformation-rate ($10^8 s^{-1}$) crack propagation in a notched Lennard-Jones glass with interaction potential of different width. The narrowing of the LJ potential well induces a ductile-to-brittle transition, i.e. a decrease in the energy dissipation with crack growth. For a reference LJ potential (Right), the initial crack blunts and a dense spatial distribution of non-affine displacements (in black) is activated around the blunted crack, resulting in a high energy dissipation. The material eventually fails at high stress by void nucleation and coalescence of these nucleated zones. For a compressed LJ potential (potential with narrower width, Left), the crack can propagate at a much smaller loading stress, it leaves a sparse wake of activated non-affine zones behind it, and results in a much lower dissipation. Void nucleation is also shown to occur, but at much smaller scale. From[2].

Experimental approaches are made complicated by the small size of the process zone in such amorphous materials (few tens of nanometers). For example, results similar to the one predicted by Rountree were obtained by Celarie & al [5]: cavities of typical size $10nm$, opening and coalescing ahead of a crack, were observed in an aluminosilicate glass using AFM. Additionally to the small size of the process zone, the visualization techniques that are able to reach these scales are very slow, which limits the study of damage to the vanishing velocities and prevents experimentalists from studying the effect of crack velocity as an additional source of dissipation.

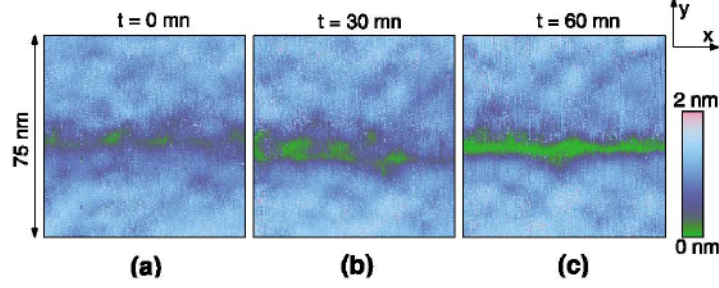


Figure 1.3: Sequence of successive topographic AFM frames showing the crack propagation at the surface of the aluminosilicate DCDC specimen. The scan size is $75 \times 75 \text{ nm}^2$ and the heights range over 2 nm. The crack front propagates from the left to the right (x direction) with an average velocity V close to 10^{-11} m/s . (a) Evidence of nanometric damage cavities before the fracture advance. (b) Growth of the cavities. (c) The crack is advancing via the coalescence of all the cavities. From [5].

In conclusion, numerical fracture experiments deal with specimens that are often smaller than the process zone and with very fast cracks, while live experimental observations only allow the observation of very slow cracks at resolutions that do not make possible the observation of the microstructure and local rearrangements. An original experimental approach is thus needed to circumvent these limitations.

1.2 Exploring the process zone

In the 2000's, Fracture mechanics made a great deal of progress in the context of Dynamic fracture. Thanks to very original experiments, Fineberg shed new light on this complex problem. Dynamic branching, fracture surface roughening, etc. were commonly accepted as consequences of the dynamic nature of crack propagation. But one had very little idea about the mesoscopic processes resulting in these macroscopic observations. Fineberg's idea is very simple: taking advantage of the decrease of the speed of sound when decreasing the shear modulus, he works with soft materials so that the dynamic effects, appearing for cracks propagating at 3000m/s in glass or at 1000m/s in stiff polymers, appears below 1m/s in soft materials such as polymer gels. This allows to perform live observations of dynamic crack propagation (see Fig.1.4), raises a new interest for dynamic fracture, and enabled to solve open questions [6, 7].

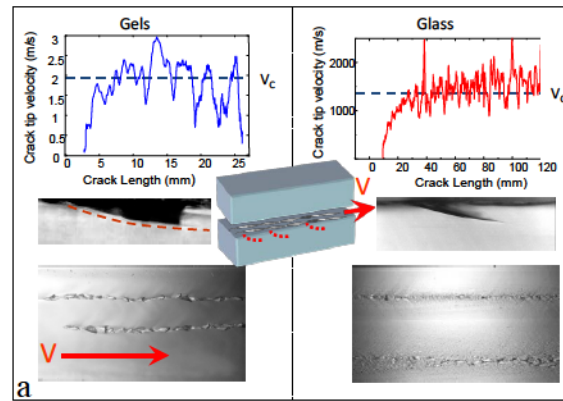


Figure 1.4: Dynamic fracture: Universality of the micro-branching instability. (a) A comparison between the instability in both soft polyacrylamide gels (left) and soda-lime glass (right). Top: the instantaneous velocity of the crack undergoes violent oscillations that correspond to the formation of micro-branches. Bottom: micro-branches and fracture facies are very similar in both materials. From [6]

Enlarging the process zone. As mentioned in the first part of this introduction, lots of questions are still open as to what is happening in the process zone. This is because, in most of the materials around us, the process zone is confined in a region of few tens of nanometers for atomic scales of the order of the Angström. But one can reasonably suggest that the size of the mesoscopic damage processes will somehow scale with the elementary microscopic scale. In soft colloidal glasses, the elementary microscopic scale is of the order of the size of the colloid ($1\mu\text{m}$). In soft gels, the entropic

elastic length (or mesh size) $\xi = (k_B T / G)^{1/3}$ (where G is the shear modulus of the material) will be the relevant microscopic scale. Typical shear moduli and length scales are given for several soft materials:

Material	Shear modulus	Microscopic scale
Polymer gel	$10kPa$	$10nm$
Colloidal glass	$10 - 100Pa$	$1\mu m$
Colloidal gel	$0.1 - 10Pa$	$10\mu m$

Therefore, using soft materials instead of hard ones allows to increase the microstructural length scale by several orders of magnitude and thus, to potentially magnify the size of all the dissipative processes at stake in the crack vicinity. This will help to gain more insight into what happens in the process zone.

This increase of the microstructural length scales has already been used in contexts other than the one of fracture. Colloidal materials have already demonstrated their great experimental potential for capturing the microscopic dynamics of a material driven out of mechanical equilibrium. These systems indeed allow to combine macroscopic stress/strain experiments with particle-resolved measurements as reported in [8], [9] (see Fig.1.5) or [10] (see Fig.1.6).

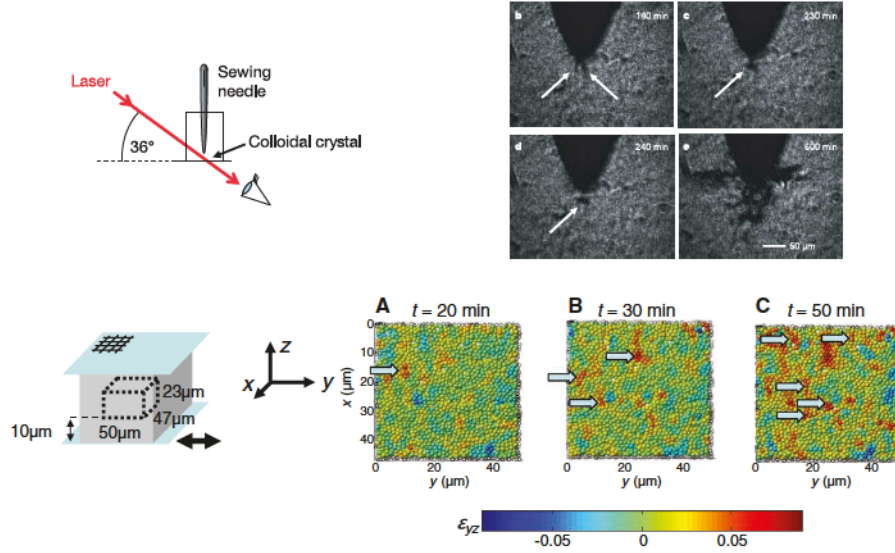


Figure 1.5: Particle-resolved experiments on colloidal materials driven out of the mechanical equilibrium. Top: Indentation of a colloidal crystal induces dislocation loops (white arrows). From [9]. Bottom: Shear step on a colloidal glass. With time, the imposed shear localizes in some mesoscopic regions called shear transformation zones.

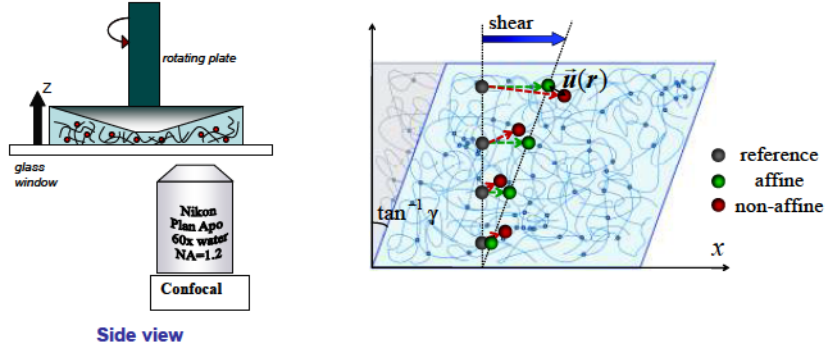


Figure 1.6: Confocal rheology setup from Yodh group. A rheometer coupled with a confocal microscope (Left) allows to track the displacement of tracers seeded in polymer gels under shear. Basu [10] showed the increase of non affinity in the nonlinear regime. A sketch of what happens when shearing a polymer gel is also shown (Right). In grey is shown the unsheared reference state. In green is shown the tracer displacements expected for the affine shear displacement field. In red are represented the non affine displacements that deviate from the shear displacement field.

Fracture of soft materials. Our novel experimental approach consists in studying fracture mechanics of soft materials, mainly polymer and colloidal gels, which have microstructures with large typical length scales. This increase in the microscopic scale will consequently increase the typical size of the process zone and make its observation easier with standard microscopy techniques (optical or confocal). The details of how the system regularizes the stress divergence at the crack tip will strongly depend on the microscopic detail of the material we will consider.

In the dynamic fracture regime of soft elastic chemical gels (with permanent cross links), there is a large separation of scales [6, 11] between the limit of validity of linear elasticity (giving the upper bound of the process zone), and the scale at which dissipation occurs (see Fig.1.7). Weak nonlinearities can start being relevant at $100 - 200\mu m$ from the crack tip while dissipation and irreversible processes occur only within $10\mu m$ from the tip. As a material undergoes some nonlinear processes before being irreversibly damaged, Livne & *al* together with Buehler [12] stressed the importance of understanding the effect of nonlinear elasticity to capture how the energy is transferred from large LEFM scales to the small scale at which damage occurs. Understanding the role of nonlinear elasticity with respect to damage processes is one of the objectives of this work.

Choice of the soft material class. Chemical gels used by Fineberg are not good candidates for our study. Indeed, as chemical gels fail by

chain scission, one does not expect much structural damage and the observed weakly rate-dependent fracture properties are mainly attributed to the chain/solvent viscous coupling at the high velocities investigated here.

In elastic physical gels, crosslinks fail at lower stresses, so that greater microscopic damage and rate-dependency can be expected while conserving a similar separation of scale. For this class of materials, we think we will have a unique opportunity to bridge the information collected at the different scales and to disentangle both nonlinear elasticity and rate-dependent dissipation occurring in the process zone.

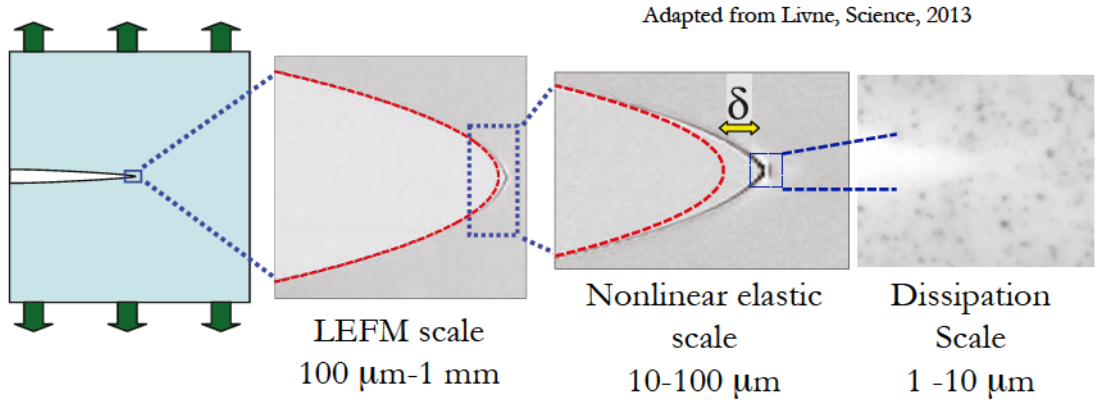


Figure 1.7: A crack tip magnified at different lengthscales. Far from the crack tip, the material is in its linear elastic regime: the crack profile can be captured by LEFM (red dashed line). Weak nonlinearities can start being relevant 100 – 200 μm from the crack tip. The crack profile departs from the LEFM prediction. Dissipation and irreversible processes occur only within 10 μm from the tip. From [11]

Our approach. To do so, we designed a novel experimental device to study crack propagation in such soft materials (Chapter 2). This experiment enables us to grow a single crack in a controlled way in a soft specimen and to look at the crack tip at high magnification in a wide range of crack velocities. Working on physical polymer gels (Chapter 3), we analyzed the crack shape and crack displacement fields (using Digital Image Correlation) at large and intermediate scales for various velocities (Chapter 4). We figured out there was a separation of scales between the scale at which LEFM applies, the scale at which elastic nonlinearities emerge, and the scale at which dissipation occurs (Chapter 5). For the moment, the scale at which irreversible processes occur could not be investigated in the case of the polymer gel. Recent experiments on colloidal gels, which have a microscopic length scale bigger than that of polymer gels, show that we are able to probe damage at the microstructural scale (Chapter 6).

2

Agar, a physical polymer gel.

Contents

2.1	Introduction	15
2.2	Biopolymer gel of Agar	17
2.2.1	Structure and conformation of agar chains in water	17
2.2.2	Sol-gel transition	20
2.2.3	Gel preparation	24
2.2.4	Structure of agar gels.	26
2.3	Mechanics of Agar gels	26
2.3.1	Linear elasticity of agar gels	26
2.3.2	Rate-dependent properties of agar gels	37
2.3.2.1	Viscoelasticity	37
2.3.2.2	Poroelectricity	38
2.3.2.3	Network relaxation	39
2.3.3	Nonlinear elasticity	42
2.3.3.1	Nonlinear stretching of polymer chains	42
2.3.3.2	Compression experiments	44
2.4	Conclusion	50

2.1 Introduction

Agar gels belong to the class of polymer gels and more precisely to the class of biopolymer physical networks. In water, below the gelation temperature, these polysaccharides molecules are able to form intermolecular H bonds, and to self assemble in a supramolecular structure swollen with water. The sol gel transition of this polymer/solvent system was extensively documented: nature of the transition, structural evolution, dynamics of the chains, viscoelastic properties of the gel... As physicists being interested in the mechanics of this class of material, we will review the gel properties trying to answer a double question: What are the characteristic time,

length and energy scales for these biopolymer gels? Are these sufficient to understand the rate dependency of the fracture properties of this class of materials?

Rate-dependent properties of these gels have been widely studied [13]. As this assembly is driven by low energy physical interactions, the 3-dimensional percolating structure is thermoreversible and may undergo rearrangements when submitted to stress. Depending on the time scales over which the gel properties are scanned, this system can show viscoelasticity, stress relaxation or even poroelasticity.

But fracture properties may not be fully understood by just knowing the linear mechanical properties of the material. Stress at a crack tip diverges and might induce locally very large deformation: characterization of the non linear mechanics of the gel is also essential to capture its ultimate properties.

This very simple material is the object of a huge and sometimes complex litterature. But this extensive characterization work makes this biopolymer physical gel a good candidate to gain a deeper understanding of the fracture properties of soft materials. In the coming chapter, we will try to give the reader a full but somehow simplified view of this material structure and properties. After briefly reviewing the chemical structure of agar molecules, we will see how the sol gel transition of this system influences the network topology. Doing this will enable us to build a model view of the material the fracture properties of which we want to characterize. This will also guide us practically in the way we prepare our samples, with a good control of thermal history. We will then focuss on our gel mechanical properties from linear viscoelasticity, nonlinear elasticity to failure properties.

2.2 Biopolymer gel of Agar

2.2.1 Structure and conformation of agar chains in water

Agar chemistry. Agar is typically extracted from red seaweeds (e.g., *Gracilaria* and *Gelidium*) and it contains two fractions. The fraction with the greatest gelling capability is termed agarose, which is an alternating copolymer of α -(1-4)-D- and β -(1-3)-L-linked galactose residues in a way that most of the α -(1-4) residues are modified by the presence of a 3,6-anhydro bridges. (Fig. 2.1). The other fraction, termed agaropectin, includes all of the remaining molecules with the same backbone structure as agarose. Each unit of the agar molecule has a molar mass $M = 306g.mol^{-1}$ and a size of order $1nm$. The molecular weight depends on the way agar is extracted. In our case, agar powder was supplied by Sigma Aldrich. The chain average molecular weight is $M_w = 120kg.mol^{-1}$ for about 400 agarobiose units.

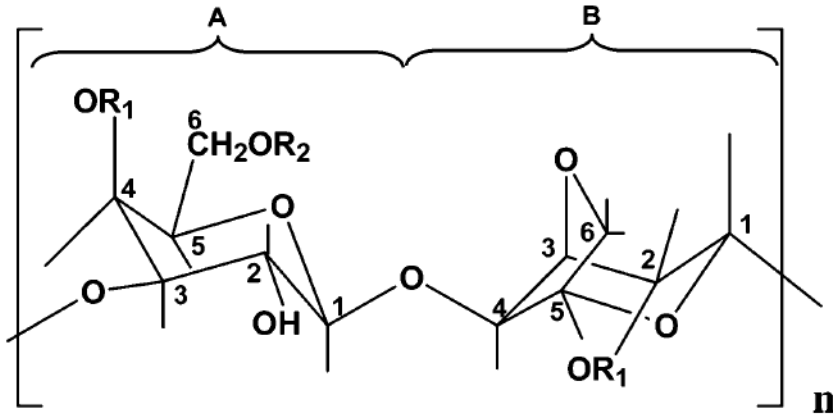


Figure 2.1: Idealized AB unit of agar molecules, ($M = 306g.mol^{-1}$). Taken from [14].

Chain Conformation in water. In water, at high temperatures, well above the gelation point ($T_{gel} = 40C$), intermolecular and intramolecular interactions are screened and agar molecules take a random coil conformation. This is what is usually called the sol state. At temperatures lower than T_{gel} , the system undergoes a coil-to-helix transition [15]: two neighbouring coils can associate through H bonds and form a left-handed double helix of $1.9nm$ pitch [16]. When this double helix is formed, -OH hydroxy groups point outwards: they can get engaged in hydrogen bonding with solvent water molecules or with a neighbouring helix. At low temperature, agar chains thus aggregate into bundles of up to 10^4 double helices [16].

A Building block for 3D network formation. Of course, association between the polymer strands is not sufficient to build a 3-dimensional network. But certain parts of the agar chain termed kinks are incompatible with double helix formation and thus lead to partner switching during association[16]. Consequently, agar molecules participate in more than one double helix and are interacting with several distinct chains. This is the elementary block for building a 3D percolating network able to sustain mechanical stress.

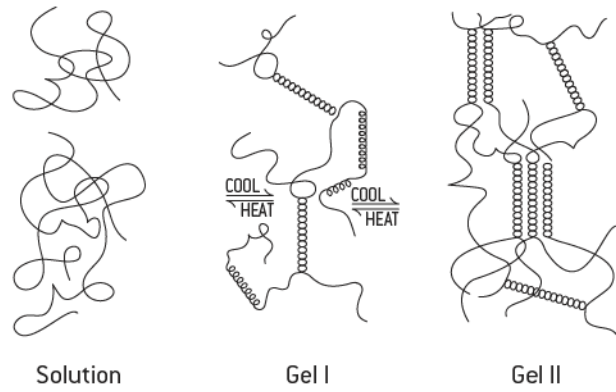


Figure 2.2: Various levels of organization: coil-to-helix transition (left) and formation of suprafibers (right).

2.2.2 Sol-gel transition

The picture of Section 2.2.1 describing network formation is simplified. In real conditions, the obtained network depends a lot on the concentration of polymer chains (usually expressed in weight concentration) and on the gel thermal history. This dependence can be somehow understood by investigating processes at stake during the sol-gel transition.

Sol-gel transition scenario. The sol-gel transition constitutes a phase change from an ergodic to a nonergodic state. In other words, agar coils undergo brownian motion in the sol while agar chains are dynamically arrested in suprafibers. The transition is summarized in Fig. 2.3 and described in Ref.[14]. When the temperature is lowered, the Brownian diffusion of the chains slows down. In the induction stage, the entanglement points of the network act as nuclei for further assembly of the fibers. In the early stage of gelation, the network is quite loose. It becomes tighter and tighter due to the aggregation of the helices into suprafibers. In the pseudo-equilibrium stage, the aggregation slows down: a few remaining dangling chains associate with the network. This state extends over an extremely long time.

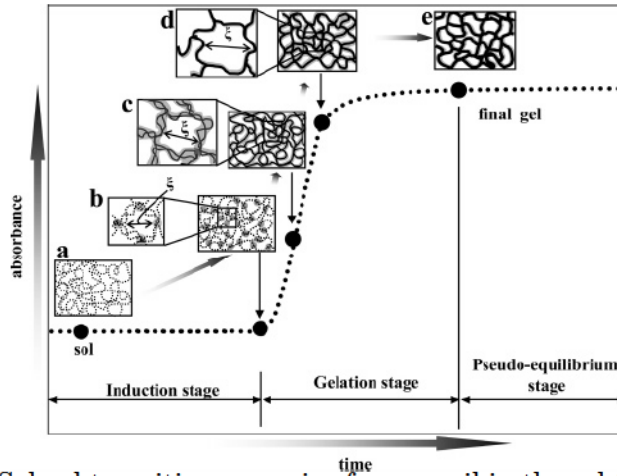


Figure 2.3: Sol-gel transition scenario: from a coil in the sol to a network of mesh size ξ . Taken from [14].

Network formation at the sol-gel transition is especially visible when measuring the material shear modulus, that is to say the material ability to sustain mechanical stress. When quenched below T_{gel} , the sol with an initial vanishing mechanical modulus experiences a sigmoidal increase of its shear modulus in the gelation stage. As the structure of the gel slowly evolves, the stiffness of the gel keeps on increasing slowly with time in the pseudo equilibrium stage (see Fig.2.4).

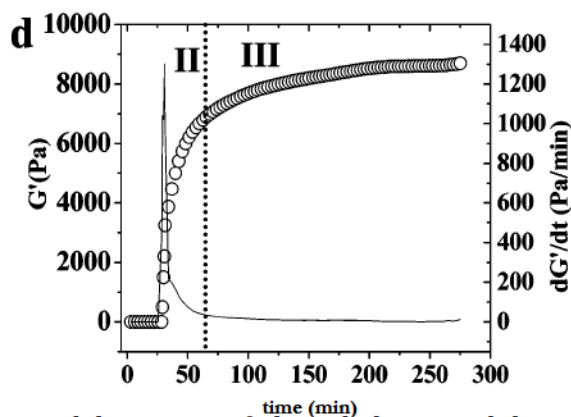


Figure 2.4: Sigmoidal increase of the gel shear modulus at the transition. Taken from [14].

Thermal history: a competition between crosslinking and demixing. The structural properties (and thus the mechanical properties) of the obtained gel result from a strong competition between two processes: demixing and crosslinking. Bulone & al [17] discussed the kinetics of the two processes with sol concentration and the quenching temperature, i.e. the temperature at which the sol is cooled down to trigger gelation.

At low to moderate agarose concentrations (up to about 1% wt), solution demixing is the first event in the sequence of processes leading to gel formation. Quenching the polymer solution in the region under the spinodal line (see Fig.2.5) causes spinodal demixion into regions of higher and lower concentrations in biopolymer. Inside the polymer-rich regions, molecular cross-linking can start. A macroscopic gel is obtained if the average concentration is large enough to enable percolation of the high concentration regions. The picture one has of the resulting gel is a collection of dense microgels elastically connected by few polymer chains.

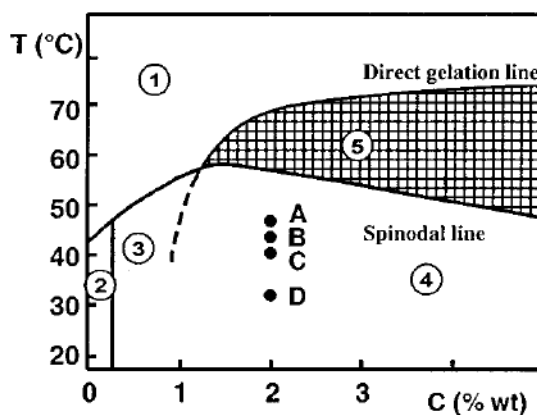


Figure 2.5: Sol-gel phase diagram. Taken from [18].

At concentrations larger than 1% wt, the chains are statistically closer to one another. Molecular crosslinking will prevail over spinodal demixing. The quenching temperature will actually tune the relative kinetics of demixing and crosslinking: very different gel structures can thus be obtained at fixed polymer concentration by changing the quenching temperature (points A,B,C and D in 2.5).

As a result, controlling thermal history is crucial to ensure reproducibility in the obtained gel. This can be easily shown with TEM images of the networks obtained with 2 different quenching temperatures (Fig. 2.6). At a quenching temperature close to T_{gel} , the system has time to demix before crosslinking happens. This result in large inhomogeneities of the network structure. At lower quenching temperatures, crosslinking is faster and inhibits demixing: the resulting network is more homogenous.

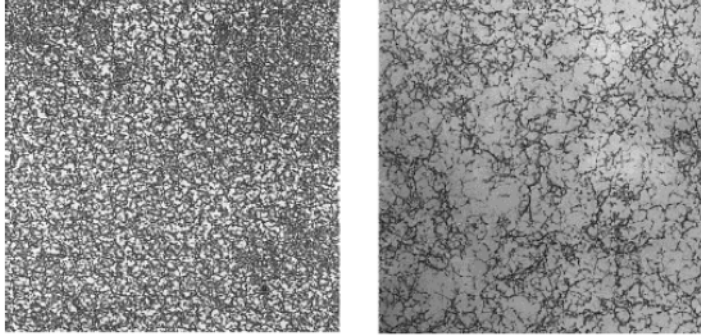


Figure 2.6: Transmission electron micrographs of 2% agarose gels formed in different conditions of thermal history: Quenching at 20 C (left) and 38 C (right). Size: $7\mu m \times \mu m$. Taken from [19].

The gelation mechanism is thus different depending on whether we work at low or high concentrations. This will be important in the discussion about the power law evolution of shear modulus with concentration.

A thermoreversible transition. Due to the very weak interaction at the origin of the network formation, the sol-gel transition of agar is thermoreversible. However, this transition shows a very large hysteresis. Again, this can be easily shown measuring the shear modulus of the gel (see Fig.2.7). The gel is submitted to thermal cycles between 20 C and 95 C. Starting from high temperature and slowly cooling the system down, the shear modulus G remains small until crossing T_{gel} where G suddenly increases. Increasing the temperature again, the gel keeps a high value of G (though slowly decreasing) until a sudden drop close to T_{melt} . The temperature T_{melt} needed for the suprafibers and helices to unbind and the network to melt is much higher than T_{gel} : $T_{melt} = 95C$. This can be easily understood: once formed and tightly packed, dissociation of these fibers is highly unlikely.

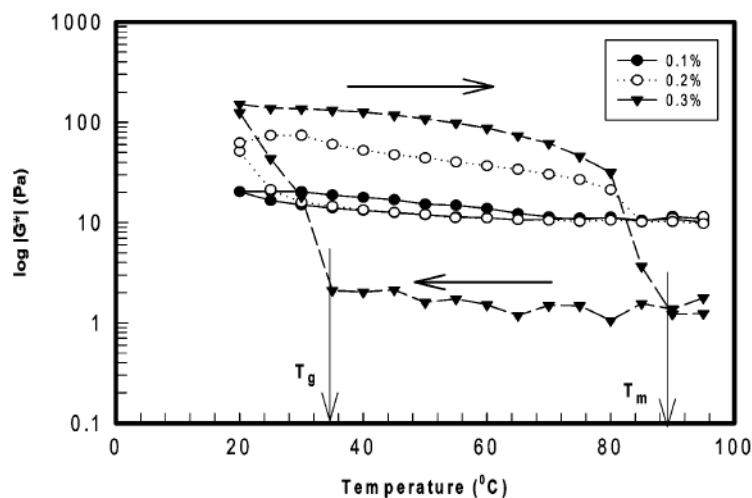


Figure 2.7: Hysteresis of gel mechanical properties when submitted to temperature cycles between T_{gel} and T_{melt} . Taken from [15].

2.2.3 Gel preparation

Preparation of sols. Agar sols are prepared by dissolving agar powder (Sigma Aldrich) in hot water. A 1.5%wt solution of agar is stirred for 1h at 95 C without any water loss. The obtained sol is then kept at 75 C overnight and used within a day. After several days, the chains showed signs of degradation, the solution taking a yellow shade. To slow this process down, we conserved the sol of agar at a temperature of 75 C, lower than the melting temperature T_m but higher than the gelation line shown in Fig.2.5. The limit of one day between the preparation of the solution and its use for experiments was a conservative value chosen to make sure that the chains had no time to deteriorate on this timescale (the yellow color typically appeared after 7 days at 75C).

Gelation procedure. As we explained in Section 2.2.2, the thermal history of the gel formation is of tremendous importance regarding the gel structure and properties. To circumvent this, we always used the same quenching procedure to cross the sol-gel transition. Starting from 65 – 70C, the temperature is decreased at a rate of 5C/min until it reaches 23C, which is well below the sol-gel temperature. This was done using a circulation of water at room temperature in a thermalized room.

2.2.4 Structure of agar gels.

In Section 2.2.1, we described the way chains interact at a microscopic scale to form the junctions. However, at a mesoscopic point of view, the length-scales characterizing the structure of agar gels are a direct consequence of the sol gel transition and of the experimental conditions for this process to occur.

What we saw in Fig.2.6 is that quenching of "high-concentration" sols at low temperature (20 C) leads to the formation of a homogenous biopolymer network with a well defined structural correlation length of order $10nm$ for a gel concentration of 2 wt%. We will see in Section 2.3.1 that this structural correlation length corresponds to the mesh size of the network and is directly related to the mechanical modulus of the gel. A question to adress is how this structural length scale evolves with polymer concentration for a given quenching procedure? Besides direct visualization with TEM, numerous techniques as turbidity measurements [14], gel electrophoresis, light scattering enables to extract structural lengthscales of the gel [14]. All of these agree on the fact that the mesh size ξ decreases when increasing the biopolymer concentration.

Junction zones composed of suprafibers are thus typically separated by a distance ξ and connected by an agar chain that is not involved in any interaction with any other chain. This chain segment of contour length Λ_{int} can be modeled as a coil with an end-to-end distance being imposed by the typical junction-to-junction distance ξ . The ratio $r = \Lambda_{int}/\xi$ will then influence the coil elasticity from ideal rubber elasticity for $r \gg 1$ to strain stiffening due to finite extensibility of the chains for $r \simeq 1$. This ratio r will be of fundamental importance to understand the gel nonlinear elasticity.

2.3 Mechanics of Agar gels

2.3.1 Linear elasticity of agar gels

Linear elasticity of gels: Theory. In this part, we investigate the gel linear elasticity. This is also studied because measuring the gel shear modulus can provide an easy access to the typical lengthscale ξ of the gel network.

Even if the physical chemistry of gels and rubbers is very different, the linear elasticity of gels can be understood in the framework of rubber elasticity. This is because, as for rubbers, the gel elasticity has an entropic origin: when stretched, chains between junctions (or between entanglements for rubbers) have an increasingly constrained conformation that decreases their entropy. This resists stretching and the chain thus behaves as a spring and wants to go back to its unstreched conformation. The idea, given by McEvoy & al[20], is that each elastically active network chain (EANC's), *i.e.* each strand being able to bear stress applied to the network, gives a contribution

of order gkT to the shear modulus. As G_{eq} is a measure of the free elastic energy stored by unit volume and that the density of EANC's is $1/\xi^3$, this provides a very simple scaling:

$$G_{eq} = gkT/\xi^3. \quad (2.1)$$

where, g is a factor of order unity which is equal to 1 for an ideal rubber. Indeed, for an ideal coil containing N monomers of length a , the gyration radius R_0 is such that $R_0^2 = Na^2$. If we impose an end-to-end vector \mathbf{R} such that $|\mathbf{R}| \ll Na$, the chain entropy can be written as:

$$S(\mathbf{R}) = -\frac{3}{2}k\frac{|\mathbf{R}|^2}{R_0^2} + cst \quad (2.2)$$

$$F(\mathbf{R}) = U - TS = \frac{3}{2}kT\frac{|\mathbf{R}|^2}{R_0^2} + cst \quad (2.3)$$

These results are true for an isolated chain submitted to a stretch. But, for gels, blob theory allows one to consider this theory as true for the strand linking two junctions at a scale smaller than ξ . Results based on Ref.[20] suggest that, for gelatin, a value of g close to unity is found, meaning that rubber elasticity applies at length scales below ξ . However, in the case of agar, it indicates a value close to $g = 20$ for the contribution of each EANC. This value $g = 20$ will be used throughout this manuscript. But, this result found in Ref.[20] is based on linear rheology measurements performed at 10% strain. We will see that contrary to gelatin, agar is at its very limit of linearity at such deformation and tends to stiffen. g could thus be lower than the claimed value but would still remain larger than unity, while it is close to unity in the case of gelatin.

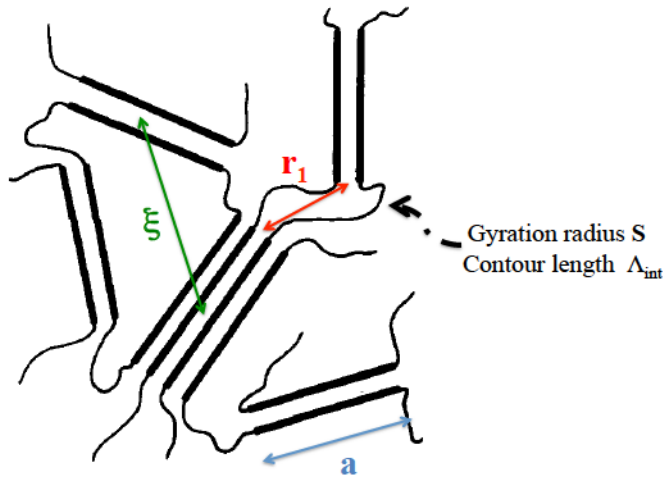


Figure 2.8: Recapitulative scheme of the mesh structure. Adapted from [21].

Why such a large g ? In Ref.[21], to take into account the size and inflexibility of junction zones, Higgs described them as rods of size a , connected by Gaussian chains with a radius of gyration S and an end-to-end distance r_1 (distance between two connected strands). The physics of the probabilistic calculation they run is very simple: for a given mesh size ξ , an increase of the junction size a decreases the gyration radius S of the coil connecting two neighbouring rods, which decreases the total number of possible conformations. They find that the Young's modulus is:

$$\begin{aligned} \frac{E}{NkT} &= 3 + \mathcal{O}\left(\frac{a^4}{S^4}\right) = 3g \quad \text{if } \frac{a^4}{S^4} \ll 1 \\ \frac{E}{NkT} &= \frac{a^2}{5S^2} + \frac{14}{5} + \mathcal{O}\left(\frac{S^2}{a^2}\right) = 3g \quad \text{if } \frac{a^4}{S^4} \gg 1 \end{aligned} \quad (2.4)$$

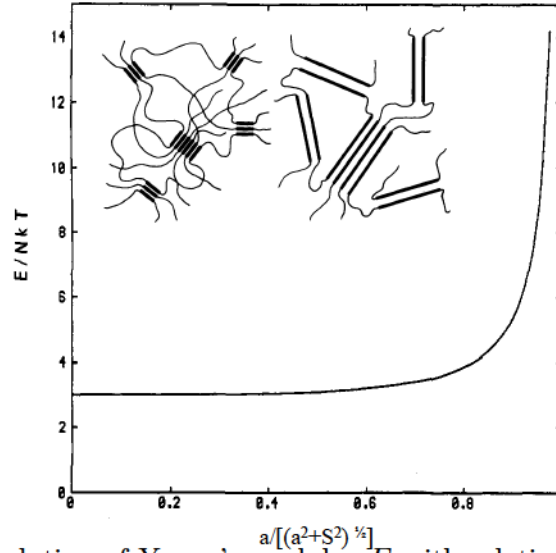


Figure 2.9: Evolution of Young's modulus E with relative rod size a for a given volume number of EANCs. Left of the insert: Case of gelatin ($a^2 \ll S^2$). Right of the insert: Case of agar ($a^2 \gg S^2$). Adapted from [21].

Fig. 2.9 shows that for a/ξ smaller than 0.75, the effect of rod size is negligible. However, for large rod sizes, E strongly increases and even diverges. Such a model of course does not hold for large a . Indeed, for such a , we would have to take into account bending of the junctions for example. Though imperfect, this simple model shows that the increase of g can be understood by an increase in the relative size of junctions compared to the mesh size. g being independent of concentration, a/S does not evolve with C and thus with ξ . This has another important consequence: when C decreases, the radius of gyration S of the connecting chains increases. Now g is known, it is possible to directly relate the equilibrium shear modulus G_{eq} to the gel characteristic length scale ξ .

Oscillatory rheology. Linear elasticity of agar gels was first characterized using small amplitude oscillatory shear using a controlled stress AR500 rheometer (TA instruments). An oscillatory shear stress $\sigma_\omega(t) = \sigma_0 \cos(\omega t)$ is imposed to the material confined within the gap of the rheometer and we measure the resulting shear strain $\gamma_\omega(t)$. In the linear regime, $\gamma_\omega(t) = \frac{\sigma_0}{|G^*(\omega)|} \cos(\omega t - \delta)$ where $G^*(\omega)$ is the complex shear modulus and $\delta = \arg(G^*(\omega))$ is the phase shift between the stress loading and the measured strain. G^* is usually decomposed as $G^* = G'(\omega) + iG''(\omega)$ where G' is the storage modulus characteristic of the elastic in-phase response, and G'' is the viscous out-of-phase response. Incidentally a purely linear elastic solid will have a $G'' \ll G'$ whereas a purely viscous liquid will have $G'' \gg G'$. Gels being solids on experimental time scales, we expect to be in the first case. We define their equilibrium shear modulus G_{eq} as their shear modulus at long times or, equivalently, as their G' for small ω .

The geometry used was a 60mm-diameter cone and plate truncated geometry. Its surface was roughened so as to prevent the gel from slipping at the boundaries. This geometry with large diameter was chosen to induce larger torques, especially at low agar concentration where the gel shear modulus vanishes. However, such an increase for the diameter induces an increase of the moment of inertia of the geometry. It implies decreasing the upper bound for pulsation to minimize the effect of inertia on our measurement at high oscillation frequencies.

The rheometer being equipped with a Peltier stage, the thermal history of gel formation can be controlled and made as close from conditions encountered during the fracture experiment. 0.6mL of sol at 65 C was poured on the rheometer stage heated at the same temperature. The temperature was then decreased at a rate of $5Cmin^{-1}$ until it reached the room temperature of 23C. The material was then left for 1 hour without doing any measurement until the material reached its pseudo-equilibrium structure. A solvent trap was used to saturate the atmosphere with water vapour and to prevent the sample from drying during the measurement.

For various agar concentrations, amplitude and frequency sweep measurements were performed.

Amplitude sweep rheology. For amplitude sweeps, the frequency of oscillation was set to 1Hz and stress amplitude σ_0 was varied between 1 Pa and 100 Pa, which are low values compared to the shear moduli in the concentration range we focused on (0.2-2 wt%). Higher stresses usually induced slippage, and loss in the quality of the measurement. We define the Linear Viscoelastic Region (LVER) of the gels, where the measured storage modulus was independent of stress. Figure 2.10 shows stress sweep experiments for different agar concentrations. It is demonstrated that, for a stress amplitude of 1Pa, each gel is in its linear viscoelastic range. This

value will consequently be chosen for the stress amplitude of the frequency sweep test.

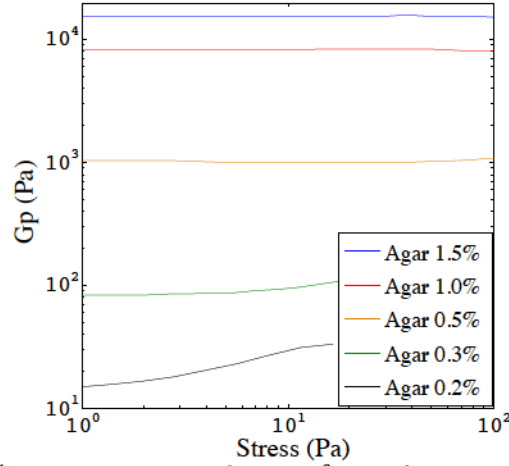


Figure 2.10: Stress sweep experiments for various agar concentration.

Frequency sweep rheology. For frequency sweep, the minimum pulsation was 0.01 rad.s^{-1} . The maximum pulsation we used was 50 rad.s^{-1} : at higher pulsation, quality of the measurements decreases due to slippage of the gel. The result of frequency sweep measurements are shown for 0.2, 0.5 and $1.5 \text{ wt}\%$ in Fig. 2.11:

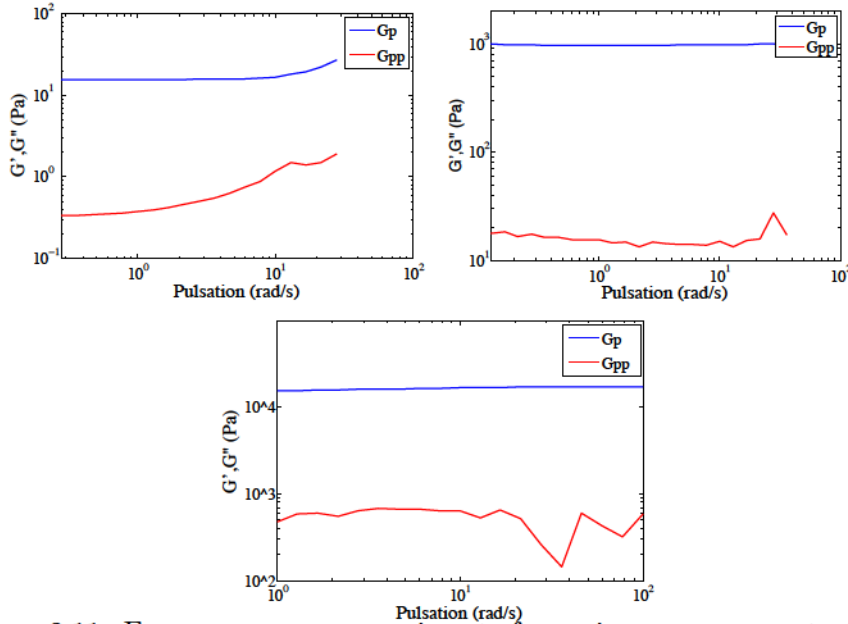


Figure 2.11: Frequency sweep experiments for various agar concentrations. Top Left: $C = 0.2 \text{ wt}\%$. Top Right: $C = 0.5 \text{ wt}\%$. Bottom: $C = 1.5 \text{ wt}\%$.

At every concentration, we have $G' \gg G''$ which confirms that, in this frequency range, the mechanics of these gels is the one of an elastic solid. High concentrations exhibit relatively low rate-dependency of both elastic and viscous properties. This means that the physical interactions holding the chains together in the junctions can be considered as permanent crosslinks over this time scale. At 0.2wt%, high frequency oscillations induce higher dissipation. In the framework of entangled polymer dynamics, this increase in dissipation is due to the Rouse relaxation of chains between the junction zones. The corresponding relaxation time scales as $\tau_e = \tau_0 N_{int}^2$, so that $\omega_e \propto 1/N_{int}^2$ decreases when N_{int} increases *i.e* when the gel concentration C decreases. This is why this relaxation process is not visible at high concentration in our frequency range but starts being perceptible at low concentrations.

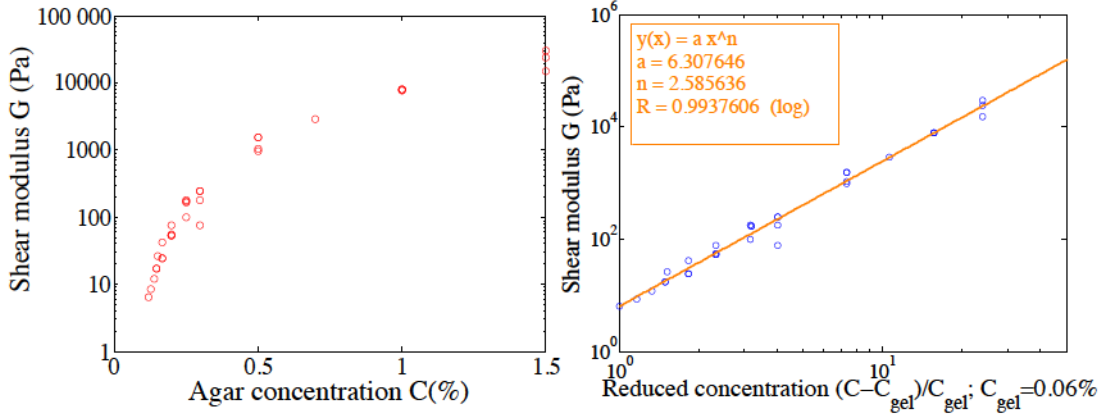


Figure 2.12: *Left*: Evolution of shear modulus versus agar concentration. *Right* Shear modulus versus reduced concentration $\frac{C - C_{gel}}{C_{gel}}$. The best fit is obtained for $C_{gel} = 0.06\%$ wt, close to the value 0.1% found in [13].

Concentration dependence of the gel shear modulus. To measure G_{eq} , a value of $\omega = 1 \text{ rad.s}^{-1}$ was chosen and G' was measured at this pulsation for each concentration. This equilibrium value is plotted as a function of the agar concentration C in Fig. 2.12 (left). As expected, there exists a concentration C_{gel} below which the polymer network does not percolate. At C_{gel} , the polymer network percolates, and the obtained gel has a vanishing shear modulus G . Above $C = C_{gel}$ the mechanical modulus of the gel increases continuously and rapidly with the polymer concentration. The sol-gel transition, as any percolation transition, is a 2nd order phase transition. Its control parameter is the relative distance to the percolation threshold and a power-law behavior is expected for G above the critical concentration. In our case, the distance to the percolation threshold writes $C_r = \frac{C - C_{gel}}{C_{gel}}$ and we expect $G \propto C_r^t$ where t is the critical percolation exponent. t is expected

to be $t_s = 1.98$ for a scalar elasticity percolation model and $t_v = 3.5 - 4.5$ for a vector elasticity model [22]. G is thus plotted versus C_r with different choices for the critical concentration C_{gel} chosen around $0.1wt\%$, which is a value commonly found in literature [13].

The optimal fit we could get is shown in Fig. 2.12. It is obtained for $C_{gel} = 0.06wt\%$ and gives $t \simeq 2.58$. We think that, in our concentration range, we lie in a crossover region in between the scalar and vector elasticity models and we thus observe an effective percolation exponent lying between t_s and t_v . Similar crossover was found in Ref. [22].

Let us now come back to the elastic length scale ξ . Thanks to Eq.(2.1), we are indeed able to relate G and the corresponding ξ . Knowing the prefactor $g = 20$ for agar gels, we show the evolution ξ versus G in Fig. 2.13.

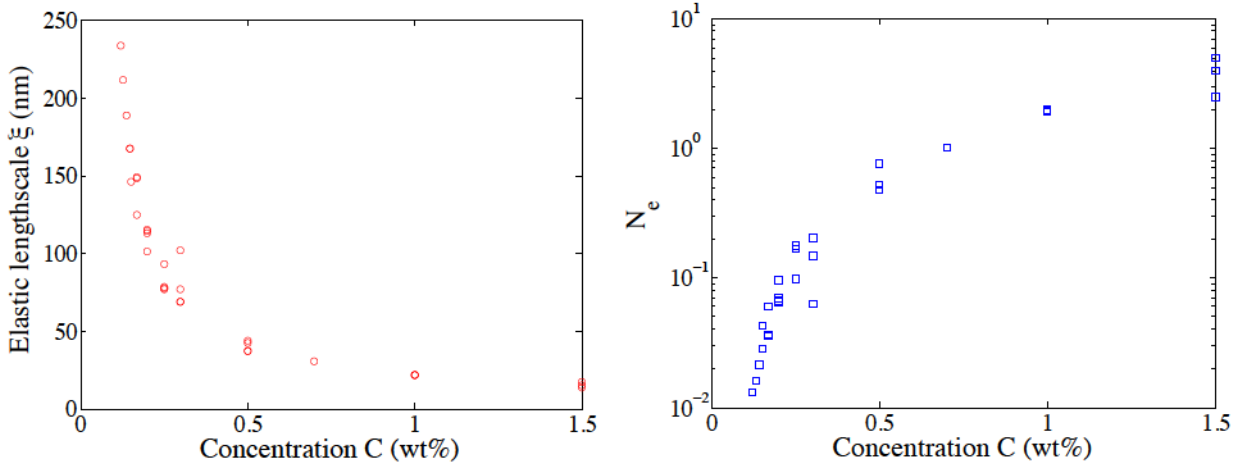


Figure 2.13: *Left* Decrease of the elastic length scale ξ with the concentration C . *Right* Evolution of the number of Elastically Active chains EANC's per primary chains with the concentration C .

For a $1.5wt\%$ concentration, ξ is around $15nm$ while it can reach $0.25\mu m$ for the lower concentrations we could reach. Even at the lowest concentration, the elastic length scale is a scale that cannot be observed with standard microscopy. However, this scale will be important to understand the mechanics of our gel.

In Eq.(2.1), $1/\xi^3$ is ν_e , the number of Elastically Active chains (EANC's) per unit volume. We previously saw that a polymer chain of agar could be involved in several junctions. We want to compute N_e , the number of EANCs per chain. To do so, we define V_{mol} as the volume of solvent per mole of polymer chains in solution prior to gelation. Knowing the molecular weight M_w of the chains and concentration C , we have $V_{mol} = M_w/C$ and

thus:

$$\nu_e = \frac{\mathcal{N}_A N_e}{V_{mol}} = \frac{\mathcal{N}_A N_e C}{M_w} \quad (2.5)$$

In Eq.(2.5), N_e is unknown, but using $1/\xi^3 = \nu_e$ enables to see how N_e evolves with concentration. In the right part of Fig.2.13, N_e starts from values of order 10^{-2} at low concentration but can reach values of order unity or more at high C . The values lower than $N_e = 1$ for concentrations below $C = 1\%wt$ mean that only some fraction of the chains contributes to the the macroscopic elasticity of the network. This is consistent with the picture of loosely connected microgels we described in Section 2.2.2. For $C > 1\%wt$, N_e is larger than unity meaning that each chain contributes to the network elasticity. At the maximum concentration we have investigated ($C = 1.5\%wt$), each agar chain is statistically involved in 2 junctions.

2.3.2 Rate-dependent properties of agar gels

Rate-dependent phenomena can be of various origins in such physical networks swollen with solvent. They can be separated into 3 classes:

- Poroelasticity: Long-range flow of solvent in a fixed network
- Viscoelasticity: Short range conformational changes of the polymer chains coupled with viscous solvent.
- Network relaxation: lifetime of the non-permanent physical crosslinks.

2.3.2.1 Viscoelasticity

We will see that viscoelasticity depends only on intrinsic timescales of the gel whereas poroelastic time scales depend also on the typical experiment duration. We thus briefly recall results from Section 2.3.1 concerning linear viscoelasticity. As we mentioned sooner, rheology experiments performed at 23°C in the $0.1 - 100 \text{ rad.s}^{-1}$ range did not show rate-dependency of both storage and loss moduli except for low concentrations. This means that on the corresponding time scales, junctions can be considered as permanent and inter-junctions chains are fully relaxed. Here follows the typical master curve of an entangled polymer taken from [23]. We expect a similar qualitative behavior between entangled polymer and physical gels by considering junction zones as entanglement points.

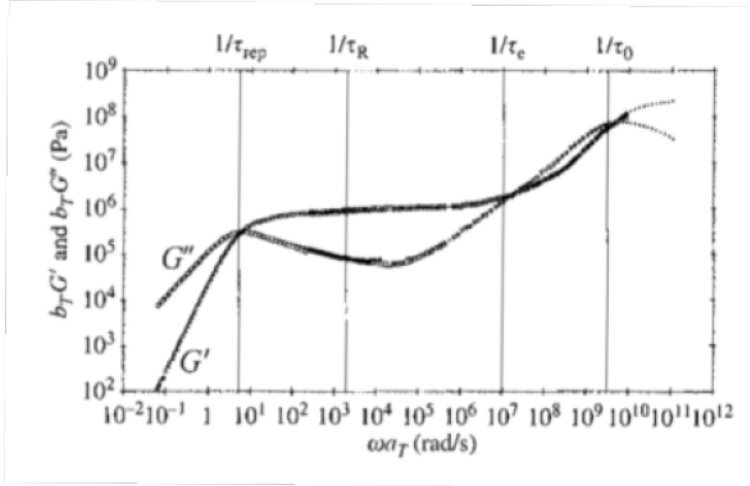


Figure 2.14: Master curve from oscillatory shear data for entangled polymer chains. Taken from [23].

In this diagram, we will come back later on the meaning of τ_{rep} . What we should notice now is that there exists a large range of pulsations lying between $\omega_{rep} = 1/\tau_{rep}$ and $\omega_e = 1/\tau_e$ where both G' and G'' slowly vary

with ω . This is where our measurements stand. What we already explained for the 0.2wt% shear data is that, for large interjunction strands (low gel concentration), ω_e decreases and enters into our experimental range. Looking at the viscoelastic spectrum for a 0.2wt% gel (Fig.2.11), we find that the pulsation ω_e at which $G'(\omega)$ and $G''(\omega)$ cross each other can be estimated to be $\omega_e = 100 \text{ rad.s}^{-1}$. This crossing point gives a measure of the Rouse relaxation time of the interjunction chain ($\tau_e(N_{int}) = \tau_0 N_{int}^2$) [23]. This means that the viscoelastic time τ_e of the strands between junctions is smaller than 10^{-2} s for $C \geq 0.2 \text{ wt}\%$.

2.3.2.2 Poroelasticity

A gel is a network of chains of typical mesh size ξ swollen by a good solvent. When compressing a cylinder of gel of diameter d , two things can happen simultaneously. At short times, the solvent does not have time to flow through the porous-like network of permeability $\kappa \propto 1/\xi^2$: the gel can be considered as incompressible. At long times though, large scale motion of the solvent relative to the network has time to occur: the material behaves as a sponge and releases its solvent, it is poroelastic [24]. While viscoelasticity is characterized by τ_v , poroelasticity is characterized by the effective diffusivity $D = \frac{G\kappa}{\eta_s}$ of the solvent in the network. We thus can define a typical length scale $\ell_p = \sqrt{D\tau_v}$ over which the solvent has time to move over the timescale τ_v . The relevance of poroelasticity depends on the experimental lengthscale L (size of the cylinder in compression experiments or specimen thickness in a fracture experiment) and the time scale t of the measurement. L^2/ℓ_p^2 and t/τ_v are the relevant parameters.

τ_v being smaller than 10^{-2} s , our material is always relaxed in terms of viscoelasticity. For a 1.5wt% gel, D is of order $10^{-10} \text{ m}^2.\text{s}^{-1}$, thus $\ell_p \simeq 1 \mu\text{m}$ (taking the upper bound 10^{-2} s for τ_v). For the crack experiment, L is of order of $300 \mu\text{m}$. The poroelastic time is so $\tau_p = L^2/D = 1.5 \cdot 10^3 \text{ s}$. The material is consequently unrelaxed regarding poroelasticity and can be considered as incompressible.

2.3.2.3 Network relaxation

Network relaxation is the ability of the network to flow when submitted to low stresses for very long experimental time scales. This flow is made possible by the transient nature of the weak physical interactions governing the network formation. Fig.2.14 indeed shows a crossover of G' and G'' at $\omega_e = 1/\tau_{rep}$ and a liquid-like response for lower pulsations. In our experiments, we were not able to see any relaxation at low pulsation. In theory, it is possible to lower the minimum value of ω but such experiments take a long time and enhance the potentiality of error (due to drying for example). In Ref. [16], Labropoulos & al used the time-temperature superposition

principle to circumvent this issue. If a relaxation process occurs over very long time scales, an increase of temperature decreases the relaxation time of the chains which makes it measurable at higher pulsations. What makes the data taken at different temperatures superimposable is the fact that all the relaxation modes of the polymer chains have the same temperature dependence. After choosing a reference temperature T_0 , the oscillatory data obtained at a temperature T can thus be easily rescaled onto a master curve with horizontal α_T and vertical b_T shift factors given by:

$$\alpha_T = [\tau_i]_T / [\tau_i]_{T_0} \quad (2.6)$$

$$G'(\omega, T) = \left(\frac{T}{b_T T_0} \right) G'(\alpha_T \omega, T_0) \quad (2.7)$$

Fig. 2.15 shows data on agar gels taken from Ref. [16].

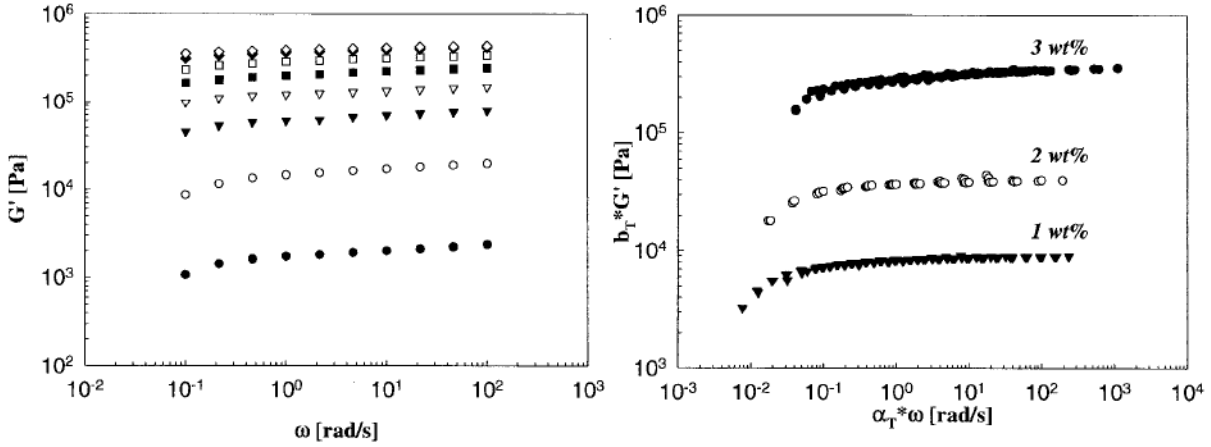


Figure 2.15: *Left:* Storage modulus G' vs ω of a 3 wt% agar gel for different temperatures (26 to 40C top to bottom). *Right:* Master curves obtained for 1, 2 and 3 wt%. Reference temperature $T_0 = 30C$. Taken from [16].

On the left subfigure, we see that increasing the temperature lowers the storage modulus and allows the capture of stress relaxation at a reasonable pulsation (0.5 rad.s^{-1}). At the reference temperature, ω_e is one order of magnitude smaller. At temperature corresponding to our experimental conditions, ω_e would be about $5 \cdot 10^{-3} \text{ rad.s}^{-1}$: the network relaxes on times scales of hours under small stresses. In a very naive Arrhenius model, we can write that the bond breaking rate ν is:

$$\nu = \nu_0 \exp \left[\frac{-(U-fa)}{kT} \right] \quad (2.8)$$

$$\text{where } \nu_0 = \frac{kT}{\eta_s a^3} = 4 \cdot 10^{10} \text{ s}^{-1} \quad (2.9)$$

with U being the binding energy and f the force exerted on the chain. Neglecting the bias due to imposed stress i.e setting f to $0N$ gives a binding

potential U of order $30kT$ i.e $0.7eV$. This is consistent with the typical order of magnitude of energy for a few H bounds (0.1eV per bond) and with bond energies found in Ref. [25]. Indeed, in [16], it is mentionned that three of the four hydroxy groups from the 3,6-anhydrogalactose are pointing outwards and are engaged in hydrogen bonding with the bulk water molecules or neighboring helices. As we neglected the imposed stress, the obtained value is a lower bound for U . The effect of imposed stress may be seen in the right panel of Fig.2.15. Indeed, for the 3 concentrations, these tests were performed at fixed strain . As a result, the stress imposed on the network increased with concentration, which may be the explanation for the shifting of the network relaxation towards larger frequencies.

2.3.3 Nonlinear elasticity

When gels are used in practice, their large-strain characteristics are far more relevant than the small-deformation ones. This is especially true for crack propagation. High stresses at the crack tip (even "infinite" stresses in theory) induce very large strains in the vicinity of the tip. It is known that the stress/strain relationship for all networks composed of semiflexible filaments is nonlinear, and in the case of stiffer filaments such as collagen, they always stiffen for strains lower than 20% [26].

2.3.3.1 Nonlinear stretching of polymer chains

In the affine assumption, i.e. when each polymer is stretched by the same amount, both linear elasticity and nonlinear strain-stiffening in gels can be understood on the single molecule level. Within this approach, when a stretch ratio $\lambda = 1 + \epsilon$ is applied to the network, the chain end-to-end distance in the cross-linked network is $R = \lambda\xi$ where ξ is the equilibrium average distance between cross-links. Λ_{int} is the average contour length of polymer segments between two neighboring junctions. The free configuration of this polymer segment has a mean end-to-end distance S .

The observed stiffening results from the collapse of the small strain hypothesis ($|\mathbf{R}| \ll Na = \Lambda_{int}$) made for computing Eq.(2.1) and Eq.(2.3). Indeed, if we relax this hypothesis and calculate the partition function of the stretched chain linking two junctions (this chain has a contour length Λ_{int} , see Fig.2.8), one finds that for a given stretching force f , the average end to end distance is [23]:

$$\langle R \rangle = Na \left[\coth\left(\frac{fa}{kT}\right) - \frac{kT}{fa} \right] \quad (2.10)$$

At small f , we recover gaussian elasticity with spring constant $\frac{3kT}{S^2}$. At large f or, equivalently, $|\mathbf{R}| \simeq Na = \Lambda_{int}$,

$$\langle R \rangle = Na \left[1 - \frac{kT}{fa} \right] \quad (2.11)$$

$$\text{and thus : } \frac{fa}{kT} \simeq \frac{\Lambda_{int}}{\Lambda_{int} - |\mathbf{R}|} \quad (2.12)$$

In this framework of the freely jointed chain, which only takes into account the entropic reduction due to imposed R , the force diverges at large f . For such f , one potentially needs to consider other deformation modes: bending and eventually stretching. The worm-like-chain model (WLC) takes into account the bending modes of the units. One introduces l_p , the persistence length quantifying the stiffness of a polymer. When $l_p \ll \Lambda_{int}$, a polymer is

flexible; when $l_p \gg \Lambda_{int}$, a polymer is very stiff, i.e. rod-like. Semiflexible polymers are such that $l_p \simeq \Lambda_{int}$. The relationship between l_p and Λ_{int} also determines mean-square end-to-end distance of a free WLC as:

$$S = \langle \mathbf{R} \rangle^2 = 2l_p\Lambda_{int}[1 - l_p/\Lambda_{int}(1 - e^{-\Lambda_{int}/l_p})] \quad (2.13)$$

and the force f to keep the end-to-end distance of a WLC at R may be written as:

$$\frac{fl_p}{kT} \simeq \left(\frac{1}{4(1 - |\mathbf{R}|/\Lambda_{int})^2} - \frac{1}{4} + \frac{|\mathbf{R}|}{\Lambda_{int}} \right) \quad (2.14)$$

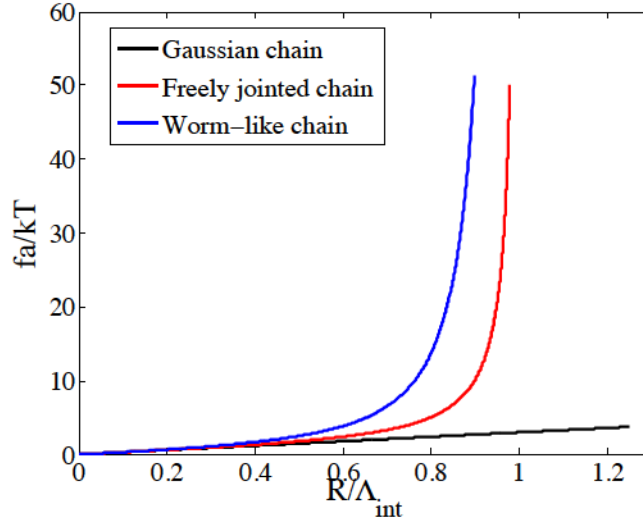


Figure 2.16: Chain elasticity in the Gaussian model (black), freely jointed chain model (red) and the Worm-like chain model (blue).

Whatever the theory chosen to model the chain mechanics, finite extensibility of the connecting chains induces a strong increase of the force stretching the polymer chains. Such forces are not sufficient to induce a chain scission of the strands ($U_{covalent} > 100kT$) but may be large enough to cause the unwinding of the junctions and the failure of the network.

2.3.3.2 Compression experiments

In the case of agar gels, which tend to slip at the walls, a characterization of their nonlinear mechanics by shear experiments is not the best way to proceed. Compression of cylindrical samples is a very common way to investigate the effect of large deformations on compliant materials. The experimental geometry is shown in Fig. 2.17. A cylinder of gel (height $h_0 = 12\text{mm}$, section $S_0 = 78\text{mm}^2$) is compressed between two glass plates, the upper one being mounted on an Instron load cell moving down at crosshead speed V and being able to measure forces F up to 10N . The nominal stress $\sigma_N = \frac{F_{meas}}{S_0}$ is then plotted with compression stretch $\lambda = 1 + \frac{\Delta h}{h_0}$.

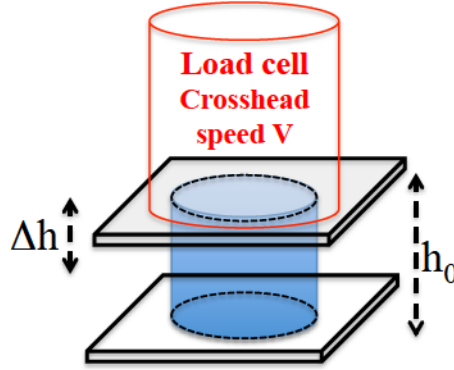


Figure 2.17: Schematic of uniaxial compression experiments.

Hall & al [27] were one of the first to point out agar nonlinear stress/strain relationship. They compared it with the stress/strain relationship of gelatin which is known to be a material for which rubber elasticity applies up to very large strains. Figure 2.18 shows their results for agar and gelatin gels having similar Young's moduli.

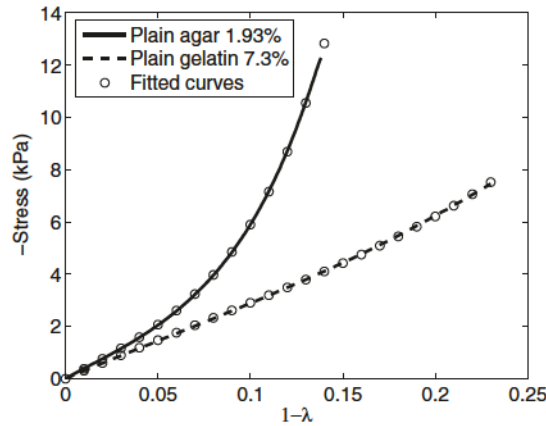


Figure 2.18: Stress/strain relationship for agar and gelatin gels. From [27].

While gelatin has a nearly linear stress/strain relationship in compression, agar has a very nonlinear response and departs from linear behavior for strains larger than a few percents. This means that the Young's modulus, defined for small strains, is not sufficient to understand the nonlinear behavior of the materials we are dealing with. In Section 2.3.3.1, forces and stresses were calculated at the chain level, which enabled one to understand from a microscopic point of view why the material showed such nonlinear stiffening. But such arguments are not sufficient to build new constitutive laws and to compute actual stresses in a material experiencing complex loading. To interpret experiments of cylindrical compression where we go beyond linear elasticity, one needs first to introduce a specific formalism to measure large deformations and second, to compute the corresponding stresses using the appropriate constitutive laws.

Defining strain and stress at large deformation. Here are the key ingredients in the modeling of nonlinear mechanics of such gels. Let us introduce:

X_i which locates points of interest in the undeformed configuration.

x_i which locates points of interest in the deformed configuration (also named current configuration).

$u_i(\mathbf{X})$ is the displacement field between undeformed and deformed configuration. We have:

$$x_i = X_i + u_i \quad (2.15)$$

Strains are computed using \mathbf{F} , the deformation gradient tensor defined by:

$$F_{ij} = \frac{\partial x_i}{\partial X_j} = \lambda_{ij} = \delta_{ij} + \frac{\partial u_i}{\partial X_j} \quad (2.16)$$

We then compute $C = F^T F$, the right Cauchy Green Tensor, which enables to measure the change of length from the reference to deformed configurations.

$$C_{ij} = F_{ki} F_{kj} = \lambda_{ki} \lambda_{kj} \quad (2.17)$$

This symmetric tensor has three invariants that are frequently used in constitutive laws:

$$I_1 = \text{tr}(C) = \sum \lambda_i^2 \quad (2.18)$$

$$I_2 = \frac{1}{2}[(\text{tr}(C))^2 - \text{tr}(C^2)] = \sum \lambda_i^2 \lambda_j^2 \quad (2.19)$$

$$I_3 = \det(C) = \prod \lambda_i^2 \quad (2.20)$$

Strain tensors and their invariants enable scientists to write constitutive work functions $U(I_1, I_2, I_3)$ for each material. U is the density of elastic energy contained in the material with a deformation state characterized by the values (I_1, I_2, I_3) . I_n depends on λ_{ij} in the specific test geometry.

U being defined, different stresses can be computed, depending on if they are computed in the reference or deformed configuration. For example, the first Piola-Kirchhoff stress tensor P , is computed from forces expressed in the deformed configuration divided by surfaces in the reference configuration. The nominal stress $\sigma_N = P^T$ is:

$$\sigma_N{}_{ij} = \frac{\partial U}{\partial \lambda_{ij}} = \frac{\partial U}{\partial I_n} \frac{\partial I_n}{\partial \lambda_{ij}} \quad (2.21)$$

In the case of compression of cylindrical specimens with a stretch ratio $\lambda < 1$, we thus have, due to cylindrical symmetry and incompressibility:

$$\mathbf{F} = \begin{vmatrix} \lambda & 0 & 0 \\ 0 & 1/\sqrt{\lambda} & 0 \\ 0 & 0 & 1/\sqrt{\lambda} \end{vmatrix} \quad (2.22)$$

hence:

$$\mathbf{C} = \begin{vmatrix} \lambda^2 & 0 & 0 \\ 0 & 1/\lambda & 0 \\ 0 & 0 & 1/\lambda \end{vmatrix} \quad (2.23)$$

$$I_1 = \lambda^2 + 2/\lambda = C_{11} + 2/\sqrt{C_{11}} \quad (2.24)$$

$$I_2 = 2\lambda + 1/\lambda^2 = 2\sqrt{C_{11}} + 1/C_{11} \quad (2.25)$$

$$I_3 = 1 \quad (2.26)$$

Neo Hookean versus exponentially stiffening models. The simplest non linear model for soft materials is the neo-Hookean model. It assumes that entropic elasticity is still valid at large deformation. The neo-Hookean work function is:

$$U = U(I_1) = \frac{\mu}{2} I_1 \quad (2.27)$$

$$2 \frac{\partial U}{\partial I_1} = \mu \quad (2.28)$$

$$N_{11} = \mu \left(\lambda - \frac{1}{\lambda^2} \right) \quad (2.29)$$

Therefore, for an incompressible solid, the only physical parameter is the linear shear modulus μ .

A very common model for biopolymer networks, taking account the strong stiffening at large deformation, is the exponential stiffening model which gives:

$$U = U(I_1) = \frac{\mu J_m}{2} [e^{\frac{I_1-3}{J_m}} - 1] \quad (2.30)$$

$$2 \frac{\partial U}{\partial I_1} = \mu e^{\frac{I_1-3}{J_m}} \quad (2.31)$$

$$N_{11} = \mu (\lambda - \frac{1}{\lambda^2}) e^{\frac{I_1-3}{J_m}} \quad (2.32)$$

where μ is the small strain shear modulus and J_m is a parameter characterizing the nonlinear regime and which is a measure of the typical strain at which the chains reach their finite extensibility. This exponential stiffening model is very commonly used because it implies few free parameters compared to the Generalized Neo Hookean or Ogden models. Figure 2.19 shows σ_N versus $1 - \lambda$ for neo Hookean and exponentially stiffening materials with $\mu = 20kPa$ and $J_m = 0.05$. If we compare Fig.2.18 and 2.19, we see that neo-Hookean model is adequate for gelatin while an exponential stiffening model suits well the agar gels.

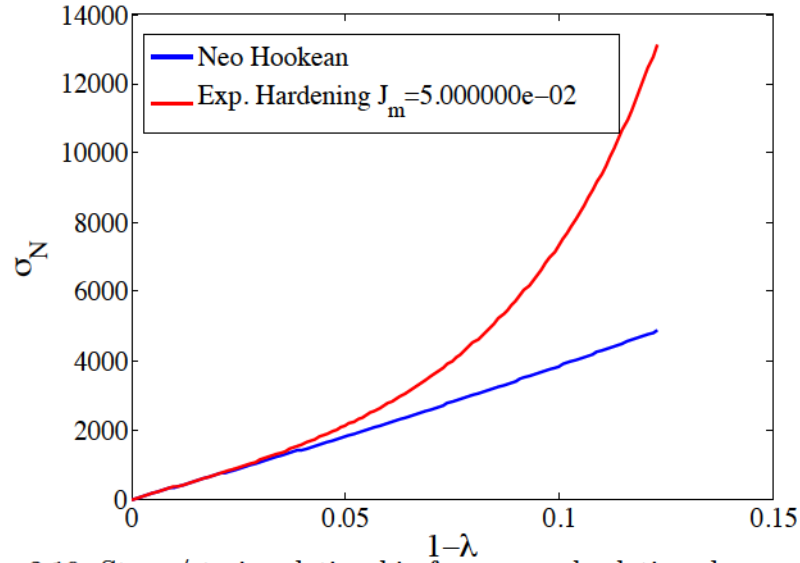


Figure 2.19: Stress/strain relationship for agar and gelatin gels, respectively good examples of exponential hardening and neo-Hookean materials.

A first observation of the dependence of nonlinear behavior with the gel concentration had already been demonstrated [28]. They were not interested in agar non linear properties but showed stress/strain measurements for agar gels of concentrations ranging from 0.5wt% to 3wt% for nominal strains smaller than 10%. It seems that the more concentrated the gel, the earlier

the material departs from its vanishing-strain linear behavior. In other words, the non linear parameter J_m used to describe these measurements with exponentially stiffening models, is decreasing with concentration. For three concentrations in the experimental range we explored, we use Eq. (2.32) and the shear moduli measured by Hall and try to find J_m that best matches the data shown in Fig. 2.20. Results are shown on the right subfigure of 2.20.

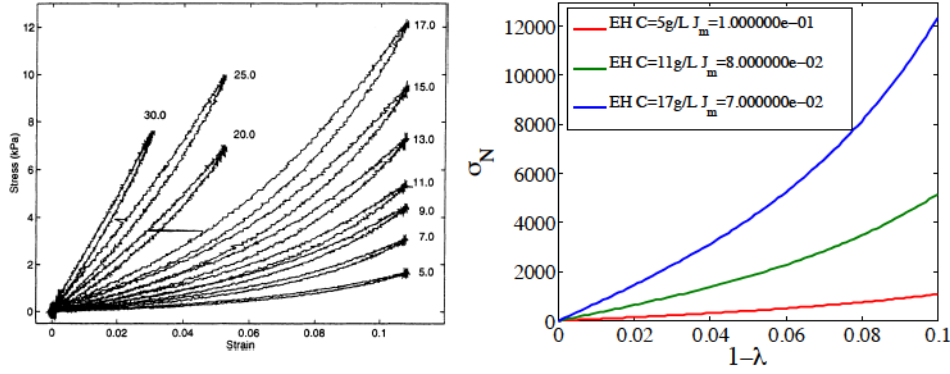


Figure 2.20: Left: Stress/strain relationship for agar gels with varying agar concentrations between $5g.L^{-1}$ (0.5wt%) and $30g.L^{-1}$ (3wt%). Taken from [28]. Right: Evolution of J_m used to match the data by Hall & al [28] for 3 different concentrations.

This confirms the weak decrease of J_m with concentration in this experimental range. At 0.5wt%, $J_m = 0.1$ corresponds to a characteristic strain $\gamma_{nl} = 5\%$. For 1.7wt%, $\gamma_{nl} = 3\%$. This evolution of J_m with concentration is due to the decrease of Λ_{int} when increasing C .

2.4 Conclusion

In the introduction, we have emphasized on the potential interest of physical polymer gels. We have focused on agar gels, whose properties are broadly referenced due to their numerous applications in microbiology and food industry. We summarize here the main characteristics that a complete review coupled with extra experiments revealed about these gels:

- Agar molecules have a contour length $\Lambda = 400nm$. In water, at low temperature, these molecules interact with each other by forming bundles of double helices called junctions. Due to partner switching in the junction, this self-assembly process eventually leads to the formation of a 3D physical network.
- When quenching a hot sol below $T_{gel} = 40C$, the sol-gel transition of agar occurs and the obtained gel structure and properties result from a competition between spinodal demixing and physical cross-linking. At low concentration, the gel can be viewed as a heterogenous assembly of loosely-connected dense microgels. At high concentration (above $C = 1wt\%$), the gel has a homogenous structure, the mesh size and the elastic modulus strongly depends on the sol quenching procedure and each chain contributes to macroscopic elasticity ($N_e \simeq 1$).
- The linear and nonlinear elastic properties of this 3D network can be understood using an affine model. The network can be viewed as stiff rods of size a (the junctions) connected by flexible segments. In the linear regime, the small-deformation elasticity ($R \ll \Lambda_{int}$) is driven by the entropy of the connecting segments. Non linear elasticity and exponential stiffening can be accounted for by considering the semiflexibility of the rods at high forces.
- The gel poroelasticity can be neglected (at high concentrations at least) and the gel is thus assumed to be incompressible. On the experimental time scales we have considered, the gel viscoelasticity can also be neglected as long as $C > 1wt\%$: the Rouse relaxation time $1/(\tau_0 N_{int}^2)$ of the connecting segments is indeed $10^{-5}s$ or shorter and the connecting segment is therefore fully relaxed. In this concentration range, it will be shown that bulk viscoelastic dissipation can be neglected and thus, that all the dissipative processes are due to structural damage confined in the process zone.
- Our gel being physical, the crosslinks can be thermally-activated or stress-activated. The typical bonding energy are the one of multiple H-bonds. Network relaxation at vanishing stress occurs on timescales of order 10^3s , which corresponds to typical interactions of order $30kT$.

Most of the experiments and results we show in this manuscript are conducted with 1.5wt% agar gels. At lower concentrations, nonlinear elasticity, viscoelasticity and even poroelasticity could enter into account simultaneously, thus making the experimental observations harder to interpret. For 1.5wt% agar gels, the material is considered to be incompressible; the Young's modulus is $E = 60kPa$. Under vanishing stress, this elastic network can show stress relaxation over timescales longer than an hour; no high-frequency bulk viscous dissipation will be considered. Additionally, this elastic solid behaves strongly nonlinearly as soon as strains go beyond a few percents: it behaves as an exponentially hardening solid with $J_m = 0.05$.

3

Fracture of Soft Materials

Contents

3.1	Fracture of soft materials: a short review	54
3.1.1	Probetack or extensional experiments	59
3.1.2	A tensile test for soft materials	61
3.1.3	Fracture in Hele Shaw geometries	64
3.2	A new experiment for fracture of soft materials	67
3.2.1	Specification list for our experiment	67
3.2.2	Toward a "on-a-chip" mechanical test	69
3.2.2.1	Choice of the appropriate fabrication technology	70
3.2.2.2	Initiation of a unique crack	72
3.2.2.3	Controlling the direction of crack propagation	75
3.2.2.4	Controlling mechanical boundary conditions	78
3.3	Design of our on a chip mechanical test	81
3.3.1	Chip geometry	81
3.3.2	Chip fabrication	85
3.3.2.1	Soft lithography	85
3.3.2.2	Microfluidic Stickers	87
3.3.2.3	Acrylamide grafting of NOA and glass surfaces	89
3.3.3	Experimental procedure	92
3.3.3.1	Injecting the soft material inside the chip.	93
3.3.3.2	A typical experiment.	99
3.3.4	Some other tested geometries	104

3.1 Fracture of soft materials: a short review

Soft condensed matter is all around us. Gels, pastes, foams, rubbers, emulsions share one major feature: they have a structure at a mesoscopic scale; this structure has a typical relaxation time in a range easily accessible experimentally and thus, this material can exhibit either liquid-like or solid-like response depending on the timescales over which they flow or are stretched. This liquid-to solid crossover is something industry tries to avoid: the jamming transition of granular materials in food or the cement industry; the fracture of extruded liquid polymer melts in the tyre industry. It can also be something they take advantage of: improving the texture of food and cosmetics while preserving flowability, enhancing oil recovery with hydraulic fracture. This is why, over the last decades, large efforts were made to understand the liquid/solid duality encountered in soft materials.

From a more fundamental point of view, the typical "microstructural" length scales involved in soft condensed matter (grain, colloid or bubble size) offer physicists the possibility to perform measurements on model systems at different scales and to correlate their macroscopic and microscopic properties. In the more particular context of fracture, we think this experimental accessibility of both microscopic and macroscopic length scales has been very little used to gain a better understanding of why a material is tough or brittle, what are the dissipative processes at play and how the material gets damaged, etc...



Figure 3.1: Some very current applications involving Soft Condensed Matter.

The developpement of rheology enabled to have a better knowledge of the mechanical behavior of soft materials, to classify them and to identify their linear and nonlinear constitutive laws. Early, it was demonstrated that

even liquid polymer melts could undergo fractures when loaded at a high shear rate (see Fig.3.2).

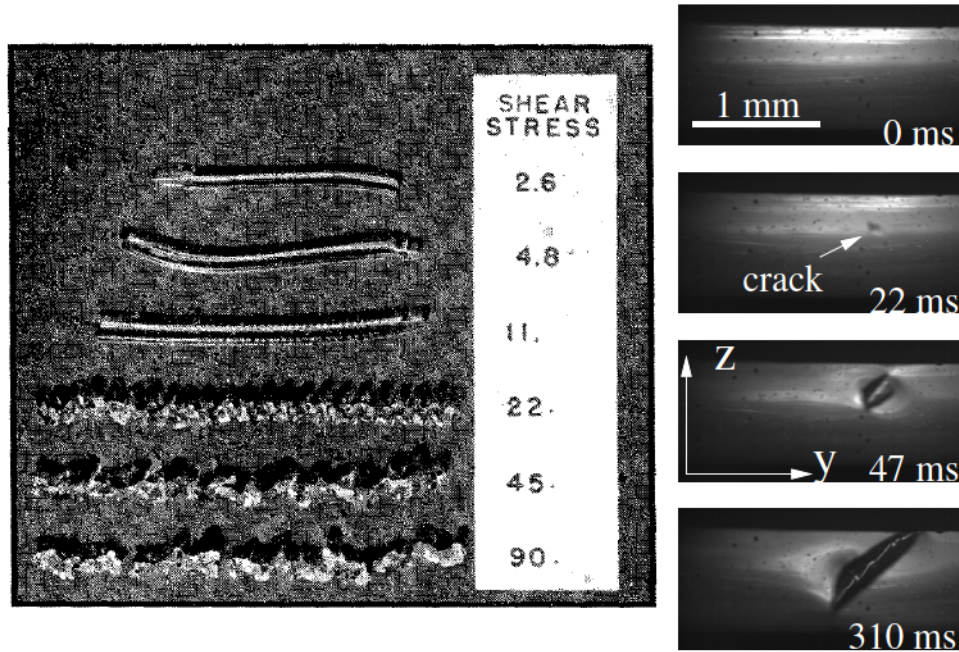


Figure 3.2: Capillary extrusion of a polymer melt for increasing shear rates. Shear induced cracks occur in the filament at high rates. Taken from [29].

Rheometers can measure torques very precisely but it is hard to visualize what is occurring in between the two shearing surfaces. However, experimental efforts have been made to couple rheometry with particle image velocimetry [30], ultrasonic imaging [31] or confocal microscopy [8]. This new ability to measure the actual spatial map of displacement fields in the rheometer helped a lot in the interpretation of non linear rheological data (creep, failure, shear banding). For example, the top of Fig.3.3 shows that a solution of wormlike micelles under shear can exhibit homogeneous flow or Taylor-like vortices for the same stress level. Similarly, within the framework of fracture, it was admitted that it is difficult to distinguish between mode II fracture and shear banding [32, 33] without a precise in situ measurement of the displacement fields. The bottom of Fig.3.3 shows PIV measurement of the velocity field in a transient polymer network sheared at imposed rate in a Couette geometry. When increasing the shear rate, the velocity map exhibits a sharp discontinuity: one part close to the moving wall that has an almost constant velocity and one part at the stationary wall which is not moving at all. This means that what is observed is a fracture. Last, shear experiments allow the study of crack initiation [34] but they make the study of crack propagation impossible: due to the complexity of the loading and

of the cylindrical geometry, there is no predictability for where the crack will nucleate and what the crack path will be.

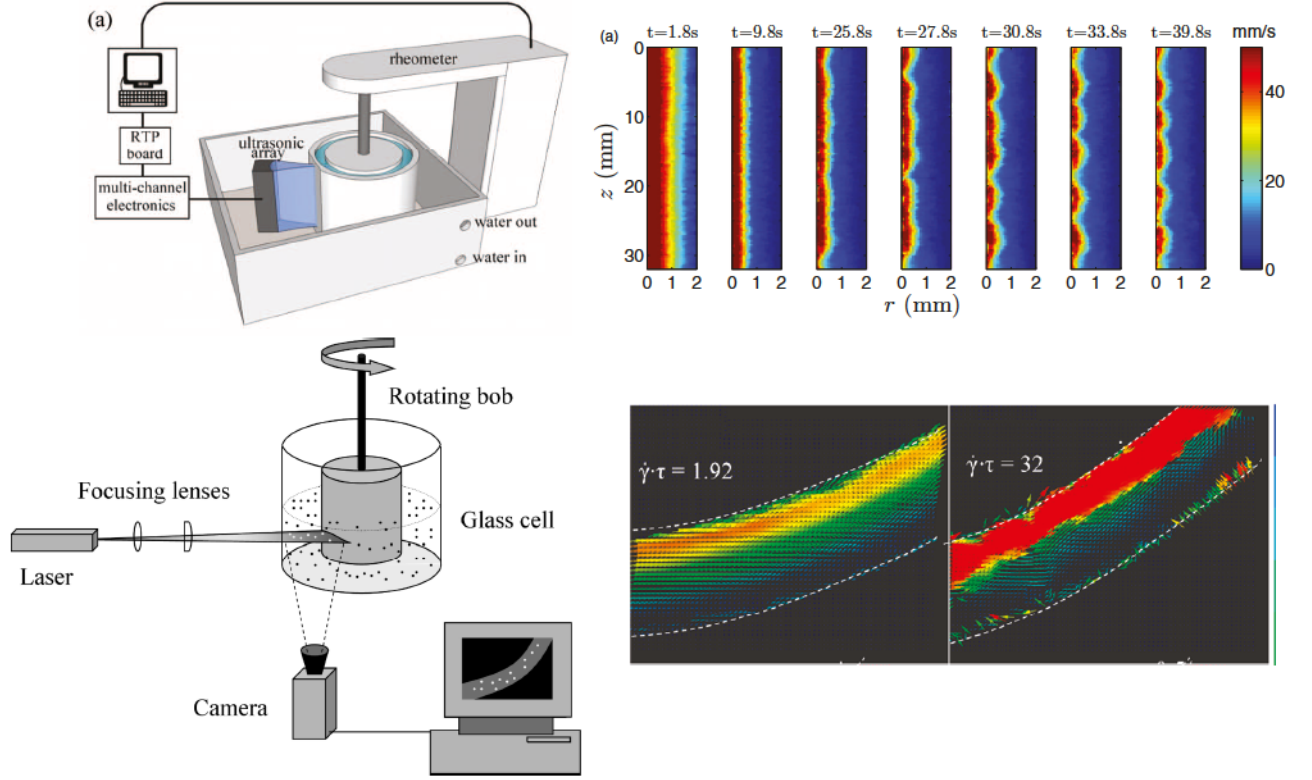


Figure 3.3: Top: Shear experiments coupled with ultrasonic imaging [31] allows mapping of the velocity field in the rheometer gap with a $0.2mm$ spatial resolution. Bottom: Shear experiments coupled with PIV setup [30]. A laser sheet allows to map the velocity field of a transient polymer network sheared in a Couette geometry.

In the following, we will focus on three original experimental devices that have led to characterize more accurately the fracture properties of soft materials. The first one is the probetack, or extensionnal geometry. The second one is a tensile test especially designed for soft materials. The last one consists in studying fracture in Hele-Shaw geometries. We will describe the advantages and the drawbacks of these various techniques. They will inspire us in the design of a new mechanical test for soft materials.

3.1.1 Probetack or extensional experiments

Probetack and extensional geometries were initially dedicated to the understanding of the mechanical properties of adhesives. The experimental geometry is shown in Fig.3.4 [35]. A thin layer of material (typically few hundreds of micrometers) is confined between two plates. The upper plate is moved upward at a fixed velocity while the bottom one remains still. Observation with a camera is performed through the bottom plate while a tensile deformation is applied on the material.

Typical observations are shown in Fig.3.4 for PDMS melts with increasing crosslink concentration [35]. At zero cross link concentration, the PDMS melt behaves as a viscous Newtonian liquid: Saffman-Taylor-like air fingers grow in the bulk from the edges toward the center of the initially circular contact. When the crosslink concentration increases, i.e. when the material starts behaving as an elastic solid, cracks propagate radially at the interface.

In a similar geometry but using colloidal suspensions close to the colloidal glass transition, Smith & al [36] showed that, at sufficiently high strain rates, cracks can nucleate and propagate in the material, the strain rate for the transition between flow and fracture decreasing with suspension volume fraction. This experimental device enables one to test failure of both viscoelastic liquids and solids in a tensile configuration. It provides information on the typical relaxation times of the material and on the ultimate force to failure. But it is very poor as for what it can teach us about crack propagation and fracture energy. This probetack geometry combines several drawbacks:

- No control of crack initiation.
- No preferential crack path, no stable crack propagation.
- Crack geometry difficult to model (complex 3D geometry with multiple planar crack front).
- No possible visualization of the crack front.
- Lack of physico-chemical control of environment

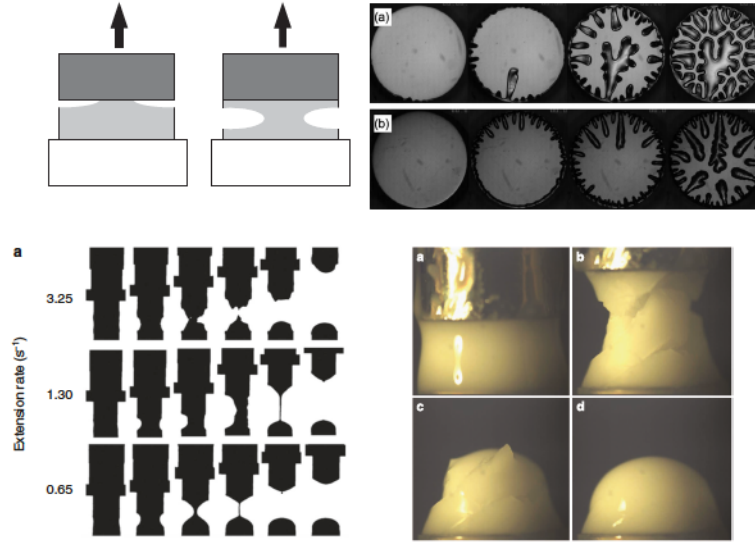


Figure 3.4: Top: Geometry of a probe-tack test. Low-reticulated PDMS shows Saffman-Taylor-like patterns while highly reticulated specimens fail by interfacial cracking. From [35]. Bottom: In a similar geometry, Smith & al [36] show a liquid-to-solid transition in dense colloidal suspensions.

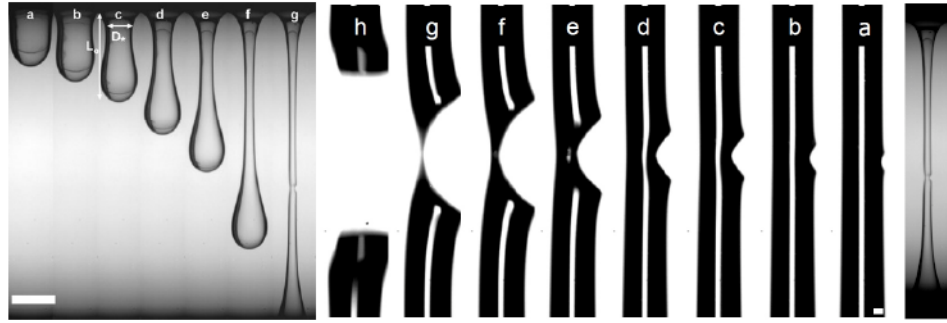


Figure 3.5: Left: Pendant drop experiments with a brittle Maxwell fluid. When the weight of the drop exceeds some value the drop elongates and the thin elongated tail ultimately fails. Right: Fast camera capture of the crack propagation in the tail. The crack shape is analyzed using a neo Hookean model. From [37].

Pendant drop experiments have a comparable geometry (see Fig.3.5). The stress generating the crack is the own weight of the pendant drop. Experiments in model complex fluids shows that a unique crack nucleates and propagates at high velocity [37]. As it is a stress-controlled experiment without any notch to initiate the crack, there is no possibility to control either the crack initiation or the crack growth rate. Besides, the propagation is

very fast and, as the initiation locus cannot be predicted, a visualization in the vicinity of the crack tip is not possible.

3.1.2 A tensile test for soft materials

More recently, Martina *& al* [38] developed a tensile test specifically dedicated to the understanding of the dynamics of crack propagation in soft gels. The specimen they used has typical dimensions $L \times 2h \times e = 300\text{mm} \times 30\text{mm} \times 10\text{mm}$. An important contribution concerns the way such soft materials are gripped: the gel is moulded in a rectangular frame with a velcro tape over the 300mm edge (see middle of Fig.3.6). This velcro tape is then glued on the vertical frame used to impose deformation. When stretching in the y-direction, a unique crack grows from an initial cut made at the top edge of the specimen, and it propagates downwards. A low-magnification camera records crack propagation: after a transient acceleration, the crack reaches a steady state.

This setup allowing to measure forces, one can compute the crack energy release rate \mathcal{G} . For an unnotched sample, the elastic energy F_{el} stored in the specimen without crack is computed by performing a numerical integration of the experimental force-elongation curve. The same strain is then applied to a notched specimen and the crack velocity V is measured. This enables Martina *& al* [38] to plot $\mathcal{G} = F_{el}/(e_0 L_0)$ versus V for different gel concentrations.

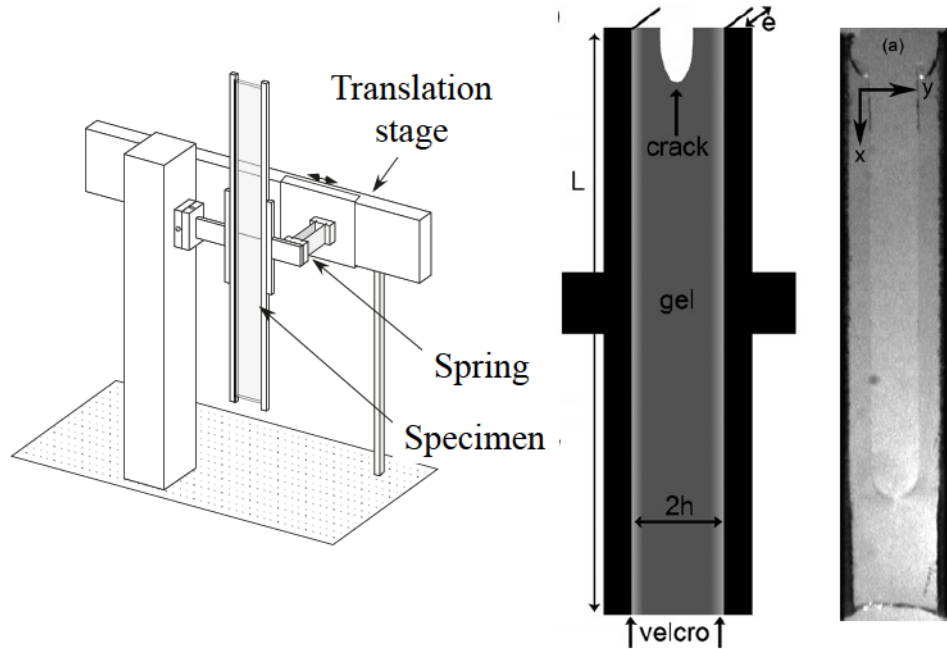


Figure 3.6: Tensile test of a notched specimen. Left: Experimental setup. Right: Snapshot of a crack in gelatin. From [38].

This experimental device constituted a major advance in the charac-

terization of fracture in very compliant materials, and contributed a lot in understanding the dynamics of crack propagation in physical reversible gels.

However, from our perspective, this device still lacks some characteristics:

- Only possible to load solids with sufficient stiffness ($G > 1kPa$ typically).
- Specimen has to be thick to allow manipulation but thin to be close to plane-stress conditions.
- Need for large quantity of material.
- Difficult high magnification visualization of the crack front.
- Lack of physico-chemical control of environment.

3.1.3 Fracture in Hele Shaw geometries

A last class of experiments consists in having the material confined between two rigid plates with a gap of a few hundreds micrometers. A hole is made in one of the plate through which a fluid is injected at given pressure or flowrate. This geometry is called radial Hele-Shaw cell (see top left corner of Fig.3.7).

Lemaire & al [39] were among the first to use this experimental geometry in order to study the viscoelasticity of clay suspensions. They injected water in clay suspensions at a fixed flow rate. They showed that an increasing clay volume fraction induced a transition from a viscous "Saffman Taylor-like" fingering to a viscoelastic multiple-crack pattern (see Fig.3.7). They observed a similar transition by increasing the injection water flowrate.

Foyart & al [40] did similar experiments in model viscoelastic liquids and observed a similar transition with the flow rate. They were able to perform low-magnification measurements of the crack tip shape by using image analysis and measurements of the crack tip displacement fields using local correlation approaches (PIV). This enabled them to characterize the liquid-to-solid transition, and to compute a velocity-dependent fracture energy on the solid side.

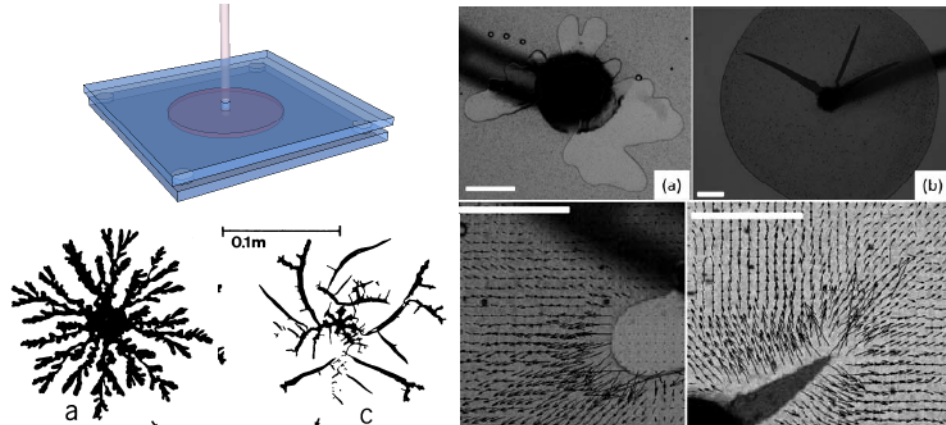


Figure 3.7: Top, Left: Radial Hele-Shaw geometry. Bottom, Left: Liquid-to-solid transition driven by volume fraction in clay suspensions [39]. Right: Liquid to solid transition with increasing the injection flow rate in Maxwell liquids [40].

Let us summarize the characteristics of this experiment:

- Possible to load both liquids and solids.
- Failure stress or strain rate can be controlled.
- Specimen is nearly 2D and confined between transparent surfaces which allows observation.

- Good physico-chemical control of the environment (possible to change injection fluid for example).

but:

- Need for large quantity of material.
- No unique crack (possible interaction between cracks).
- No privileged crack direction.
- Difficult high magnification visualization of the crack front.
- No control of the boundary conditions of the gel on the glass plates.

3.2 A new experiment for fracture of soft materials

From the previous review, and given the experimental challenges we want to pursue, we have identified a minimal list of four specifications that we should satisfy in the design of our new experiment.

3.2.1 Specification list for our experiment

1. Performing fracture experiments on different classes of soft materials: From viscoelastic liquids to soft solids with vanishing mechanical moduli.

The purpose of the experimental device we want to build up is to study damage and fracture of materials which are close to a liquid-to-solid transition. The sol-gel transition or the glass transition are typical examples of liquid-to-solid transitions. In these two cases, the material has a zero shear modulus at the transition and the shear modulus continuously grows when getting deeper into the solid phase. One naive approach consists in starting from the solid side of the transition and study crack propagation when one gets closer to the transition. The advantage of working with such soft materials is that their microstructural length scale reaches easily observable length scales. For example, a rubber with $10Pa$ shear modulus will have a typical mesh size of a few tens of micrometers!

2. Controlling the physical chemistry of the experimental conditions

Soft materials offer experimentalists the unique possibility to control their structure, the mesoscopic interactions governing the material assembly, or their typical relaxation time for example. And, for numerous soft materials, mastering physico-chemical conditions and maintaining them all along the experiment is the key to control the material mechanical properties, and to assure the reproducibility of the mechanical test. For example, pH or temperature history of some polymer gels will be shown to be critical parameters as for the gel shear modulus. In the case of colloidal materials, temperature changes of order $1C$ can change the colloidal sedimentation velocity or the van der Waals interactions between the colloids. Evaporation induces an increase of the suspension volume fraction, which can be of crucial importance when getting very close to the jamming or to the colloidal glass transition.

3. Visualizing the material at mesoscopic/microscopic scales during crack propagation.

3.2. A NEW EXPERIMENT FOR FRACTURE OF SOFT MATERIALS 53

In our approach, each observation scale can bring us a great deal of information on damage in the material. At low magnification, we will see that measuring the crack shape over the first few millimeters can give us an access to the energy dissipated during crack propagation. At intermediate scales (hundreds of micrometers), analyzing the displacement fields can give us information on the nonlinear processes occurring at the crack tip. At high magnification, we can access the microstructural scales of the material, and observe the elementary processes responsible for energy dissipation. This is easily feasible with standard microscopy techniques. Here are some orders of magnitudes of pixel size and size of field of view for observations at different magnifications. A 4x magnification has a poor resolution ($1.5\mu m$ pixel size) but allows fields of view as large as $3mm$ by $3mm$ and large working distances (distance between the objective and the plane observed). In the very high magnification range, 100x objectives with high numerical aperture allows submicronic resolution but fields of view are restricted to $(100\mu m)^2$ and working distances that can be as low as $200\mu m$. Both the size of the field of view and the working distance are very important indeed, because if we want to visualize crack propagation at high magnification, we have:

- (a) to control crack propagation and to make sure the crack path crosses the field of view.
 - (b) to design a mechanical test for which the objective lens with small working distance can be approached enough to the sample.
4. Building a mechanical test requiring low volumes of material.

In practice, a colloidal synthesis can produce batches of a few tens of milliliters of dry colloidal volume (dry colloidal volume is the volume of the colloids without the solvent they are suspended in). Above this range of volumes, colloidal synthesis is more difficult to control because of inhomogeneities in the stirring or in the heating of the batch. This results in large colloidal polydispersity, bad colloidal stability,... On top of that, colloidal synthesis is very sensitive to numerous parameters (temperature, pH, ionic force, presence of impurities,*etc.*...), so much so that it is very difficult for chemists to perform exactly the same synthesis twice. One cannot guarantee that two different syntheses with the same protocol will produce colloids with the same size and polydispersity, the same density, the same refractive index, the same interaction,... Thus, the best way not to introduce any bias due to the synthesis is to perform all the experiments on the same batch. To do so, we expect our new device to require only a very small amount of material per test. A goal of $100\mu L$ per test is fixed.

3.2.2 Toward a "on-a-chip" mechanical test

These points are essential specifications that our experimental device should satisfy. In the technological review that was just made, specifications (1) and (2) were already addressed in some experiments.

In rheology experiments, in the Hele-shaw and probe-tack devices, the material is confined between two rigid plates separated by a few millimeters at the most. This confinement prevents liquid materials to flow out and soft solid materials to buckle under their own weight.

Moreover, confinement helps in controlling the physico-chemical environment of the material by limiting evaporation. To have a full control of the environment, confinement, however, is not sufficient. We should think of a closed system that would guarantee a perfect control of the material physico-chemistry.

However, this strong confinement of the material raises the question of the boundary conditions at the wall during the mechanical test. Is the material adhering to the wall? Is it slipping? In rheology, for example, it is very common to make the walls rough in order to prevent slippage of the material under shear. In the case of the radial Hele-Shaw cell described in Section 3.1.3, the mechanics of crack opening is very different if the material slips perfectly, or if it adheres to the walls. We think this issue has never been addressed so far in such experiments.

Points (3) and (4) of the specification list are particular to our study. These are the points that make the experiment we want to design original. Regarding our wish to associate high magnification observation and low volume of material required for the mechanical test, we thought about an experimental device fabricated using microfluidic/millifluidic technologies. The total size of this on-a-chip mechanical test should thus be the size of a glass slide (40mm by 70mm typically). Finally, on a chip systems also present the advantage of being closed and their small size is in favor of fast thermal and chemical homogenization: this will help us a lot in controlling physical-chemistry of our environment. Of course, building an on-a-chip mechanical test is not enough to guarantee that one can observe the crack tip at high magnification: one also needs to initiate a unique crack and to know approximatively what the crack path will be.

To summarize, a closed and confined on-a-chip mechanical test satisfies points (1),(2) and (4). The previous discussion has raised some other important issues:

5. Fabricating the device using microfluidic technologies.
6. Initiating a unique crack.
7. Controlling the direction of crack propagation.
8. Controlling the mechanical boundary conditions at the wall.

3.2.2.1 Choice of the appropriate fabrication technology

Numerous microfabrication technologies are currently available to make on-a-chip microfluidic/millifluidic systems. The choice of the good technology and of the good material depends on the compatibility of this material with the solvents used, on the constraints related to observation or on the constraints related to the limitations of the fabrication technology itself.

Table 3.1 is a short list of the materials available, with their corresponding properties:

Material	Shaping	Young Mod.	Chem comp.	Refraction index	Thermal cond	Cost
PDMS	moulding	2MPa	w:++ org:-	1.41	0.2W/mK	low
NOA	moulding	1GPa	w:++ org:+	1.56	0.2W/mK	low
glass	μ machining	70GPa	w:++ org:++	1.50	1.05W/mK	high
PMMA	moulding/ μ machining	2.5GPa	w:++ org:-	1.49	0.2W/mK	med
copper	μ machining	120GPa	w:- org:-	-	401W/mK	high
steel	μ machining	200GPa	w:+ org:+	-	20W/mK	high

Table 3.1: Mechanical, chemical, optical and thermal properties of the materials available for chip fabrication

In this list, fabrication based on glass and metals was not considered due to its cost and to the very long times needed to design a new prototype: indeed, nearly 2 years of this PhD project were spent on designing new prototypes, testing their abilities and robustness, improving their design, etc... We could not afford to lose time on the fabrication itself. For this project, the chips were made in a UV photocurable glue called NOA thanks to Microfluidic Stickers technology (see Part.3.3.2.2). This choice results from multiple considerations.

The first consideration is linked to the mechanical properties of the chip. Because the material under study is stretched, it will undergo shrinking and its thickness will decrease by Poisson effect. This may lead to a bending of the chamber, which has to be avoided. We now estimate this bending by computing the typical upper plate deflection when deforming a soft material confined in between the two plates.

Let us consider a deformable material of Young modulus E confined between two plates. The bottom plate is considered as infinitely stiff and, thus, cannot undergo any deformation. The top one has a Young modulus E_p and a thickness h which means that its bending modulus is $D \propto E_p h^3$. Now consider we apply strain ϵ to the soft material in the direction of the red arrows in Fig.3.8. The tensile strain induces a contraction in the direction normal to stretching. If we assume that the gel is bound to the deformable upper plate, we can calculate the upper plate deflection by arguing that the stress inducing deflexion is $\propto E\epsilon$ and find that the maximum deflexion $w_{max} \propto \frac{Eb^4\epsilon}{E_ph^3}$. For b of order $10mm$ and $E \simeq 1kPa$, $w_{max} \simeq \frac{10^{-5}}{E_ph^3}$. In the

following table, we have reported the values of w_{max} for the most common materials used in microfluidics.

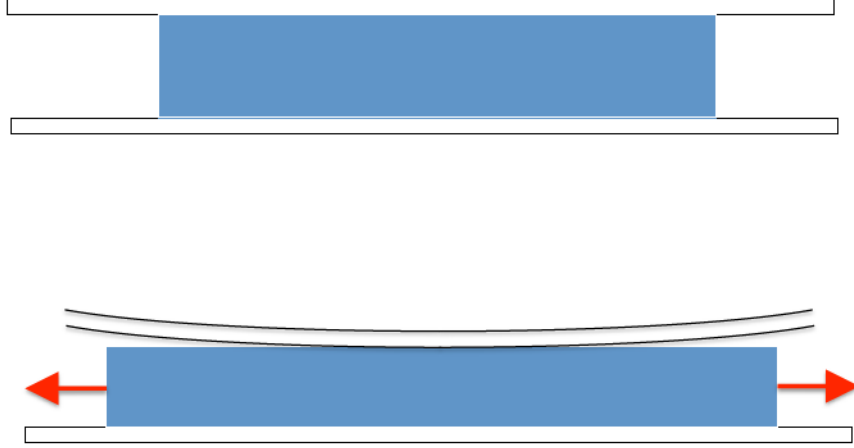


Figure 3.8: Upper plate deflection induced by the deformation of the confined soft material.

Material	thickness h	Young Mod.	w_{max}
PDMS	5mm	2MPa	$40\mu m$
glass	1mm	70GPa	$0.14\mu m$
PMMA	1mm	2.5GPa	$4\mu m$

Table 3.2: Typical deflection induced by soft material deformation during the tensile test

These values of deflection are to be compared with the typical gap where the soft material is confined (typically $300\mu m$). Considering this, the PDMS technology, which is very common in microfluidics does not seem appropriate for this application.

The second consideration is linked to the observation of the crack. The experimental device must allow observation with a microscope. It must be transparent for transmission microscopy or at least semi-transparent for reflection microscopy. NOA, glass and PMMA are transparent. For an observation in fluorescence or confocal microscopy, the chosen material should show low levels of autofluorescence [41]. NOA and glass do not autofluoresce. PMMA, as lots of others polymeric materials, exhibit high levels of autofluorescence.

From the point of view of chemical compatibility, our device should not have its mechanical and optical properties altered by the presence of any solvent used in colloidal or polymer materials. These solvents can be both aqueous (for polymer gels) or organic (halogenated solvent used for PMMA

colloidal suspensions). Metals undergo corrosion with water and other solvents; PDMS and PMMA chips are swollen by lots of organic solvents. NOA and, ultimately glass, have very stable chemical bonds (Si-O for glass, S-S for NOA) which make them very stable in inorganic and organic environments.

Last criteria for choosing the good material is of technological order: the material and the associated fabrication technology should be able to generate the desired chip geometry. Moreover, as we already mentioned, the creation of a new experimental device implies prototyping. This prototyping should be fast to converge rapidly toward a functional and performant solution. Microfluidic stickers technology is very efficient from this point of view compared to glass micromachining. Moreover, shaping of glass with etching or micromachining have some limitations regarding the structure shapes and sizes that are possible. For example, it is very complicated to build the notch or the grooves (see Part 3.2.2.2 and 3.3.3.1) which are large aspect ratio structures (large height compared to width). And last, typical cost for a glass chip with non-standard patterns is above 1000 euros per chip and the delivery time is about 1 month. On the contrary, we will see that microfluidic stickers are cheap and that the time needed to build a new prototype is about 1 week.

3.2.2.2 Initiation of a unique crack

As we saw in the review on fracture of soft materials, there is very little experimental geometries where a unique crack nucleates during the mechanical test. This is due to the fact that it is very difficult to initiate a crack in soft materials, especially when the material is confined. This, of course, induces poor reproducibility in the experiments.

When an unnotched specimen is loaded, it first undergoes an elastic deformation and may even undergo, afterwards, plastic strains. If the loading keeps increasing, the material eventually fails. For a brittle material (no plasticity) without any defect, macroscopic failure will occur at a stress corresponding to the theoretical stress needed to break one bond. This barely occurs since defects always exist, and they trigger failure at a much lower stress than expected theoretically. As a simplification, one can consider a rectangular specimen with a unique defect of length a and width b with $a \gg b$. If one applies a stress σ_{inf} to the specimen, the local stress at the tip of the defect is amplified by a factor $\sqrt{a/b}$. Locally, the material reaches its ultimate stress for σ_{inf} much smaller than the theoretical value. Failure of an unnotched specimen thus strongly depends on the distribution of defect sizes in the specimen.

In fracture mechanics, which usually deals with crack propagation rather than crack initiation, one experimentally gets rid of the distribution of defects in the specimen by inserting a macroscopic defect in the specimen, prior to loading. Depending on the material, a cut can be made in the ma-

terial [38] or a sharp notch with controlled geometry can be machined in the specimen. This will enable initiating a reproducible crack.

In soft material fracture, when the specimen is confined between two plates, it is difficult to make such notches. We found no paper mentioning any experimental technique other than laser ablation, which is used in totally different contexts. The solution we developed consists in building in the gap space, a thin elongated structure of controlled length and radius of curvature at the tip (see Fig.3.9). This structure around which the material will be moulded, will act as a macroscopic defect.

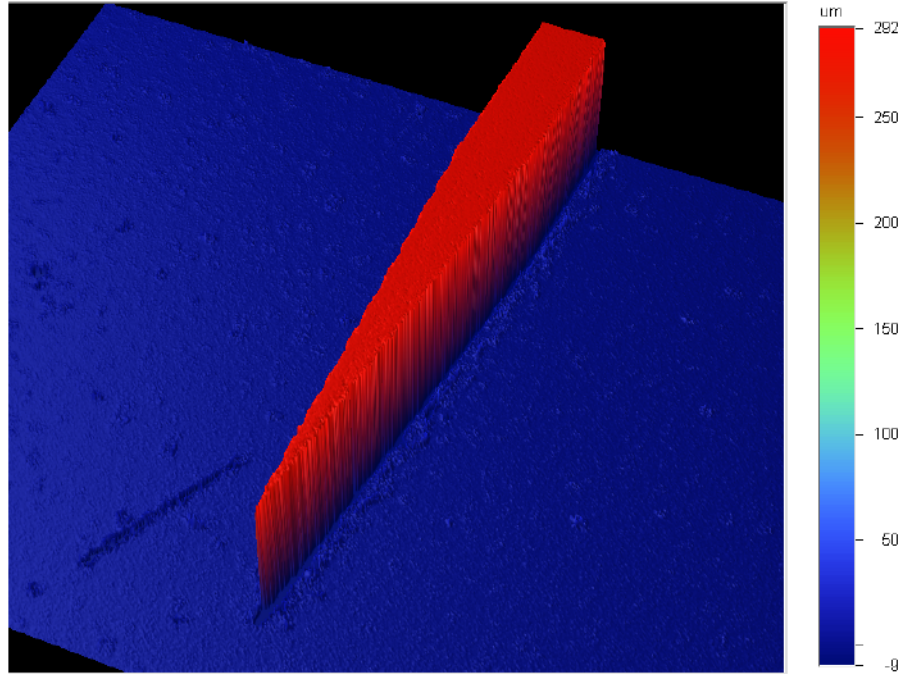


Figure 3.9: 3D structure of the built-in notch obtained with optical profilometry.

The material injected in the chamber solidifies around this elongated structure: the specimen is thus moulded with a macroscopic defect in it. This structure is built in the chip from the lithography step. The length of the defect ℓ , its radius of curvature at the tip ρ and, consequently, the stress amplification factor $\sqrt{\ell/\rho}$ can be tuned depending on how hard it is to initiate a crack in the material. The shape of the defect was also modified but it did not have a clear influence on crack nucleation, providing that the compared notches had similar lengths and radii of curvature at their tip.

3.2.2.3 Controlling the direction of crack propagation

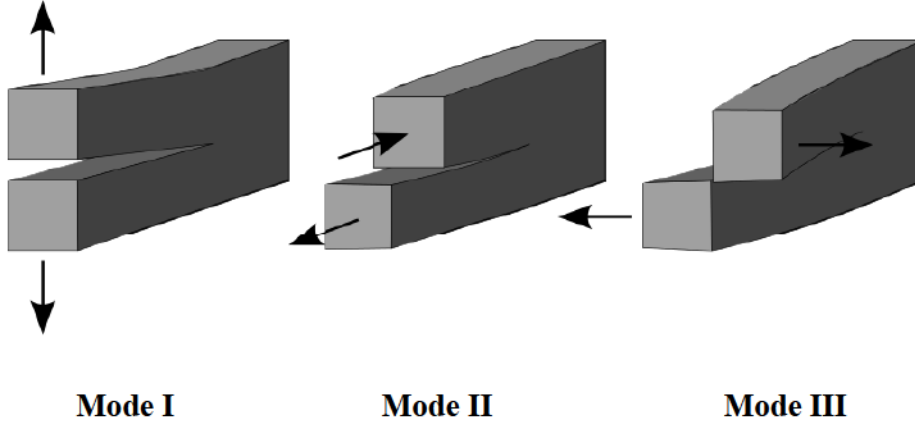


Figure 3.10: Three elementary fracture modes. Mode I: tensile crack opening. Mode II: Sheared crack. Mode III: Teared crack.

When a specimen with a unique crack inside is loaded in a complex way, one can always decompose this loading onto a stress field basis containing 3 modes. Mode I is the opening mode. Mode II corresponds to pure shear of the crack within the fracture plane. Finally, Mode III corresponds to tearing: an out-of-plane shear of the crack.

A crack path usually follows the principle of local symmetry: a crack loaded in mixed mode spontaneously turns so that it locally opens in pure Mode I. As a result, to have a crack propagating along a straight path, the loading of the specimen should have Mode I symmetry:

$$\sigma_{xx}(-x) = -\sigma_{xx}(x) \quad (3.1)$$

$$\sigma_{xy}(-x) = \sigma_{xy}(x) = 0 \quad (3.2)$$

In our experiment, there is negligible mode III because out of plane deformations are constrained a lot. Only Mode I and II are possible. We took inspiration from pure Mode I geometries to build our mechanical test. Mode I fracture geometries are shown in Fig. 3.11. One stretches a rectangular specimen of width l and length L with a notch in the direction perpendicular to stretching. The notch can be either on one side of the plate or in the middle of it. The mechanical stress can be applied either at the specimen boundaries (infinite loading) or on the mouth of the crack (inner loading).

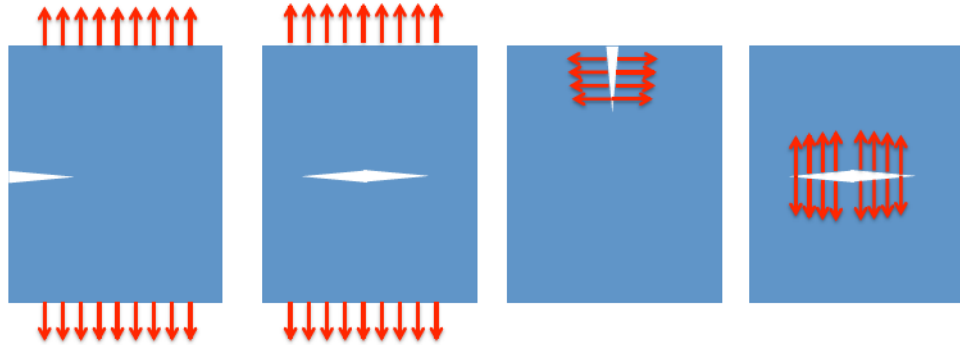


Figure 3.11: Several tensile geometries for Mode I fracture. Left: Edge-notched and central-notched plates remotely loaded. Right: Edge-notched and central-notched plate with inner-loaded cracks

As we saw previously, most fracture experiments with soft materials do not allow the control of the direction of crack propagation. The loading mode is often mixed, which makes the crack path complex. Moreover, numerous cracks propagating simultaneously interact elastically. We are going to present experimental solutions to solve these two problems (Part 3.3.1).

3.2.2.4 Controlling mechanical boundary conditions

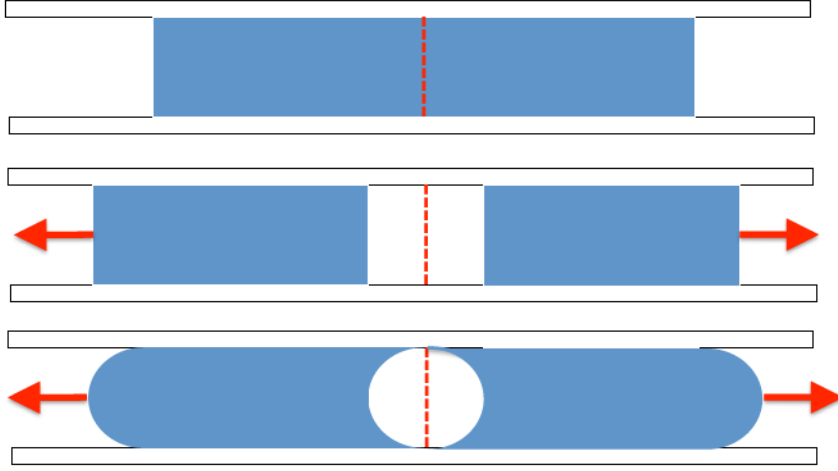


Figure 3.12: Mechanical deformation of a confined specimen. Top: Cross section of an undeformed specimen between two rigid walls. Red dashed line is the crack front with crack in a closed state. Middle: case where material slips at the walls: the crack opens and there is no material deformation in the confinement direction. Bottom: case where material adheres to the walls: the crack opens and there is large deformation in the confinement direction.

The problem of crack propagation in a confined specimen is very dependent on the boundary conditions at the bottom and top walls confining the material. Depending on slippage or adhesion of the soft material on the walls, the energy stored in the material when deformed will have very different dependences. Two extreme cases are shown in Fig. 3.12. Adhesion of the material on the walls will be critical when trying to open a crack: adhesion to the boundaries will induce large deformations at the walls and cost a lot in elastic energy. We will thus try to promote slippage at the walls.

Finally, we can wonder about the boundary conditions at the crack mouth. In classical fracture mechanics, crack lips are surfaces where normal and tangential stresses vanish. In soft materials, boundary conditions could be somehow different: when dealing with extremely soft materials, surface tension can become relevant at specific lengthscales. We can indeed introduce an elasto-capillary length $l_c = \gamma/G$ where γ is the surface tension between the solid and the surrounding fluid and G is the material shear modulus. The interpretation of l_c is the following: at scales larger than l_c , elasticity applies; at scales smaller than l_c , capillarity dominates. For a gel with few tens of Pa in contact with air, l_c can be as large as 1mm ! To illustrate this, Mora [42] moulded very soft agar cylinders with sharp corners. When plunging the cylinders+mould in toluene, the outer mold dissolves.

In blue, Figure (3.13) shows the smoothing of the sharp corners due to surface tension between toluene and the water-based gel. The smoothed zone is larger when the gel is softer. In the context of fracture, it means that if one observes a crack tip with air inside at length scales smaller than 1mm , the crack tip will be blunted by capillary forces!

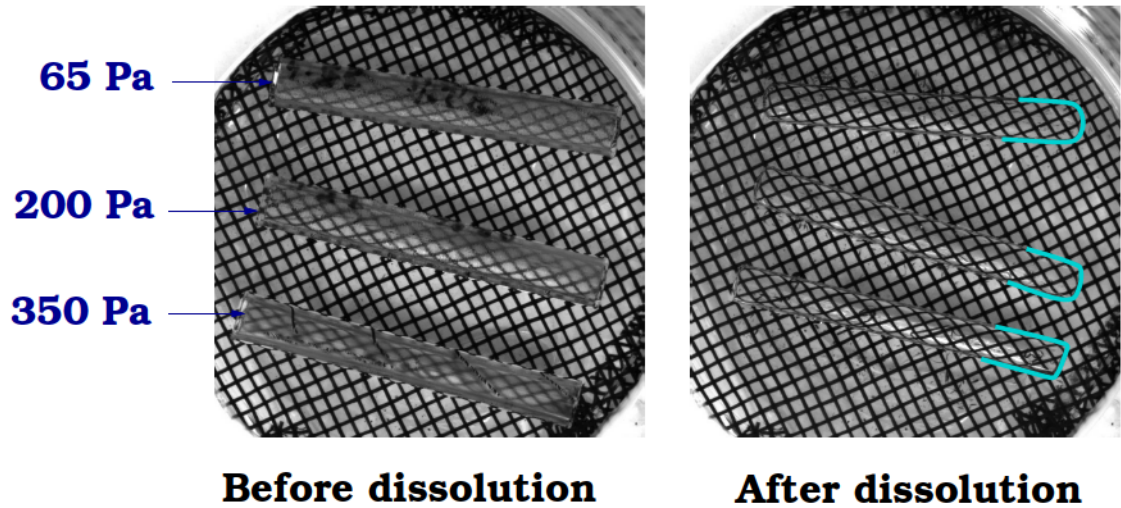


Figure 3.13: Mora showing the surface-tension-induced smoothing of sharp corners for very soft objects.

As a result, if one wants to grow cracks in very soft materials and observe the crack tip, one needs to get rid of surface tension forces by injecting a liquid showing very low surface tension with the soft solid. For instance, for a water-based gel like agar, water should be injected in the crack while it is growing.

3.3 Design of our on a chip mechanical test

3.3.1 Chip geometry

The geometry of the microfluidic chip we designed is a miniaturized version of the tensile geometry used by Martina [38].

Let us consider a square chamber of 25mm in length and thickness $e = 350\mu\text{m}$. The edges of the chamber along the y -direction are closed by walls. The edges along x -direction remain open. Top and bottom of the chamber are 1mm -thick glass slides (not represented here).

In the middle of the chamber, a rectangular specimen made of the studied material (in red in Fig.3.14) is confined between the two rigid glass plates. The specimen width is 7mm (in the y -direction) and its length is 25mm (in the x -direction). The rectangular specimen is thus touching the chamber walls along y -direction but its two other boundaries are free. Stretching is to be applied by imposing a normal displacement in the y -direction on the specimen boundaries along x -direction.

As in radial Hele-Shaw experiments, a hole is drilled in the upper plate: it will be the starting point of our crack and it will enable us to inject a liquid (water in all the experiments we are considering now) in the crack while it is growing.

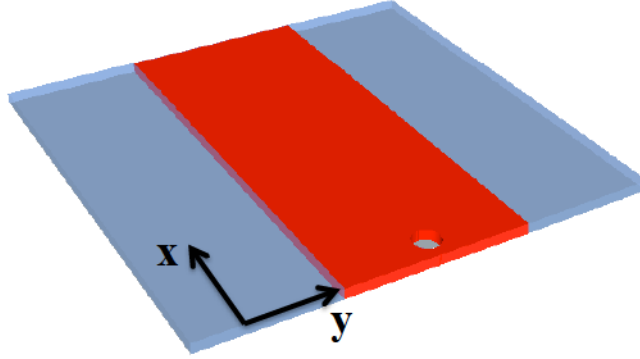


Figure 3.14: $350\mu\text{m}$ -high square chamber with 14mm (along y) \times 25mm (along x) rectangular specimen inside (red). A hole is drilled in the upper plate.

We need to find a solution to grip our material and to apply a tensile stretch to our specimen. As a matter of fact, we cannot design small mobile parts able to grip the specimen at its boundaries. First, it would be a technical challenge. Second, one cannot grip a liquid or a very soft material.

We therefore developed a new method to stretch soft materials: we call it "liquid pistons" and it enables us to prescribe displacements on the free boundaries of the rectangular specimen.

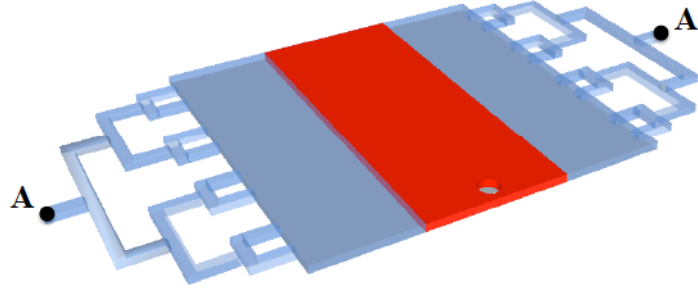


Figure 3.15: Each side of the chamber is filled with fluorinated oil and is connected via tree-like channels to syringe pumps that will draw the oil out of the chamber.

The open sides of the chamber are connected with tree-like channels (see Fig. 3.15). The channels and empty spaces of the chamber on both sides of the specimen (in blue on Fig. 3.15) are filled with fluorinated oil (FC3283). This liquid is used for two of its properties: it is incompressible and it is completely immiscible with most of other solvents. This liquid will be used as a piston: two syringe pumps connected to points A draw the oil out of the sides of the chamber. Due to oil incompressibility, this aspiration induces forced displacement along y -direction on the boundaries of the soft specimen. Contrary to standard grips, this liquid piston does not constrain the displacement of the boundaries in the x -direction.

As this piston is very soft, we are not in fixed-grip conditions: until the crack opens, the applied displacement is homogeneous along the boundaries of the specimen but, as soon as the crack starts opening, the applied displacement becomes larger in the wake of the crack tip (see Fig. 3.16).

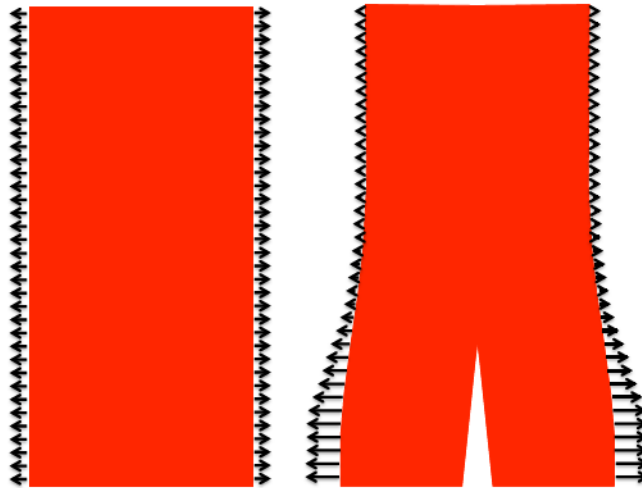


Figure 3.16: Schematic view of the displacements prescribed by liquid pistons before (left) and after (right) the crack starts propagating.

To help initiating a unique crack, the notch described in Part 3.2.2.2 is built in the experimental device just below the hole drilled in the upper plate (see Fig.3.17). The crack will start from the notch tip and grow in the x -direction. Fig.3.17 shows the whole design of the microfluidic chip made to perform a tensile test on soft materials.

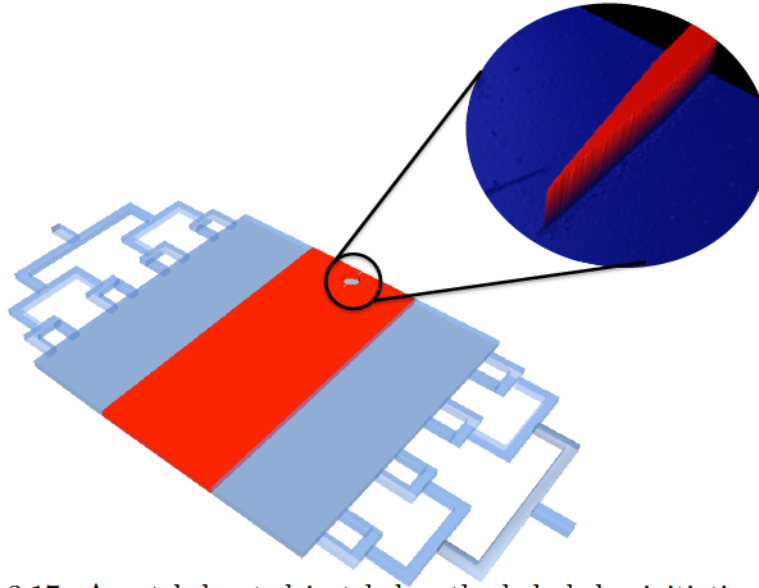


Figure 3.17: A notch located just below the hole helps initiating an edge crack into the specimen.

Let us summarize the new possibilities this chip provides and what would still need to be improved:

- Possible to load both liquids and solids.
- Strain rate can be controlled
- Specimen is nearly 2D and confined between transparent surfaces which allows observation
- Good physical-chemical control of environment (no evaporation, possible to change injection fluid for example)
- Need for small amount of material ($50\mu\text{l}$ of material per experiment).
- Unique crack propagating in a given direction.
- Possibility of high magnification visualization of the crack front.
- Close to plane stress approximation.

but:

- No direct measurement of applied force.

3.3.2 Chip fabrication

In this section, we describe the technologies used to build this new kind of experimental chip. In the description, we focuss on some technical difficulties encountered in the fabrication steps. Fabrication can be summarized in 3 steps:

- Generating a mould with soft lithography.
- Replicating the device using microfluidic stickers technology.
- Promoting gliding of the gel by applying a surface treatment on the inner walls of the chip.

3.3.2.1 Soft lithography

Photolithography is a process that allows to form a relief structure on a substrate (usually a silicium wafer). It uses light to transfer a geometric pattern from a photomask to a light-sensitive chemical "photoresist", or simply "resist," deposited on the substrate. The obtained structures are 2.5D: they have vertical walls through the thickness of the resist. The final resist pattern is binary: parts of the substrate are covered with resist while other parts are completely uncovered.

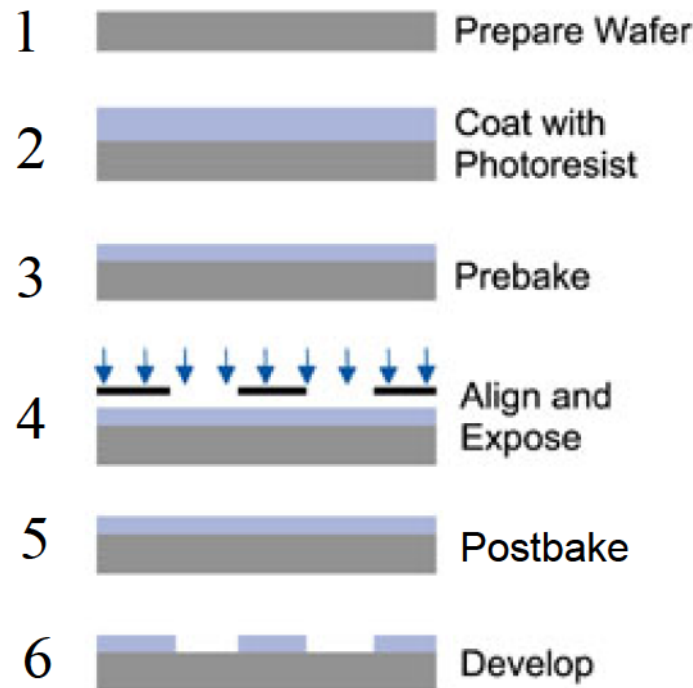


Figure 3.18: Main steps for soft lithography. The Si wafer is shown in grey. The resist is in blue.

Fig. 3.18 briefly recaps the main steps to get an N-layer mould with photolithography: before the first layer, the clean wafer is dehydrated to improve adhesion of the structures. For the i^{th} layer, a homogeneous layer of photoresist is spincoated (thickness e_i). Prebake consists in heating the wafer+photoresist to evaporate part of the solvent contained in the photoresist. The mask corresponding to the layer we are adding is then placed a few micrometers above the surface of the photoresist. If needed, it is aligned relatively to the previous layer using a mask aligner. The photoresist is then exposed with collimated UV light. The polymer we use is SU8; it is a negative photoresist, meaning that the polymer only crosslinks in the zone where it is insolated. If a multilayer structure is made, steps 2 to 4 are repeated for each layer until reaching the top layer. Then, we move to a postbake step: the wafer with insolated photoresist is heated to improve the kinetics of crosslinking. Finally, the photoresist that has not reticulated is washed away using a development bath. We obtain what we call a master. It is used to obtain soft negative replica of the pattern; these replica are usually made of PDMS: liquid PDMS and crosslinker are mixed, poured onto the master and thermally cured for two hours at 70C. When completely reticulated, PDMS can be lifted off from the master and used as a stamp for NOA microfabrication (see Part 3.3.2.2)

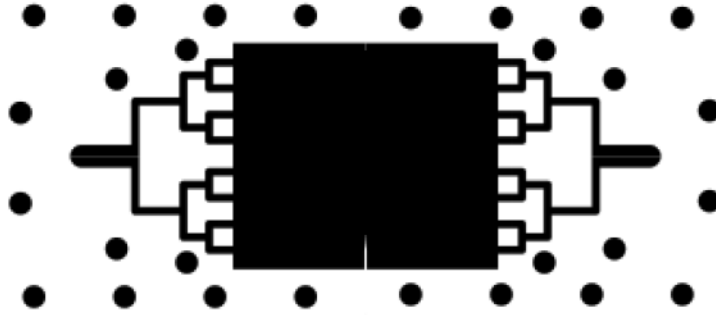


Figure 3.19: High resolution mask used for lithography.

Fig.3.19 shows the mask used for photolithography. We recall that white patterns are the positive relief on the wafer while black patterns are the wafer surface. We immediately notice the difficulty in making the notch: it is a thin structure of high aspect ratio (height/width > 5) and it should have the sharpest tip as possible. The insert of Fig.3.17 is a 3D picture of the notch made of photoresist (acquired with an optical profilometer). The radius of curvature at the crack tip was estimated to be $10\mu m$.

The major difficulty originated in the large thickness of our structures ($> 100\mu m$): this resulted in large inhomogeneities of the structure height (10–20% variation) and in large residual stresses in the obtained structures. These residual stresses even provoked debonding of some structures from

the wafer. To reduce thickness inhomogeneities, we mainly improved the horizontality of the heating plates used for baking the photoresist. At such large thicknesses, a small tilt of the wafer is enough to induce surface flows of the heated photoresist ($V \propto \frac{\rho g \sin(\alpha) e^2}{\eta}$). To reduce residual stresses in the photoresist, we tried to avoid thermal shocks of the photoresist during the postbake step. The photoresist was thus cured by increasing temperature from ambient to 95C at 5C/min, left at 95C for the required time and cooled down at about the same speed.

3.3.2.2 Microfluidic Stickers

The stickers are made by soft imprint lithography using an UV reticulable glue named NOA81 [43]. As mentioned earlier, this material combines several interesting properties: it is two orders of magnitude stiffer than PDMS, it is compatible with most solvents, its surface chemistry is similar to the one of glass and it is compatible with prototyping (short fabrication time and low cost).

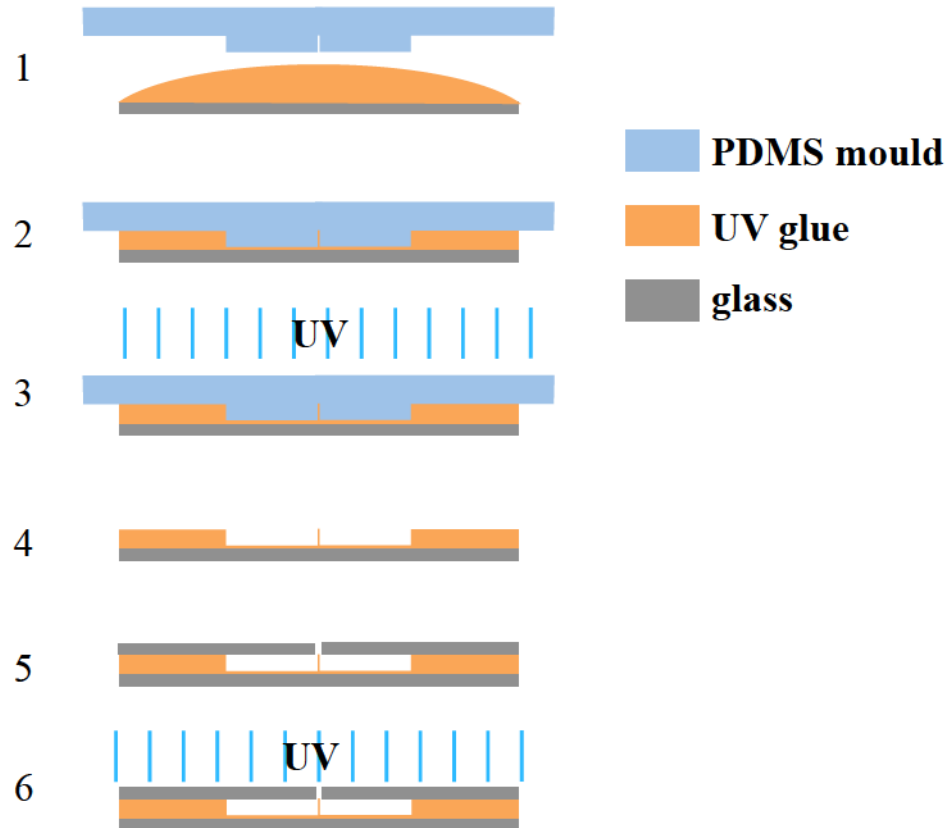


Figure 3.20: Making NOA chips

Here is how we proceed to make one chip (see Fig.3.20). A drop of the photocurable monomer is deposited onto a flat glass slide. A structured PDMS stamp moulded from the previous lithography master is then gently pressed onto the drop. To cure the polymer film, the liquid is insolated with UV (365nm) through the transparent PDMS stamp. Since oxygen inhibits the free-radical polymerization of the glue, the gas permeability of PDMS ensures that an ultra thin superficial layer of glue in contact with the PDMS stamp remains uncured. After this first insolation, the PDMS stamp can be detached and a glass slide with drilled holes (corresponding to the ins and outs of the chip) is used to close the chip. A second insulation allows reticulation of the superficial layer and complete sealing of the system.

3.3.2.3 Acrylamide grafting of NOA and glass surfaces

We explained in Part.3.2.2.4 the importance of controlling boundary conditions to simplify the interpretation of our mechanical test. The ideal boundary condition is a perfect slippage of our soft material relative to the wall. M. Leocmach working at ENS Lyon on the mechanics of confined layers of casein gels introduced me to a surface treatment consisting in growing polyacrylamide brushes on glass surfaces. Casein gels have a strong adhesion with glass and polyacrylamide brushes strongly reduce this adhesion.

On glass, this surface treatment is a 2-step reaction consisting in:

1. Silanization step: immobilization on the glass surface of a silane with reactive C-C double bond.
2. Polymerization step: growing of acrylamide brushes from the immobilized silanes.

Glass is a 3D Si-O-Si network. In contact with oxydizing environment (air for instance), its surface shows Si-OH groups instead of Si-O-Si bridges (Fig.3.21). These chemical groups are very reactive and are frequently used for chemical grafting of silane species. OH surface groups react onto the silane group of the silane precursor in solution and form new Si-O-Si covalent bonds. A self-assembled monolayer of precursors forms at the glass surface.

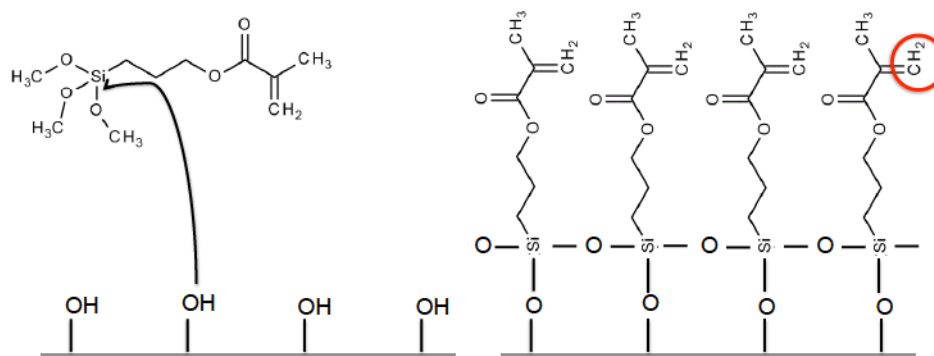


Figure 3.21: Immobilization of silane precursors on the glass surface.

The second step is the growth of acrylamide chains from the grafted silane precursor. This reaction occurring in water is a free-radical polymerization. Polymerization is initiated by ammonium persulfate and TEMED (tetramethylethylenediamine): TEMED accelerates the rate of formation of free radicals from persulfate and these, in turn, catalyze polymerization. A persulfate free radical thus converts the reactive C=C double bond of one grafted silane (in red on Fig. 3.21) into a radical that reacts with an unactivated monomer (see Fig. 3.22) and begins the polymerization chain reaction. The elongating polymer chains grows in about 30 min at room temperature following the reaction described in Fig. 3.23.

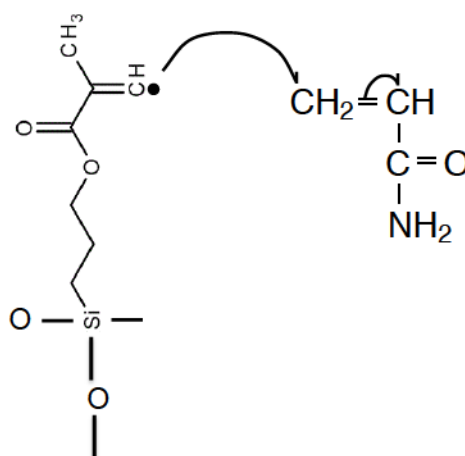


Figure 3.22: Initiation of the polymerization.

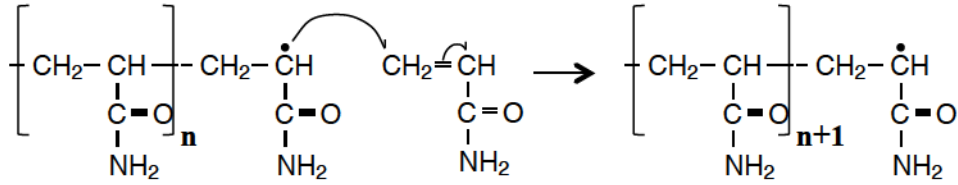


Figure 3.23: Propagation of the reaction: growth of the acrylamide brushes

The walls in our chip are not all made of glass: some are made of cured NOA. We thus needed to adapt the protocols in the case of NOA surfaces, covered with SH groups instead of OH ones. Our main contribution was to add a plasma step before the silanization of NOA surfaces in order to activate the SH groups and to favor binding of Si groups to SH groups (S and O belong to the same column in the periodic table and thus have a similar reactivity). The acrylamide polymerization step remained unchanged.

3.3.3 Experimental procedure

In the previous sections, we described the various experimental setups we have worked with, and introduced the reader to how these experimental devices are fabricated. We now address the question of how this on-a-chip mechanical test can be performed and focus on the particular case of a thermoreversible physical gel (agar or gelatin for example). Two particular aspects of a typical experiment need to be described:

- Loading of the soft material inside the chip.
- A typical fracture experiment.

3.3.3.1 Injecting the soft material inside the chip.

The first requirement is that our material can flow inside the tensile test chip. There is obviously no problem for viscoelastic liquids. For most of the soft solids we are considering, this is not a big constraint either, since they are often prepared from a liquid solution which undergoes a liquid-to-solid transition. The example we will consider next is the one of a thermoreversible physical polymer gel which can be flown at high temperatures. Similarly, some liquid-to solid transitions of colloidal materials are controlled by temperature: the suspension can remain liquid providing we maintain the temperature below some critical value (or above depending on the system). For silica gels prepared by electrostatic destabilisation of silica suspensions, the time of gel formation can be tuned with salt concentration [1] and thus gives the experimentalist a time window during which the gel in its still liquid form can be injected. Most of the materials that we have worked with

were controlled with temperature. We thus give the reader details on the procedure adapted to this specific case.

Procedure in the case of a thermoreversible gel. We first describe the injection procedure for a gel without considering the problem of temperature control: we proceed with a material in its liquid state at ambient conditions. The filling procedure is described with the help of Fig. 3.24.

Two synchronized syringe pumps filled with FC3280 fluorinated oil are connected to the extremities of the chip. The main chamber is filled with fluorinated oil (in light blue in Fig. 3.24) at high flow rate. The excess of oil can flow out from the central hole and fill a reservoir directly connected to it. Great care is taken to get rid of every bubble stuck in the chamber. This can be understood easily: if a bubble remains in the chamber with the soft specimen inside, drawing out the oil will induce the bubble inflation instead of deforming the gel.

The gel-forming solution is then poured into the reservoir above the oil in excess. The two pumps are then reversed and one withdraws oil from the chip until the middle of the chamber is filled with the correct amount of the gel forming solution ($50\mu L$). Pumps are then stopped and, if needed, gel formation is triggered (by temperature quench for example).

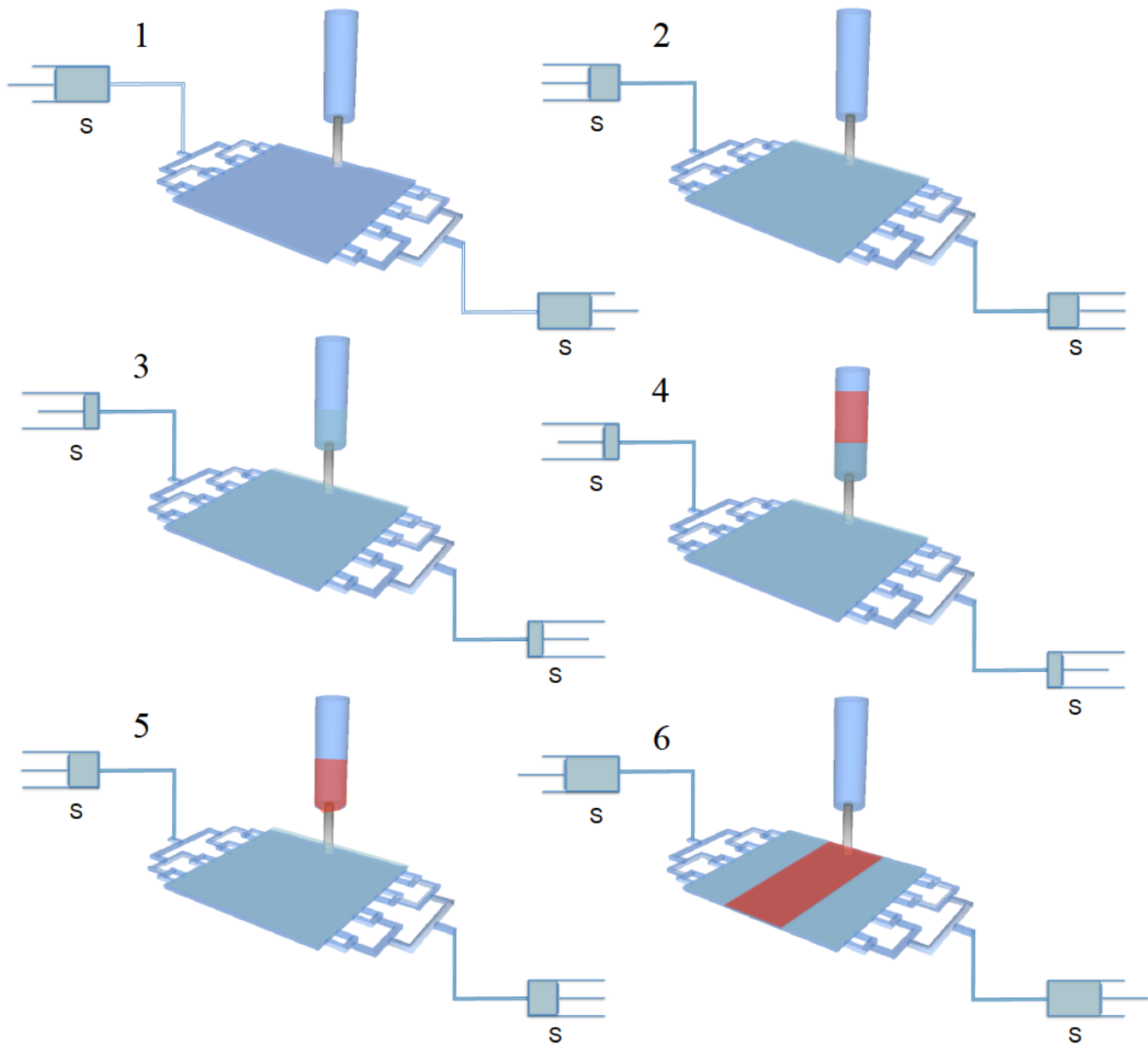


Figure 3.24: Main injection steps (read from left to right and from top to bottom). 1: empty chip with connected syringe pumps full of oil and empty reservoir connected to the hole. 2: chip is filled with oil... 3:...until reservoir is half filled with oil. 4: the gel forming solution (sol) is poured into the reservoir. 5: oil is sucked back in the syringes... 6: ...until the sol occupies the inside of the chamber.

Let us consider now the case of agar. Agar is a thermoreversible physical gel that has its sol-gel transition (liquid-to-solid transition) at about 40°C . In

order to keep the material flowable and with a low viscosity, we need to maintain it at about 60°C . To do so, one needs first to thermalize the chip, and, second, to thermalize the reservoir in which the agar solution is poured.

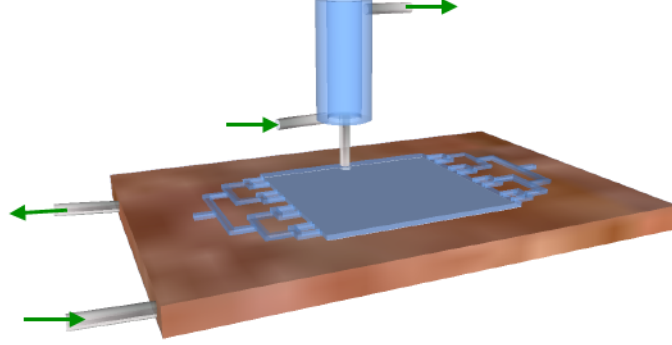


Figure 3.25: Thermalization system. Thermalized water at 60°C circulates in a copper heating stage below the chip and in the glass reservoir connected to the central hole of the chip.

To perform the injection procedure previously described, the whole system is maintained at 60°C . We built a thermal stage to thermalize the chip. The chip is taped on a copper plate with water circulation inside connected to a water bath maintained at 60°C . As for the reservoir plugged to the middle hole, it is a glass pipette with double walls. The content of the pipette is thermalized by water circulating in between the two glass walls. This water comes from the same water bath used for the thermal stage, ensuring that both chip and reservoir are at the same temperature. This double heating system is shown in Fig.3.25.

After the gel-forming agar solution is injected into the chip, the thermal stage is connected to a cold water bath (23°C) while the reservoir is maintained hot. In addition to the triggering of gelation, cooling from 60 to 23°C first induces a slight contraction of the chip: keeping the reservoir at high temperature enables to compensate for this volume change. Indeed, before gelation, a few microliters of the agar solution (corresponding to volume change due to cooling) flow back into the hot reservoir. The reservoir is connected to the cold bath as soon as the thermal stage reaches 23°C (5 minutes typically). The gel then starts forming in the middle of the chamber. We use rheological data to estimate the time needed for gel formation and for reaching of the pseudo equilibrium.

How to get a rectangular specimen? In Section 3.3.1, we mentioned that, before starting the fracture experiment, the gel specimen was rectangular with dimensions 0.35mm in thickness, 25mm in length and 7mm in width. The main reason why we chose a rectangular specimen is that lots

of attempts to implement numerical fracture experiments of these very soft compliant materials were inspired by Martina's geometry [38] and are thus dealing with a rectangular slab of material.

Of course, as described in the previous part (3.3.3.1), the injection does not spontaneously result in a specimen with a rectangular shape. It would rather spontaneously result in a specimen with semicircular shape (see Left of Fig.3.26) centered about the middle hole.

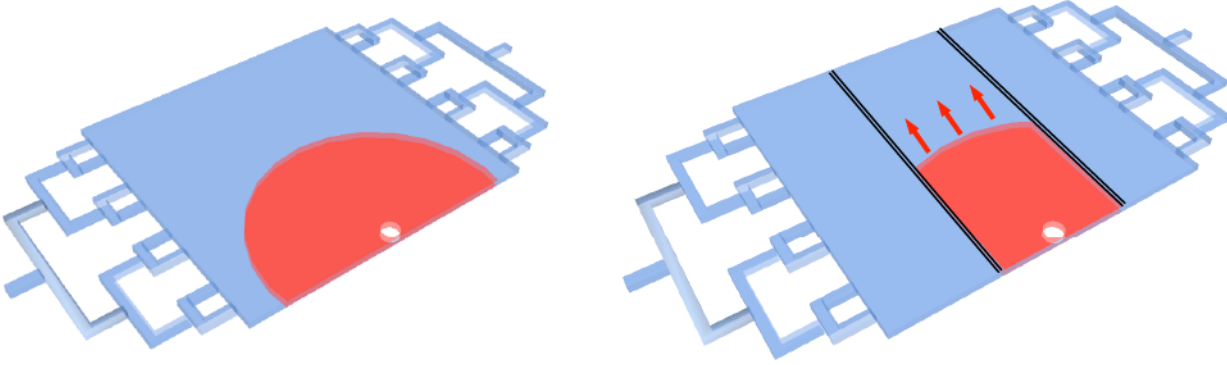


Figure 3.26: Specimen shape obtained after the injection procedure. Left: without grooves. Right: with grooves.

To achieve this, we found a convenient way to proceed. Two grooves (represented in black on the right of Fig.3.26) with width $50\mu m$ and depth $100\mu m$ lie at the bottom surface of the chamber: they delimitate the specimen boundaries by pinning the interface between the oil that fills the chip and the gel-forming solution we are injecting from the middle hole.

The explanation of the pinning is simple. The interface between oil and the solution has a fixed advancing contact angle. This is illustrated in Fig.3.27: we show the oil/solution interface (in red) moving at velocity U . When this interface tries to cross the groove, this groove acts as a topological defect: crossing the groove with fixed contact angle θ implies a large deformation of the meniscus and is thus very unlikely. As a result, the injection of the gel-forming solution occurs as sketched on the right of Fig.3.26. The solution is stopped by the "topological defect" and then fills the rectangular space delimited by the two grooves. As a consequence, it is possible to control the specimen dimensions by changing the distance between the two grooves. The grooves are $50\mu m$ wide, $100\mu m$ deep and are added right from the lithography step. This controlled filling occurs at low capillary number $Ca = \eta U / \gamma = 10^{-5}$ so that the effect of surface tension takes over the effect of viscosity.

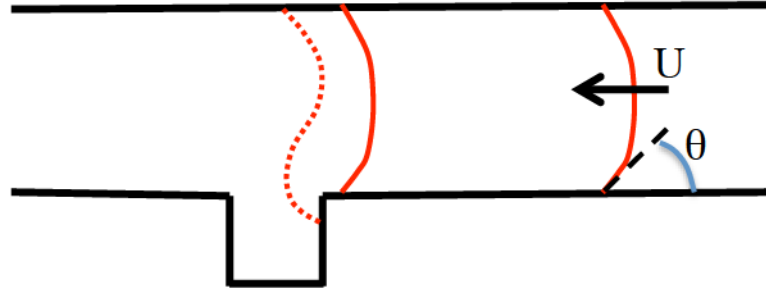


Figure 3.27: The groove in the bottom acts as a topological defect. Red line: Advancing sol-oil interface with fixed contact angle θ with the bottom wall. Dashed red line: deformed contact line trying to go over the groove.

3.3.3.2 A typical experiment.

After injection and gelation of the gel-forming solution, the rectangular specimen is surrounded by immiscible fluorinated oil. The oil being immiscible with the gel, the interfaces between the fluid and the material remain sharp. The two synchronized syringe pumps connected to points A (Fig. 3.28) draw the oil out of the chamber at a prescribed flow rate Q .

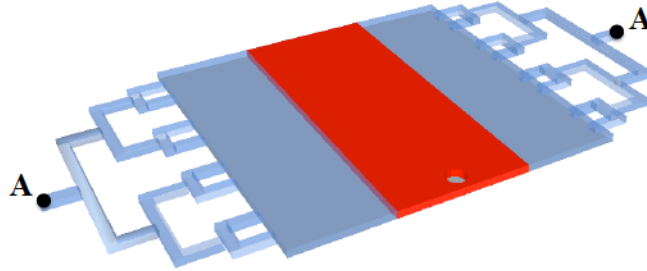


Figure 3.28: Initial experimental conditions. A chip full of fluorinated oil with the specimen in the middle. Each point A is connected to a syringe pump.

Acting as a tensile machine of low stiffness, the oil outflow imposes a velocity of displacement proportional to Q to these two boundaries. However, as already mentioned, due to the low rigidity of the tensile system, the displacement along the oil/gel interface is non uniform as soon as a crack starts propagating. Under deformation, a single mode I crack is initiated from the built-in notch. We also recall that the central hole is connected to a water reservoir so that the propagating crack is filled with water instead of air. As a consequence, our gel being mostly made of water, we suppress surface tension forces that might generate a spurious blunting of the crack tip, smoothing it at scales smaller than the elastocapillary length $\gamma/E = 1.2\mu\text{m}$.

We show in Fig.3.29 snapshots at very low magnification (macro camera objective) of the crack nucleating at the notch and propagating in the mode I direction. The gel is dyed with indian ink, giving it a dark colour.

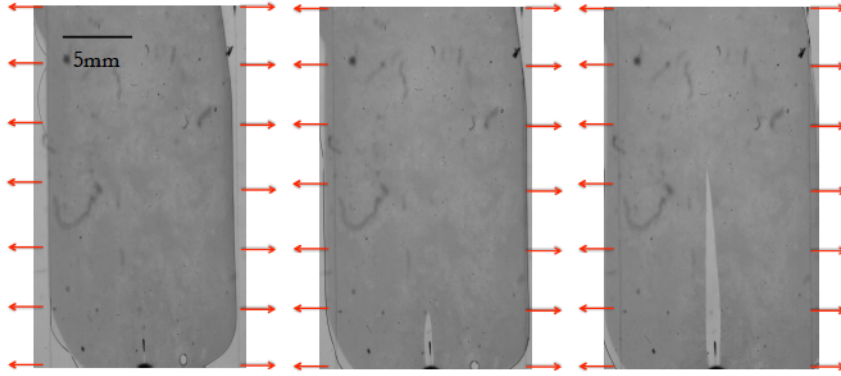


Figure 3.29: Typical nucleation and crack growth observed at low magnification.

Observation of the crack. While the crack is propagating, its crack tip is observed under a transmission microscope with a $4\times$ magnification (observation field 9 mm^2 , pixel size $1.5\mu\text{m}$). The field of view with a $4\times$ objective is represented in red on the left of Fig.3.30 in a picture acquired with macro lens. The same crack is observed at $4\times$ magnification (right of Fig.3.30). Pictures are acquired with a 2040×2048 pixel 8 bit CCD camera; the frames are directly transferred to hard disks able to record in streaming at 60 frames per second in full resolution.

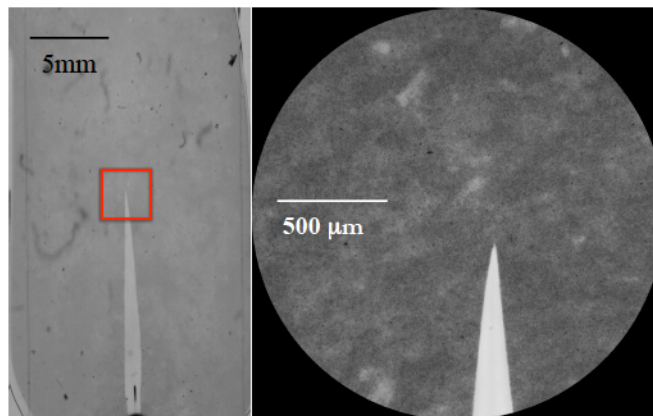


Figure 3.30: Left: Crack observed at low magnification. The red square depicts the field of view with a $4\times$ microscope objective. Right: magnified $4\times$ field of view. The crack appears bright and grows in a dyed gel with a texture provided by carbon-black powder.

On the left of Fig.3.30, we realize that the $4x$ field of view is a small fraction of the specimen and so, that we cannot have both a large field of view and a high magnification. This means we have to choose where to observe during the tensile test. To record a sequence of pictures showing crack propagation, a first possible strategy is to observe at a fixed location of the specimen, to start deformation and to wait for the crack to cross the field of view. This strategy presents a high probability one miss the crack. The second strategy is to continuously record the crack growth from initiation at the notch until it reaches the opposite wall. This can be done by translating the microscope stage while the crack is propagating. We opted mainly for the second strategy except for high-velocity cracks ($V > 1\text{mm/s}$) where it happened to be difficult to follow the crack manually.

Quasi-static cracks. At fixed Q , after a transient acceleration, the crack reaches a propagation regime where the crack velocity V varies very slowly with time, until it starts feeling the edges of the specimen. Within the steady-state regime, sequences of images are captured and processed with a home-made image analysis routine detecting the crack lips. Changing the control parameter Q from 0.1 to $1000\mu\text{L/min}$ enables one to tune V between $1\mu\text{m.s}^{-1}$ and 1cm.s^{-1} : V being always much smaller than the Rayleigh wave speed $V_R \simeq 1\text{m.s}^{-1}$, crack propagation can be considered as quasi-static and dynamic effects always remain negligible. Note that for velocities lower than $1\mu\text{m.s}^{-1}$, crack propagation becomes intermittent: under stress, junctions in the agar gel have time to unzip and the network to relax. For V higher than 1cm.s^{-1} , it becomes difficult to reach steady state.

How to model this crack? In mechanics, a flat thin sheet of material of thickness h is called a plate. The midplane lies halfway between the bottom and top faces. The direction normal to the midplane is the transverse direction. Directions parallel to the midplane are called in-plane directions. Axes x and y are placed in the midplane. A plate loaded in its midplane is said to be in a state of plane stress if the following assumptions hold:

- All loads applied to the plate act parallel to the midplane, and are symmetric with respect to the midplane.
- In-plane displacements, strains and stresses can be taken to be uniform through the thickness.
- The normal and shear stress components in the z direction are zero or negligible.

A practical condition is that the thickness h should be small, typically 10% or less, than the shortest in-plane dimension. In our experiment, the thickness is 5% of the shortest in-plane dimension.

The last condition could have been reasonably questioned if one had not promoted perfect slippage of the gel on the bottom and upper walls using acrylamide brush coating. As a quantitative check that the boundary condition at the wall is a slipping boundary condition, a microPIV control experiment was performed. The micro-PIV system is able to measure the near-wall velocity profile of a gel slab when this specimen is forced to translate in the chamber. A microscope with $1\mu m$ depth-of-field objective scans the specimen while it is translating in the microfluidic device. At every depth, it measures, using a PIV technique, the velocity of fluorescent tracers seeded in the specimen. In fig.3.31, we show the gel velocity with the depth within the specimen: it shows a flat velocity profile on the first $20\mu m$, which means the gels slips on the coated wall.

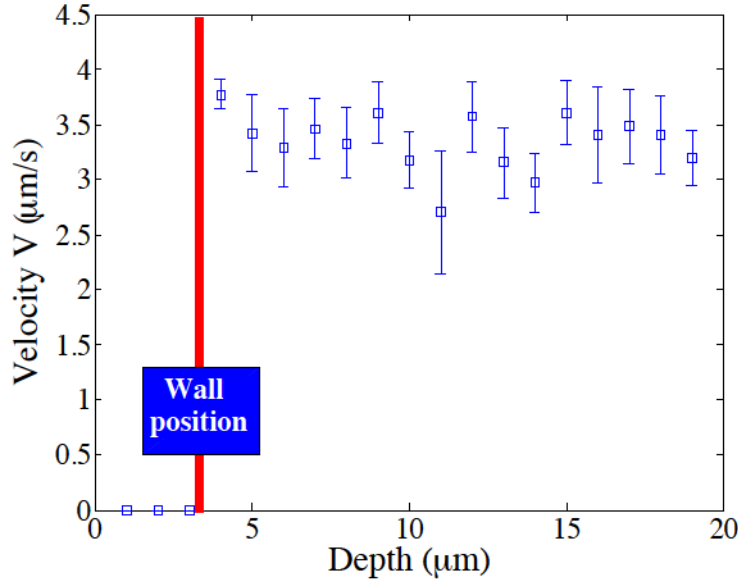


Figure 3.31: Transverse velocity profile for a translating agar gel specimen. The red line signals the glass wall position.

For each experiment, the crack opening displacement (COD) is extracted from the observed shape of the crack, while the full displacement field around the crack tip is determined by using the CorreliQ4 Digital Image Correlation (DIC) code [44]. Full DIC results will be reported later (Chapter 4). The dominance of mode I over mode II ($K_I=50 K_{II}$) will be shown. In this plane stress configuration, we can thus relate directly the energy release rate $\mathcal{G} = K_I^2/E$ [45] with the stress intensity factor (SIF) K_I . K_I can indeed be extracted from the measurement of the displacement along the crack direction, behind the crack tip (see Chapter 4).

3.3.4 Some other tested geometries

A lot of other fracture devices were designed during this PhD. Here one focuses on a specific one, which is shown in Fig.3.32. This device also allows crack nucleation and control of crack propagation. Yet, this Hele-Shaw-like chip is not closed and thus allows only modest physico-chemical control. The whole chip is filled with the agar gel (in red); the hole located above the notch is connected either to a water syringe pump (flow rate controlled crack growth) or to a pressure-controlled water reservoir. When water flows in the chip, a crack initiates from the notch and propagates along the notch direction.

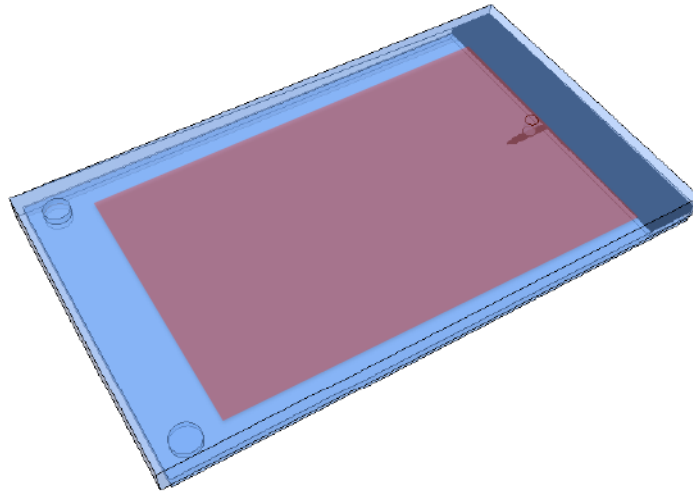


Figure 3.32: Another micromechanical test: an open Hele-Shaw-like chip with lateral hole and built-in notch (in black).

4

Crack tip Displacement Fields

Contents

4.1	Introduction	106
4.2	Learning from the crack shape	108
4.2.1	Mode I Crack profiles in soft materials	108
4.2.1.1	Linear elastic crack tip	108
4.2.1.2	Dugdale-Barenblatt crack tip	113
4.2.1.3	De Gennes' viscoelastic trumpet	119
4.2.2	Crack shape analysis	121
4.2.2.1	Crack mouth detection	121
4.2.2.2	Crack opening displacement	128
4.2.3	Crack opening displacement in agar gels.	132
4.2.3.1	Crack at vanishing velocity: linear elastic case	132
4.2.3.2	Departure from linear elasticity at high crack velocities	136
4.3	Crack displacement fields measured with DIC	141
4.3.1	FE-DIC: a new tool in Soft Matter	143
4.3.1.1	Global versus local approaches	143
4.3.1.2	FE-DIC	145
4.3.2	Performances of FE-DIC applied to our specimen	146
4.3.2.1	Providing texture to our specimen	146
4.3.2.2	How precise is the technique?	149
4.3.3	Capturing displacement field at the crack tip.	154
4.3.4	Projecting the measured field on known displacement fields	160
4.3.4.1	Displacement field libraries	161
4.3.4.2	Projection procedure	165
4.4	Conclusion. A comparison of COD and DIC	178

4.1 Introduction

In the previous chapter, we have shown the possibility to control crack initiation and crack propagation. This ability gives us the unique opportunity to observe cracks at magnifications never reached before. However, capturing a crack tip at high magnification is not a goal *per se*. The challenge is to be able to investigate the elastic, nonlinear elastic and damage processes at stake at the different scales.

From the point of view of the material structure, two scales can be defined. Most theories applying to fracture mechanics deal with the scales at which the material can be defined as a continuum.

1. the matter in the body is continuously distributed and fills the entire region of space it occupies.
2. mean physical quantities such as Young's modulus, volume fraction are well defined and do not depend on the chosen element.

At this scale, measured crack-induced strains are affine (or homogenous). They give experimentalists a way to test material linear and nonlinear constitutive laws, to measure failure criteria or fracture energies, etc. At scales where this continuum approximation breaks down, the material is heterogeneous and the measured strains can show non-affinity. This scale is usually the scale at which structural damage and elementary dissipative processes can be investigated (see Fig. 4.1).

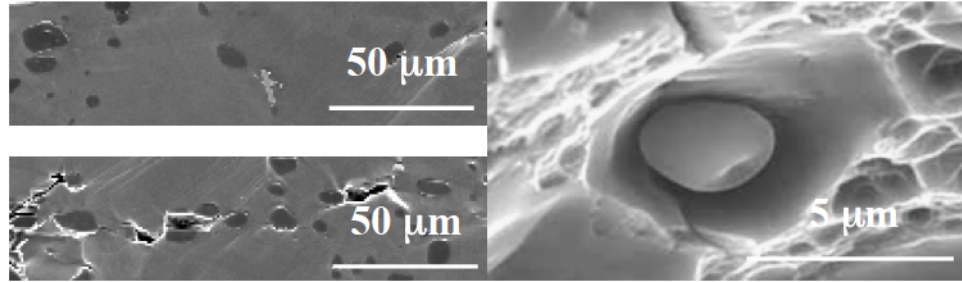


Figure 4.1: Upper left side: SEM image of a Ti₃Al-based alloy showing second phase precipitates (dark spots). At this scale, the material is heterogeneous. Bottom left side: close to the crack surface, this material shows signs of damage. Localized void formation by fracture of the brittle precipitates or at the precipitates/matrix interfaces occurred due to large stresses ahead of the main crack tip (far left). Right: fracture surface of an Al-Si alloy, showing several dimples characteristic of ductile fracture; a precipitate can be seen at the bottom of a deep dimple, which results from a damage cavity nucleated and grown at the matrix/precipitate interface.

Whatever the scale at which the observation is made, one needs a toolbox

allowing to measure material displacements close to the crack tip. To do so, we designed and/or improved two tools.

First technique consists in detecting the crack edges and analyzing the crack shape. Another complementary technique, called *Q4 Digital Image Correlation* and originally developed by F. Hild and S. Roux, allows to precisely map the displacement fields around a crack tip. In this chapter, we will illustrate these two techniques by discussing the case of cracks in a $C=1.5\text{wt}\%$ agar gel observed at scales where continuum mechanics applies.

4.2 Learning from the crack shape

As we previously argued and as we will justify with more details in Section 4.3, the cracks we are dealing with are: (1) mode I cracks, (2) embedded in an agar gel specimen, (3) in a plane stress configuration. In this framework, we will first review the predictions for the crack shape in the framework of three theories that are often referred to in the context of fracture of soft materials:

- Linear Elastic Fracture Mechanics
- de Gennes' viscoelastic trumpet
- Dugdale-Barenblatt crack

4.2.1 Mode I Crack profiles in soft materials

These three theories are based on linear elasticity arguments. We should thus start with recalling the key features of LEFM.

4.2.1.1 Linear elastic crack tip

Let us now examine analytical predictions for the stress and displacement fields around the tip of a slit-like crack embedded in a thin sheet of an ideal Hookean material. The crack configuration and the coordinate systems are shown in Fig.4.2.

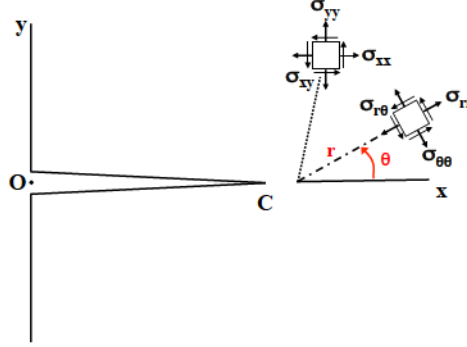


Figure 4.2: Stress field at the crack tip: rectangular and polar coordinates.

Here we need to find the 2D linear elastic displacement and stress fields for a planar problem. The very classic approach is to find the correct "stress function" Φ that satisfies the biharmonic equation (in the absence of body forces) expressed in polar coordinates [46]:

$$\left(\frac{\partial^2}{\partial r^2} + \frac{1}{r} \frac{\partial}{\partial r} + \frac{1}{r^2} \frac{\partial^2}{\partial \theta^2} \right)^2 \Phi = 0 \quad (4.1)$$

This equation expressed in the natural polar coordinates of the undeformed configuration (infinitely thin slit) is a fourth-order differential equation embodying the condition for equilibrium, strain compatibility and Hooke's law. In this calculation Φ is a scalar function of space that allows stress field calculation through:

$$\sigma_{xx} = \frac{\partial^2 \Phi}{\partial y^2}; \quad \sigma_{yy} = \frac{\partial^2 \Phi}{\partial x^2}; \quad \sigma_{xy} = -\frac{\partial^2 \Phi}{\partial x \partial y} \quad (4.2)$$

The boundary conditions are traction-free crack mouths and thus:

$$\sigma_{\theta\theta}(\theta = \pm\pi) = \frac{\partial^2 \Phi}{\partial r^2} = 0; \quad \sigma_{r\theta}(\theta = \pm\pi) = \frac{\partial}{\partial r} \left(\frac{1}{r} \frac{\partial \Phi}{\partial \theta} \right) = 0 \quad (4.3)$$

Trying a solution of the form:

$$\Phi = r^{n+1} f(\theta) \quad (4.4)$$

and reinjecting it in Eq.4.1, we find a function f of the form:

$$\begin{aligned} f(\theta) = & A_1 \cos(n+1)\theta + A_2 \sin(n+1)\theta \dots \\ & \dots + A_3 \cos(n-1)\theta + A_4 \sin(n-1)\theta \end{aligned} \quad (4.5)$$

where we recognize a symmetric part corresponding to mode I, and an anti-symmetric part corresponding to mode II. The stress components are:

$$\begin{aligned} \sigma_{\theta\theta} = n(n+1)r^{n-1}(A_1 \cos(n+1)\theta + A_2 \sin(n+1)\theta \dots \\ \dots + A_3 \cos(n-1)\theta + A_4 \sin(n-1)\theta) \end{aligned} \quad (4.6)$$

$$\begin{aligned} \sigma_{r\theta} = nr^{n-1}[(n+1)(A_1 \sin(n+1)\theta - A_2 \cos(n+1)\theta) \dots \\ \dots + (n-1)(A_3 \sin(n-1)\theta - A_4 \cos(n-1)\theta)] \end{aligned} \quad (4.7)$$

Using the boundary conditions, one can find that n must satisfy $\sin(2n\pi) = 0$ i.e. $n = \pm 1/2, \pm 1, \pm 3/2, \dots$

We see that solutions with $n \geq 1$ generate stresses that do not decay far from the crack tip. They will thus depend on the configuration of the crack remote loading. Besides, LEFM usually rejects solutions with $n < 0$ claiming they correspond to unbounded strain energies. Hui & Ruina have shown that these terms can indeed be rejected in the approximation of Small Scale Yielding [47], i.e., in the case where deviations from linearity occurs in a very small region compared to the specimen dimensions.

For each n , the boundary conditions also allow us to find a relation between A_1 and A_3 :

$$n = 1/2, 3/2, 5/2, \dots; A_1 = -(n-1)A_3/(n+1) \quad (4.8)$$

$$n = 1, 2, 3, \dots; A_1 = -A_3 \quad (4.9)$$

Irwin's Asymptotic term. We first focus on the $n = 1/2$ -term which is called the Irwin's asymptotic term. It is the only term that vanishes far from the crack tip and that does not correspond to diverging strain energies. However, this term induces a diverging stress at the crack tip. For mode I and mode II asymptotic terms, we define the respective amplitudes of the diverging term as K_I and K_{II} , which are called Stress Intensity Factors (SIF). Asymptotic stresses thus write:

$$\begin{aligned} \begin{Bmatrix} \sigma_{xx} \\ \sigma_{yy} \\ \sigma_{xy} \end{Bmatrix} = \frac{K_I}{(2\pi r)^{1/2}} \begin{Bmatrix} \cos(\theta/2)(1 - \sin(\theta/2) \sin(3\theta/2)) \\ \cos(\theta/2)(1 + \sin(\theta/2) \sin(3\theta/2)) \\ \sin(\theta/2) \cos(\theta/2) \cos(3\theta/2) \end{Bmatrix} \\ + \frac{K_{II}}{(2\pi r)^{1/2}} \begin{Bmatrix} -\sin(\theta/2)(2 + \cos(\theta/2) \cos(3\theta/2)) \\ \sin(\theta/2) \cos(\theta/2) \cos(3\theta/2) \\ \cos(\theta/2)(1 - \sin(\theta/2) \sin(3\theta/2)) \end{Bmatrix} \end{aligned} \quad (4.10)$$

The mode I asymptotic displacement field, in a material of Young's modulus E and Poisson's ratio ν , is:

$$\begin{Bmatrix} u_x \\ u_y \end{Bmatrix} = \frac{K_I}{2E} \left(\frac{r}{2\pi} \right)^{1/2} \begin{Bmatrix} (1+\nu)[(2\kappa-1) \cos \theta/2 - \cos 3\theta/2] \\ (1+\nu)[(2\kappa+1) \sin \theta/2 - \sin 3\theta/2] \end{Bmatrix} \quad (4.11)$$

and the corresponding mode II field is:

$$\begin{Bmatrix} u_x \\ u_y \end{Bmatrix} = \frac{K_{II}}{2E} \left(\frac{r}{2\pi} \right)^{1/2} \begin{Bmatrix} (1+\nu)[(2\kappa+3)\sin\theta/2 + \sin 3\theta/2] \\ -(1+\nu)[(2\kappa-1)\cos\theta/2 + \cos 3\theta/2] \end{Bmatrix} \quad (4.12)$$

Our material being considered as incompressible: $\nu = 1/2$ and, in plane stress, we thus have $\kappa = (3-\nu)/(1+\nu) = 5/3$. Considering a mode I crack, we can write the displacement of the crack mouth as:

$$\begin{Bmatrix} u_x \\ u_y \end{Bmatrix} (\theta = \pm\pi) = \pm \frac{K_I}{2E} \left(\frac{r}{2\pi} \right)^{1/2} \begin{Bmatrix} 0 \\ 8 \end{Bmatrix} = \pm \frac{4K_I}{E} \left(\frac{r}{2\pi} \right)^{1/2} \mathbf{e}_y \quad (4.13)$$

Here, we find that the Irwin's term corresponds to a parabolic crack opening. It is important to note that, in the near field, details of the applied loading (specimen geometry and nature of the loading) enter only through the value of K_I . However, if, at intermediate distance from the crack tip, we want to match the stress and displacement fields with the applied loading, higher-order terms need to be included in the expansion. These higher order terms are the one corresponding to $n \geq 1$.

William's expansion. In the previous paragraph, we have focused on the Irwin term corresponding to $n = 1/2$ and emphasized the importance of higher order terms to match the far-field stresses. Now, we focus on a pure mode I plane stress crack and compute its shape when including the higher order terms.

Following William's approach [48], we start from the solution of Coker [49] in which it is shown that displacements in polar coordinates are related to the stress function Φ by:

$$2Gu_r = \frac{\partial\Phi}{\partial r} + (2/3)r\frac{\partial\Psi}{\partial\theta} \quad (4.14)$$

$$2Gu_\theta = -\frac{1}{r}\frac{\partial\Phi}{\partial\theta} + (2/3)r^2\frac{\partial\Psi}{\partial r} \quad (4.15)$$

where the displacement potential Ψ is such that:

$$\nabla^2\Phi = \frac{\partial}{\partial r} \left(r \frac{\partial\Psi}{\partial\theta} \right) \quad (4.16)$$

Using Eq. (4.4), Eq. (4.5) (with $A_2 = 0$ and $A_4 = 0$ in pure Mode I), we can write Ψ as a similar series as Φ :

$$\Phi(r, \theta) = r^{n+1}(A_1 \cos[(n+1)\theta] + A_3 \cos[(n-1)\theta]) \quad (4.17)$$

$$\Psi(r, \theta) = r^m(a_1 \cos(m\theta) + a_2 \sin(m\theta)) \quad (4.18)$$

Substituting Eq.(4.18) into Eq.(4.16), we find $a_1 = 0$, $a_2 = 4A_3/(n-1)$ and $m = n-1$. Using Eq. (4.15), we can compute u_r and u_θ :

$$2Gu_\theta = r^n[A_1(n+1)\sin[(n+1)\theta] + A_3(n-1)\sin[(n-1)\theta]] \\ + (8/3)A_3r^n\sin((n-1)\theta) \quad (4.19)$$

$$2Gu_r = (n+1)r^n(A_1\cos[(n+1)\theta] + A_3\cos[(n-1)\theta]) \\ + (8/3)A_3r^n\cos[(n-1)\theta] \quad (4.20)$$

We calculate displacements of the crack lips ($\theta = \pm\pi$). We first consider terms with $n = 1/2, 3/2, 5/2$, which satisfy Eq. (4.9) and thus, Eq. (4.20) becomes:

$$2Gu_\theta(r, \pm\pi) = \pm(8/3)A_3r^n\sin((n-1)\pi) \quad (4.21)$$

$$2Gu_r(r, \pm\pi) = 0 \quad (4.22)$$

Terms with $n = 1, 2, 3$ satisfy Eq. (4.9) and thus, Eq. (4.20) becomes:

$$2Gu_\theta(r, \pm\pi) = 0 \quad (4.23)$$

$$2Gu_r(r, \pm\pi) = (8/3)A_3r^n\cos[(n-1)\pi] \quad (4.24)$$

For $n = 1/2$, we immediately recover the Irwin's term found in Eq.(4.13). The first additionnal term is the " $n = 1$ "-term. It corresponds to a stress amplitude $4A_3$ that does not vary with the distance to the crack tip and which is called T-stress. It does not contribute to u_θ ; its contribution to u_r is $(4A_3/E)r = Tr/E$.

To summarize, the terms contributing to the crack opening are the terms $n = 1/2, 3/2, 5/2, \dots$ and the terms $n = 1, 2, 3, \dots$ contribute to u_r :

$$u_\theta(r) = \frac{4K_I}{E} \left(\frac{r}{2\pi}\right)^{1/2} + A_{3/2}r^{3/2} + A_{5/2}r^{5/2} + \dots \quad (4.25)$$

$$u_r(r) = \frac{Tr}{E} + A_2r^2 + A_3r^3 + \dots \quad (4.26)$$

4.2.1.2 Dugdale-Barenblatt crack tip

Cohesive zone formalism. The previous section dealt with a crack embedded in a linear elastic material and one of its main conclusions was that, sufficiently close from the crack tip, the stress and displacement fields were dominated by Irwin's term in the approximation of Small Scale Yielding. As this term is predicting a diverging stress at the crack tip, it necessarily implies there is a region, in the vicinity of the crack tip, where linear elasticity breaks down.

Dugdale-Barenblatt models developed a way to regularize the diverging fields at the crack tip. They introduce what they call a cohesive zone: in this zone, there is a balance between the opening stresses (transmitted from infinity through the linear material) and some closing stresses, also called cohesive stresses. Cohesive stresses are intrinsic attractive surface forces that exert between the two material planes that are to be separated after crack extension. These cohesive stresses help maintaining the material integrity in the crack tip vicinity.

A typical cohesive stress-separation curve is plotted in Fig. 5.9: it shows the typical variation of the cohesive stress when separating two neighboring atomic planes. The stress-separation curve is linear for low separation; it starts showing non linearity, exhibits a maximum (as $2(u - u_0)$ increases) at some yielding point, and goes back to zero when the separation distance exceeds some length scale δ .

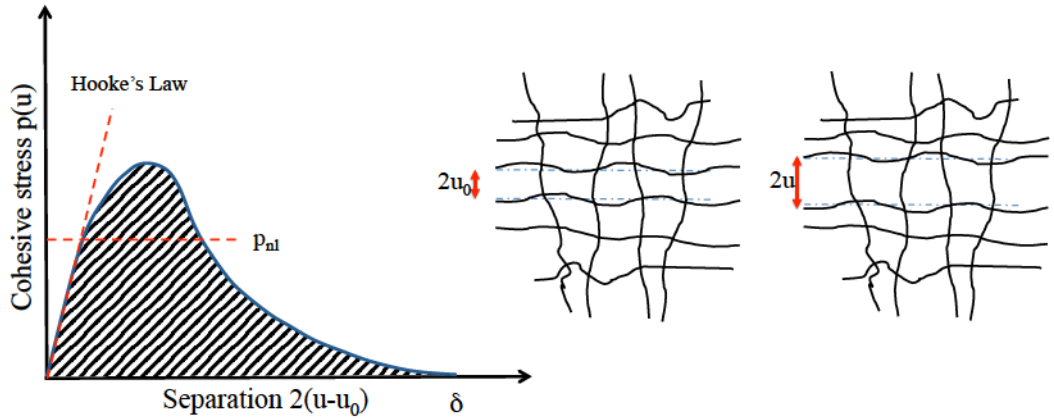


Figure 4.3: Cohesive stress with separation $2(u - u_0)$ for two atom planes. $2u_0$ refers to the equilibrium distance between the two planes while $2u$ is the imposed distance between the two material planes. Work to separate planes beyond $2(u - u_0) = \delta$ defines the work of cohesion R_0 . In Dugdale model, one assumes that $p(u) = \sigma_{yd}$ such that $R_0 = \sigma_{yd}\delta$.

As mentioned in Part. 4.2.1.1, providing we are very close to the crack tip and that the cohesive zone is small, there is a zone where Irwin's term

dominates. In this zone, knowing the external stress intensity factor K_{Iout} is sufficient to know the local fields: the cracked specimen with complex geometry and complex loading can thus be profitably replaced by an equivalent specimen with remote stresses (in blue) such that the local K_I field applies. To model the cohesive zone at the tip, one considers a zone of size λ (in red) where a distribution of cohesive stresses $p(X)$ (X being the distance to the crack tip) helps closing the crack and cancelling out Irwin's singularity. The balance between external and intrinsic stress is illustrated in Fig. 4.4.

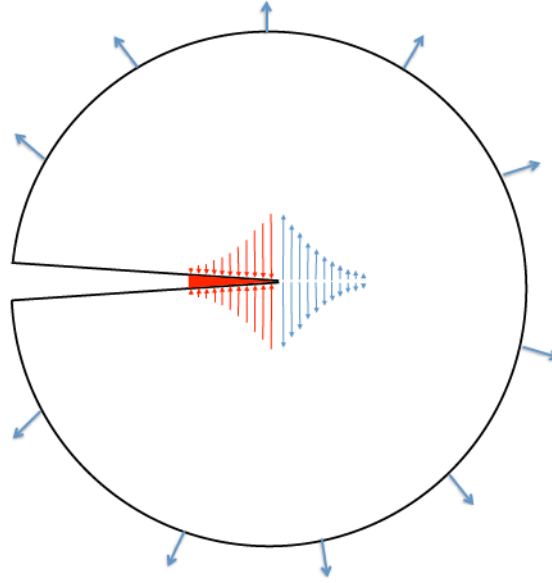


Figure 4.4: Local balance between the external stress field (in blue) and the cohesive stress field (in red) over a distance λ at the crack tip. These two superimposed stress fields of opposite sign predict divergences of the stress field. At equilibrium, the two divergences should cancel out.

One can show [46] that the internal cohesive loading of the crack in the cohesive zone is equivalent to a negative stress intensity factor K_0 such that:

$$K_0 = (2/\pi)^{1/2} \int_0^\lambda \frac{p(X)}{X^{1/2}} dX \quad (4.27)$$

with corresponding dominant term for the crack opening in plane stress:

$$u_y(X) = \frac{4K_0}{E} \sqrt{\frac{X}{2\pi}} \quad (4.28)$$

The Barenblatt requirement for equilibrium is that $K_{Iout} = -K_0$. In other words, the singular term due to cohesive stress inside the crack is cancelled out by the singular term due to external loading. It is thus necessary to proceed further in the power expansions of σ_y and u_y .

A cusp-like crack tip. To solve this problem, one consider a linear elastic plane stress crack of size a subjected to an internal pressure distribution $p(x)$. The crack thus lies between $x = 0$ and $x = a$. It can be shown that [46]:

$$\begin{aligned} x \leq a, \quad u_y(x, 0) &= \frac{4}{\pi E} \int_x^a \frac{tg(t)dt}{\sqrt{t^2 - x^2}} \\ &= \frac{4}{\pi E} \left[g(a)\sqrt{a^2 - x^2} - \int_x^a g'(t)\sqrt{t^2 - x^2} \right] \end{aligned} \quad (4.29)$$

$$\begin{aligned} x \geq a, \quad \sigma_y(x, 0) &= \frac{-2}{\pi} \frac{d}{dx} \int_0^a \frac{tg(t)dt}{\sqrt{x^2 - t^2}} \\ &= \frac{2x}{\pi} \left[\frac{g(a)}{\sqrt{x^2 - a^2}} - \int_0^a \frac{g'(t)dt}{\sqrt{x^2 - t^2}} \right] \end{aligned} \quad (4.30)$$

where:

$$g(t) = \int_0^t \frac{p(s)ds}{\sqrt{t^2 - s^2}} \quad (4.31)$$

$$g'(t) = \frac{1}{t} \int_0^t \frac{sp'(s)ds}{\sqrt{t^2 - s^2}} \quad (4.32)$$

As, in 4.32, $p(s)$ is non zero over a distance λ from the crack tip

$$g(t) = \int_{t-\lambda}^t \frac{p(s)ds}{\sqrt{t^2 - s^2}} \quad (4.33)$$

$$g'(t) = \frac{1}{t} \int_{t-\lambda}^t \frac{sp'(s)ds}{\sqrt{t^2 - s^2}} \quad (4.34)$$

Let us derive the asymptotic shape of a Barenblatt crack. In the expression 4.30, as $\lambda \ll a$, t is very close to a and $g'(t)$ is close to $g'(a)$ when x is close to a . Hence:

$$\int_x^a g'(t)\sqrt{t^2 - x^2} \simeq g'(a)\sqrt{(2a)} \int_x^a \sqrt{t - x} dt \quad (4.35)$$

i.e :

$$u_y(x, 0) \simeq \frac{4}{\pi E} \left[g(a)\sqrt{a^2 - x^2} + \frac{2}{3}g'(a)\sqrt{2a}(a - x)^{3/2} \right] \quad (4.36)$$

Using Eq. (4.27), we easily prove that $K_0 = 2\sqrt{\frac{a}{\pi}}g(a)$. Therefore, at Barenblatt equilibrium, when superimposing the crack opening due to external field and the one due to internal pressure distribution, the first term in 4.36 disappears. The remaining term is a term is proportionnal to $X^{3/2}$. This means that Barenblatt cohesive zone model predicts a cusp-like shape at the very crack tip.

Dugdale Case. There is one special case for which the entire crack shape can be solved analytically: that of a constant cohesive stress σ_{yd} over the cohesive zone between $x = a - \lambda = c$ and $x = a$. This assumption results in very simple relationships:

$$K_{Iout} = -K_0 = \left(\frac{8}{\pi}\right)^{1/2} \sigma_{yd} \lambda^{1/2} \quad (4.37)$$

$$\text{or } \lambda = \frac{\pi E}{8} \frac{\mathcal{G}}{\sigma_{yd}^2} \quad (4.38)$$

These relations have a remarkable property: they do not depend on the crack geometry but only on the microscopic details of failure.

One can write:

$$g(t) = \sigma_{yd} \arccos c/t \quad (4.39)$$

$$g'(t) = \frac{\sigma_{yd} c}{t \sqrt{t^2 - c^2}} \quad (4.40)$$

The displacement of the crack mouth is:

$$u_y(X) = (2\sigma_{yd}/\pi E) \left[c \log \left(\frac{|\xi - 1|}{\xi + 1} \right) - x \log \left(\frac{|c\xi - x|}{c\xi + x} \right) \right] \quad (4.41)$$

with

$$\xi = \sqrt{\frac{a^2 - x^2}{a^2 - c^2}} \quad (4.42)$$

$$\text{for } x \simeq a, \xi \simeq \sqrt{\frac{a - x}{a - c}} = \sqrt{\frac{X}{\lambda}} \quad (4.43)$$

On the edge of the cohesive zone, $X = \lambda$ and $2u = \delta$ with:

$$\delta = \frac{8\sigma_{yd}}{\pi E} \lambda \quad \text{i.e. } \mathcal{G} = \sigma_{yd} \delta \quad (4.44)$$

In agar gels, Dugdale model is simple but reasonably relevant. It is expected that the physical junctions yield at a moderate (but still unknown) stress, that is sufficient to unzip the physical bonds. It is also likely that the length scale δ introduced in Fig. 5.9, which is the maximum opening of the cohesive zone, is of the order of the chain contour length $\Lambda = 450\text{nm}$. Assuming σ_{yd} of order E would give $\lambda \simeq 1\mu\text{m}$ and $\mathcal{G} = 3.10^{-2} \text{J/m}^2$.

Fig. 4.5 shows asymptotic Dugdale crack profiles plotted using Eq. (4.41). The maximum opening of the cohesive zone is fixed at $\delta = \Lambda = 450\text{nm}$ and the yield stress σ_{yd} is varied between $\sigma_{yd} = E/10$ (black) and $\sigma_{yd} = E$ (blue). In ξ , the crack size a is chosen at 10mm and $c = a - \lambda$ is computed using Eq. (4.38). \mathcal{G} is computed using Eq. (4.44).

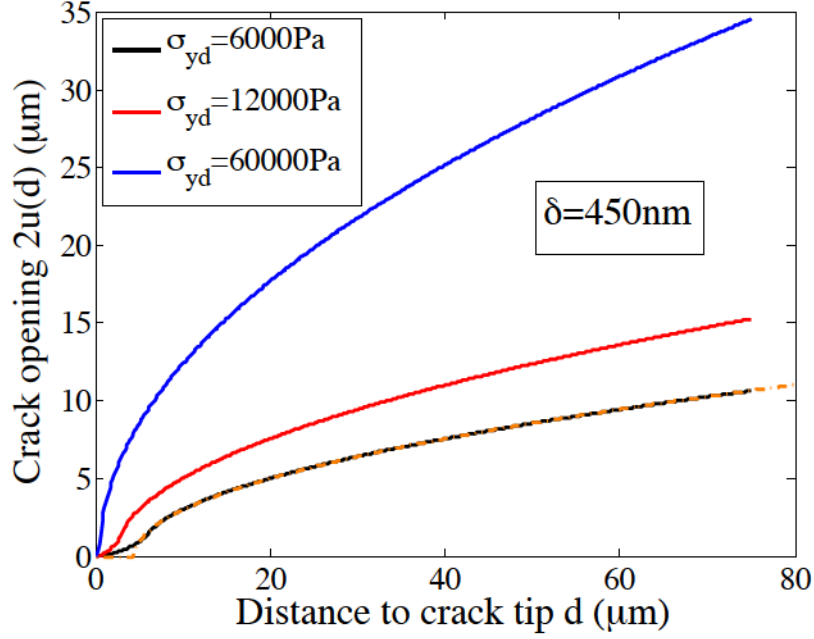


Figure 4.5: Asymptotic Dugdale crack profiles at our experimental resolution. The maximum opening of the cohesive zone is fixed at $\delta = \Lambda = 450 \text{ nm}$ and the yield stress σ_{yd} is varied between $\sigma_{yd} = E/10$ (black) and $\sigma_{yd} = E$ (blue). In the far-field, a parabolic profile (shown in orange dashed dots in Fig.4.5) is recovered.

Here, we realize that, at fixed δ , the resulting crack shape depends a lot on the yield stress. For low $\sigma_{yd} = E/10$, the cusp-like region is $7 \mu\text{m}$ long and is thus clearly visible. In the far-field, a parabolic profile (shown in orange dashed dots in Fig.4.5) is recovered. For higher σ_{yd} , the cohesive zone can hardly be detected and the profile is nearly perfectly parabolic.

4.2.1.3 De Gennes' viscoelastic trumpet

In the 90's, de Gennes [50] proposed a very simple model predicting the crack shape and fracture energy in a linear viscoelastic material. The material complex modulus $\mu(\omega)$ is the one of a standard linear solid with a unique relaxation time τ . It qualitatively well reproduces the high frequency rheology of rubbers or entangled polymer melts (see Fig.2.14).

$$\mu(\omega) = G_0 + (G_\infty - G_0) \frac{i\omega\tau}{1 + i\omega\tau} \quad (4.45)$$

The linear oscillatory rheology response of such a material is shown in Fig. 4.6. At low frequencies, the material behaves as a soft solid of shear modulus G_0 . At high frequencies, one recovers a hard solid ($G = G_\infty$). We define $r = G_\infty/G_0$. When $1/(r\tau) < \omega < 1/\tau$, the material behaves as a liquid of viscosity $\eta = (G_\infty - G_0)\tau$.

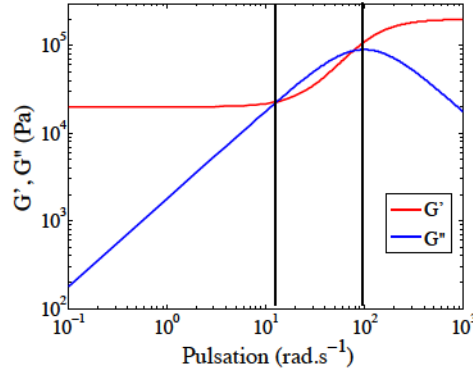


Figure 4.6: Linear oscillatory rheology of a linear standard solid with $G_0 = 20kPa$, $G_\infty = 200kPa$ and $\tau = 0.01s$.

As the equations describing mechanical equilibrium ($\nabla\sigma = 0$) and compatibility equations do not depend on the material constitutive law, the relation $\sigma(r) \simeq K_0/(r^{1/2})$ still holds, where the stress intensity factor K_0 , in a Dugdale Barenblatt vision, is associated with the local dissipative processes happening in the process zone of size λ .

Let us now find the overall shape of this crack. One uses the fact that, for a material point at a distance x of the tip of a crack propagating at velocity V , the local pulsation is $\omega = V/x$. Thus, for $\lambda < x < V\tau$, the material point is in the strong solid zone and $u = (K_0/G_\infty)x^{1/2}$. In the liquid zone, $\sigma = \eta V \frac{d^2u}{dx^2}$ and thus $u \propto x^{3/2}$. For $x > rV\tau$, the material is back in the soft solid zone and $u = (K_0/G_0)x^{1/2}$. The crack shape is shown in Fig. 4.7.

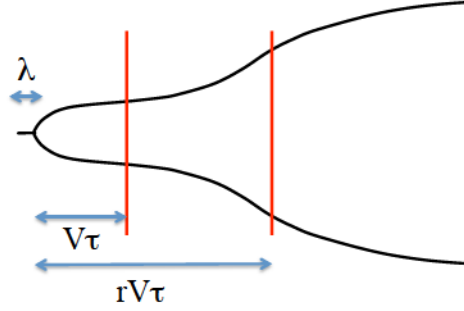


Figure 4.7: Viscoelastic trumpet for a crack propagating at a velocity V in a standard linear viscoelastic solid with a single relaxation time τ .

In our case, regarding our material viscoelastic characterization (see Part. 2.3.1), the only part of the spectrum where $G'' > G'$ is its high frequency range, above $\omega_e = 1/(\tau_0 N_{int}^2)$. We have seen previously that, for a 0.2wt% gel, ω_e was about 100 rad.s^{-1} . For the concentration at which we work ($C = 1.5 \text{ wt\%}$), N_{int} will decrease, so that ω_e is expected to strongly increase. For a crack propagating at 1 mm/s , a minimal value of $\omega_e = 1000 \text{ rad.s}$ gives a maximal size of hard solid zone of $1 \mu\text{m}$: we will not be able to see the strong solid zone!

The overall crack shape then depends on r . If r is large enough (but we do not have any means to measure it) the crack tip we will observe will have a cusp shape with $u \propto r^{3/2}$. if r is close to 1, the viscous regime disappears and one recovers the parabolic profile of the soft solid.

4.2.2 Crack shape analysis

In the previous section, we reviewed some of the standard theories giving predictions for crack shapes in soft linear elastic materials. LEFM predicts a parabolic crack tip. Meanwhile, Dugdale Barenblatt cohesive zones and de Gennes viscoelastic model can, under some circumstances, predict a regime where $u \propto r^{3/2}$ at the very crack tip. In any case, measuring the crack shape and comparing it with the previous models will enable us to gain insight into where we stand and to know more about the way the material fails.

4.2.2.1 Crack mouth detection

As mentionned in the Experimental Chapter, the crack tip is observed under a transmission microscope using a $4\times$ magnification objective. The gel is dyed with a few ppm of indian ink, which makes it dark. Meanwhile, the inside of the crack is filled with undyed water. Before each experiment, lighting is tuned to improve the contrast between the gel and the fracturing liquid. A typical picture and its corresponding histogram are shown on Fig. 4.8.

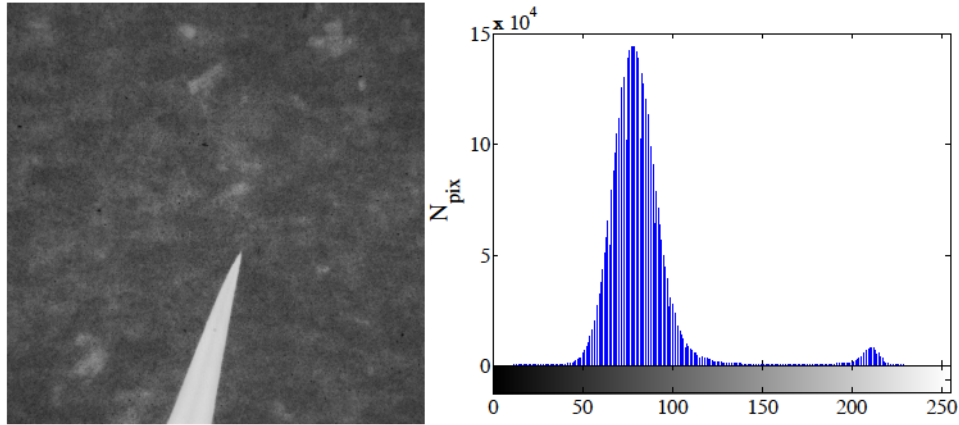


Figure 4.8: Left: Snapshot of a low-velocity crack (white) in a dyed 1.5%wt agar gel. The interior of the crack is filled with water. Right: Histogram of the acquired image. There is a good separation between the dark pixels corresponding to the dyed gel and the bright ones corresponding to the inside of the crack.

The challenge is to be able to detect the crack edges until the very tip of the crack. In Fig. 4.9, the grey level profiles along 2 different lines are shown. First, the dark and bright values can be different depending on the position of the cross-section line. Behind the tip, the bright value is more than 200. At the tip, it can go down to 150. The choice of threshold grey levels for binarizing the image is thus not obvious. Furthermore, due to the

gel texture and its associated gray level variation, it could be delicate to determine where the crack edges really are. At the crack tip, it might be difficult to distinguish between pixels that are inside the crack from the ones that are inside the material.

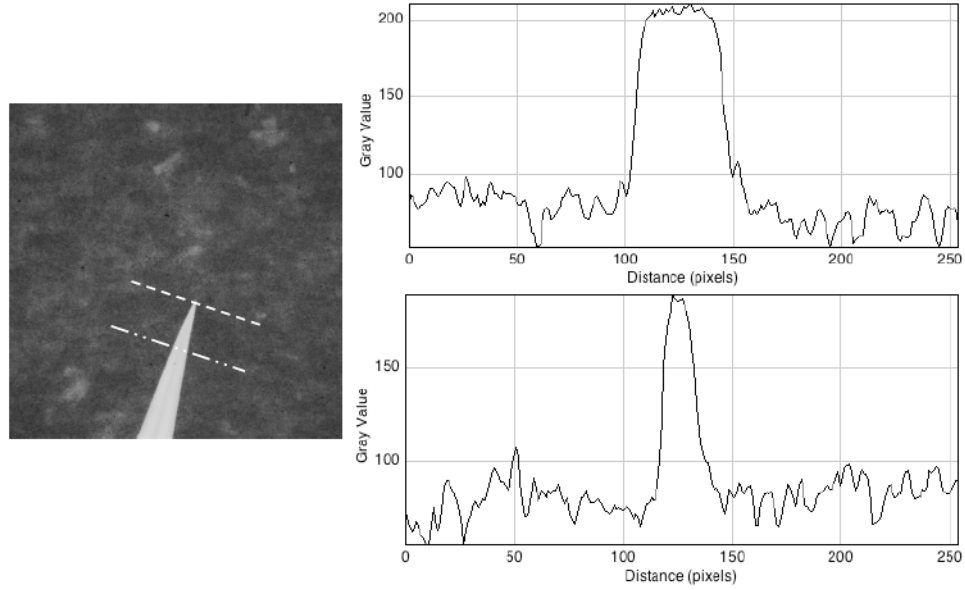


Figure 4.9: Left: Position of the two cross-section lines used to plot the profiles on the right. Top Right: Gray level profile along the line crossing the crack far behind its tip. Bottom Right: Gray level profile along the line crossing the crack close to the tip.

To determine properly the crack shape, one proceeds as follows:

- Background subtraction.

Regarding the histogram just above (Fig. 4.8), we have to define a criterion allowing us to determine if a given pixel belongs to the inner crack or to the outer crack. On the raw picture (uncorrected), the graylevel in the gel has fluctuations due to the gel texture: it can typically vary between 50 for the darkest graylevels and 140 for the brightest ones. The brightest pixels, corresponding to the inside of the crack, have gray levels between 190 and 220. However, there does exist a few pixels with gray values in between 140 and 190. One need to choose a cutoff graylevel GL_c in between 140 and 190 (Rule(1)). The first operation is to subtract from the image the constant graylevel GL_c : here we choose a graylevel of 150 (see Fig. 4.10).



Figure 4.10: Image with substracted background.

We then show magnifications of the crack tip for pictures without and with substraction (Left of Fig. 4.11). Graylevel profiles along a section line very close to the crack tip are shown for uncorrected and corrected pictures (Right of Fig. 4.11).

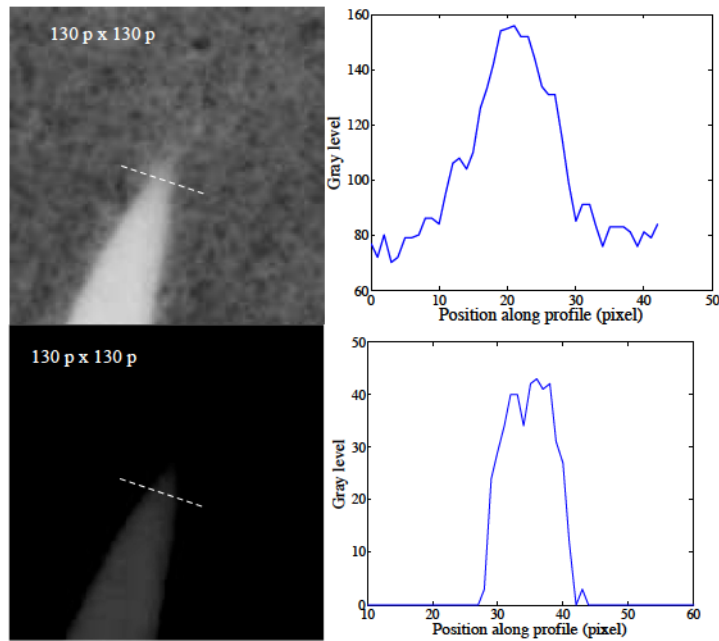


Figure 4.11: Cross section profiles without and with substracted background.

After substraction, the edges are much simpler to detect due to the reduction of gray level fluctuation outside the crack.

- Image adjustment.

One shall now choose two thresholds (threshmin and threshmax) for image adjustment. All pixels below threshmin are set to 0. All pixels above threshmax are set to 255. Pixels with intermediate gray values are attributed a gray value $255 * \frac{GL - \text{threshmin}}{\text{threshmax} - \text{threshmin}}$. Rule(2): Choosing threshmin and threshmax that delimits the steepest part of the gray level profile.

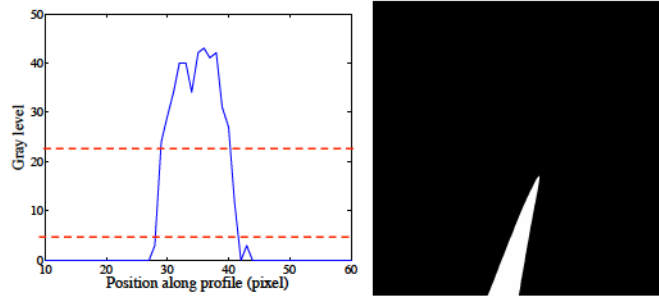


Figure 4.12: Left: Choice of the two thresholds (threshmin and threshmax) for image adjustment. All pixels below threshmin are set to 0. All pixels above threshmax are set to 255. Pixels with intermediate gray values are attributed a gray value $255 * \frac{GL - \text{threshmin}}{\text{threshmax} - \text{threshmin}}$. Right: Resulting picture.

- Image binarization.

The previous image is binarized using a gray level threshold of 256/2. Fig. 4.13 shows a zoom of the original image multiplied by the negative of the binarization result. It allows to compare the original and binarized crack shape and to check quantitative agreement. The procedure is able to capture the crack shape with good precision. We estimate the detection error $\pm 2\text{pixels}$ at the most.

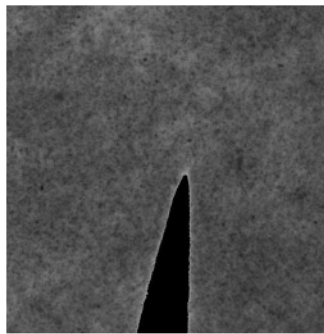


Figure 4.13: Left: Original image multiplied by the negative of the binarization result. The image is 500pixel x 500pixel. The bright shell around the binarized zone is about 2 pixel size.

For each sequence of images, the set of proper parameters is determined and used to perform the binarization of all the images. The procedure for determining the good set of parameters is semi-automatic. First, the parameters are first chosen on the basis of the histogram. Then, if a large discrepancy is observed between the binarized crack and the "observed" crack, the parameters are fine tuned until we get a good agreement. We did not observe a large effect of the choice of parameters providing one follows rules (1) and (2). More systematic way to determine GLc would imply analyzing the histogram more carefully.

4.2.2.2 Crack opening displacement

Plotting the crack opening displacement consists in plotting the crack opening u or $2u$ versus the distance to the crack tip. To do so, one needs to stand in the natural frame of the crack; which is known if both the crack tip position and the crack axis are determined (see Fig.4.2).

Crack tip detection. First step consists in detecting the crack tip. Once binarized, the sequence of binary frames is turned into a sequence of text files, each of this text file containing the x-y coordinates of the crack edges. But, as mentioned earlier, the crack is not always propagating in the vertical direction. It may have some angle with the vertical direction, as for example in the case of Fig.4.12. To have a first estimate of the crack tip position, one rotates the frame such that the crack points toward the vertical direction (see Fig.4.14). The crack tip position X_{CT} is simply defined as the upper point of the contour. One then defines a size of interest $l_{sizebox}$. This will set the upper length scale at which the crack profiles will be studied.

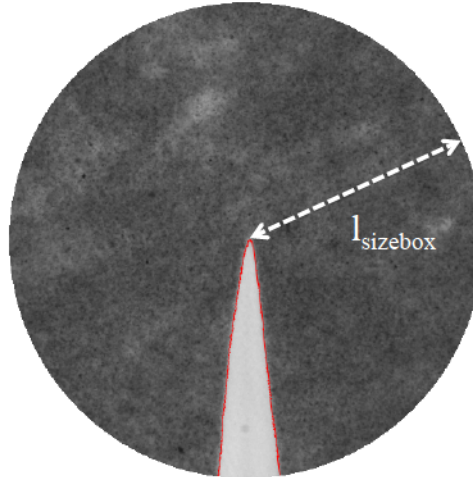


Figure 4.14: Original picture with superimposed contour of the crack (in red). The picture has been rotated such that the crack points toward the vertical direction. The parts of the picture and contour points at a distance larger than $l_{sizebox} = 450pixels$ from the crack tip have been cropped.

Now the crack tip and crack orientation are known, it is possible to plot the crack in the crack natural frame.

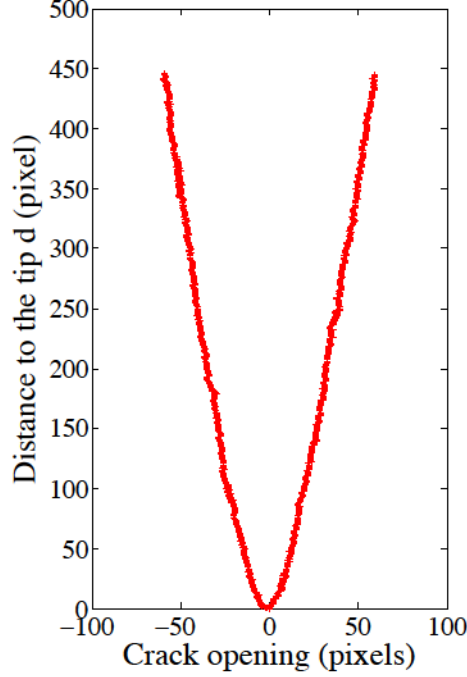


Figure 4.15: Plot of the crack shape in its natural frame.

Measurement of the crack velocity. The crack velocity is computed from the crack tip positions recorded at successive times. The camera acquisition frame rate f can be varied between $1Hz$ and $60Hz$ depending on the crack velocity. At $4\times$ magnification, the pixel size is $1.5\mu m$ and the crack tip position can be determined within a circle of radius 2 pixels. If the velocity $V = \frac{\Delta x}{\Delta t}$ is computed using two consecutive positions, Δx will be the distance over which the crack has propagated over a time $\Delta t = 1/f$. In that case, the relative uncertainty is:

$$\left| \frac{\delta V}{V} \right| = \left| \frac{\delta x}{\Delta x} \right| + \left| \frac{\delta t}{\Delta t} \right| \quad (4.46)$$

For a crack propagating at $3\mu m/s$, the motion is captured at a frame rate of $1Hz$: we can reasonably neglect the temporal relative uncertainty. Spatial uncertainty is $\delta x = 2\text{pixels}$ while the crack extension is $\Delta x = 2\text{ pixels}$. Relative uncertainty is thus close to 100%. Crack velocity measurements are shown on the upper left side of Fig.4.16 for 50 consecutive images. It shows fluctuations comparable to the mean signal amplitude.

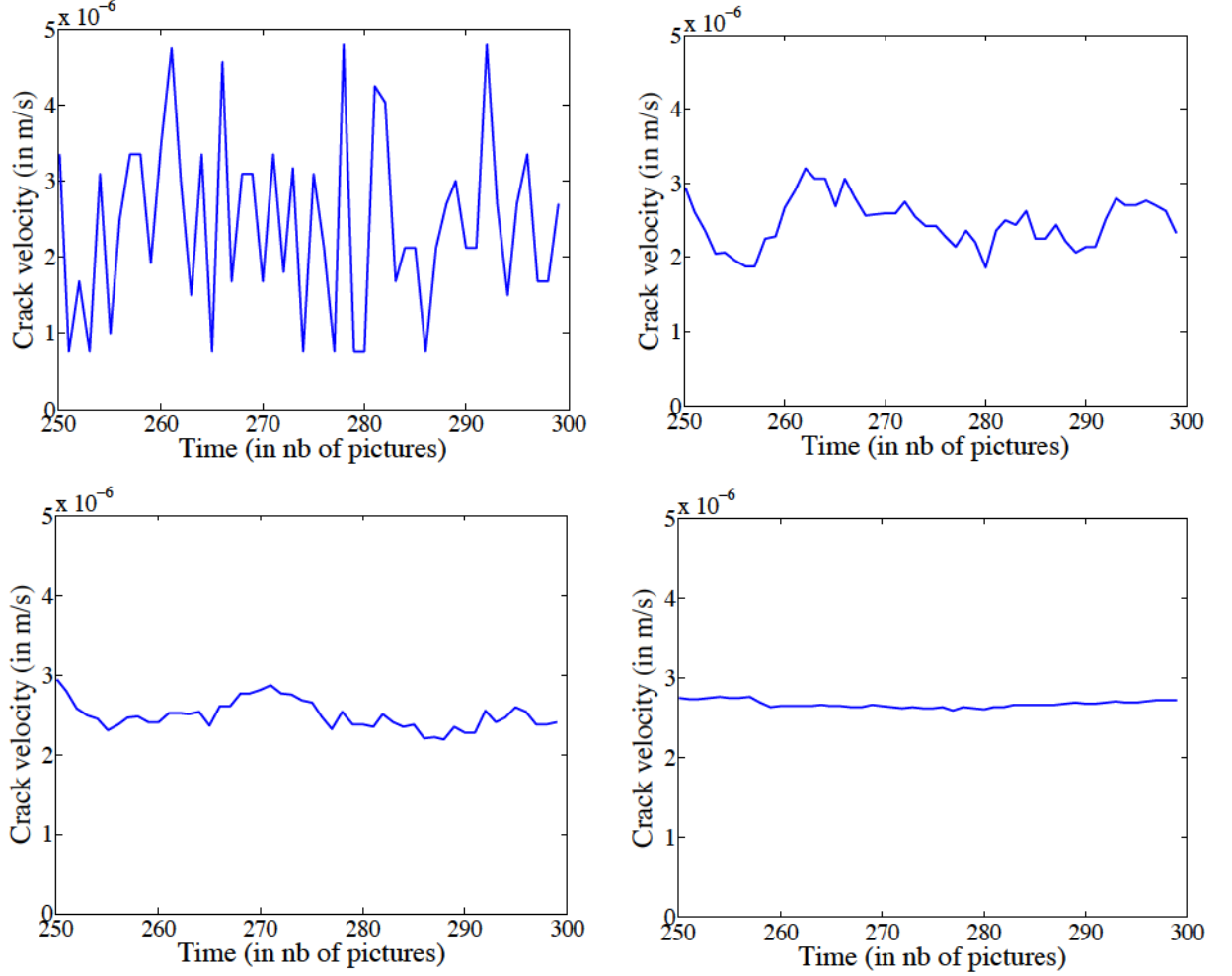


Figure 4.16: Velocity measurement: from instantaneous velocity to velocity averaged over n time steps. From top to bottom and from left to right: $n = 1$; $n = 10$; $n = 20$; $n = 100$.

To improve the crack velocity measurement, one can of course increase the time interval over which we measure the change in crack position. Keeping the same uncertainty on crack tip detection, Δx is increased such that velocity fluctuations decrease. In Fig.4.16, are shown velocity measurements using 1, 10, 20 and 100 time steps for Δt (from left to right and top to bottom). For 20 time steps, the standard deviation of the fluctuations are 5% of the mean value and $\delta x / \Delta x = 1/20$, which seems satisfactory. For the experiments at higher velocities, the uncertainty on acquisition time is still negligible and δx does not vary: one always chooses the time interval Δt in order to have $\delta x / \Delta x = 1/20$ i.e., $\Delta x = 40 \text{ pixels}$.

4.2.3 Crack opening displacement in agar gels.

Previously, we have explained how the crack profile could be measured. We now take the example of quasi static cracks propagating in a physical polymer gel of agar. We show that the prediction of LEFM for the crack shape holds at vanishing crack velocity but starts collapsing as soon as the crack velocity increases (still in the quasi-static regime).

4.2.3.1 Crack at vanishing velocity: linear elastic case

Figure 4.18 shows a typical snapshot of a crack in the low velocity range ($V=3\mu\text{m.s}^{-1}$). The corresponding Crack Opening Displacement (COD), i.e. the crack width $2u$ versus the distance d to the crack tip, is shown in Fig.4.17.

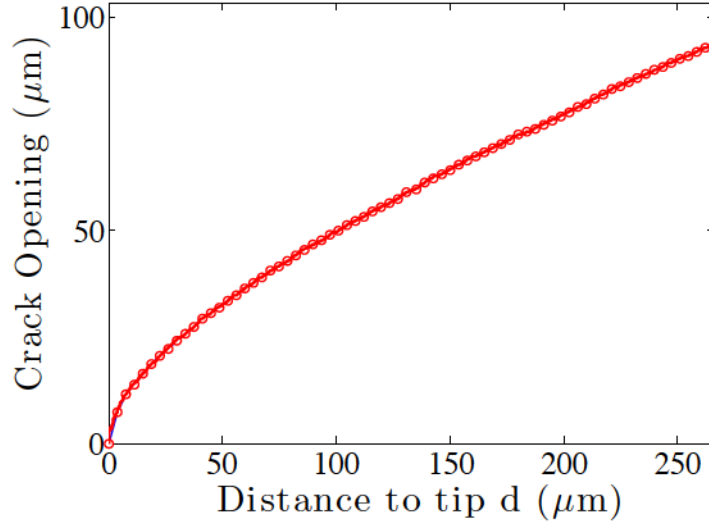


Figure 4.17: **Slow crack** ($V=3\mu\text{m.s}^{-1}$). Crack opening (displacement along the crack mouth) as a function of the distance d to the crack tip. Red line with circles: experimental results.

Here, the COD was plotted differently than in Fig.4.15. Due to crack symmetry (which is itself a consequence of local Mode I), one does not lose any information by plotting the width of the crack $2u$ versus d . Besides, it makes the data lot more convenient to fit with mathematical expression such as the one in Eq.(4.52). The size of the circular markers used to plot the experimental crack profile is larger than the typical uncertainty for the crack edge detection.

What we immediately notice is the relatively large slope of the COD at the very crack tip. From this respect, the measured profile should not be in contradiction with the LEFM asymptotic prediction of a parabolic crack

tip. More generally, we recall Williams prediction [48] for the crack opening displacement u :

$$u_\theta(r) = \frac{4K_I}{E} \left(\frac{r}{2\pi}\right)^{1/2} + A_{3/2}r^{3/2} + A_{5/2}r^{5/2} + \dots \quad (4.47)$$

$$u_r(r) = \frac{Tr}{E} + A_2r^2 + A_3r^3 + \dots \quad (4.48)$$

We recall here that (r, θ) are the polar coordinates in the undeformed configuration. As a result, the distance to the tip in the deformed configuration is :

$$d = r + u_r(r) = r + \frac{Tr}{E} + A_2r^2 + A_3r^3 + \dots = r(1 + T/E + A_2r + \dots) \quad (4.49)$$

We show now that a non-zero T stress can have a very important effect on the apparent curvature of the crack tip. Let us consider first that $A_2 = 0$ for simplicity's sake. Then r can be expressed in function of d :

$$r = d/(1 + T/E) \quad (4.50)$$

The opening Irwin term then becomes:

$$u_{Irwin}(d) = \frac{4K_I}{E(1 + T/E)^{1/2}} \left(\frac{d}{2\pi}\right)^{1/2} \quad (4.51)$$

One immediately realizes that, if K_I is measured using the crack tip radius of curvature (what we propose to do next!), neglecting the effect of T-stress can cause an underestimation (if $T > 0$) or an overestimation (if $T < 0$) of the SIF K_I . We will see later that the T-stress can reasonably be neglected. We should emphasize that the value of the T-stress cannot be inferred from the crack shape measurements as the T-stress only induces a dilation or contraction of the crack in the propagation direction.

In the case we can neglect the T-stress, the crack opening displacement can be written as an expansion of the form:

$$2u(d) = \frac{2K_I}{E} \sqrt{\frac{8}{\pi}} d^{1/2} \left[1 + \frac{d}{d_1} + \left(\frac{d}{d_2}\right)^2 + \dots \right] \quad (4.52)$$

where d is the distance to the crack tip, and E is the gel's Young modulus. Here, we have turned the expansion in odd powers of $d^{1/2}$ into a new form by introducing length scales d_1 and d_2 . This new form easily allows to compare the relative importances of the three terms.

Thus, we will first focus on the values of d_1 and d_2 . Fig. 4.18 shows a fit of the experimental profile based on the first three terms of William's expansion. Agreement is good both at the crack tip and far from it (Regression coefficient $R=0.9999$), which means that LEFM applies in that case. For this low-velocity crack, d_1 and d_2 are respectively $850\mu\text{m}$ and 2mm .

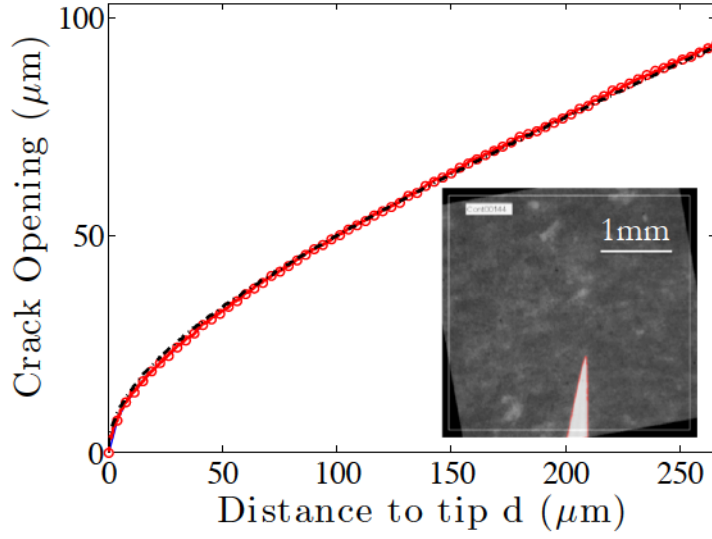


Figure 4.18: **Slow crack** ($V=3\mu\text{m.s}^{-1}$). Crack opening (displacement along the crack mouth) as a function of the distance d to the crack tip. Red line with circles: experimental results. Black dashed line: fit with the LEFM expression (4.52). *Inset*: Picture of a low-velocity crack (white) in a dyed 1.5%wt agar gel. The interior of the crack is filled with water. The contour of the crack is superimposed in red.

We can thus plot the respective contributions of each term to the total crack opening displacement. This is done in Fig. 4.19.

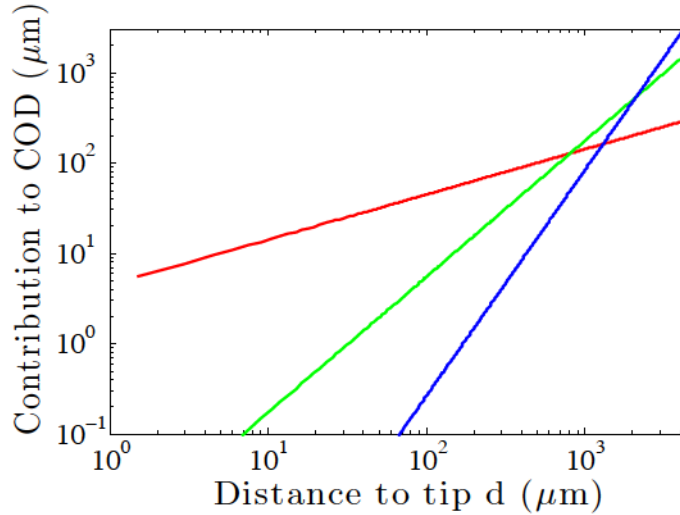


Figure 4.19: Log-log plot of the respective contributions of each of the three terms to the total crack opening displacement. Red: $d^{1/2}$ term. Green: $d^{3/2}$ term. Blue: $d^{5/2}$ term.

This result shows that, even if they are essential to capture the measured crack opening displacement, these two extra terms are only dominant far from the crack tip. This is illustrated by Fig. 4.20, where we have removed the $d^{5/2}$ term from the expansion (in blue) and compared with the measured profile.

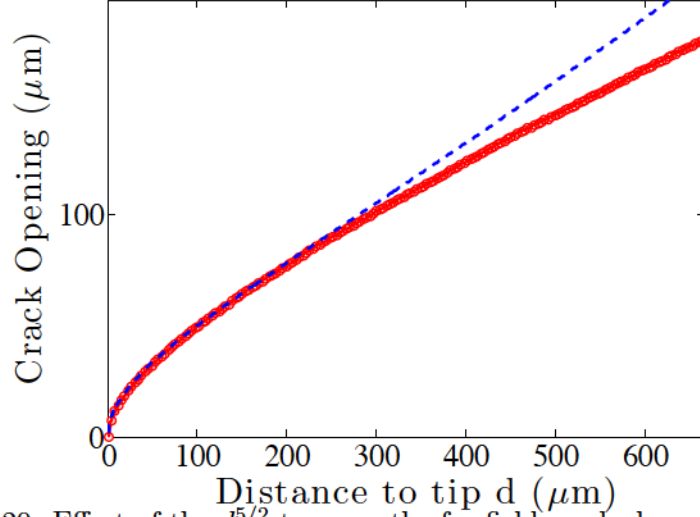


Figure 4.20: Effect of the $d^{5/2}$ term on the far field crack shape. The crack profile is in red. In blue, we show the William's expansion until order $3/2$ with the values of K_I and d_1 determined from the fit in Fig. 4.18. The effect of the $d^{5/2}$ term starts being important for $d > 300\mu\text{m}$.

Figure 4.19 also shows the existence of a zone of K_I -dominance at the crack tip, i.e. a region of space in which the Irwin $d^{1/2}$ term dominates. Indeed, Figure 4.19 proves that, until $d \simeq 100\mu\text{m}$, the $d^{3/2}$ contribution is more than 10 times smaller than the Irwin contribution. Hence, this is a perfect case where Small Scale Yielding approximation holds and one can claim that K_I can be deduced directly from the COD measurement using Eq.(4.52).

Using Eq.4.52, the prefactor $P = \frac{2K_I}{E} \sqrt{\frac{8}{\pi}}$ of Irwin's term is found to be $P = 4.46$. Knowing that $E = 60\text{kPa}$ from linear oscillatory rheology, one can compute the SIF $K_I = 84\text{ Pa}\sqrt{\text{m}}$. We emphasize that this value of P corresponds to a radius of curvature at the crack tip of $P^2/8 = 2.5\mu\text{m}$: due to uncertainties in the crack edge detection, such a low value could not have been computed by direct computation of the local curvature along the crack edge.

4.2.3.2 Departure from linear elasticity at high crack velocities

At low velocity (the lowest we could reach), it was shown that the crack shape was compatible with LEFM prediction. When increasing the applied strain rate, crack velocity consequently increases and induces a marked change of the crack shape in the vicinity of the tip. A typical crack shape for a crack propagating at $V \simeq 1\text{cm/s}$ is shown in Fig.4.21.

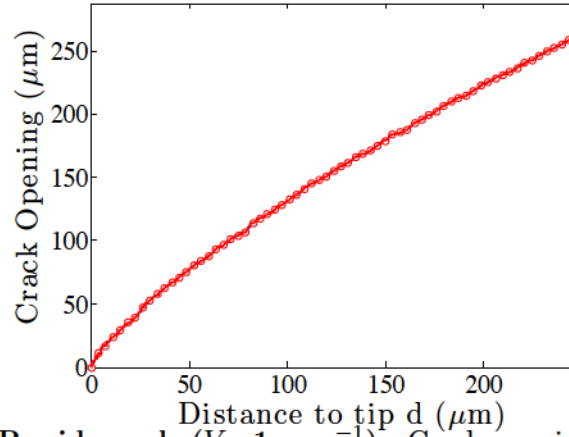


Figure 4.21: **Rapid crack** ($V=1\text{cm.s}^{-1}$). Crack opening (displacement along the crack mouth) as a function of the distance d to the crack tip. Red line with circles: experimental results.

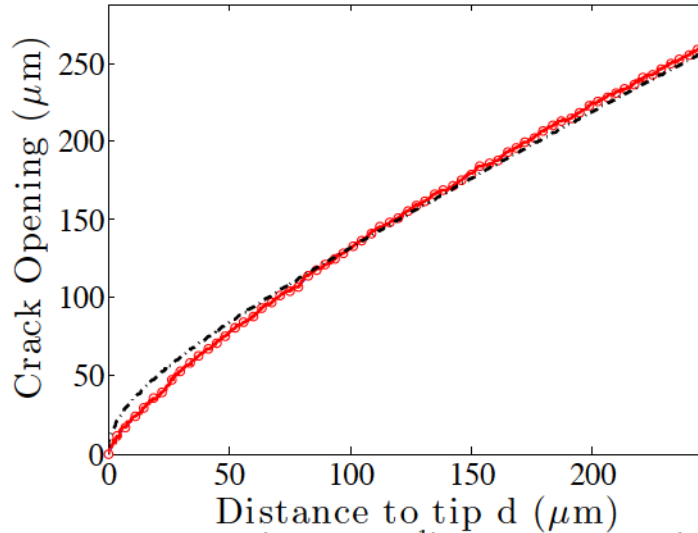


Figure 4.22: **Rapid crack** ($V=1\text{cm.s}^{-1}$). Crack opening (displacement along the crack lips) as a function of the distance d to the crack tip. Red line with circles: experimental results. Black dashed-dotted line: fit of the data with the LEFM prediction (4.52), which clearly does not work either close to the crack tip or in the far field.

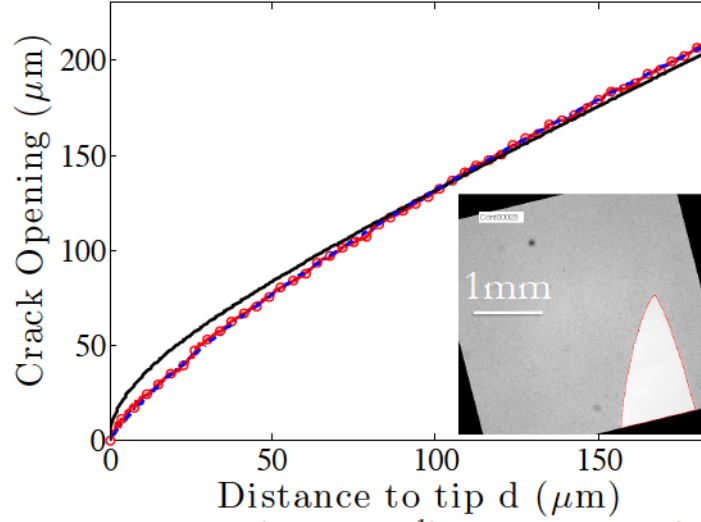


Figure 4.23: **Rapid crack** ($V=1\text{cm.s}^{-1}$). Crack opening (displacement along the crack mouth) as a function of the distance d to the crack tip. Red line with circles: experimental results. Black line: fit of the data with the LEFM prediction (4.52), which clearly does not work close to the crack tip; Blue dashed line: fit of the data with the modified William's expansion (4.53). *Inset*: Picture of a high velocity crack in a dyed 1.5%wt agar gel. The interior of the crack is filled with water. The contour of the crack is superimposed in red.

When increasing V , the crack shape departs from the LEFM prediction. Fig. 4.21 shows the COD for a high velocity crack ($V=1\text{cm.s}^{-1}$). A snapshot of a high velocity crack in a dyed 1.5%wt agar gel is shown in the inset of Fig. 4.23. Instead of an “infinite” slope (at the experimental resolution) as for a LEFM crack tip, fast cracks propagating in agar gels exhibit a finite slope at the apex with $u(d) \propto d$. The crack profile therefore cannot be captured by William's expansion (see Fig. 4.22), whatever the number of terms used in the LEFM expansion.

A central point of Chapter 5 will be to determine the very nature of this region close to the crack tip. Is it a Dugdale Barenblatt cohesive zone? Is this new crack shape due to the material viscoelasticity – the so-called de Gennes trumpet [50, 51] –? Or is it an effect of large strains at the crack tip [52]?

In any case, it is clearly distinct from the Dugdale crack shapes described by Eq. (4.41) and plotted in Fig. 4.5. Using $\delta = \Lambda$ in the Dugdale model, we could not find parameters resulting in a wedge-like crack tip. Furthermore, one already discussed that, considering the viscoelastic characterization of the agar gels, it was *a priori* irrelevant to take into account the material bulk viscoelasticity as a cause of a change in crack shape. In addition, viscoelasticity would result in $u(d) \propto d^{3/2}$, which does not match our observation.

Based on our phenomenological observation, we write a modified William's expansion series:

$$\tilde{u}(d) = d \left[\frac{A}{1 + (\frac{d}{\tilde{d}^*})^{1/2}} + \left(\frac{d}{\tilde{d}_1} \right)^{1/2} + \left(\frac{d}{\tilde{d}_2} \right)^{3/2} \right] \quad (4.53)$$

where \tilde{d}^* is a crossover length between the linear apex and the classical LEFM expansion. A is a measure of the finite slope at the apex.

While the crack opening profile may look like a perfectly linear elastic one at large scale, it is obviously not the case at distances smaller than \tilde{d}^* . Equation 4.53 fits well the COD over the whole velocity range. \tilde{d}_1 and \tilde{d}_2 hardly change with crack velocity. They are both of order $10^5 \mu\text{m}$ with $\tilde{d}_1 < \tilde{d}_2$. In Fig.4.24, we show a log-log plot of the respective contributions of the three terms in the modified Williams expansion for the highest velocity (largest \tilde{d}^*). The two higher order terms ($d^{3/2}$ and $d^{5/2}$) dominate at distances larger than 1mm. The modified Irwin's term exhibits a slow crossover from $u(d) \propto d$ to $u(d) \propto d^{1/2}$. Here again there is a region of space where the $d^{1/2}$ term dominates.

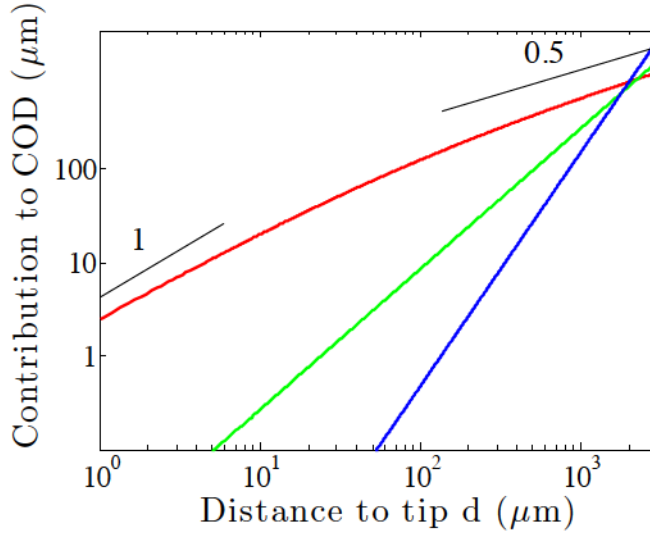


Figure 4.24: Log-log plot of the respective contributions of each of the three terms to the total crack opening displacement for the modified William's expansion. Red: Modified Irwin's term. Green: $d^{3/2}$ term. Blue: $d^{5/2}$ term.

As the modified William's expansion can capture the crack shape on the whole velocity range, $A(V)$ and \tilde{d}^* are systematically measured for the different crack velocities. Each crack propagating at velocity V will be fully characterized by a couple $(A(V), \tilde{d}^*(V))$.

4.3 Crack displacement fields measured with DIC

In the following section, we will detail a technique called Digital Image Correlation (DIC), that aims at measuring displacement fields. In our case, this technique is used to capture the displacement fields of cracks propagating in the studied soft materials. The measured fields can then be projected on analytical or numerical displacement fields. This technique will be illustrated using the low and high-velocity cracks we have just considered.

The general goal of 2D-Digital image correlation can be defined very simply. One considers two images (see Fig.4.25) showing the evolution of a texture between a reference state and a deformed state. One wants to find the displacement field that describes the best the transition from the reference texture to the deformed texture. When this technique is to be applied to measure the deformation of a solid, the main hypothesis is that the texture (either natural or artificial) is bounded to the solid and that it will undergo the same deformation than the solid it is bounded to.

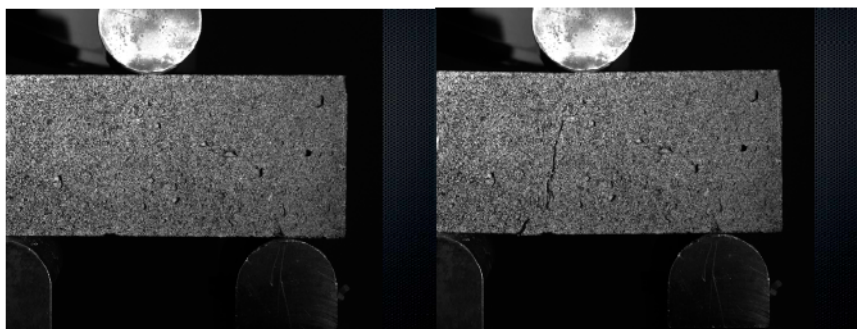


Figure 4.25: Reference (Left) and deformed (Right) images of a concrete specimen undergoing a 3-point flexion test. The reference picture shows the undeformed specimen. In the deformed state, a crack has appeared. *From M. François, "Correlation d'images".*

DIC is a very general appellation that encompasses lots of very different approaches for solving this problem. Finite Element DIC (FE-DIC) is one of them. With FE-DIC, and more particularly with CorreliQ4, Hild & Roux developed a "global" way to solve the problem. Most of the techniques used in the context of soft matter physics being "local" approaches, it is useful for the reader to get more insight into the advantages of a global approach over a local one. We will thus first shortly explain the different approaches for measuring displacement fields and second, focus on the FE-DIC technique. Then, one will describe how a texture was provided to our specimens. Finally, we will try to estimate the typical experimental uncertainties and resolution that we can expect from FE-DIC technique in our particular case.

4.3.1 FE-DIC: a new tool in Soft Matter

4.3.1.1 Global versus local approaches

In this introduction, we mentioned two types of approaches to Digital Image correlation. Let us first describe the formalism in which the two techniques can be compared.

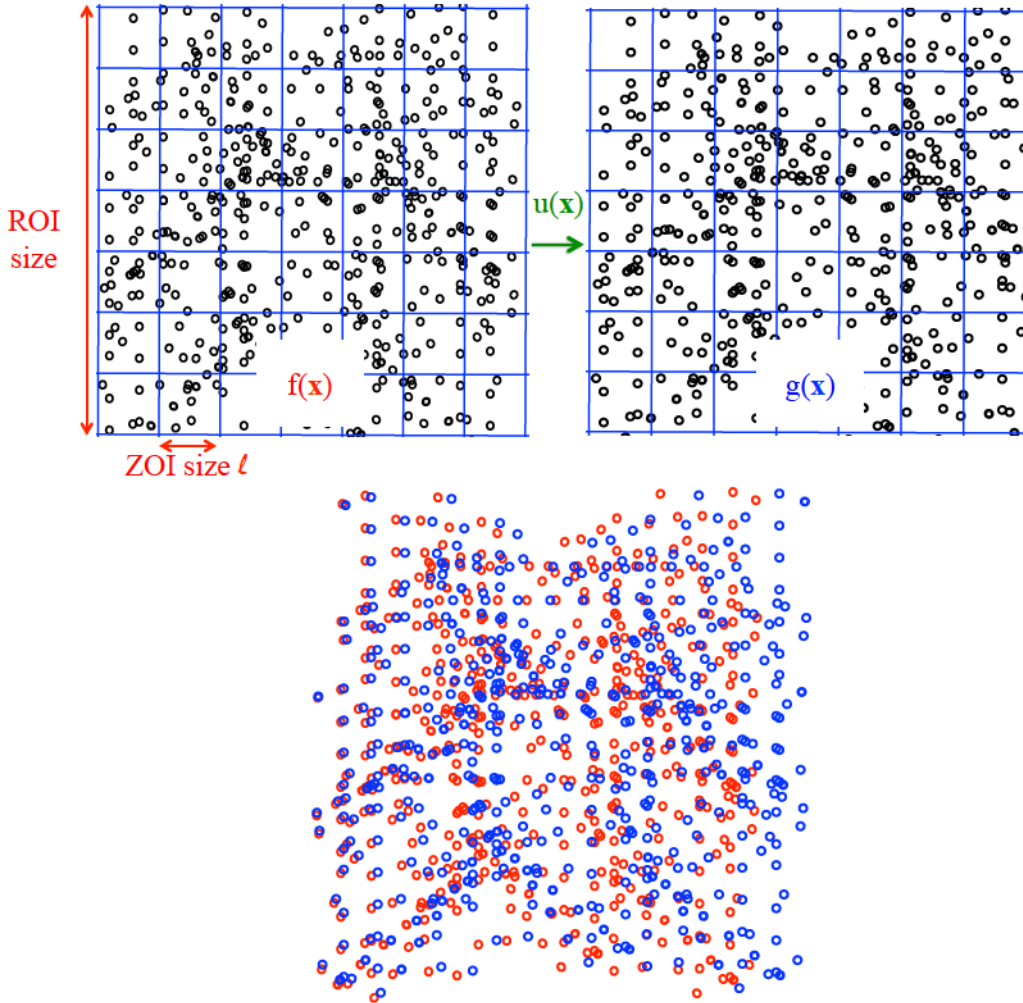


Figure 4.26: Formalism for Digital Image Correlation. $f(x)$ and $g(x)$ respectively describe the textures in the reference (left) and deformed (right) configurations. Bottom: superposition of the reference (blue) and deformed (red) textures. The goal is to find $u(x)$ that best describes the transformation from reference to deformed configuration. For both local and global approaches, the total Region of Interest (ROI) is divided into Zones of Interest (ZOI, size ℓ).

In Fig.4.26, we show the texture in the reference and deformed configurations, and introduce $f(\mathbf{x})$ and $g(\mathbf{x})$, that respectively describe the reference (undeformed) and deformed textures. The Region of interest (ROI) is $N \times N$ pixels. The introduced mathematical objects f and g are thus 2D $N \times N$ matrices: each element of these 2 matrices is the grey level value of the corresponding pixel. Here, the applied loading consists in applying a stretch on the right boundary of the linear elastic specimen. The challenge is to find the displacement field $\mathbf{u}(\mathbf{x})$ that best describes the transformation from reference to deformed configurations. A more mathematical way to translate that consists in writing the grey level conservation for each pixel:

$$f(\mathbf{x}) = g(\mathbf{x} + \mathbf{u}(\mathbf{x})) \quad (4.54)$$

Here, we see that if the picture (assuming it is square) contains N^2 pixels, the number of unknowns $2N^2$ for knowing each component of $\mathbf{u}(\mathbf{x})$, exceeds the number of equations N^2 . The correlation approach consists in seeking a displacement field interpolated as:

$$\mathbf{u}(\mathbf{x}) = \sum u_n \Psi_n(\mathbf{x}) \quad (4.55)$$

where Ψ_n are chosen vector fields, and u_n the associated degrees of freedom. The unknowns u_n are then sought trying to minimize $f(\mathbf{x}) - g(\mathbf{x} + \mathbf{u}(\mathbf{x}))$ with respect to the u_n using a given norm. The used norm can be the sum of squared differences or simply the cross correlation (which gave its name to DIC). Here, we use the sum of squared differences and the quantity we will try to minimize is:

$$\mathcal{T} = \int_{\Omega} [f(\mathbf{x}) - g(\mathbf{x} + \mathbf{u}(\mathbf{x}))]^2 d\mathbf{x} \quad (4.56)$$

The choice for Ω , the spatial domain on which the norm is calculated, is the main difference between local and global approaches. More concretely, for experimentalists, it is the main difference between Particle Image Velocimetry techniques (PIV) and FE-DIC.

In local approaches as PIV, the integration domain Ω will be a Zone of Interest (ZOI, see Fig.4.26), i.e. a square (or rectangular) subdivision of size ℓ pixels of the total Region of Interest (ROI). Each of the two components (in 2D) of the vector functions Ψ_n is often chosen as a bilinear interpolation function $ax + by + cxy + d$ where x and y are the local coordinates in the ZOI. Thus, for each ZOI independently, the values of a , b , c and d for each of the components of the Ψ_n have to be determined (8 unknowns). Using such a local technique, only the value found for the displacement field in the center of each ZOI is reliable [53].

In global approaches as FE-DIC, Ω is the whole Region Of Interest: \mathcal{T} is minimized when defined on the total ROI. In the correli-Q4 version of

the code (the one we use), the Ψ_n are now defined using a square Finite Element-like mesh made of 4-noded elements. Degrees of freedom are the displacements of the nodes and displacements are interpolated with bilinear functions in between the nodes. The main consequence of this global approach is that the continuity of the displacement field is directly assumed. Enforcing global continuity of the sought field will be what makes this technique more robust (more resistant to noise) and more precise.

4.3.1.2 FE-DIC

Let us now give more details on the minimization procedure that allows finding the unknown amplitudes u_n [54]. This minimization problem being nonlinear, a Newton iterative procedure will be followed using $\nabla f \cdot \Psi_n$ as the search direction. Here is why.

After a certain number of iterations, let us call $\tilde{\mathbf{u}}$ the displacement field found at this step. At the next step, the corrected displacement field will be $\tilde{\mathbf{u}} + \delta \mathbf{u}$. We can thus use a Taylor expansion and write:

$$g[\mathbf{x} + \tilde{\mathbf{u}}(\mathbf{x}) + \delta \mathbf{u}(\mathbf{x})] \simeq g[\mathbf{x} + \tilde{\mathbf{u}}(\mathbf{x})] + \nabla g(\mathbf{x} + \tilde{\mathbf{u}}(\mathbf{x})) \delta \mathbf{u}(\mathbf{x}) \quad (4.57)$$

$$= \tilde{g}[\mathbf{x}] + \nabla \tilde{g}(\mathbf{x}) \delta \mathbf{u}(\mathbf{x}) \quad (4.58)$$

Due to Eq.(4.55), $\delta \mathbf{u}$ reads as $\delta \mathbf{u}(\mathbf{x}) = \sum \delta u_n \Psi_n(\mathbf{x})$ and \mathcal{T} can thus be written as:

$$\mathcal{T} = \sum_{ROI} \left[f(\mathbf{x}) - \tilde{g}(\mathbf{x}) - \nabla \tilde{g}(\mathbf{x}) \sum_n \delta u_n \Psi_n(\mathbf{x}) \right]^2 \quad (4.59)$$

Here appears $\rho = f(\mathbf{x}) - \tilde{g}(\mathbf{x})$. ρ is the residual of the minimization procedure; it is a spatial map of the grey level error due to the difference between the currently computed $\tilde{\mathbf{u}}$ and the real one. It should ideally be zero at the end of the procedure. The unknowns here are the increments δu_n , and the minimum should be found with respect to the u_n . To simplify the procedure and because we know that, when getting closer to the good \mathbf{u} , $\nabla \tilde{g}$ converges toward ∇f , $\nabla \tilde{g}$ is, from the beginning, advantageously replaced by ∇f . Minimization with respect to δu_j allows to write:

$$0 = \frac{\delta \mathcal{T}}{\delta u_j} = 2 \sum_{ROI} \left[f(\mathbf{x}) - \tilde{g}(\mathbf{x}) - \nabla f \sum_i \delta u_i \Psi_i(\mathbf{x}) \right] \nabla f \Psi_j(\mathbf{x}) \quad (4.60)$$

which can be readily transformed into a matrix equality:

$$M_{ji} \delta u_i = b_j \quad (4.61)$$

where:

$$M_{ji} = \sum_{ROI} \Psi_j(\mathbf{x}) (\nabla f)^2 \Psi_i(\mathbf{x}) \quad (4.62)$$

$$b_j = \sum_{ROI} \rho(\mathbf{x}) \nabla f(\mathbf{x}) \Psi_j(\mathbf{x}) \quad (4.63)$$

This matrix $[M]$ is computed once for all whereas \mathbf{b} is updated at each iteration and enables to compute the new \tilde{g} for next iteration. The iterative procedure stops when the norm of $\delta\mathbf{u}$ is below some threshold value.

All this minimization procedure is based on a Taylor expansion of g , and on the associated assumption that the sought displacement field is small in amplitude. As it is not always the case, a powerful coarse graining approach is used. An image is coarsened at n^{th} order by attributing to a "superpixel" of size 2^n pixels \times 2^n pixels, the mean gray level value of the real pixels it contains. Between order k and $(k + 1)$, superpixels are twice larger, so that the displacements measured in superpixel get smaller from a factor 2. As a consequence, starting from the coarsest accessible scale allows to write the Taylor expansion on the superpixel displacement fields even if it is not valid with the displacements expressed in terms of real pixels. The minimization procedure thus easily converges at the coarse grained scale. The superpixel convergence result is then used as a starting point for the minimization procedure at finer scale and so on until reaching the real scale. This ability to capture large displacements will be of tremendous importance in the case of our very compliant materials observed at large magnifications.

4.3.2 Performances of FE-DIC applied to our specimen

4.3.2.1 Providing texture to our specimen

As we have just explained, what drives the minimization procedure is ∇f i.e. the spatial gradient of the texture. The quality of the displacement measurement mainly depends on the spatial properties and on the quality of the texture. But of course, finding an ideal texture depends on the scales at which we want to measure displacements. Let us for example consider the texture shown in Fig.4.26. We divide it into subimages of size ℓ . This example is poor: here, we are in the case where fluctuations at scale ℓ are not sufficient. At this scale, too many subimages such as the one shown in red do not carry enough information to allow a good measurement.

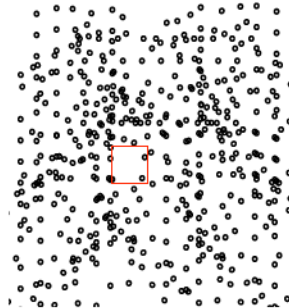


Figure 4.27: Example where ZOI size ℓ (in red) is too small to satisfy fluctuation criterion.

Most of our materials do not have a proper texture (agar gels are transparent at the observation scale), we thus have to confer them an artificial one. It is not possible to spray some pattern on the surface of the specimen confined between two transparent surfaces. We thus use an other technique. On top of adding a few microliters of indian ink to dye the gel, we mix it with a few picograms of carbon black powder containing spheres ranging from ten nanometers to 1 micrometer. After some optimization process, we ended up with the result shown in Fig.4.28.

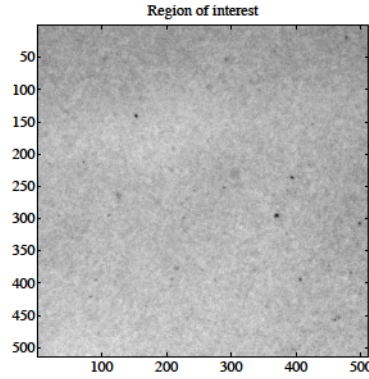


Figure 4.28: Texture of agar gels dyed with home made indian-ink/carbon black suspension.

This optimization of texture was driven by two quantitative criteria suggested by Besnard & al [55]: the correlation radius criterion and the fluctuation criterion. The importance of fluctuation criterion has just been illustrated with Fig.4.27. The importance of the correlation radius criterion can be illustrated showing a schematic case (Fig.4.29) where the ZOI (red mesh) has decent fluctuation properties but where neighboring zones have the same texture. We understand easily that if local displacement reaches one ZOI size, the minimization procedure might diverge. For a given texture, the ideal ZOI size can be chosen based on these two criteria.



Figure 4.29: Example of ZOIs that exhibit high spatial correlations.

The fluctuation properties are shown hereafter (Fig. 4.30). The normalized RMS value with respect to the dynamic range of the picture (80 in our case) is plotted as a function of the element size. A practical limit is chosen to be at least 1% of the dynamic range of the camera. Below this value, it is believed that the measurement is not possible (i.e., there are not enough gradients to capture displacements). With this limit, it is concluded that all ZOI sizes meet this criterion.

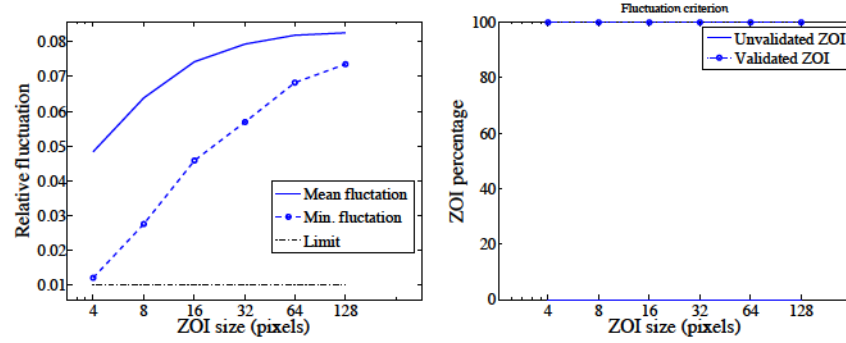


Figure 4.30: Minimum and mean relative RMS fluctuations as functions of the element size in the analyzed picture. Percentage of validated elements regarding the fluctuation criterion.

Second, the principal correlation radii ℓ_c normalized by the element size ℓ are shown (Left of Fig. 4.31). It should be as low as possible but a practical limit is chosen to be at most 25% of the element size. Above this value, the measure is not reliable. With this limit, it is concluded that about 15% of all 8-pixel elements do not meet this criterion. With 16-pixel and larger elements, this second criterion is always satisfied.

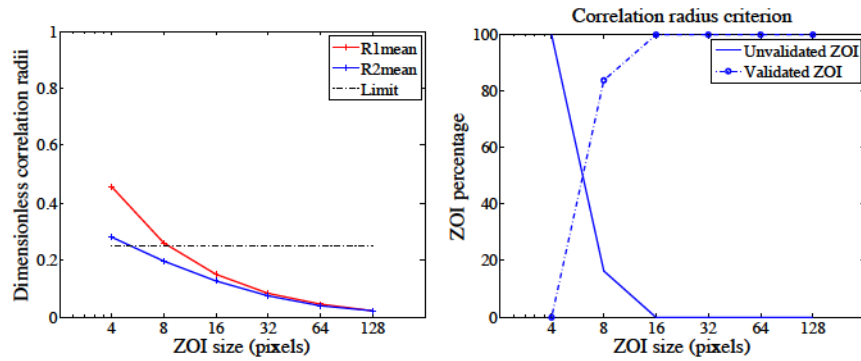


Figure 4.31: Mean correlation radii as functions of the element size. Percentage of validated elements.

With these two simple criteria, it is concluded that 16-pixel elements are the smallest ones to meet the two criteria. It is worth noting that 8-pixel

elements are close to meet these somehow arbitrary criteria. To gain a better resolution and because the displacements we want to capture are large, we will try to use 8-pixel elements and check for convergence of the procedure.

4.3.2.2 How precise is the technique?

Errors and uncertainties. In the previous paragraph, we had a semi-quantitative but arbitrary approach to determine the best size of ZOI. We will now be more quantitative and assess the abilities of this measurement technique for a given experimental texture. The limitations are of different nature. First there are intrinsic causes (at fixed texture) such as texture imperfections or the choice of interpolation functions, etc. Once these parameters are set, one can compute what Besnard & al call an "a priori" uncertainty or an "a priori" error. These are computed by translating the reference image from a prescribed displacement u_{presc} (in unit of pixel) in the diagonal direction. FE-DIC is then used to measure the displacement u_{meas} that best matches the passage from the reference to the artificially deformed image. One then computes the systematic error $\delta_u = \|\langle u_{meas} \rangle_{ROI} - u_{presc}\|$ and the standard uncertainty $\sigma_u = \langle \|u_{meas} - \langle u_{meas} \rangle_{ROI}\|^2 \rangle_{ROI}^{1/2}$ for different ZOI sizes ℓ and different u_{presc} . Here, $\langle u_{meas} \rangle_{ROI}$ designates the average over all the elements of the ROI. The results are shown in Fig.4.32.

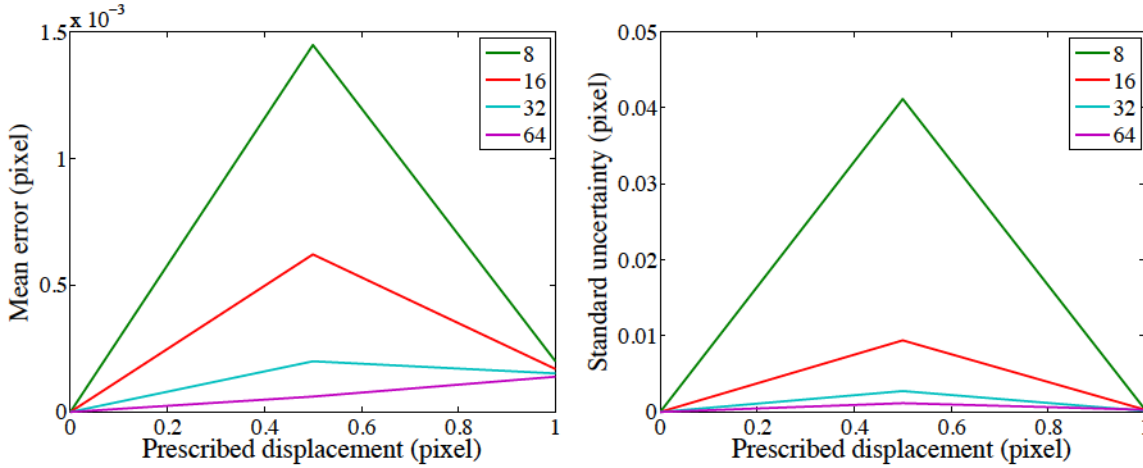


Figure 4.32: Mean displacement error and standard deviation as functions of the prescribed displacement for different element sizes.

Both quantities reach a maximum for $u_{presc} = 0.5$ pixel, and are approximately symmetric with respect to this maximum. This maximum for a half pixel displacement is mainly due to systematic errors due to grey level interpolation. Integer valued displacements imply no interpolation: error goes down to 0.02%. Systematic errors of the order of $1.5 \cdot 10^{-3}$ and $0.5 \cdot 10^{-3}$ pixel

are reached for element sizes respectively equal to 8 and 16 pixels. Standard uncertainties are of the order of $4 \cdot 10^{-2}$ and 10^{-2} pixels, for element sizes respectively equal to 8 and 16 pixels.

These performances only reflect the code ability to precisely map displacement fields for a given texture and given interpolation functions, in some kind of ideal experimental conditions where the texture itself is purely advected without any change in its gray level values. Unfortunately, the conservation law is never strictly satisfied and the minimum one tries to seek is not strictly zero. Experimentally, one of the main reasons for non-conservation is the noise associated with the image acquisition. One can test sensitivity to noise by transforming the reference image and adding it a spatially non-correlated Gaussian noise with standard variation σ_g ranging from 1 to 8 gray levels. The standard deviation of the displacement field σ_u computed by the Q4-DIC is plotted versus σ_g for different element sizes (see Fig.4.33). In our experimental conditions the noise level is about 2 grey levels. This results in σ_u lower than 0.1 pixel for ZOI sizes ℓ larger than 8 pixels. We can conclude that, in our case, the main contribution for uncertainties comes from sensitivity to noise.

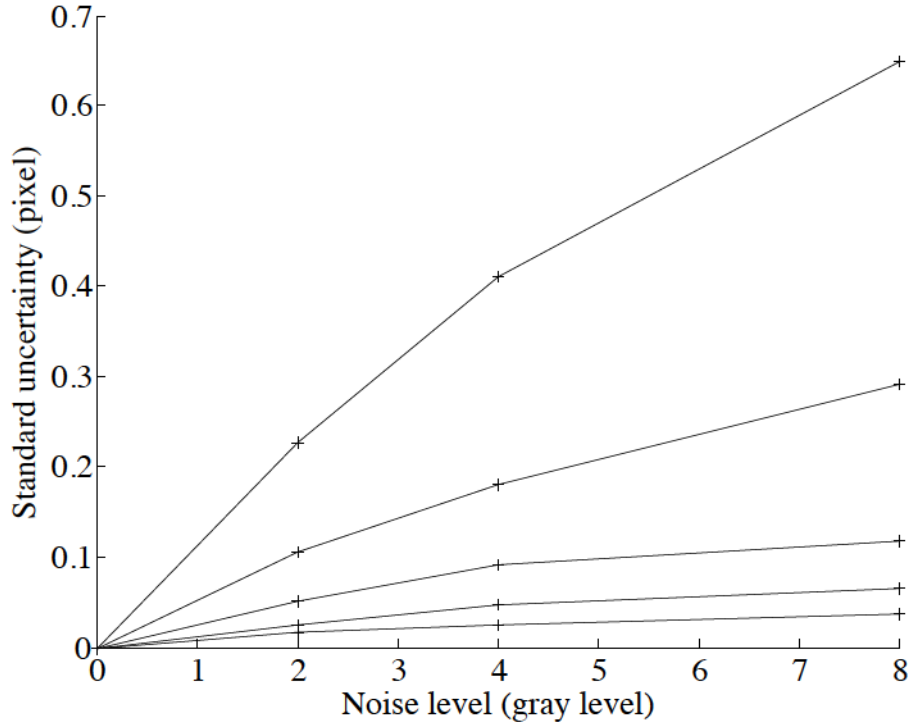


Figure 4.33: Sensitivity to noise of the displacement field measurement for different ZOI sizes. From top to bottom, the curves correspond to $\ell = 4, 8, 16, 32, 64$

The noise we have introduced to do the previous test had some given properties and it is doubtful this noise can reliably model the experimental noise in our case. Another way to test the sensitivity to noise consists in capturing, in real conditions, a sequence of 50 images for which one does not apply any deformation. One measures the displacement field \mathbf{u} for each parts of image and compute the corresponding standard uncertainty calculated at the nodes. A typical map is shown in Fig.4.34 for $\ell = 8\text{pixels}$. One finds $\sigma_u = 0.15$ pixel (averaged over the 50 images of the sequence). This a value close to the one expected following the previous approach. One also checks the residual map provided by Correli (see Fig.4.34). A very important output of the displacement measurement obtained from a minimization procedure is indeed, that the optimization procedure is able to provide a spatial map of the residuals. This error is, for each pixel, the difference in grey levels (normalized by the gray level dynamic range) that remains unexplained after converging toward the estimated displacement field. The mean value of the error maps is 0.015 normalized grey level value. In real grey level, this results in a typical error of 1 gray level value. This is of the order of our acquisition noise.

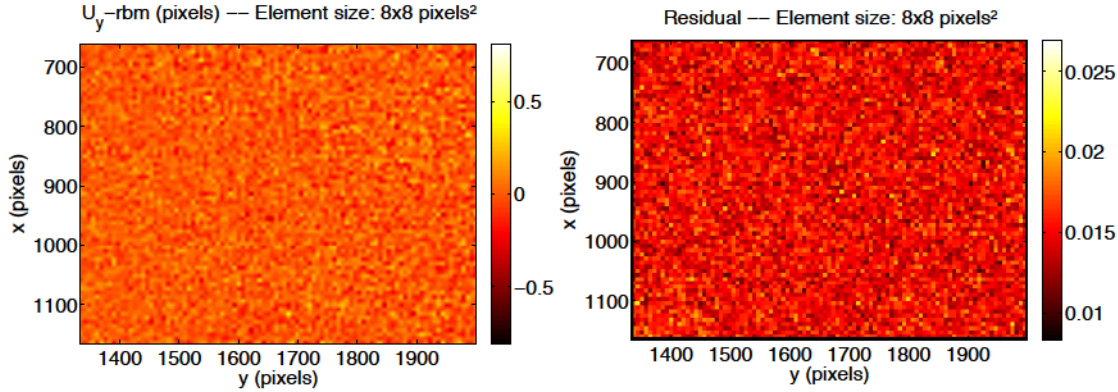


Figure 4.34: Left: typical u_y component of the displacement field measured when no deformation is applied to the specimen. Standard uncertainty $\sigma_u = \langle \|u_{meas} - \langle u_{meas} \rangle_{ROI}\|^2 \rangle_{ROI}^{1/2}$ is computed using this map. Right: residual map in the absence of deformation.

4.3.3 Capturing displacement field at the crack tip.

Let us now use DIC as a tool to measure the displacement field around cracks. One will consider several examples of cracks in agar gels, with velocities ranging from $1\mu\text{m/s}$ to 1cm/s . Above all, one will introduce two ways of measuring displacement fields.

In the context of Fracture mechanics, the first way is standard: it consists in having a picture with an unloaded specimen (closed slit-like crack or no crack) as the reference configuration and a loaded crack as the deformed configuration. This is the way the fields $u(r, \theta)$ are defined in textbooks: $u(r, \theta)$ is the displacement undergone by a material point located at coordinates (r, θ) in the undeformed reference configuration. We call this displacement field "absolute" (see Fig.4.35).

This field is distinct from what we call the "incremental" displacement field, which is the displacement field of material points in between a reference configuration where a crack is already open and a deformed configuration where the stationary crack has propagated over a distance δ . In that case both reference and deformed pictures are thus mechanically loaded (see Fig.4.36).

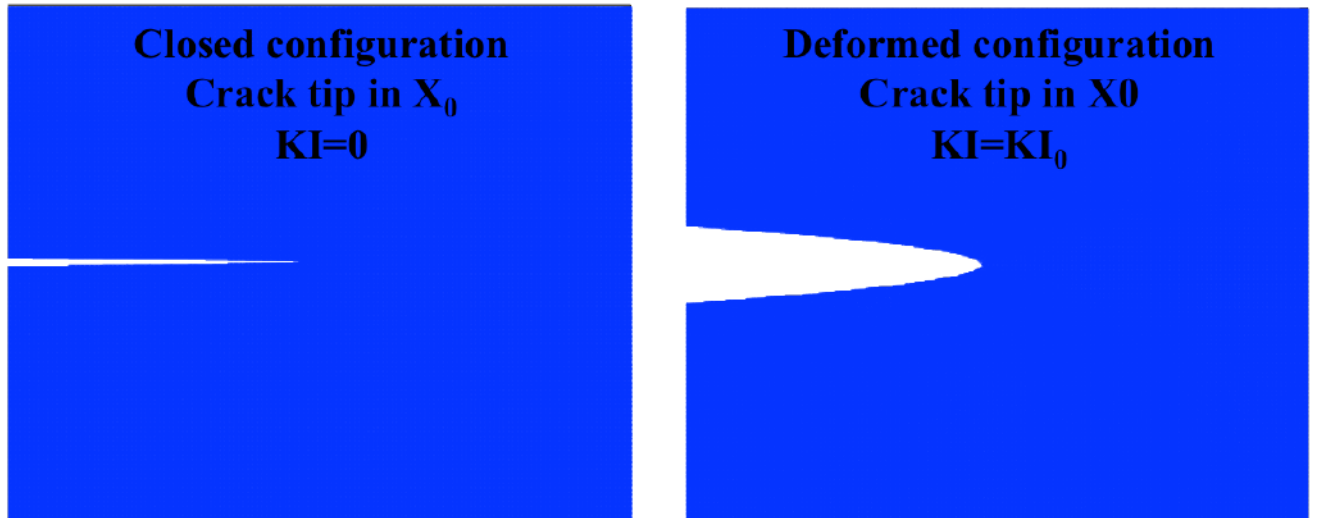


Figure 4.35: Measuring the "absolute" displacement field: reference ($K_I = 0$) and deformed $K_I = K_{I0}$ configurations for a crack in a linear elastic material.

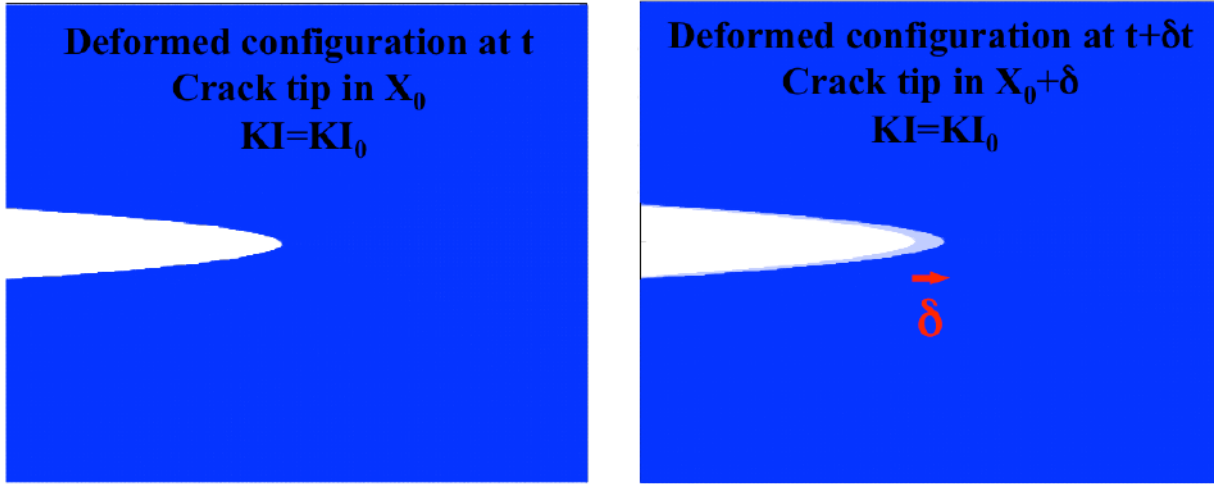


Figure 4.36: Measuring the "incremental" displacement field: between the reference and deformed configurations, the stationary crack propagates over a distance δ .

Due to the high magnification at which one observes the crack tip, one generally follows the crack while it is propagating. This has a very important consequence: one loses the memory of the unloaded reference configuration. In this manuscript, we mainly deal with "incremental" displacement fields. This is why we will mainly focus with on this non-standard way to proceed. Here follows a pair of experimental images:

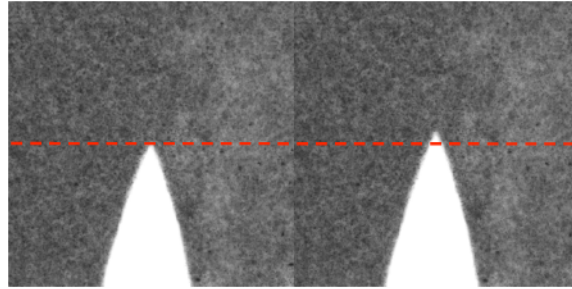


Figure 4.37: Pair of experimental images for measuring "Incremental" displacement field.

As mentioned earlier, to make this incremental analysis possible, the chosen image sequence should correspond to a crack propagating in a stationary way. Starting from a reference image 0 with a loaded crack, the displacement field to transit to image 1 is computed (see Fig. 4.38). In this figure, the inside of the crack is masked (in black). This is done because the texture inside the crack usually has very low spatial gradients so that Correli is in trouble for converging if this zone remains unmasked.

The same procedure is followed from image 1 to image 2, from image 2 to 3, etc. The displacement field to go from image 0 to image n can be obtained by cumulating the intermediate displacement fields. The resulting displacement fields u_x and u_y for $n = 1$, $n = 5$ and $n = 18$ are shown in Fig. 4.38, 4.39 and 4.40.

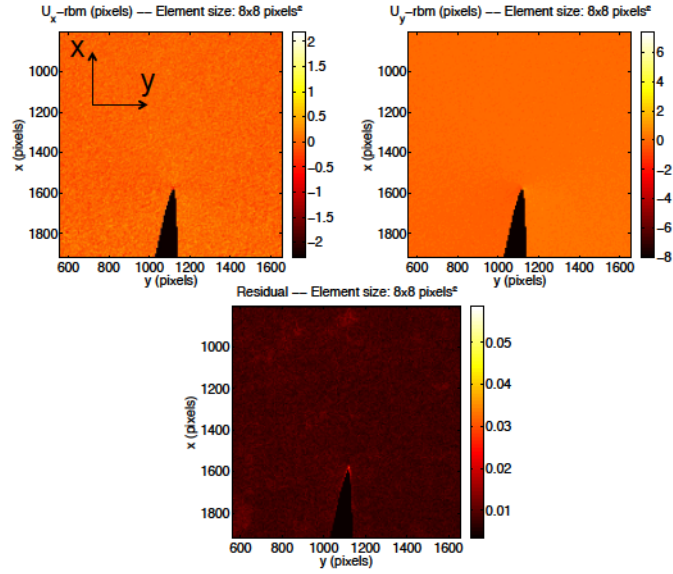


Figure 4.38: "Incremental" displacement field for $n = 1$.

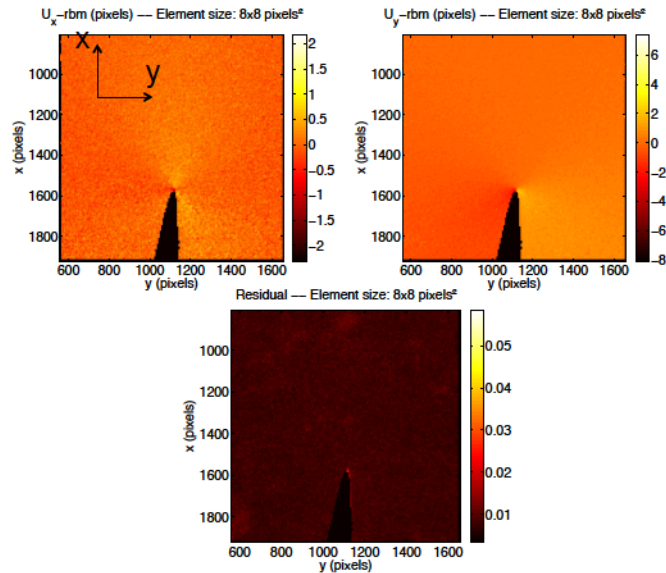


Figure 4.39: Cumulated "incremental" displacement field for $n = 5$.

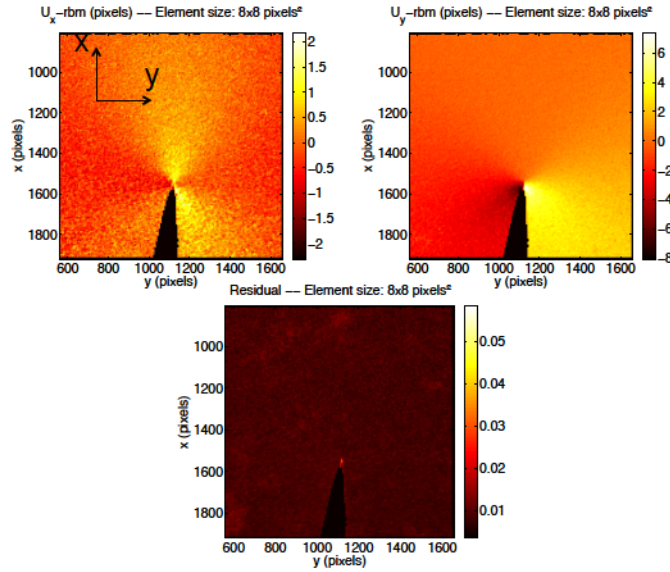


Figure 4.40: Cumulated "incremental" displacement field for $n = 18$.

Of course summing these intermediate displacement fields has an impact on the errors that also cumulates: the larger n , the larger the amplitude of the measured displacement field but the larger the uncertainty. Error maps are shown in the previous figures; they correspond to the normalized residuals for the estimated field to go from $n - 1^{th}$ to n^{th} image. Each of them has typical mean errors of order 0.02 to 0.03 which correspond to a value of about 2 grey levels. If one now considers the spatial features of the residual map, two things can be noticed. First, there are some spots far from the crack tip where the residuals have a slightly higher values: these spots correspond to zones of the specimen where the texture has lower gradients, which results in larger uncertainties. Second, there is also a small zone with larger errors at the crack tip. This can be easily explained by the fact that the displacement field continuity breaks down in the elements that are crossed by the crack tip: this results in high local residuals. One should mention that this residual signal can help to locate the crack tip.

One shall also consider cases where the "absolute" displacement field can be measured. This is a difficult experiment at this scale because, in these very compliant materials, the material undergoes very large displacements (rigid body motions and deformation) before the crack start to propagate. As a result, if the observation point remains fixed at some place, let us say, in the middle of the specimen, there is high chance that the material points under observation before loading are not in the observation field anymore when the crack crosses the field of view! On top of that, one is not even sure that the crack will go through the field of view especially if the observation field is far from the notch. To increase the probability of success,

the observation field is focused on the tip of the notch at the beginning of the experiment and one captures an image sequence from the moment the loading is started until the moment the crack propagates.

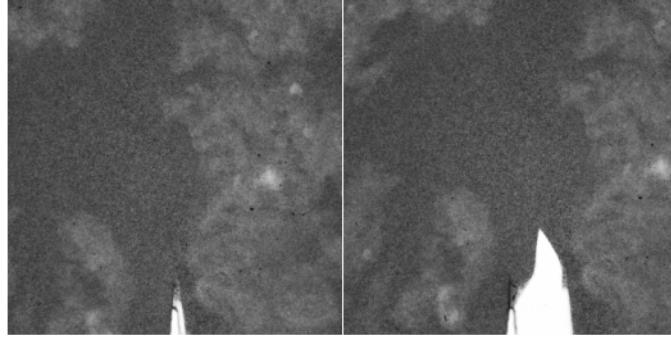


Figure 4.41: Couple of experimental images for measuring "absolute" displacement field. Left is the notched unloaded specimen. Right shows a crack propagating under mechanical loading.

4.3.4 Projecting the measured field on known displacement fields

May one measure the "absolute" or "incremental" crack displacement field, one of the great possibilities is to check how the measured field can compare with known displacement field. This may enable us to check if linear elasticity applies, if there is a zone in which linear elasticity fails, if so, to test for other constitutive laws etc... To do so, a tool is needed to analyze the fields measured with *Correli-q4*. This tool called *fissurefit* is a Matlab code written by Hild & Roux (IJF, 2006). The principle of this code is simple: a rough estimate of the crack tip and of the crack direction are given and one is able to project the displacement fields measured with DIC over a basis of analytical or numerical crack displacement fields. As received, it allowed to post-process the measured absolute fields and to project them over a basis of LEFM fields. Before giving more details about the projection procedure, let us specify the content of the displacement field library.

4.3.4.1 Displacement field libraries

Of course the displacement field library will depend on our material constitutive law (Hookean, Neo Hookean, etc...), on the scale at which one observe the crack, the loading configuration (plane stress, plane strain, 3D,...) etc...but above all, the chosen basis will depend on the chosen reference for the displacement field. In other words, is it an absolute or incremental displacement field?

Undeformed versus deformed crack configuration. The basis for the absolute displacement fields is the easiest to define. As was already mentioned, when computing a crack displacement field, one takes the undeformed state as a reference. In the case of LEFM, let us recall the displacement fields that were computed in section 4.2.1.1. In what follows, fields will be expressed in the frame of the crack: in this frame, the crack tip is at coordinate $(0,0)$, the crack lips lie in $\theta \pm \pi$, the material points M with coordinate (r, θ) are represented in a complex plane by $z = re^{i\theta}$ and the in-plane displacements reads $\mathbf{u} = u_x + iu_y$.

One first considers the solid body motions (translations and rotation):

$$\mathbf{u}_1 = 1 \quad (4.64)$$

$$\mathbf{u}_2 = i \quad (4.65)$$

$$\mathbf{u}_3 = iz \quad (4.66)$$

Then come the mode I and mode II Irwin asymptotic displacement fields that can be written as:

$$\mathbf{u}_4 = \sqrt{r}[2\kappa e^{i\theta/2} - e^{3i\theta/2} - e^{-i\theta/2}] \quad (4.67)$$

$$\mathbf{u}_5 = i\sqrt{r}[2\kappa e^{i\theta/2} + e^{3i\theta/2} - e^{-i\theta/2}] \quad (4.68)$$

the displacement field due to T-stress:

$$\mathbf{u}_6 = (\kappa - 1)z + 2\bar{z} \quad (4.69)$$

and finally, the higher order subsingular terms:

$$\mathbf{u}_7 = r^{3/2}[2\kappa e^{3i\theta/2} - 3e^{i\theta/2} - e^{-3i\theta/2}] \quad (4.70)$$

$$\mathbf{u}_8 = ir^{3/2}[2\kappa e^{3i\theta/2} + 3e^{i\theta/2} - 5e^{-3i\theta/2}] \quad (4.71)$$

where $\kappa = \frac{3-\nu}{1+\nu}$ in plane stress and $\nu = 1/2$ is the Poisson ratio for an incompressible material. In Fig.4.42, one shows the absolute displacement field for a plane stress pure mode I crack ($K_I = 80 \text{ Pa.m}^{1/2}$).

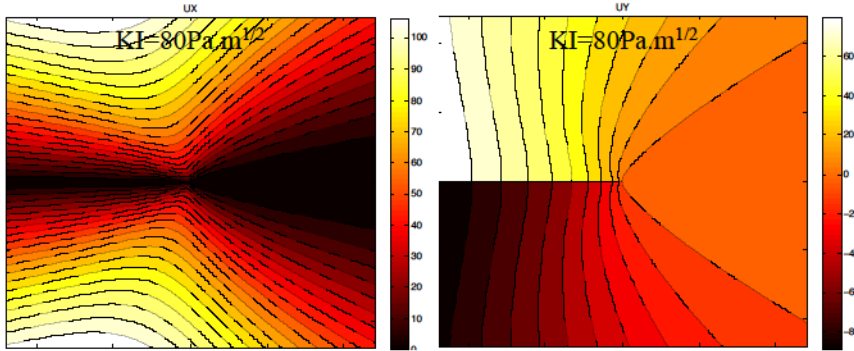


Figure 4.42: Analytical prediction for the absolute displacement field of a Mode I crack loaded with $K_I = 80 \text{ Pa.m}^{1/2}$. The crack lies on the left of the horizontal axis with crack tip in the middle of the frame.

Incremental displacement field for a stationary crack. In the absolute displacement field basis, the only free parameter is the choice for the crack frame i.e, the combination of the crack tip location and of the crack direction. In the incremental case, there is one more parameter which is the distance δ over which the crack propagates between the two images. As one assumes that the crack is stationary, the crack frame in the deformed configuration is a translation of the reference one over a distance δ in the direction of crack propagation. To be able to compute the incremental displacement fields, one can decompose the crack extension into three steps (see Fig.4.43). The first consists in closing the crack; the second step is an advance of a slit-like crack over a distance δ ; the last is the opening of a crack with crack tip shifted δ compared to the previous crack tip position.

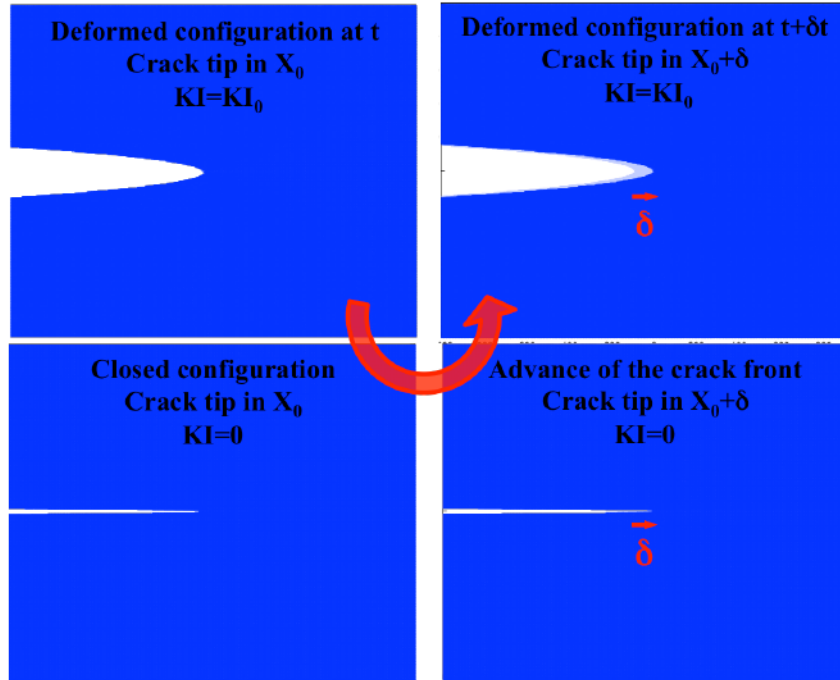


Figure 4.43: Incremental displacement field is equivalent to a cycle with closure of the existing crack, propagation of the slit-like crack and reopening of the crack.

Once this elementary propagation step is decomposed, the calculation of the corresponding displacement field is obvious. Again, let us take the LEFM example and consider a mode I crack. If one takes as $(0,0)$, the crack tip position in the reference image, the closure of the crack induces a displacement $-K_{I0}\mathbf{u}_4$, where K_{I0} is the stress intensity factor for this propagating mode I crack. Step 2 does not contribute to the displacement. Finally, as one assumes crack propagation is stationary, the SIF for the

reopening crack will also be K_{I0} . However, the crack tip being now shifted a distance δ , the reopening displacement field is:

$$\mathbf{u}_{\text{open}} = \sqrt{r'}[2\kappa e^{i\theta'/2} - e^{3i\theta'/2} - e^{-i\theta'/2}] \quad (4.72)$$

where (r', θ') are the new coordinates of the material points in the undeformed configuration, expressed in the new crack frame (with crack tip located at $(\delta, 0)$). The total mode I incremental displacement field (shown in Fig.4.44) is thus:

$$\tilde{\mathbf{u}}_4 = -\sqrt{r}[2\kappa e^{i\theta/2} - e^{3i\theta/2} - e^{-i\theta/2}] + \sqrt{r'}[2\kappa e^{i\theta'/2} - e^{3i\theta'/2} - e^{-i\theta'/2}] \quad (4.73)$$

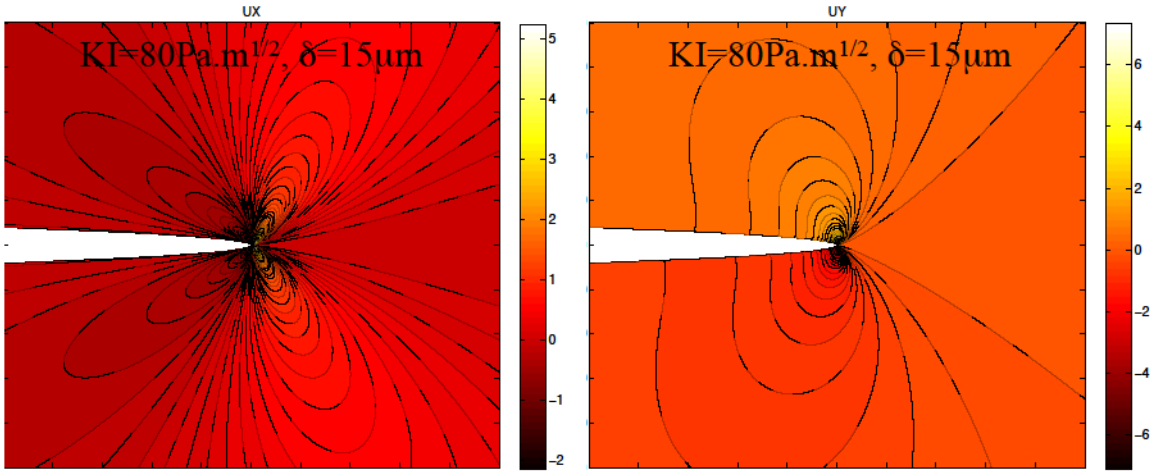


Figure 4.44: Analytical prediction for the incremental displacement field of a crack loaded with $K_{I0} = 80 \text{ Pa} \cdot \text{m}^{1/2}$ propagating over $\delta = 15 \mu\text{m}$.

One can note that this displacement field has some close similarities with the one measured in the case of agar and shown in Fig.4.40.

4.3.4.2 Projection procedure

This qualitative agreement between measured and predicted displacement fields is not enough. One wants to make a quantitative analysis of the measured displacement field. Using the elastic library will enable us to address numerous questions: is the crack loaded in pure Mode I or is there mode mixity? Is the T-stress (previously neglected) really negligible? Is LEFM applicable? What are the order of magnitude of the strains at the crack tip? In the following, one will be able to find answers to these questions. Considering the example of a low velocity crack propagating in a 1.5% agar gel, one is going to show how one can project the measured displacement field on the LEFM fields of the incremental library. One is then considering the

high-velocity case. Using the measured COD, it was shown that LEFM does not apply any more. Is it the same when investigating the 2D displacement field?

Minimization of residuals & Crack tip detection. Let us consider the low velocity case and show the measured incremental displacement field (Fig 4.45) for $n = 5$. Choosing $n = 5$ enables a good measure of crack front displacement δ while keeping a reasonably low uncertainty level on the measurement itself.

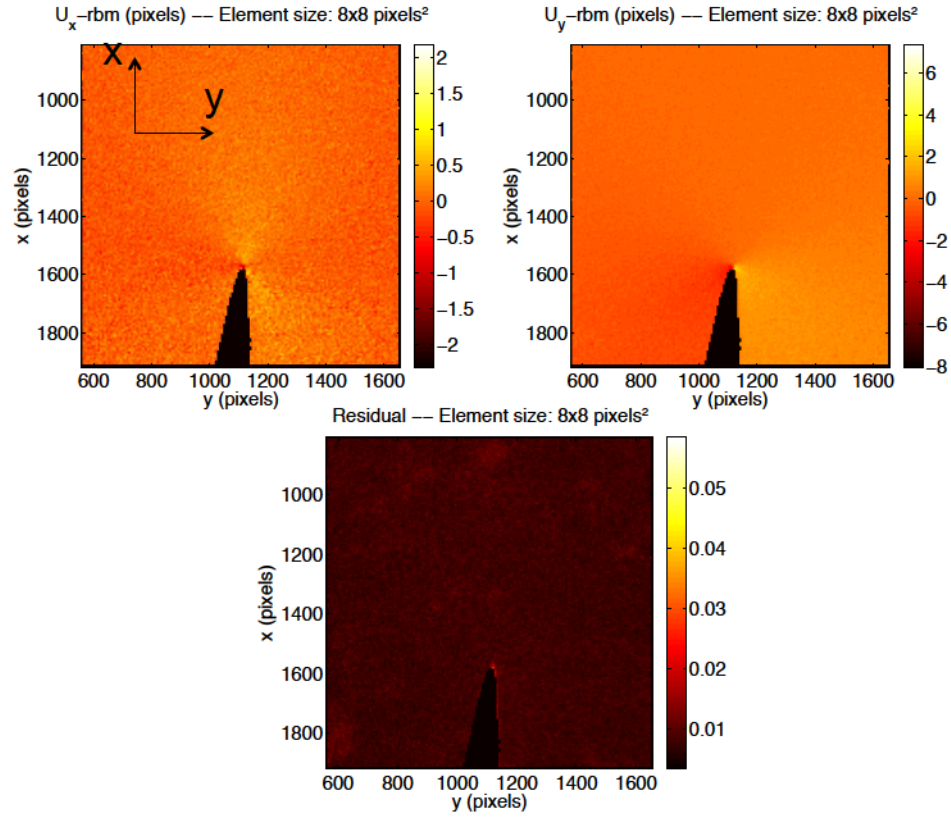


Figure 4.45: "Incremental" displacement field for $n = 5$. Choosing $n = 5$ enables a good measure of crack front displacement δ while keeping a reasonably low uncertainty level

This measured displacement field is now going to be post-processed: following a minimization procedure similar to the one described in Section 4.3.1.2, one is seeking for the combination of the $\tilde{\mathbf{u}}_k$ that best reproduces the measured field $\tilde{\mathbf{u}}_{\text{meas}}$.

The goal is to find:

$$\tilde{\mathbf{u}}_{\text{est}}(r, \theta, \delta) = \sum_k a_k \tilde{\mathbf{u}}_k(r, \theta, \delta) \quad (4.74)$$

that best matches $\tilde{\mathbf{u}}_{\text{meas}}$. The minimization procedure thus tends to minimize $\|\tilde{\mathbf{u}}_{\text{meas}} - \tilde{\mathbf{u}}_{\text{est}}\|$ with respect to the a_k .

However, as mentioned earlier, the incremental basis $\tilde{\mathbf{u}}_k$ depends on the crack tip position and δ . Here the value allocated to the propagation distance δ is computed using the crack tip positions determined by the edge detection procedure. In this version of the code, there is no minimization with respect to δ . However, there is, additionally to the minimization with respect to the amplitudes a_k , a minimization with respect to the crack tip position in the deformed configuration. This enables to search for the real crack tip position, i.e. the place where, in the framework of LEFM, the stress is thought to diverge.

This is how one typically proceeds. The starting value for the crack tip position is the crack tip measured with crack edge detection on the deformed image. The crack tip detection procedure is then allowed to look for the "LEFM crack tip" in a rectangular bounding box of given size surrounding the starting position. For every crack tip position in the bounding box, the minimization with respect to the a_k is conducted and the mean residual value is recorded. One can thus get a map of the mean residuals for each crack tip position chosen in the bounding box (see Fig.4.46).

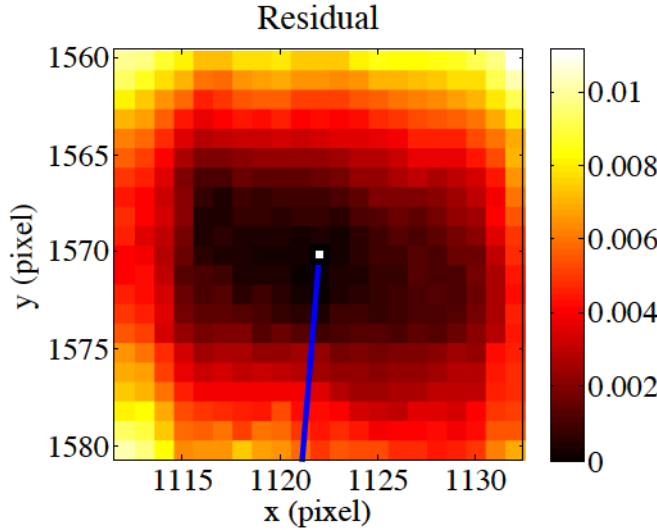


Figure 4.46: LEFM crack tip detection. The residual map (bounding box 20 pixels \times 20 pixels) is shown. For every crack tip position in the bounding box, the minimization with respect to the amplitudes a_k is conducted and the mean residual value is recorded. The LEFM crack tip is the minimum of the residual map. Here, the procedure finds a clear minimum in the residuals and the LEFM crack tip position can be clearly identified. It is signaled by the white square. The crack direction is indicated by the blue line.

The LEFM crack tip is chosen as the crack tip position that minimizes the residual value. This procedure is started again until it finds a real minimum so that the LEFM crack tip position is stable when starting the minimization again and again. Fig.4.46 shows the residual map once the LEFM crack tip position is stable: the procedure has found a clear minimum and the LEFM crack tip position can be clearly identified. In the low velocity case, it is noticeable that the LEFM crack tip found by the minimization procedure is identical to the crack tip found thanks to the crack edge detection.

Once the minimum is identified, one can access the corresponding values of the amplitudes a_k (see Fig.4.47), reconstruct $\tilde{\mathbf{u}}_{\text{est}}$ using Eq.(4.74) (see Fig.4.48), and compare it with $\tilde{\mathbf{u}}_{\text{meas}}$ using a residual map (see Fig.4.49).

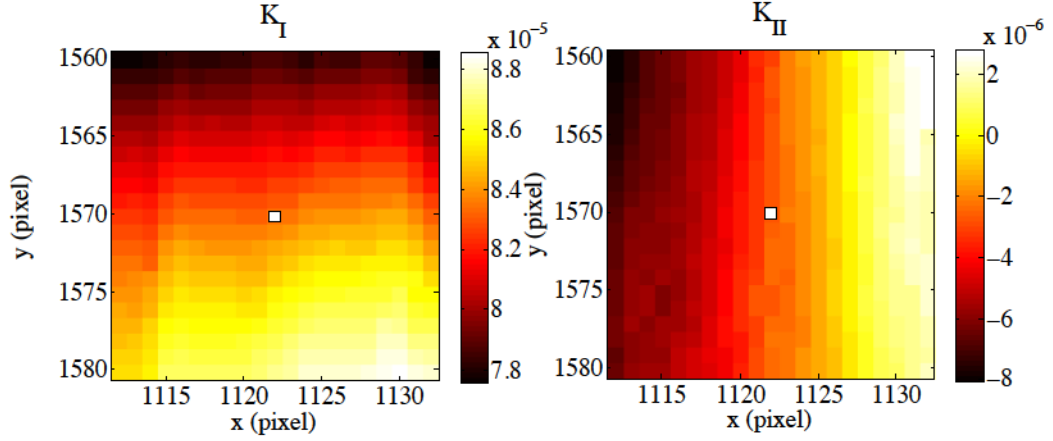


Figure 4.47: Map of the estimated K_I and K_{II} for the different crack positions in the bounding box. White square is the LEFM crack tip position after convergence of the minimization procedure.

Here one shows a map of the K_I and K_{II} values estimated by the minimization procedure for the different crack positions in the vicinity of the LEFM crack tip position. The white square signals the position of the LEFM crack tip: it corresponds to $K_I = 83 Pa.m^{1/2}$ and to $K_{II} = -3 Pa.m^{1/2}$. In Fig.4.46, one can realize the LEFM crack tip position can be determined within a disk of radius about 5 pixels. This gives a typical uncertainty for the amplitudes a_k : $K_I = 83 \pm 1.5 Pa.m^{1/2}$ and $K_{II} = -3 \pm 2 Pa.m^{1/2}$. The first important result provided by this projection over LEFM fields is that $K_{II} \ll K_I$: the crack is thus opening in pure mode I. Similarly, the estimation of a_6 provides us with a value of T-stress $T = -7 Pa$ which is very small compared to the Young modulus $E = 60 kPa$ and thus can be neglected.

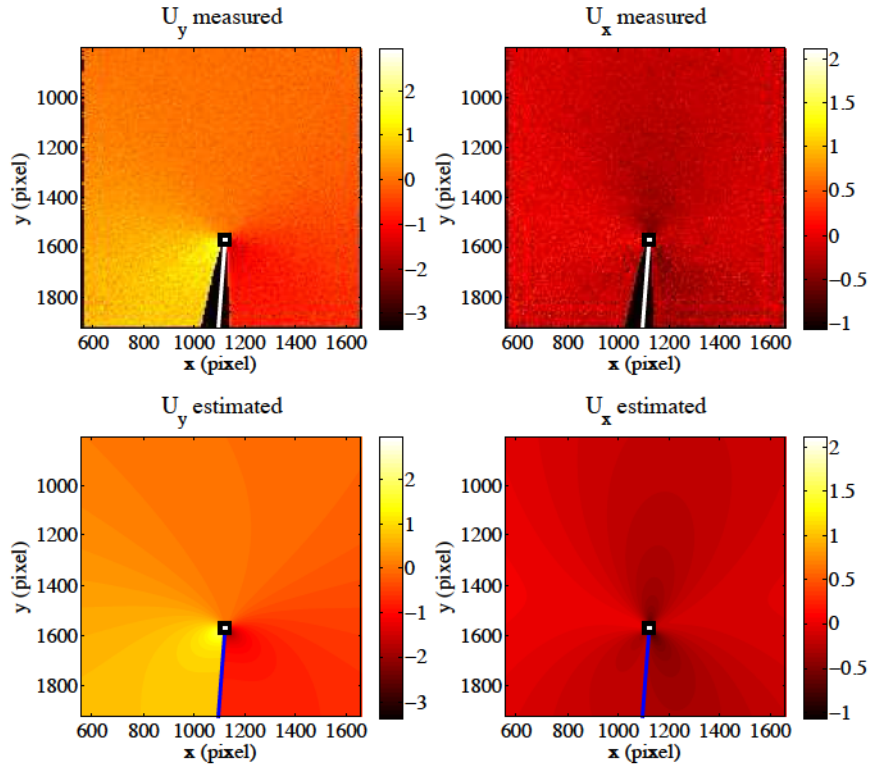


Figure 4.48: Comparison of the measured and estimated u_x and u_y displacement fields for a slow crack.

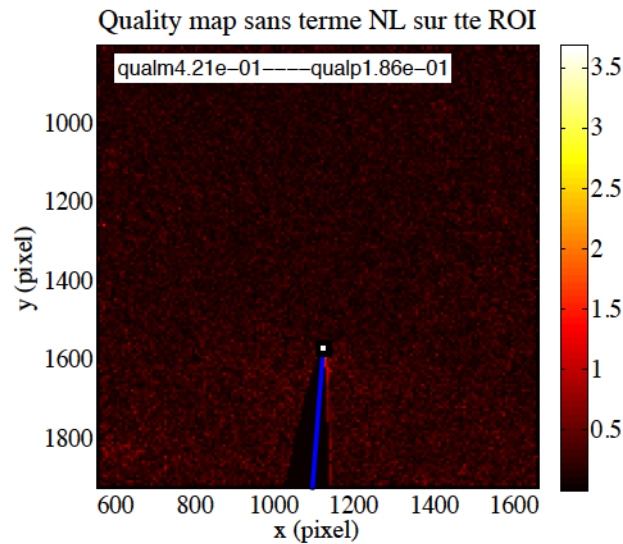


Figure 4.49: Error map: difference between the measured and estimated displacement fields in pixels

Figure 4.48 shows a good quantitative agreement between the measurement and the estimation. This is confirmed by Fig.4.49 which shows a map of $\|\tilde{\mathbf{u}}_{\text{meas}} - \tilde{\mathbf{u}}_{\text{est}}\|$ for each pixel. This error map does not show any relevant difference between the measurement and the estimation. One recalls that the projected displacement field was the sum of five measured incremental displacement fields ($n = 5$). Each of them being characterized by a typical uncertainty $\sigma_u = 0.15\text{pixel}$, the total uncertainty is thus $\sigma_{\text{tot}} = 0.15\sqrt{5} = 0.33\text{pixel}$, which correspond to the mean value of 0.4 pixel observed in Fig.4.49. The fact that the error map shows no significant signal proves that LEFM and the combination of Mode I, Mode II, T-stress and subsingular terms are sufficient to understand the structure of the displacement field in the vicinity of the crack tip propagating at low velocity. Because a "good" minimum has been found, one can trust the values of K_I , K_{II} , T , etc.

Displacement field projection: Learning from errors. In agar gels, analysis of the crack opening displacement (COD) had suggested a departure from LEFM in the high velocity case. For a crack propagating at $V = 2\text{mm/s}$ in a 1.5wt% agar gel, one measures its incremental displacement field and project it on the LEFM displacement field basis. First, the projection is done on the whole ROI, and the results are shown in Fig. 4.50.

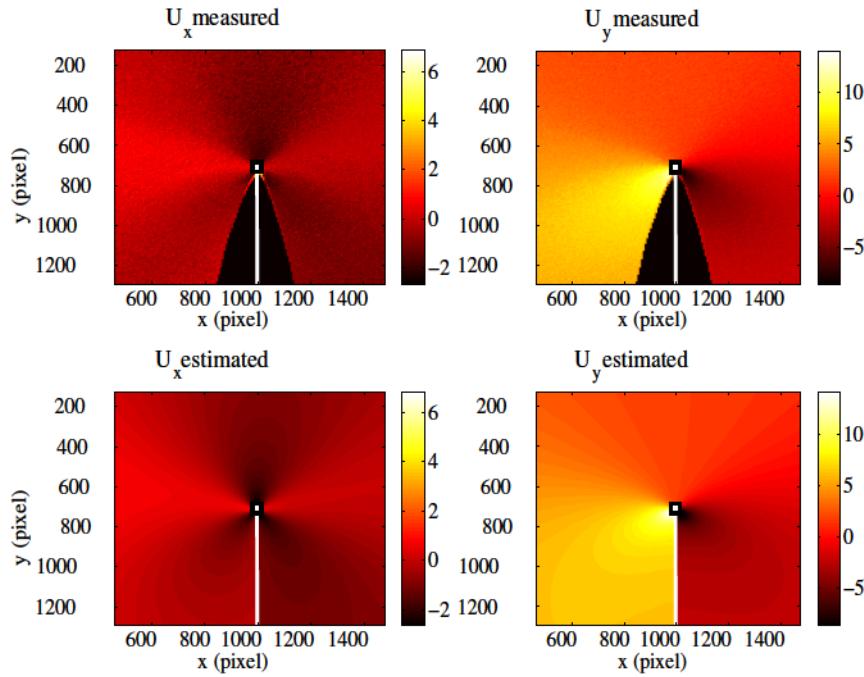


Figure 4.50: Comparison of measured (top) and estimated (bottom) u_x and u_y components of the displacement fields

Here again, a good qualitative and quantitative agreement is obtained between the measurement and the estimation. However, this agreement is only approximate. Fig.4.51 shows a quality map of the projection. The quality map (Left) reveals large projection errors in the very vicinity of the crack tip (that can reach a magnitude of 14-pixel differences). The scale of the error map was changed (Right) to show the large errors also made in the crack far field. It seems LEFM is not able to capture both small scale and large scale displacement fields in the case of high velocity cracks.

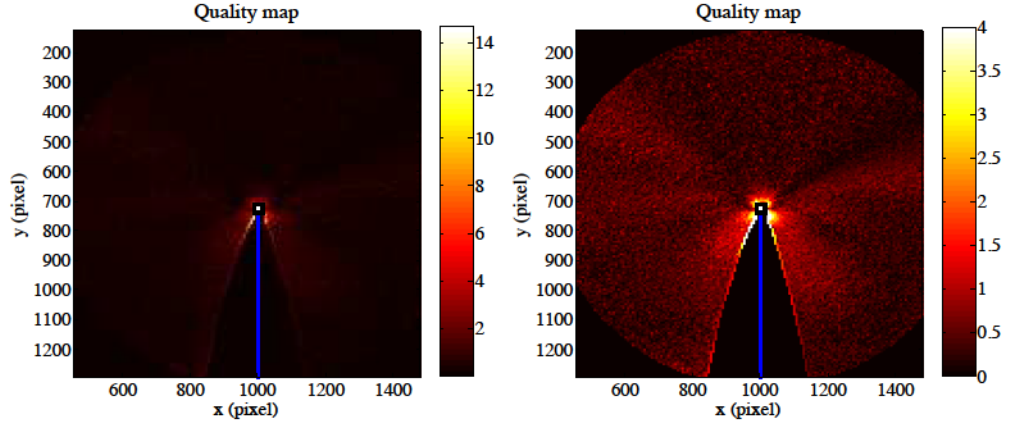


Figure 4.51: Quality map: norm of the difference between the measured and estimated displacement fields (in pixels) for a high velocity crack. Here, the projection was done using the whole ROI field.

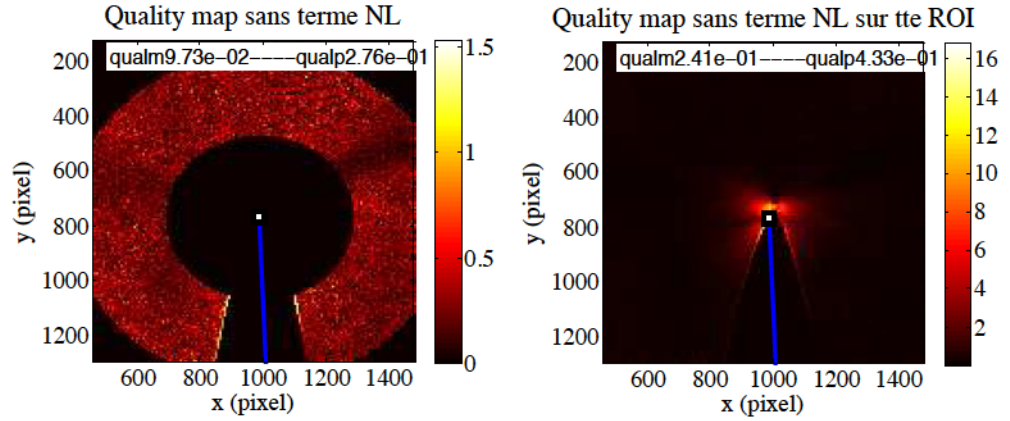


Figure 4.52: Quality map: norm of the difference between the measured and displacement fields (in pixels). Here, the projection was done using the unmasked region of the ROI. The hidden zone close to the crack tip has a 300 pixel radius. Left: Quality map in the shell-like zone between $\ell_{maskmin}$ and $\ell_{maskmax}$. Right: Quality map on the whole ROI.

Inspired by the results we had on COD measurements, one assumes there is a zone where the crack departs from linear elasticity. In the case of COD measurements, a phenomenological way to account for the wedge-like crack shape was proposed, and a modified Williams expansion was introduced. Such a phenomenological approach is not possible for such a complicated 2D displacement field. We used another approach. As the material departs from linear elasticity close to the crack tip, only the far-field displacement field is used to do the projection. This is done using a mask so that only

the data at distances from the crack tip comprised between $\ell_{maskmin}$ and $\ell_{maskmax}$ are used for the projection. The corresponding quality map of the projection is shown in Fig.4.52.

On the left of Fig.4.52, one shows the resulting quality map with a masked zone of radius $\ell_{maskmin} = 300$ pixels around the crack tip. One gets a rather homogenous quality map with low magnitude, which means the estimated LEFM displacement field is in agreement with the measured displacement field in this far field region. To assess at which lengthscale LEFM starts to break down, we systematically change $\ell_{maskmin}$ between 12 pixels (1.5 element size used to get Fig.4.51) and 500 pixels. In Fig.4.53 is shown the evolution of the quality map with the size of the masked zone in the crack tip vicinity.

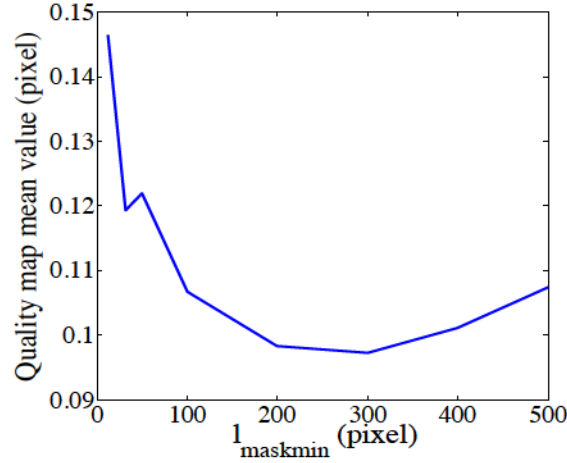


Figure 4.53: Evolution the quality map with the size of the masked zone in the crack tip vicinity.

At small $\ell_{maskmin}$, one recovers the bad agreement between LEFM and the measured displacement field. However, when increasing $\ell_{maskmin}$, this curve goes through a minimum around $\ell_{maskmin} = 300$ pixels. Let us focus on this minimum and show the corresponding values for the amplitudes a_k (see Fig.4.54).

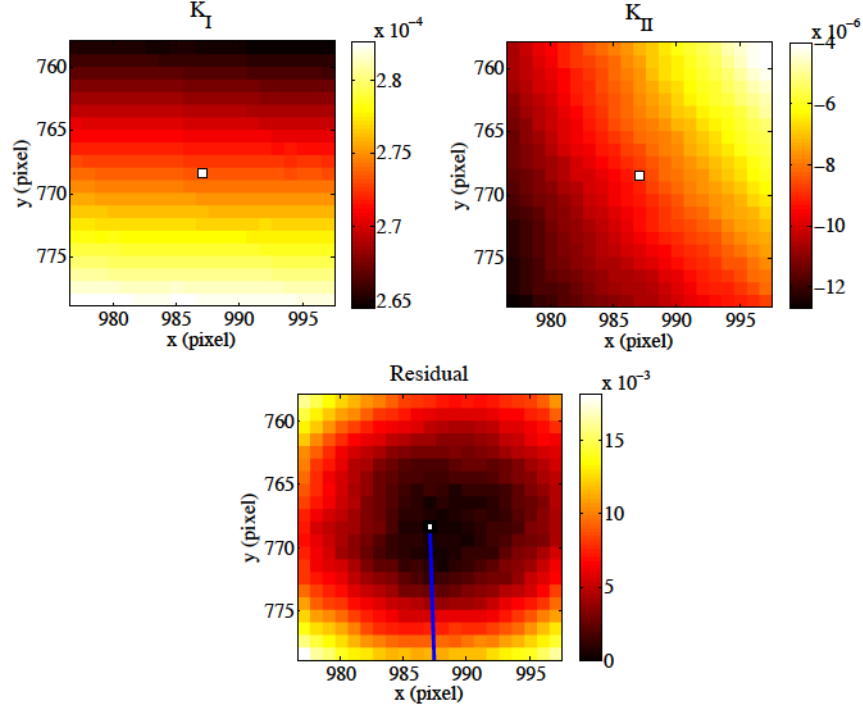


Figure 4.54: Resulting values for K_I and K_{II} with $\ell_{maskmin} = 300$ pixels.

Figure 4.54 shows that, here again, the crack is nearly in pure Mode I. K_I is found to be $273 \pm 3 \text{ Pa.m}^{1/2}$ whereas $K_{II} = -8 \pm 2 \text{ Pa.m}^{1/2}$. Meanwhile, the T-stress is again negligible. We shall note that this value of K_I is very comparable with the one that is found when analyzing the crack profile: $260 \text{ Pa.m}^{1/2}$. Figure 4.55 shows that reducing the size of the hidden zone from 300pixels to 12 pixels can cause a 20% decrease of the measured K_I value.

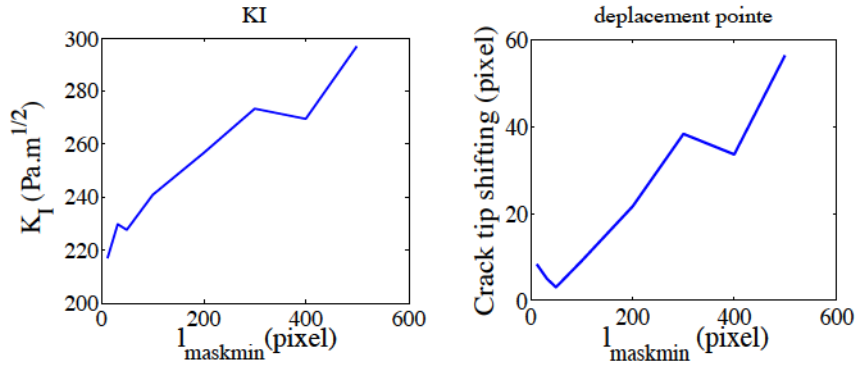


Figure 4.55: Evolution of K_I and crack tip shifting with size of the hidden zone $\ell_{maskmin}$ around the crack tip.

Another interesting result provided by this analysis is the location at which the LEFM crack tip is found: the LEFM crack tip is found $38 \pm 3\mu m$ from the detected crack tip and lies inside the crack. One can wonder how this can be compared with the $d^* = 40\mu m$ characterizing the typical length scale over which the crack had a wedge-like shape!

4.4 Conclusion. A comparison of COD and DIC

In this chapter, two techniques based on the measurement of crack displacement fields were implemented in the context of the fracture of compliant materials. The first technique consists in measuring the crack opening displacement and comparing it with theoretical predictions by proceeding in a non linear fit of the crack shape. The second technique consists in measuring the displacement field near the crack tip using Digital Image Correlation and decomposing the measured field over a basis of known displacement fields (linear elastic ones for instance).

Simplicity of Crack opening displacement. The main difficulty in the COD approach is the detection of the crack edges. However, in the context of the fracture of soft materials, where, by definition, the crack openings are large, it is a profitable technique that allows to get a more precise idea of the phenomena at stake at the crack tip. Additionnally, several theoretical contributions focused on the crack shape and provided relatively simple predictions for the crack morphology in many kind of soft materials (linear viscoelastic [50], weakly non linear elastic [56], neo-Hookean[57, 11]) and at different length scales (linear elastic [45], Dugdale-Barenblatt [58, 59]). The problem of this approach lies in its simplicity: measuring the crack shape provides data that are easy to deal with, but it may give a very simplified view of the reality.

Shortcomings of the COD approach. Two examples illustrating this idea are now given. The first one is a surprising similarity between the prediction for the crack shape in a linear elastic material and the asymptotic non linear shape of a crack in a Neo-Hookean material. Both profiles are supposed to be parabolic [57, 60], but the interpretation of the tip curvature in terms of energy release rate is very different! The second example was mentionned in Section 4.2.3.1, where we have demonstrated the effect of the T-stress on the apparent radius of curvature of a Mode I linear elastic crack tip. The knowledge of the curvature of a linear elastic parabolic crack tip is not sufficient to compute the corresponding stress intensity factor K_I : At given E , an infinity of (K_I, T) will result in the same crack shape providing $\frac{4K_I}{E(1+T/E)^{1/2}}$ is constant.

DIC provides complementary information. These two examples illustrate some shortcomings of the COD approach: the crack shape does not contain enough information to get a complete view on the material behaviour. It can be useful providing that some assumptions are made: assuming that the T-stress is zero, that the crack is in pure Mode I or checking that the strains at the crack tip are small enough to justify that LEFM ap-

plies. This additional information can only be provided by a full analysis of the displacement fields thanks to DIC (see Chapter 5). This analysis is somehow more complicated: measuring the displacement field and post-processing it, requires experimental effort and computer time. Therefore, when possible, one advocates for a complementary use of both techniques.

Equivalence between COD and DIC. What we have shown previously is that, provided that the right assumptions are made, crack opening displacement and Digital Image correlation can give similar results. For cracks at vanishing velocity, for which LEFM applies, one could show that the value of K_I obtained with the two techniques were identical. For cracks at higher velocities, each of the techniques was able to measure the same K_I but also to inform us on the typical length scale d^* below which the material departs from LEFM. Fig.4.56 is an attempt to explain why DIC found a crack tip position behind the observed one: at scales larger than d^* , the crack shape can be fitted with a parabola; the tip of this parabola is distinct from the observed one. It is at a distance δ behind it.

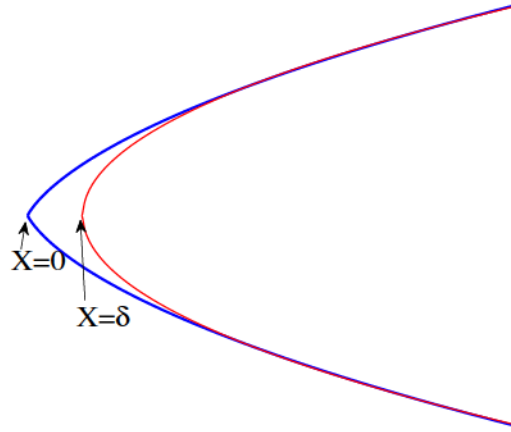


Figure 4.56: Equivalence between the COD and the DIC approaches. In blue, a typical high velocity crack shape is plotted with tip at $X = 0$. In red, we plot Irwin's Parabola that matches the far-field profile for $X > d^*$. Irwin's Parabola has its tip shifted a distance δ from the measured one.

DIC: Learning from errors. As DIC and the post-processing step goes through a minimization procedure, both can give access to maps of the errors remaining after minimization (Correli residual map, Fissurefit residual map and quality map). In Section 4.3.4.2, we have already emphasized on the interest of using the quality maps given by the post-processing step. These maps give a spatial view of where discrepancies remain between the measured and the estimated displacement fields. For instance, these maps enable us to discuss where the material departs from LEFM around the crack tip.

However, from the measurement step with DIC, one should explain about some situations of interest where *Correli-Q4* makes errors. The error maps provided by *Correli-Q4* can indeed allow to get some physical signal. For instance, let us consider a displacement field which locally exhibits typical gradients over a lengthscale λ (in the case of non affine displacement for instance). If λ is larger than the element size ℓ , DIC will be perfectly able to capture the displacement field. For λ smaller than ℓ however, the ability to capture the displacement will depend, for example, on the very shape of the interpolation function and will certainly result in anormal residual levels. Thus, *Correli-Q4* could help get some information about some localized mesoscopic features that would be of spatial extent comparable or smaller than the element size.

In the next chapter, we will show how the use of COD and DIC approaches can help us investigating the physics of fracture of the considered physical gels.

5

Rate-dependency and large strains disentangled

Contents

5.1	Introduction.	182
5.2	Macroscopic Dissipation at the crack tip	183
5.2.1	Measuring the energy release rate without measuring forces	183
5.2.1.1	Griffith energy-balance concept	183
5.2.1.2	Equivalence of \mathcal{G} and K parameters.	185
5.2.1.3	Crack configuration in our mechanical test	186
5.2.1.4	Investigating $\mathcal{G}(V)$	187
5.2.2	How can one explain $\mathcal{G}(V)$?	194
5.2.2.1	$\mathcal{G} - \mathcal{G}_e = f(V)$	194
5.2.2.2	Baumberger model	197
5.2.2.3	Bouchbinder's approach	202
5.3	Large strains at the crack tip.	207
5.3.1	COD and DIC: interpretation of d^*	208
5.3.2	Crack tip nonlinearities in a stiffening material	214
5.3.2.1	Weakly Nonlinear theory for CT displacement fields	214
5.3.2.2	Strongly NL crack tips	220
5.4	Conclusion: disentangling dissipation and large deformations	225

5.1 Introduction.

In this chapter, the fracture properties of a physical biopolymer gel (in the case of agar gels) are investigated. In the previous chapters, two tools with different complexity, but both based on the crack tip observation, were described: one could show that these two techniques lead to the same conclusions but also that they could be complementary. For example, one showed that the crack shape measurement very simply allowed to check if Linear Elastic Fracture Mechanics applied at the scale at which the crack was observed. In the case of agar gels, when LEFM did not apply, a phenomenological approach gives ones a measurement of the lengthscale δ over which the material departed from linear elasticity. But, of course, this phenomenological approach was unfounded, which gave poor significance to the measured δ . At the same time, using crack displacement fields obtained with Digital Image correlation, one did observe the same discrepancy with respect to LEFM and, by investigating where the linear elastic field was valid, one could even get, without any assumption, another measure of the same lengthscale δ .

The original experiment allows the study of plane-stress Mode I cracks propagating at controlled velocity in compliant materials. We will show that this simple crack configuration gives us the opportunity to confront our measurements with numerical simulations and with theoretical models derived in these very simple conditions. By cross-checking the information provided by high-magnification measurements of crack shape and displacement fields, one can thus shed new light on the way soft materials get damaged. First, we will demonstrate how the fracture energy increases with velocity and discuss models that try to account for this increase. Second, we will investigate how the elastic energy necessary to propagate a crack is conveyed from the far field to the crack tip. Finally, we will confront all the collected information to try to understand how this elastic energy is dissipated at the microscopic scale.

5.2 Macroscopic Dissipation at the crack tip

5.2.1 Measuring the energy release rate without measuring forces

5.2.1.1 Griffith energy-balance concept

In 1921, Griffith [61] developed an energy balance concept by modeling a static crack as a reversible thermodynamic system. His goal was to determine a criterion for crack equilibrium or crack growth. The theory developed thus deals with propagation of an existing crack without considering its initiation.

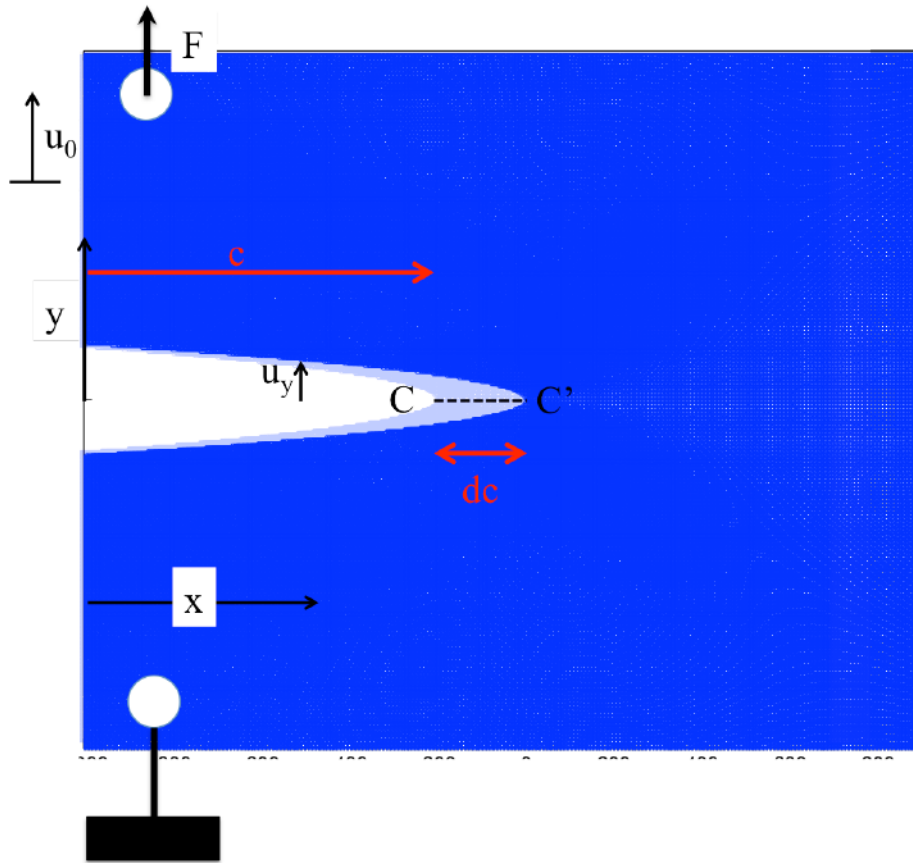


Figure 5.1: Cracked specimen and its loading system. One consider virtual crack extension between C and C' .

He considered an elastic specimen containing a planar crack of surface S and length c submitted to a load applied at infinity (see Fig.5.1). He postulated that the crack configuration at equilibrium (and thus at the limit

of extension) was the configuration that minimised the total free energy U of the system [cracked specimen+loading system].

For a system with potential surface creation (crack extension), the total energy writes:

$$U = U_M + U_S \quad (5.1)$$

where U_M is the total mechanical energy of the system [cracked specimen+loading system] and U_S is the free energy cost for creating the crack surface. U_M can itself be decomposed into two parts:

$$U_M = U_E + U_A \quad (5.2)$$

where U_E is the strain potential energy stored in the elastic body and U_A is the potential energy of the loading system.

The Griffith energy-balance concept consists in writing that the mechanical equilibrium corresponds to a minimum of U with respect to a virtual crack extension dc :

$$dU/dc = 0 \text{ i.e. } dU_M = -dU_S \quad (5.3)$$

Let us consider again the crack system of Fig.5.1 and give more details on the loading system. Consider the lower specimen boundary to be fixed and the upper end to be loaded with a tensile force F applied to the point P. One can now compute the mechanical energy U_M if one prevents the crack from extending. In that case, according to Hooke's law the specimen containing a crack of length c behaves as a spring of compliance $\lambda(c)$ and, u_0 , the displacement of the loaded point P writes as:

$$u_0 = \lambda(c)F = \lambda F \quad (5.4)$$

As a result the strain energy U_E is:

$$U_E = \int_0^{u_0} P(u)du \quad (5.5)$$

In the case of a constant force loading, let us now compute the change in U_A and U_E with respect to a crack extension dc . As the applied force F remains constant while the crack grows, crack extension is causing a displacement du_0 of the loaded point and thus $dU_A = -F du_0 = -F^2 d\lambda$. Using Eq.(5.5), one finds $dU_E = \frac{1}{2}F^2 d\lambda$. In the fixed-grip condition ($u_0 = cst$), one has $dU_A = 0$ and $dU_E = -\frac{1}{2}F^2 d\lambda$.

In both cases, the total change of U_M is therefore $dU_M = -\frac{1}{2}F^2 d\lambda$. Please note that conclusions would be the same if neither F nor u_0 remained constant. This means that: (1) some mechanical energy is released during crack extension and that: (2) this release is independent of the loading configuration. One thus defines a quantity called energy release rate \mathcal{G} such that:

$$\mathcal{G} = \frac{-dU_M}{dC} \quad (5.6)$$

with C being the crack interfacial area. \mathcal{G} thus has the dimension of energy per unit area. As it does not depend on the crack loading configuration, it can profitably be written in the fixed-grip case as:

$$\mathcal{G} = \left(\frac{-\partial U_E}{\partial C} \right)_{u_0} \quad (5.7)$$

At Griffith equilibrium, one has $\mathcal{G} = \frac{dU_S}{dC}$: the elastic energy released is used for surface creation.

5.2.1.2 Equivalence of \mathcal{G} and K parameters.

In this section, it is to be demonstrated that, in the theoretical framework of LEFM, it is equivalent to measure the energy release rate \mathcal{G} and the Stress Intensity Factor K .

To show this result, one can follow Irwin's approach described in [45]. Figure 5.1 shows a LEFM crack of length $c + \delta c$ at mechanical equilibrium. If one wants to close back the crack over distance δc , one needs to apply stresses on the crack mouth between $x = c$ and $x = c + \delta c$. The virtual operator that wants to close the crack back between $x = c$ and $x = c + \delta c$ must therefore exert a work to compensate for strain energy released for extension between c and $c + \delta c$ so that:

$$\delta U_E = 2 \int_{c+\delta c}^c 1/2(\sigma_{yy}u_y + \sigma_{xy}u_x + \sigma_{zy}u_z)dx \quad (5.8)$$

per unit width of the front. The factor 2 comes from the fact that the two crack lips should be sent back to $y = 0$. Here the relevant stresses are the one ahead of the crack tip (along CC') prior to the crack extension and the relevant displacements are those prior to crack closure. Using asymptotic σ_{ij} and u_i computed for plane stress cracks in Chapter 4, one shows:

$$\mathcal{G} = -(\partial U_E / \partial c) = \mathcal{G}_I(K_I) + \mathcal{G}_{II}(K_{II}) + \mathcal{G}_{III}(K_{III}) \quad (5.9)$$

$$= K_I^2/E + K_{II}^2/E + K_{III}^2(1+\nu)/E \quad (5.10)$$

Therefore, measuring the stress intensity factors K gives us a measure of the energy necessary to grow a crack from an infinitesimal surface dC . Furthermore, linearity gives that the different modes are additives. Usually, the SIF are computed knowing the cracked specimen geometry and the applied forces on the specimen boundaries. The interest of our method lies in our ability to directly measure the stress intensity factors from the measurement of the displacement fields.

5.2.1.3 Crack configuration in our mechanical test

Let us recall the major results provided by the post-processing analysis of the crack displacement fields measured with DIC in agar gels.

For low crack velocities ($V = 2 - 3 \mu m/s$) and for larger ones (few mm/s), it could be shown that the T-stress was negligible. The T-stress is a stress that appears in σ_{xx} where x is the crack direction of propagation (see Fig.5.2): it can be either positive, which corresponds to a tension of the specimen along the x -direction, or negative, which corresponds to a compression. The amplitude and sign of the T-stress usually depends on the biaxiality of the loading. Here, one gives a simple explanation of its origin. Let us consider the loading of the following cracked specimen (Fig.5.2).

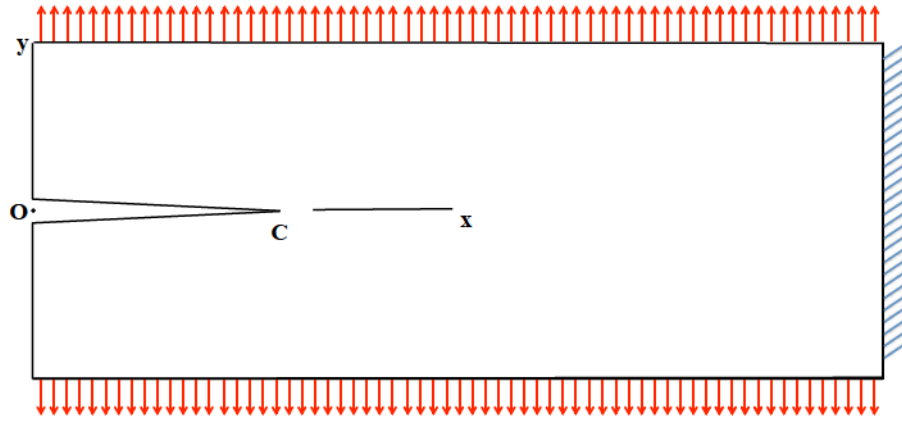


Figure 5.2: Physical origin of T-stress

The specimen is a rectangular planar body with a crack starting from one of its edge and lying along the x -direction. One of the specimen boundaries is located ahead of the crack, at finite distance from it. Its displacement is constrained by a wall to which it is bounded (see blue hatches). The two specimen boundaries along x -direction are bounded to a frame which imposes a uniform tensile displacement in the y -direction. One is interested in the stress field close to the crack tip. It is obvious that, locally, at the crack tip, the dominant stresses are the tensile σ_{yy} ones. Due to non-zero Poisson coefficient $\nu = 1/2$, and due to the fact that the boundary ahead of the crack is constrained, a non zero σ_{xx} will be non negligible in the crack tip vicinity. In this example, the constraint for the specimen boundary displacement induces biaxiality and results in tension of the crack in the x -direction.

In our case, the fact that we do have negligible T-stress results from two things. First, due to acrylamide coating of the walls, the specimen ahead of the crack is free to unbind. Second, to impose our tensile deformation, a rigid frame would, on top of imposing u_y , also constraining u_x to be zero.

The soft pistons we use leave the specimen completely free to contract in the x -direction, and the T stress is therefore close to zero!

We recall from Eq.4.51 that:

$$u_{Irwin}(d) = \frac{4K_I}{E(1 + T/E)^{1/2}} \left(\frac{d}{2\pi} \right)^{1/2} \quad (5.11)$$

Therefore, if one ignores the effect of the T-stress, the measurement of K_I can be affected by a factor $\frac{1}{(1+T/E)^{1/2}}$. However, in our case, T is, at most, equal to $10Pa$. Thus, forgetting $(1 + T/E)^{-1/2}$ results in less than 0.1% error for the measurement of K_I in the case of a Mode I crack.

Additionally to the negligible T-stress, it was shown that K_I was at least 10 times larger than K_{II} . This has a double advantage. The first one is that, with mixed mode I and II, one would not be able to measure them independently using the opening of the crack $u(d)$. Besides, the crack would not have a stable rectilinear path. Second, one just showed Eq.5.10. Therefore if K_I is negligible compared to K_{II} , it is all the more justified to neglect $\mathcal{G}_{II} \propto K_{II}^2$ compared to $\mathcal{G}_I \propto K_I^2$.

It thus seems that all the conditions are met in our plane stress mechanical test to directly infer the value of K_I and the crack energy release rate \mathcal{G} from the crack shape only!

5.2.1.4 Investigating $\mathcal{G}(V)$

To compute the crack energy release rate \mathcal{G} , one has shown that a measure of K_I was sufficient. In this part, we take advantage of the crack shape analysis conducted in Part.4.2 to extract the value of K_I .

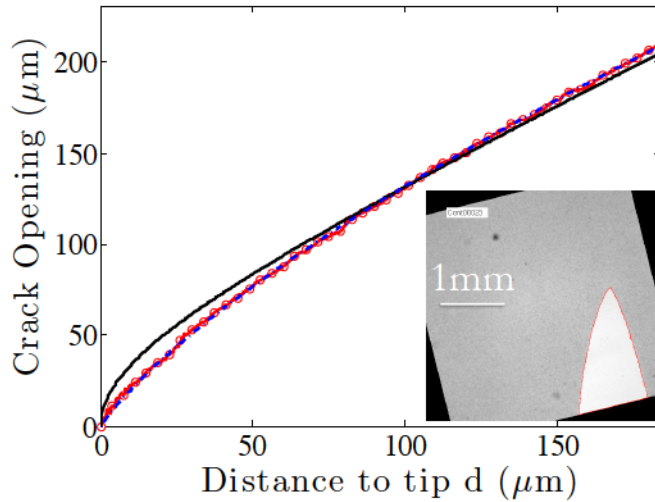


Figure 5.3: Crack opening profile at high velocity showing a wedge-like shape at the crack tip.

One recalls the modified William's expansion, which is able to capture crack profiles in the whole velocity range ($1\mu\text{m/s} - 1\text{cm/s}$ typically):

$$\tilde{u}(d) = d \left[\frac{A}{1 + \left(\frac{d}{d^*}\right)^{1/2}} + \left(\frac{d}{\tilde{d}_1}\right)^{1/2} + \left(\frac{d}{\tilde{d}_2}\right)^{3/2} \right] \quad (5.12)$$

Both crack profile analysis and analysis of displacement fields have shown that, at distances from the crack tip below d^* , linear elasticity is not valid anymore. For $d \gg d^*$, LEFM is recovered. Each crack propagating at velocity V is fully characterized by a couple $(A(V), d^*(V))$ and one wants to measure how these parameters evolve with V .

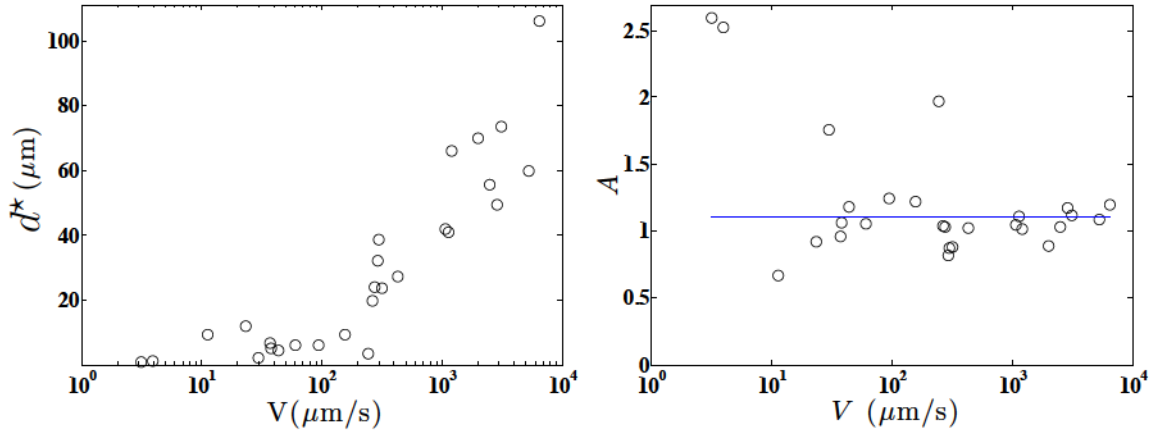


Figure 5.4: **Parameters of the modified William's expansion as a function of crack velocity V .** *Left.* Evolution of d^* with V . *Right.* Evolution of A with V . The blue line is a guide for the eye showing that A is nearly V -independent.

Values of A and d^* are shown in Fig. 5.4. Except for very low velocities, for which it is difficult to define a linear apex, A appears to be constant of order unity over the whole velocity range. Meanwhile, a continuous increase of d^* with V can be observed (Fig. 5.4, left). d^* appears to be a dynamical length scale that vanishes at small velocities and may reach up to $100\mu\text{m}$ at high velocity.

At distances from the crack tip that are large compared to d^* , but for which the 2nd term of Eq. (5.12) is still negligible, the dominant contribution to the opening is found to be $\sim A(d^*d)^{1/2}$. The question is then: does this region exist?

One could assume that, as d^* increases with increasing velocity V , d^* will eventually meet \tilde{d}_1 thus suppressing Irwin's dominant zone. Fig. 5.5 is shown again:

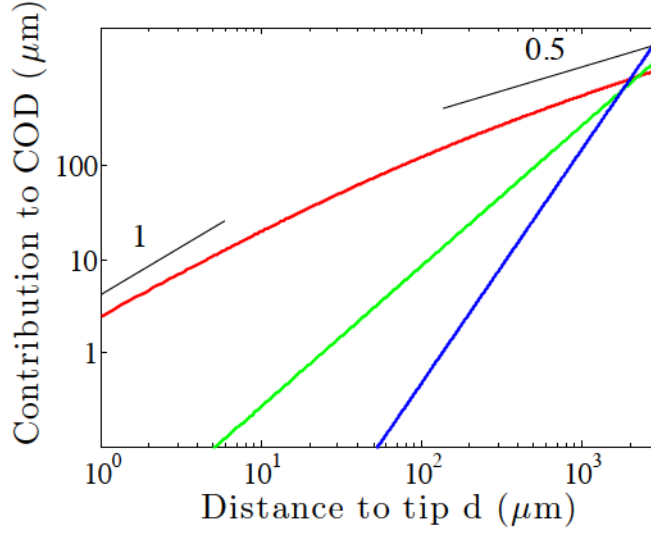


Figure 5.5: Log-log plot of the respective contributions of each of the three terms to the total crack opening displacement for the modified Williams expansion. Red: Modified Irwin term. Green: $d^{3/2}$ term. Blue: $d^{5/2}$ term.

This plot represents the respective contributions of the three terms of Eq.(5.12) on a log-log scale for one of the highest velocities one could get. It definitely confirms that there exists a spatial region close to the crack tip where Irwin's term dominates and that, therefore, it is relevant to compute K_I from the crack profile.

By analogy with the Irwin term $\frac{2K_I}{E}\sqrt{\frac{8}{\pi}}d^{1/2}$, we can thus compute the SIF $K_I(V)$:

$$K_I(V) = A(V)d^*(V)^{1/2}E\sqrt{\frac{\pi}{8}} \quad (5.13)$$

The mode I stress intensity factor K_I is computed using Eq. (5.13). Furthermore, it was shown that, in this mechanical test, crack is loaded in pure Mode I and thus, the energy release rate simply writes $\mathcal{G} = K_I^2/E$.

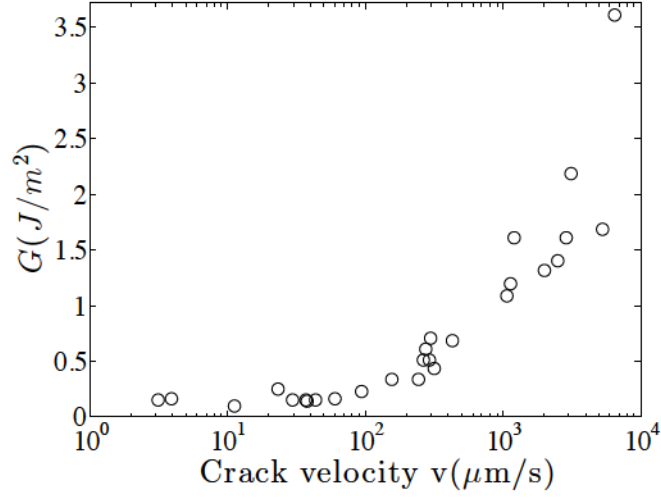


Figure 5.6: **Evolution of \mathcal{G} with V .** Black circles are the experimental results computed using Eq. (5.13).

The evolution of \mathcal{G} as a function of V is shown in Fig. 5.6. At low velocity V , \mathcal{G} seems to reach a finite limit \mathcal{G}_c below 0.1J/m^2 . At high velocity, $\mathcal{G} \gg \mathcal{G}_c$, it seems relevant to do a very common hypothesis, that it is possible to write:

$$\mathcal{G} = \mathcal{G}_c + \mathcal{G}_{diss}(V) \quad (5.14)$$

where \mathcal{G}_c would be a critical energy release rate at the onset of crack propagation and $\mathcal{G}_{diss}(V)$ would be an additional energy dissipated by the crack propagating at velocity V . $\mathcal{G}(V)$ is shown in semilog plot to emphasize the fact that, in this range of velocity, the crack energy release rate \mathcal{G} has a weak dependence on V . Indeed, for four decades increase of the crack velocity V , one observe less than 2 decades of increase of \mathcal{G} . However, one of our objectives is understand and model the increase of dissipated energy for non vanishing velocities. \mathcal{G} could increases with V due to viscous dissipation within the bulk of the material. It could also be due to dissipative processes at the crack tip.

It can be noted that the results obtained for $\mathcal{G}(V)$ by analyzing crack profiles in agar gels are qualitatively similar to those obtained by integrating force-elongation curves measured during fracture experiments on other biopolymer or physical gels [62, 63]. The results are shown in Fig. 5.7.

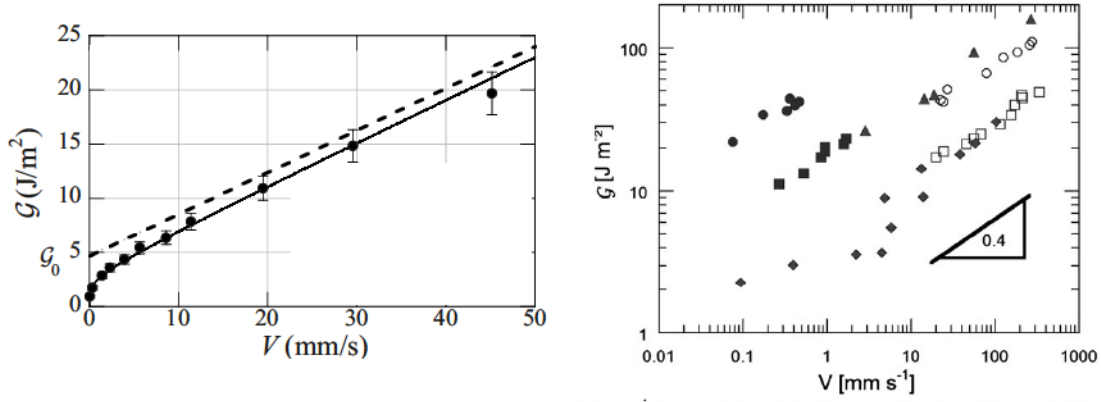


Figure 5.7: Some similar $\mathcal{G}(V)$ curves for other physical gels. Left: $\mathcal{G}(V)$ curve for a gelatin gel, physical gel with triple helix junctions. Right: $\mathcal{G}(V)$ of triblock-copolymer gels, physical gels with junctions consisting of endblock aggregates. Adapted from [62, 63].

To simplify comparison with Fig.5.7, our results for agar gels are plotted on the same axis in Fig.5.8:

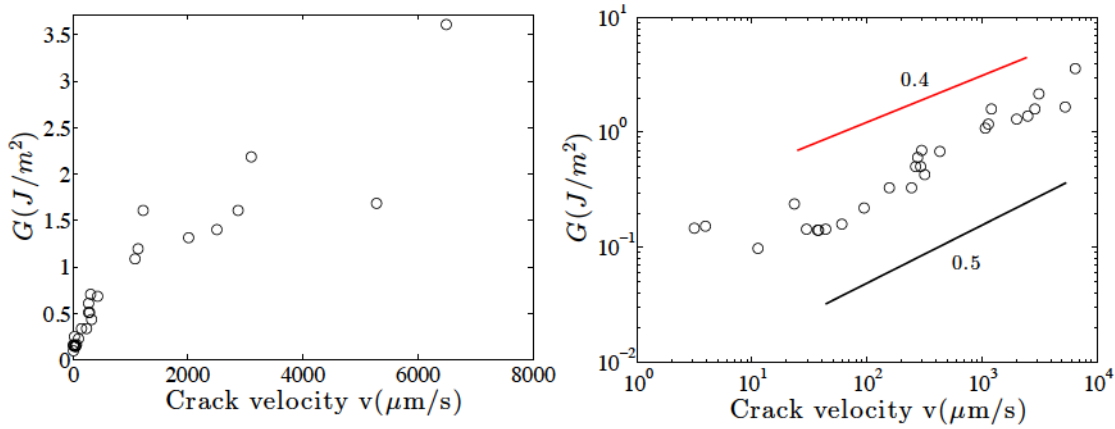


Figure 5.8: $\mathcal{G}(V)$ of agar gels represented in linear (Left) and logarithmic scales (Right).

The first comment is that these 3 materials belong to the class of physical gels. Second, when one analyses the variation of the energy release rate \mathcal{G} with V , it seems they share some characteristics: after a fast increase in the low velocity range, $\mathcal{G}(V)$ increases more softly for large velocities. If one compares Left of Fig.5.7 and Left of Fig.5.8, there is a strong similarity between the measurements in agar gels and the measurements in gelatin for velocities smaller than 10 mm/s . If now one compares Right of Fig.5.7 and Right of Fig.5.8, the power law with exponent 0.4, that is claimed to be

observed for these copolymer gels could also be valid for agar gels. In any case, these similarities between $\mathcal{G}(V)$ obtained by crack shape analysis and $\mathcal{G}(V)$ obtained by standard techniques seems to validate our measurement based on crack morphology.

5.2.2 How can one explain $\mathcal{G}(V)$?

5.2.2.1 $\mathcal{G} - \mathcal{G}_c = f(V)$

Griffith energy balance. In the Griffith energy-balance concept, a crack is in equilibrium if the crack energy release rate \mathcal{G} , i.e. the elastic energy released for a unit crack area extension, perfectly equals the energy required to create this unit crack area dU_S/dC . But Griffith does not give any way to calculate dU_S/dC .

Let us remind the existence of cohesive stresses in the crack tip vicinity and let us plot again the cohesive stress p versus the separation $2(u - u_0)$ for two material planes in a brittle solid.

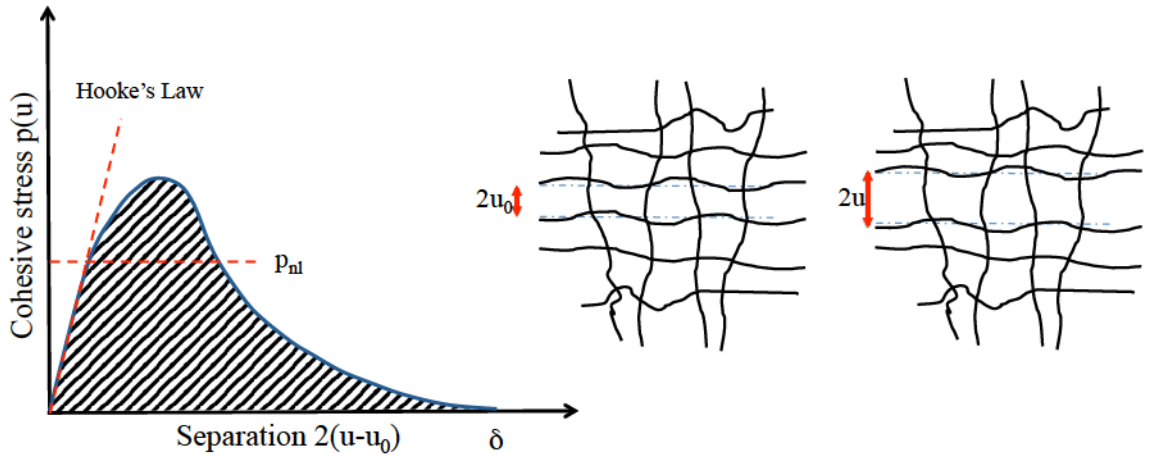


Figure 5.9: Cohesive stresses p versus the separation $2(u - u_0)$ for two material planes in a brittle solid.

Given the shape of this curve, it is trivial to compute dU_S/dC . The work to separate planes beyond distance δ defines a work of cohesion R_0 and one can write:

$$R_0 = \int_0^\delta p(u) d(2u) = 2 \int_0^{\delta/2} p(u) d(u) \simeq \sigma_y \delta \quad (5.15)$$

One can thus write the total energy change as:

$$dU = -\mathcal{G}dC + R_0dC = -gdC \quad (5.16)$$

Here, the quantity g defines the crack extension force. At Griffith equilibrium, $g = 0$ or $\mathcal{G} = \mathcal{G}_c$ where $\mathcal{G}_c = K_c^2/E = R_0$. For $g > 0$, the crack is unstable: it *a priori* grows in an uncontrolled way.

Here was only considered the surface energy cost to separate the two materials planes on each side of the fracture plane. This is *a priori* true for brittle solids, for which fracture occurs by bond rupture ahead of the crack tip. For tougher materials, Eq.(5.15) is not enough to capture all the energy cost associated to the creation of a unit crack area. Indeed, when the crack extends, damage and dissipative processes occur not only on the fracture plane ahead of the crack tip, but also in the process zone of size ℓ_{PZ} all around the crack tip. Therefore, in 1958, Irwin and Orowan simultaneously proposed an extension of Griffith's concept.

Irwin-Orowan model. Their challenge was to take into account all the nonlinear, irreversible and dissipative processes occurring in the process zone while maintaining the framework of Linear Elastic Fracture mechanics used by Griffith. This is known as the Irwin-Orowan model, where the crack system is divided into two zones: an outer zone, linear elastic, that transmits stresses and strain elastic energy to an inner zone, where all energy dissipative processes occur. They showed that, provided that the inner zone remains small, the mechanical energy release rate could be computed using LEFM while the inner zone, where the work of separation is spent, behaves as if it is embedded in an effective K dominated field. They replaced the surface energy cost R_0 by a generalised crack-resistance energy R that takes into account both bond rupture at the crack plane and all the secondary energy-absorbing phenomena in the process zone. One thus has $\mathcal{G} = R = \mathcal{G}_c$ at crack equilibrium, R being a measure of the material toughness.

V -dependent dissipation, $\mathcal{G}_{diss}(V)$. The cracks considered previously were cracks on the verge of stability and thus they were cracks with zero velocities. Let us now consider a case where $g > 0$ and the crack is unstable. In some materials and some configuration, the crack will grow in an uncontrolled way. In some others, the crack with velocity V will activate other dissipative processes (viscoelasticity, shielding, flow, etc) that will limit the crack kinetic energy: a stable state of steady crack propagation can eventually be reached. In that case the Irwin-Orowan inner zone simply translates with the crack tip and the dissipative work is a V -dependent characteristic material parameter.

As the crack is propagating in a stable way, one can write an energy balance. This results in the following relationships, often used in the case of viscoelastic materials [64, 65, 66], for a crack in steady-state extension at velocity V :

$$\mathcal{G} = \mathcal{G}_c + \mathcal{G}_{diss}(V) \quad (5.17)$$

In other words, for such a propagating crack, there is a constant balance between the energy release rate on one side, the energy necessary to create new crack surface plus the extra dissipated energy on the other side.

In Fig.5.6 or Fig.5.7, it seems that, in the case of agar gels and other physical gels, such a relationship seems to be satisfied. However, as we have shown in Chapter 2, agar gels do not exhibit any viscoelasticity on the experimental timescales. There is thus *a priori* no reason to observe rate-dependency of the fracture properties, as it is expected in viscoelastic materials. As one does observe V -dependence, there must be other dissipative processes due to crack steady-state extension.

5.2.2.2 Baumberger model

The existence of dissipation sources other than viscoelasticity was for example considered by Baumberger & al [67, 63] in the case of gelatin and alginate gels. We briefly review their rate-dependent cohesive zone model and compare their predictions with our results.

Description of the model. One considers a polymer network with chain average contour length Λ and areal chain density $\Sigma_0 = 1/\xi^2$ crossing the fracture plane. These chains are bounded to each other by extended physical junctions containing n subunits. Each of the junction subunit has a typical size a and binding energy U (see Fig.5.10). Due to the weak nature of the physical links, fracture of this class of gels is expected to occur via yielding of the junctions rather than chain scission.

Baumberger & al assume a wedge-like shape in order to have a simple kinetic relation between the crack velocity V and the speed \mathcal{V} at which the chains crossing the fracture plane are unreeled from the junction. Assuming this, the pullout velocity \mathcal{V} is thus directly proportionnal to the crack velocity $\mathcal{V} = \alpha V$. This assumption is common, but questionable, as we showed in Sec.4.2.1.2, that the Dugdale Barenblatt model predicts a cusp-like shape. It is additionally assumed that α does not depend on V . As already mentioned, the pullout of the chains occurs by unzipping of the weak bonds in the junctions. Each unzipping event allows the chain to be pulled out over a distance of the order of the size of one residue. We can thus write a relation between the pullout velocity \mathcal{V} and the rate ν at which the H bonds unzip: $\mathcal{V} = a\nu$.

The fracture energy is computed using Dugdale's viscoplastic theory and thus assumes a constant yield stress σ_{yd} over the cohesive zone of size λ_{DB} . Closure of the problem requires to relate σ_{yd} to ν . This is done by estimating the cohesive force f_Y exerted on an individual chain.

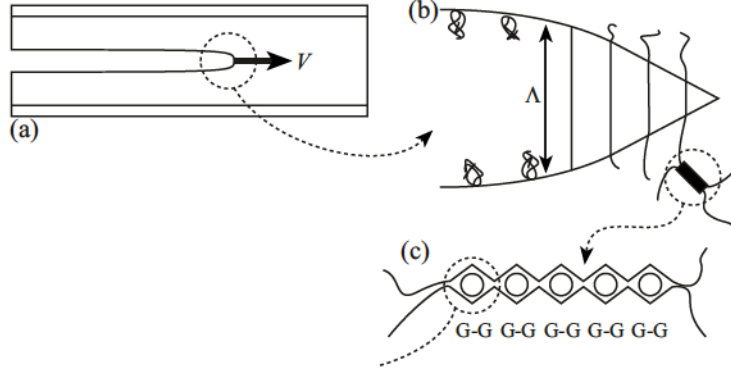


Figure 5.10: Chain pullout at the tip of a crack (a) propagating in a physical gel at velocity V . (b) The chains with contour length Λ are fully stretched when the junction zone collapses. A junction in alginate gels is shown in (c): it consists in an egg-box structure with several ionic cross-links of individual energy $U = 12kT$. From [63].

f_Y takes into account the viscoplastic yield stress (that is allowed to be V -dependent and which one of the unknowns) and viscous friction on the chain of length Λ being pulled out from the elastic mesh swollen with solvent,

$$f_Y = \frac{\sigma_{tip}}{\Sigma_0} - \eta\Lambda\mathcal{V} \quad (5.18)$$

and we relate ν to f_Y , by assuming the debonding event (interaction energy U) can be stress-activated:

$$\nu = \nu_0 \exp \left[-\frac{U - af_Y}{k_B T} \right] \quad (5.19)$$

This model thus predicts:

$$\mathcal{G} = \Lambda\sigma_y = \mathcal{G}_0 \left[1 + \frac{k_B T}{U} \ln(V/V^*) + \gamma\eta V \right] \quad (5.20)$$

with

$$\mathcal{G}_0 = \frac{U\Lambda\Sigma_0}{a}, \quad V^* = \frac{a\nu_0}{\alpha}, \quad \gamma = \frac{a\Lambda\alpha}{U} \quad (5.21)$$

At high velocity, a linear dependence of \mathcal{G} with V is expected: in this regime, the dissipation results from the friction of the chain with the viscous solvent when pulled out, and the effective viscosity is thus $\eta_{eff} = \gamma\mathcal{G}_0\eta = \alpha\Sigma_0\Lambda^2\eta \simeq 10^4\eta$.

At vanishing velocities ($V \ll V^*$), the logarithmic term induces a reduction of \mathcal{G} compared to the value \mathcal{G}_0 that would be obtained from the simple extrapolation of the linear dependence observed at high velocities. In Fig. 5.11 is shown a semilog plot of the V -dependence of the fracture energy of alginate gels. The solid line is the best linear fit for the highest crack velocities. Linear extrapolation to vanishing velocities gives an apparent $\mathcal{G}_0 \simeq 5 \text{ J/m}^2$. Due to the negative logarithmic term for $V < V^*$, the measured \mathcal{G} is lower than \mathcal{G}_0 . This means the crack propagation is subcritical: due to stress activated processes, a crack can propagate even if $\mathcal{G} < \mathcal{G}_0$, *i.e.* even if $\sigma < \sigma_{yd}$ in the cohesive zone.

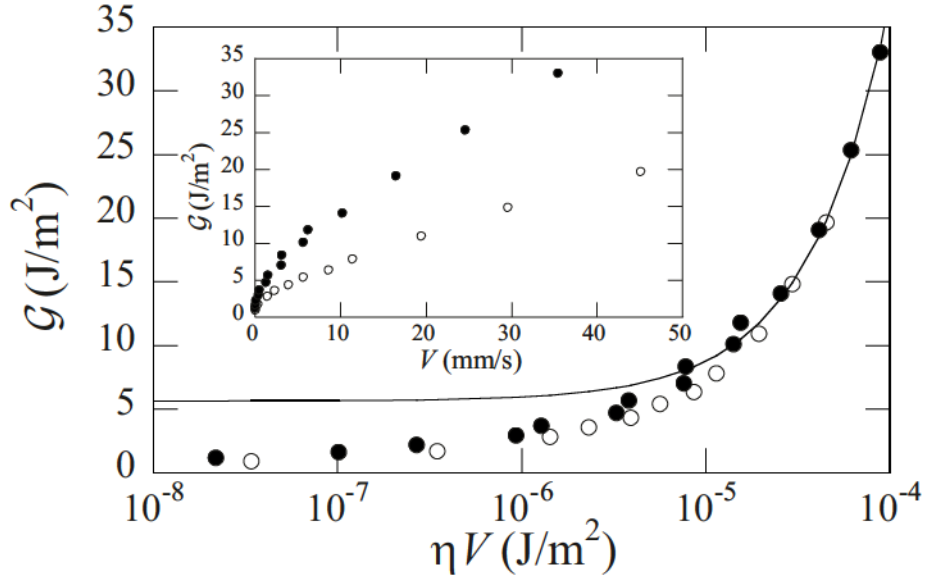


Figure 5.11: Semilog plot of the V -dependence of the fracture energy of alginate gels, from [63].

Discussion of the results. If we write the fracture energy as $\mathcal{G} = \sigma_{yd}\Lambda$, and if we use $\mathcal{G} = 1 \text{ J.m}^{-2}$ as a typical fracture energy for these gels and $\Lambda = 500 \text{ nm}$ as the chain contour length, one finds a yield stress $\sigma_{yd} = 2 \text{ MPa}$! For alginate gels, this corresponds to 1000 times the shear modulus. For agar gels with $\Lambda = 400 \text{ nm}$ and $G = 20 \text{ kPa}$, this corresponds to $\sigma_{yd} = 125G$! The conclusions are the following: (1) the chains are almost fully stretched when the chains unreel and when they are pulled out from the material (see Fig. 5.10); (2) at such level of stress, the framework of linear elasticity used for deriving Dugdale theory may collapse.

On top of the very high stresses at the crack tip, this model gives some puzzling results in the case of alginate gels. On the one hand, the obtained value of the critical energy release rate $\mathcal{G}_0 = 5 \text{ J/m}^2 = \frac{U\Lambda\Sigma_0}{a}$ gives $\Sigma_0 =$

$2 \cdot 10^{17} \text{m}^{-2}$ if we take $U = 12kT$, $\Lambda = 500\text{nm}$ and $a = 0.9\text{nm}$ (as proposed in Ref. [63]). But if, on the other hand, we compute Σ_0 using the measured mesh size $\xi = 14\text{nm}$, we find $\Sigma_0 = 5 \cdot 10^{15} \text{m}^{-2}$, a value 40 times smaller than be expected, which would correspond to \mathcal{G} lower by 2 decades ($\mathcal{G}_0 = 0.12 \text{J/m}^2$)!

There must be something wrong. Here the chosen value for U corresponds to the interaction potential of one binding unit (one subunit of the eggbox structure shown in 5.10). Owing to the high stresses computed previously, and as we only took into account the highest velocities (and thus highest stress levels) to find \mathcal{G}_0 , we should maybe consider that all the $n = 25$ subunits of the eggboxstructure collapse simultaneously. Therefore U would rather be $300kT$, and the new computed value of Σ_0 would be closer to the expected value.

A last remark concerns the logarithmic regime of $\mathcal{G}(\eta V)$ at low velocities. We consider Fig. 5.11 and Fig. 5.12 where $\mathcal{G}(\eta V)$ is plotted on semilog axes. In Fig. 5.11, the slope is small but non zero while in Fig. 5.12, it is much smaller. This means that, for alginates, the contribution of the logarithmic term is larger than for agar gels and thus, that the binding energy U to be considered for agar junctions is larger than the one of alginates.

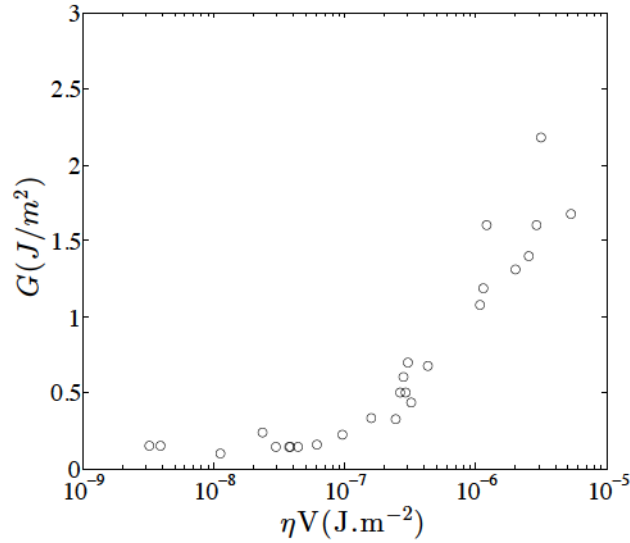


Figure 5.12: Semilog plot of the ηV -dependence of the fracture energy of agar gels.

This model has interesting properties, but the large number of microscopic parameters involved makes its use difficult. Still, it is one of the first to introduce a coupling between the stress level in the cohesive zone and the rate at which the chains are pulled out. However, what we think is not taken into account in this stress activated model, is the change of cooperativity

with crack velocity. At low velocities (and low crack tip stresses), one can expect the subunit residues to be extracted one by one ($n = 1$). At higher velocities (and higher stresses), the cooperativity could increase and all the subunits could fail at the same time ($n = 25$). In other words, the binding energy to be considered would depend on the number n_{coop} of units failing at the same time, which would itself depend on V . This detail can be of little importance when considering physical gels with small junctions; we think it will strongly modify the crack dynamics for extended junctions as the one of agar gels.

As already mentionned, in our case, there is apparently no influence of the logarithmic term at low velocities. A model with a critical \mathcal{G}_c at low velocities seems more relevant. Following a derivation by Bouchbinder & al, we try to model our experimental data with an expression of the form of Eq.5.17.

5.2.2.3 Bouchbinder's approach

Another derivation of $\mathbf{G(V)}$. We now come back to the case of agar gels and discuss the V -dependence of \mathcal{G} . As suggested in Section 5.2.2.1, the energy release rate for a crack growing at velocity V can be written as:

$$\mathcal{G} = \mathcal{G}_c + \mathcal{G}_{vis}(V) \quad (5.22)$$

where \mathcal{G}_c is the critical energy release rate (fracture energy at vanishing crack velocity) and $\mathcal{G}_{vis}(V)$ is the rate-dependent energy (per unit crack surface created) dissipated during steady-state propagation at velocity V .

Following Ref. [68], we estimate the bulk dissipation for a stationary crack (for which time derivatives can be replaced by space derivatives, i.e. $V \partial t = \partial r$) propagating at vanishing velocity V in the following way:

$$\mathcal{G}_{vis} = \frac{\eta}{V} \int (\partial_r \dot{u})^2 r dr \quad (5.23)$$

$$= \eta V \int_{r=d_c}^{r=\infty} (\partial_{rr} u)^2 r dr \quad (5.24)$$

where we have not taken into account the angular variation of u since, once integrated in Eq.(5.24), it will only modify the prefactor. It is important to note that this procedure is perturbative in nature since the static crack solution is calculated without taking into account viscous deformation, and is used to estimate the dissipation arising from viscous deformation.

In Ref. [68], η is an effective material viscosity that, here, encompasses all the bulk viscous dissipation but also all the dissipative processes at the crack tip. d_c is the microscopic length scale where the linear theory fails. In Bouchbinder & al paper d_c is the size of the process zone; it is a free parameter. Thanks to our study of crack displacement fields, d_c is not a free

parameter anymore. It is the length scale d^* that we have measured in our experiment.

In this perturbative approach, one can use the elastic asymptotic crack displacement field $u(r) \propto (K_{IC}/E)\sqrt{r}$, and $\partial_{rr}u \propto -K_{IC}/Er^{-3/2}$; Hence:

$$\mathcal{G}_{vis} \propto \frac{\mathcal{G}_c \eta}{Ed^*(V)} V \quad (5.25)$$

where $\mathcal{G}_c = K_{IC}^2/E$.

Computing $\mathcal{G}_{vis}(V)$ at higher velocity is a more delicate task. Indeed, at finite V , local dissipation at a distance r from the crack tip depends on the local strain rate at pulsation $\omega = V/r$ [69]. Moreover, the perturbative approach, valid when $\mathcal{G}_{vis} \ll \mathcal{G}_c$ does not hold when $\mathcal{G} \gg \mathcal{G}_c$.

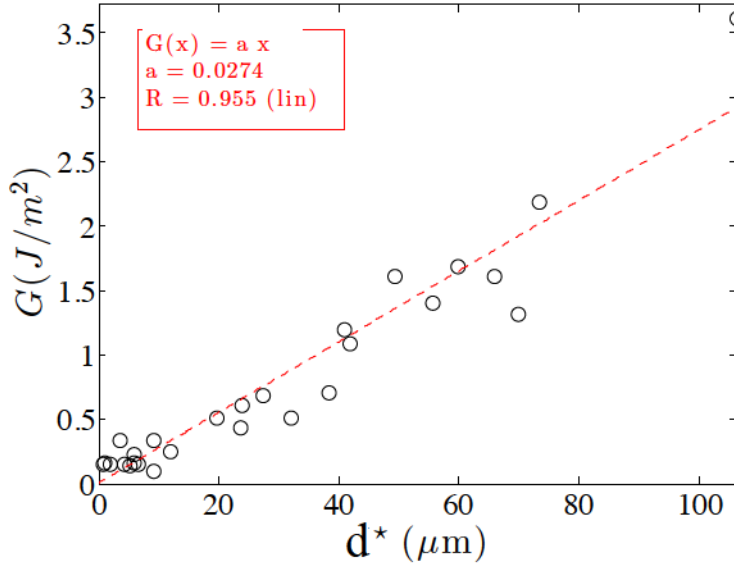


Figure 5.13: \mathcal{G} versus d^* for different velocities V .

Fig. 5.13 shows \mathcal{G} versus d^* . A linear relation $\mathcal{G}(V) = \alpha d^*$ fits indeed the data with $\alpha = 2.7 \cdot 10^4 Pa$. Thus $\mathcal{G}(V)/E \propto d^*$.

For large V , as $\mathcal{G} \sim \mathcal{G}_{vis}$, we have:

$$\frac{\mathcal{G}_{vis}(V)}{\mathcal{G}_c} = \frac{d^*(V)}{d^*(V=0)} \quad (5.26)$$

Matched asymptotics enable to eliminate $d^*(V)$ in Eq. (5.25) using Eq. (5.26), and we get, for high velocities:

$$\mathcal{G}_{vis} \sim \mathcal{G}_c \sqrt{\frac{\eta V}{Ed^*(V=0)}} \quad (5.27)$$

Over the whole velocity range, we thus have:

$$\mathcal{G} \sim \mathcal{G}_c \left(1 + \sqrt{\frac{\eta V}{E d^*(V=0)}}\right) = \mathcal{G}_c \left(1 + \sqrt{\frac{V}{\tilde{V}}}\right) \quad (5.28)$$

where

$$\tilde{V} = \frac{E d^*(V=0)}{\eta} \quad (5.29)$$

Agreement between the measured fracture energy $\mathcal{G}(V)$ and Eq. (5.28) is good within the explored velocity range (Fig. 5.14).

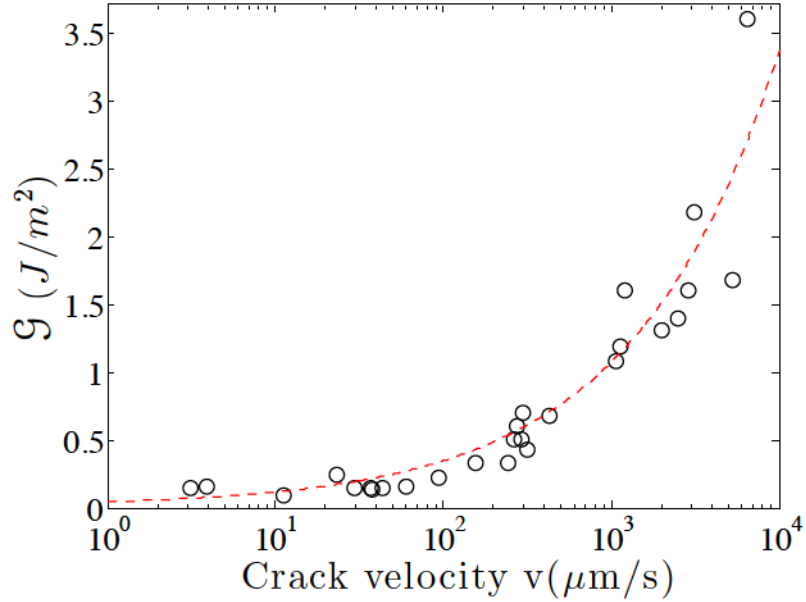


Figure 5.14: \mathcal{G} versus crack velocity V for agar gels with $C = 1.5\text{wt}\%$. Black circles: Experimental data. Red dashed line: Fit using Eq. 5.28.

Discussion of the resulting parameters. We now discuss the parameters obtained by fitting $\mathcal{G}(V)$ with the two-parameter Equation (5.28).

The resulting value for the critical energy release rate $\mathcal{G}_c = 0.01\text{J/m}^2$ is reasonable. Let us recall that, in the absence of surface tension between the fluid inside the crack and the soft material, \mathcal{G}_c is the surface energy needed to break the bonds crossing the fracture plane at vanishing velocity. Given the weakness of H-bonds compared to the covalent bonds, fracture of these physical gels is reported to occur via unzipping of the junctions of energy U_H [38]. The model of Lake & Thomas [70] states that all the energy stored in a chain containing n residues is dissipated at rupture. Thus, \mathcal{G}_c should scale like $(U_H \Lambda)/(\xi^2 a)$ where ξ is the distance between the junctions and a

is the size of a residue. With $U_H = 0.1\text{eV}$, $\Lambda = 400\text{nm}$ and $a = 1\text{nm}$, we find $\mathcal{G}_c = 1.5 \cdot 10^{-2} \text{J/m}^2$ which is in good agreement with the value measured thanks to our model. This means that, at low velocities, bond rupture on the fracture plane is enough to capture a good value of \mathcal{G}_c and that there is no additional mechanisms of dissipation at low velocities.

The fit also gives a value for $\tilde{V} = 0.1\mu\text{m.s}^{-1}$ which is below the minimum crack velocity that we could reach. For a crack of velocity \tilde{V} , \mathcal{G} is expected to be twice \mathcal{G}_c . What we observe experimentally instead, is in fact an intermittent crack propagation regime. At such small velocities, we suspect that a moderate stress relaxation of the network is sufficient to dissipate elastic energy and to decrease \mathcal{G} below its critical value \mathcal{G}_c causing the crack to grow intermittently. From Eq. 5.29, we get $\eta = Ed^*(V=0)/\tilde{V}$. When $V \rightarrow 0$, $d^* \rightarrow 0$, no large strain is expected at the crack tip and the limitation to LEFM is thus the extent of the Dugdale–Barenblatt cohesive zone $\ell_{DB} = \mathcal{G}_c/\sigma_y = \mathcal{G}_c/E \simeq 0.1\mu\text{m}$. Consequently, η is found to be $E\ell_{DB}/\tilde{V} \sim 6 \cdot 10^4 \text{Pa.s}$.

We can wonder how a material with rate independent G' and G'' exhibit rate-dependent fracture properties. The answer lies in the rate-dependency of the highly non linear processes occurring in the vicinity of the crack tip. One of them was already discussed: it is the viscous chain pull-out, proposed by Baumberger & al in the case of gelatin [63]. It results in an effective viscosity scaling like $\eta_S \Lambda^2/\xi^2 = 10^4 \eta_S$ where $\eta_S = 10^{-3} \text{Pa.s}$, is the solvent viscosity. For our agar gel, this effective viscosity is orders of magnitude too low.

Another option is to consider that dissipation stems from the dynamics of agar chain segments confined in the junction zones. Indeed, reptation processes result in an effective viscosity $\eta_{eff} = G'\tau_{rep}$ [23] where τ_{rep} is the chain reptation time. In our case, the reptation time is the time at which our biopolymer network relaxes. At our working concentration, Labropoulos & al[16] found that agar networks relax on timescales of $10^2 - 10^3 \text{s}$. This results in $\eta_{eff} = 10^7 - 10^8 \text{Pa.s}$ which is now far larger than our measurement and confirms that our material does not flow on experimental timescales. But if we now consider the material in the vicinity of the crack tip, stress-aided reptation of the strongly deformed chains may significantly decrease τ_{rep} by 1 or 2 orders of magnitude, which would lead to η_{eff} in the measured range.

In this vision, it seems that the fracture energy and the crack dynamics are mainly controlled by the microscopic details of chain failure in the cohesive zone. A better knowledge of the processes at stake at a distance from the tip smaller than d^* is therefore required to gain a better understanding of the conditions of stress at which the unzipping events occur.

5.3 Large strains at the crack tip.

Similar emergence of a region where the material departs from LEFM has already been observed by Bouchbinder & al [56, 11] in the context of the dynamic fracture of chemical gels. In this study, the dynamic propagation of cracks with large K_I induces a breakdown of LEFM near the crack tip (see Fig.5.15): the crack strongly departs from the parabolic LEFM shape (top figure, red dashed line) on some lengthscale δ .

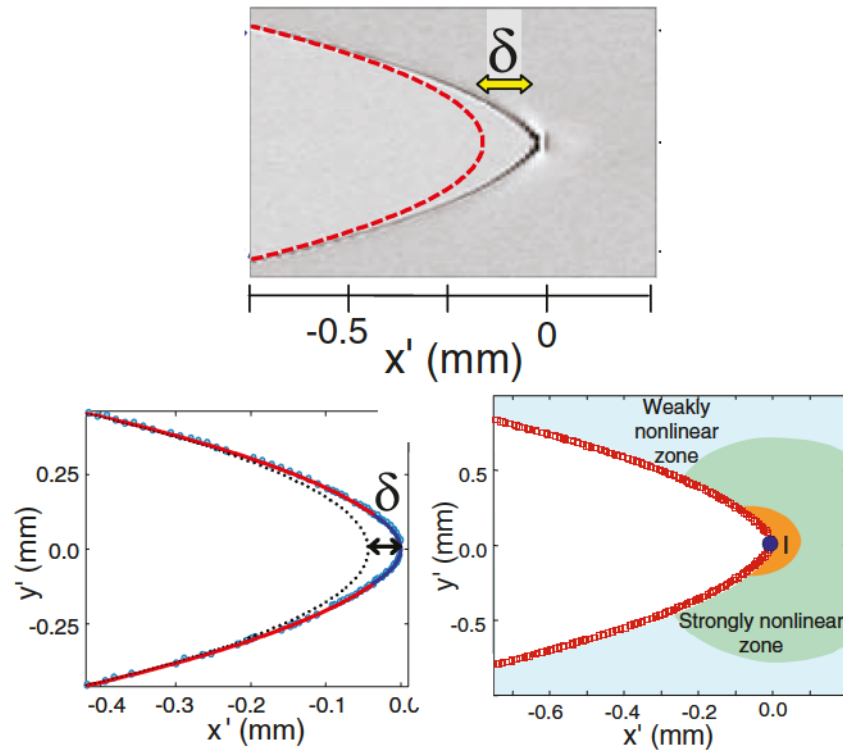


Figure 5.15: Top: Snapshot of a dynamic crack in an acrylamide gel showing a strong departure from the LEFM parabolic profile (in red) over a typical distance δ . Bottom Left: Reconstruction of the crack profile using LEFM (black dotted line), WNL theory (red line) and SNL theory (blue line). Bottom right: Map showing WNL (light blue), SNL (green) and damage (orange) zones. From [11].

Below a distance to the tip smaller than a few δ , the material enters into a weakly non linear (WNL) zone (light blue zone in bottom right figure). Below δ , elastic non linearities become greater and greater: the material is deep in a strongly nonlinear (SNL) zone but all the deformations remain reversible (green zone). Eventually, the material damages at even smaller length scales (orange zone). We will see later on that, in the case of neo-

Hookean materials, the whole crack shape can be reconstructed using LEFM, a WNL theory and the SNL prediction.

It is the first time that such a similar departure from LEFM is observed for the quasi-static propagation of cracks in a soft material. We will check that this departure is indeed due to large strains and study if the WNL and SNL theories apply to our case.

5.3.1 COD and DIC: interpretation of d^*

As already mentioned, the wedge-like shape of the crack tip cannot be explained by cohesive zone nor viscoelastic models. Another assumption is that the large deformations at the crack tip induce a departure of the material from its linear elastic behaviour. Let us thus assume that d^* marks a domain of large strains in the crack tip vicinity, which leads to a strong deviation from LEFM.

In linear elasticity, the strain ϵ at a crack tip scales as $\epsilon \simeq \frac{K_I(V)}{E\sqrt{2\pi r}}$. From Eq. (5.13), at a distance $r > d^*$ ahead of the crack tip, *i.e.* within the linear elastic zone, the strain scales as:

$$\epsilon(r) = \partial_r u(r) = \frac{K_I(V)}{E\sqrt{2\pi r}} = \frac{A(V)}{4\sqrt{r/d^*}} \quad (5.30)$$

A being independent of V , with $A \sim 1.2$, we find that $\epsilon(d^*)$ is about 30 %, which is a deformation large enough to justify that LEFM does not apply in this zone. Indeed, in the WNL theory, Bouchbinder & al [56] have shown that the effect of large deformations becomes measurable within the 10 – 20% range. At distances $d < d^*$, the crack tip shape depends strongly on the nonlinear constitutive law of the material.

This scaling approach indicates that d^* gives an order of magnitude of the distance from which nonlinear elastic effects start becoming relevant. Using Eq.(5.30) and $\mathcal{G} = K_I^2/E$, it can be shown that $d^* \propto \mathcal{G}/E$, which is known to be a nonlinear length scale [71].

There is no way to compute the material strain from the crack shape only. A more direct approach consists in using Digital Image Correlation to measure the absolute displacement field $u(r, \theta)$ around the crack tip and to compute the strain with the distance to the crack tip. To do so, following Sec.4.3.3, the absolute displacement field between a reference undeformed image and a deformed image with a crack is sought using DIC. Fig.5.16 shows the absolute fields U and V for a crack nucleating from the notch and propagating at $50\mu\text{m/s}$ and for which d^* is $20\mu\text{m}$.

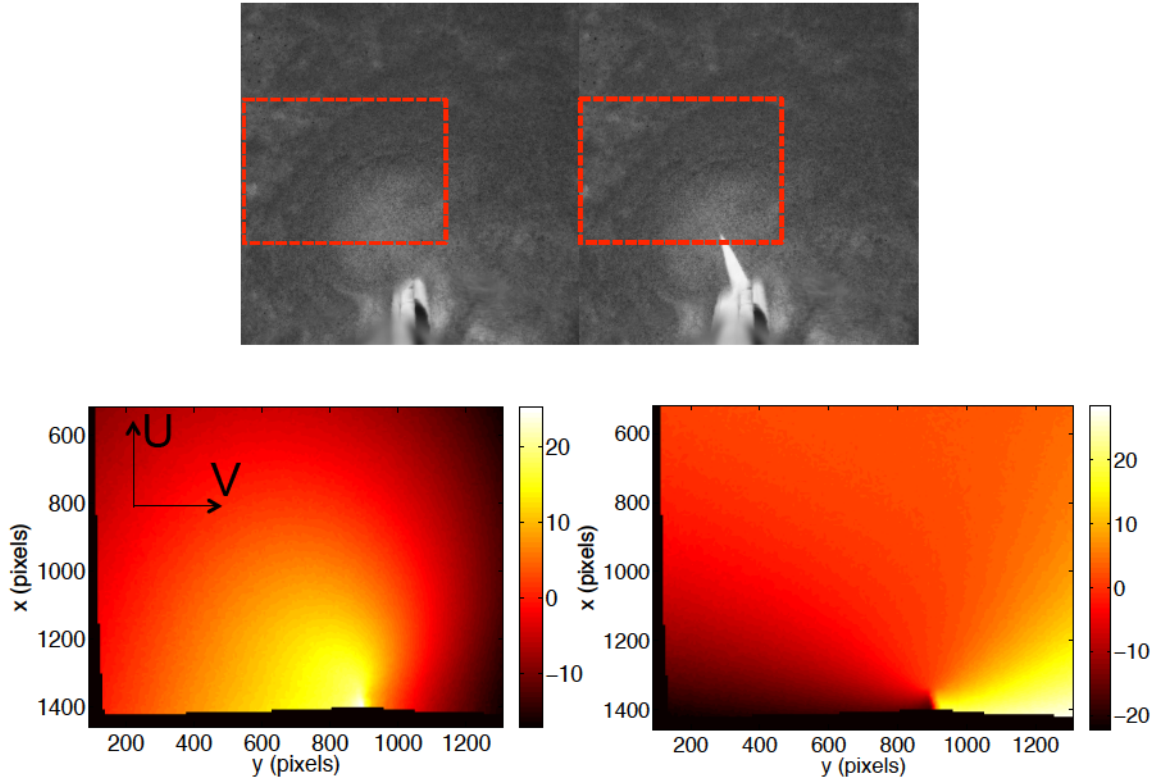


Figure 5.16: Top: Undeformed and deformed images. The rectangular ROI is shown in dashed red. Bottom: Components U (Left) and V (Right) of the measured displacement field.

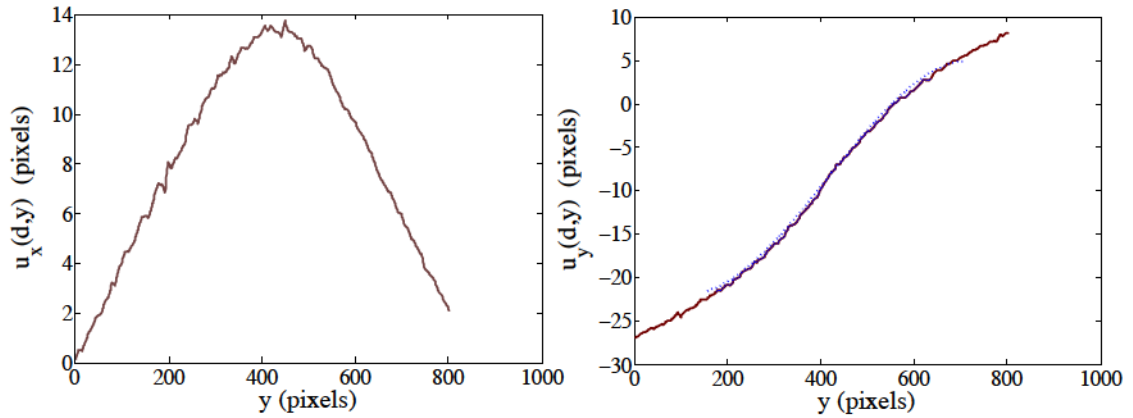


Figure 5.17: $u_x(d,y)$ and $u_y(d,y)$ are respectively shown on the Left and Right. $u_y(d,y)$ is fitted with a 3rd order polynomial with odd power terms only (dashed blue line) and the sought strain is extracted from the prefactor of the y term.

In the natural crack frame coordinate (x being the crack direction and y being the normal to it), we plot $u_y(d, y)$ and $u_x(d, y)$ for various values of $x = d$ ahead of the crack ($d > 0$). As expected for a mode I crack, $u_y(d, y)$ is antisymmetric in the y -direction while $u_x(d, y)$ is symmetric (Fig.5.17).

Our goal is to compute $\epsilon_{yy} = \frac{\partial u_y}{\partial y}(d, y = 0)$. This is done by fitting each $u_y(d, y)$ with a 3rd order polynomial with odd power terms only. The sought strain is extracted from the prefactor of the y term (see Fig.5.17). Fig.5.18 is a plot of $\epsilon_{yy}(d, 0)$ with d for this crack.

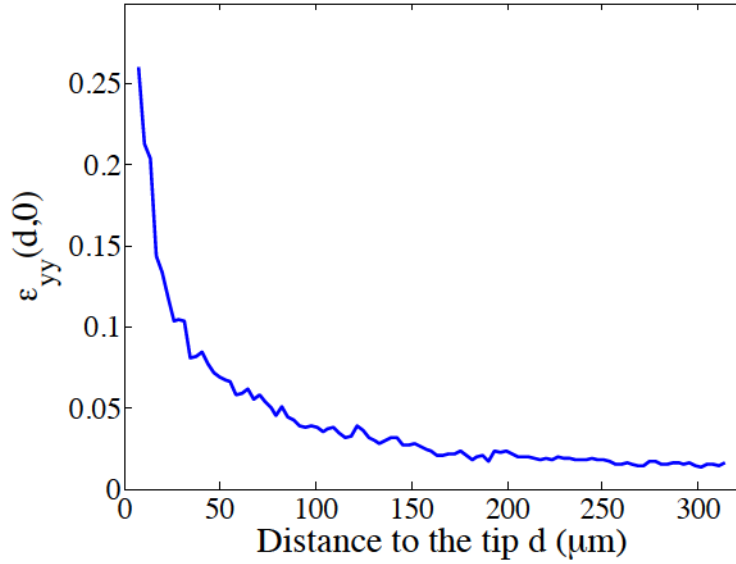


Figure 5.18: Strain $\epsilon_{yy}(d, 0)$ ahead of the tip.

Provided that we have access to the underformed state of the specimen, we are able to compute the opening component of the strain. With an element size $\ell = 8\text{pixels}$, the measure is reliable for distances to crack tip greater than $15\mu\text{m}$. Here, we are able to measure strains at the crack tip of order 25%. This value is well above the nonlinear threshold, which, in the case of agar, goes down to about 5%. At $d = d^*$, the measured strain is 8%.

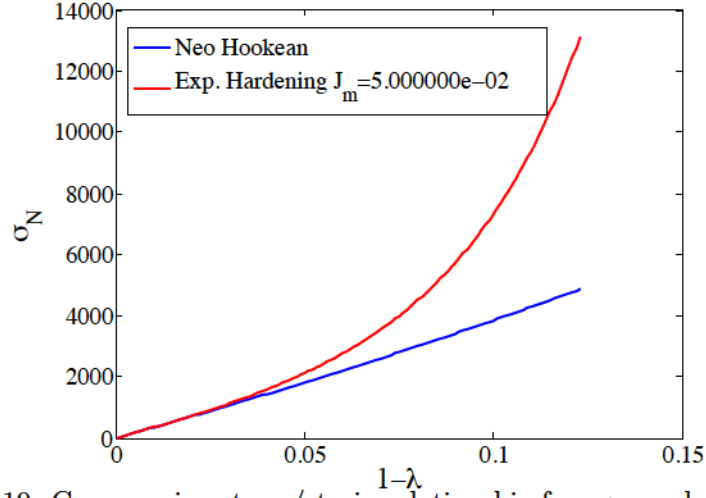


Figure 5.19: Compression stress/strain relationship for agar and gelatin gels, respectively good examples of exponential hardening (EH) and neo-Hookean (NH) materials. For a 1.5wt% agar gel $\mu = 20\text{kPa}$ and $J_m = 0.05$.

One recalls the nonlinear characterisation of Chapter 2. Agar gels stiffen exponentially and their work function is:

$$U = U(I_1) = \frac{\mu J_m}{2} [e^{\frac{I_1-3}{J_m}} - 1] \quad (5.31)$$

where I_1 is the first invariant of the right Cauchy Green tensor $C = F^T F$ and $F = \lambda_{ij} = \delta_{ij} + \frac{\partial u_i}{\partial X_j}$ is the deformation gradient.

For the gel under consideration, $J_m = 0.05$. This means that, for $J_1 = I_1 - 3 > 0.05$, the material stiffens strongly. What does it mean in terms of strain at the crack tip? What we will see next is that, in all the non linear theories we will consider, λ_{22} , which is the stretch in the opening direction, dominates over λ_{11} , λ_{12} , etc. In the crack tip vicinity, we thus have $J_1 \simeq \lambda_{22}^2 - 1 = (0.2)^2$ what allows us to compute a stress/strain relationship in the crack tip vicinity.

The true tensile stress σ^T , *i.e.* the stress computed in the deformed configuration, ahead of the crack tip is thus:

$$\sigma^T_{22} = \lambda_{22}^2 (\lambda_{22} - 1) \mu [e^{\frac{\lambda_{22}^2 - 1}{J_m}} - 1] \quad (5.32)$$

In Fig. 5.20, the true stress at the crack tip is plotted versus the local tensile stretch at the crack tip

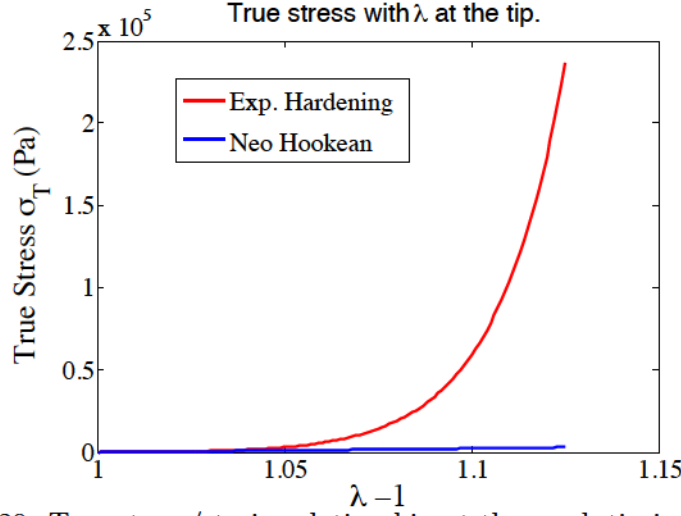


Figure 5.20: True stress/strain relationship at the crack tip is plotted with the local tensile stretch. For a 1.5wt% agar gel $\mu = 20\text{kPa}$ and $J_m = 0.05$.

Figure 5.20 illustrates the very strong impact of strain hardening on the stress-strain relationship. For $J_m = 0.05$, there is a clear distinction between the neo-Hookean and the strain-stiffening behaviours for tensile stretches as low as 3%. $\sigma^T = E$ is reached for 10% stretch and, for $J_1 = J_m$, $\sigma^T = 200E$. These are huge levels of stress: in this model, σ^T increases so strongly with the strain that $J_1 = J_m$ corresponds to stresses that no material can sustain. However, due to stiffening, the strains measured with DIC remain moderate (see Fig. 5.18): stiffening allows to prevent large strains that could threaten the material integrity. This explains why strain stiffening is a property shared by several biopolymer networks and biological tissues [26].

Agar gels are therefore ideal candidates to test the predictions for stress and strain fields, and displacement fields around a crack tip embedded in an exponential stiffening material. We thus briefly review recent work aiming at predicting their weakly nonlinear and strongly non linear behaviour in the framework of fracture.

5.3.2 Crack tip nonlinearities in a stiffening material

Nonlinearities must be experienced by any material undergoing fracture and, in soft materials, elastic nonlinearities appear way before the material gets irreversibly damaged. Understanding hyperelastic effects in the crack vicinity is of tremendous importance to understand how the energy flows from infinity to the crack tip. Simulations of cracks in model materials that could be made either softening or inversely stiffening in their nonlinear regime, were made by Buehler & *al* [12]. Comparing with a purely elastic material, they have shown that the net energy flow toward the crack tip is higher (respectively lower) for cracks propagating in a stiffening (respectively softening) material. Furthermore, they have discovered that the energy flow ahead of the crack almost vanishes in the softening case compared to the stiffening case. We can guess that the spatial distribution of damage in the material will be strongly influenced by the way the energy flows into the damage zone.

In acrylamide gels, which are well modeled by a neo-Hookean constitutive law, Livne & *al* [11] could identify and investigate three regions of space where the strains remained reversible but where three distinct constitutive laws could be used to understand the material behaviour. The first region is the far field region where LEFM, which is a theory of first order with the strain, applies. The second one is a weakly nonlinear zone where strains exceeds 10 – 20% and where second order elastic nonlinearities start being non-negligible. Finally, in the strongly non linear zone, the second order expansion is not sufficient anymore and the solutions are derived in the mathematical framework of hyperelasticity. In this section, we will briefly review the Weakly Nonlinear theory, which is expected to be universal, and the strongly nonlinear theory in the case of exponential stiffening materials.

5.3.2.1 Weakly Nonlinear theory for CT displacement fields

A weakly nonlinear region necessary lies between the linear elastic region and the strongly nonlinear zone. We follow a scaling approach by Bouchbinder & *al* [56] to give the reader a simple intuition of the calculation.

Emergence of a dynamic length scale. The first nonlinear strain can be described by the second-order nonlinear elasticity. To model this behaviour, we expand the stress s as:

$$s = \mu \partial u - \bar{\mu} (\partial u)^2 + \mathcal{O}((\partial u)^3) \quad (5.33)$$

where u denotes a displacement, ∂ denotes a spatial derivative, and μ and $\bar{\mu}$ are the first and second order moduli. We also expand the displacement u in powers of the displacement gradient $\epsilon = \partial u$:

$$u \simeq \epsilon u^{(1)} + \epsilon^2 u^{(2)} \equiv \tilde{u}^{(1)} + \tilde{u}^{(2)} \quad (5.34)$$

To first order, the momentum balance equation $\partial s = 0$ writes:

$$\mu \partial^2 \tilde{u}^{(1)} = 0 \quad (5.35)$$

This equation together with the traction-free boundary conditions on the crack mouth leads to Irwin's asymptotic solution:

$$\partial \tilde{u}^{(1)} \propto \frac{K}{\mu \sqrt{r}} \quad (5.36)$$

where K is the stress intensity factor and r is the distance to the crack tip.

To second order in ϵ , $\partial s = 0$ becomes:

$$\mu \partial^2 \tilde{u}^{(2)} - \bar{\mu} \partial (\partial \tilde{u}^{(1)})^2 = 0 \quad (5.37)$$

The second term plays the role of an effective force the magnitude of which decreases with the distance to the tip. It induces a supplementary stretch of the crack tip. Due to Eq.(5.36), this force scales as:

$$\bar{\mu} \partial (\partial \tilde{u}^{(1)})^2 \propto \frac{\bar{\mu} K^2}{\mu^2 r^2} \quad (5.38)$$

which admits a solution of the form:

$$\partial \tilde{u}^{(2)} \propto \frac{\bar{\mu} K^2}{\mu^3 r} \quad (5.39)$$

Nonlinear contributions start being relevant when $\partial \tilde{u}^{(2)} / \partial \tilde{u}^{(1)}$ exceeds 10%. This criterion, using Eq.(5.36) and Eq.(5.39), states that there exist a length scale ℓ_{nl} below which elastic 2nd order nonlinearities become important. ℓ_{nl} writes:

$$\ell_{nl} \propto \frac{\bar{\mu}^2 K^2}{\mu^4 0.1^2} \quad (5.40)$$

This length scale ℓ_{nl} has the particular property of being a dynamic length scale. Indeed, it depends on the stress intensity factor K_I and is thus function of the rate dependency of the fracture properties. This is what has already been observed in Sec.5.3.1. The physics of the length scale d^* is the same as the one of ℓ_{nl} : both give an order of magnitude of the distance below which nonlinearities become important, and both are dynamic length scales: they depend on the crack velocity via K_I or \mathcal{G} .

WNL displacement fields. Full derivation of the weakly nonlinear fields can be found in Ref. [72] in the case of a quasi-static mode I crack embedded in an incompressible neo-Hookean plane-stress sheet. It reads:

$$\begin{aligned} u_x(r, \theta) = & \frac{K_I \sqrt{r}}{4\mu\sqrt{2\pi}} \left[\frac{7}{3} \cos \frac{\theta}{2} - \cos \frac{3\theta}{2} \right] \\ & + \left(\frac{K_I}{4\mu\sqrt{2\pi}} \right)^2 \left[-\frac{1}{15} \log(r) - \frac{52}{45} \left(\log(r) + \frac{3}{4} \sin^2(\theta) \right) \right] \\ & + \left(\frac{K_I}{4\mu\sqrt{2\pi}} \right)^2 \left[-\frac{103}{48} \cos \theta + \frac{26}{15} \cos 2\theta - \frac{3}{16} \cos 3\theta \right] \end{aligned} \quad (5.41)$$

$$\begin{aligned} u_y(r, \theta) = & \frac{K_I \sqrt{r}}{4\mu\sqrt{2\pi}} \left[\frac{13}{3} \sin \frac{\theta}{2} - \sin \frac{3\theta}{2} \right] \\ & + \left(\frac{K_I}{4\mu\sqrt{2\pi}} \right)^2 \left[\frac{\theta}{15} - \frac{52}{45} \left(\frac{\theta}{4} - \frac{3}{8} \sin(2\theta) \right) \right] \\ & + \left(\frac{K_I}{4\mu\sqrt{2\pi}} \right)^2 \left[-\frac{61}{48} \sin \theta + \frac{26}{15} \sin 2\theta - \frac{3}{16} \sin 3\theta \right] \end{aligned} \quad (5.42)$$

The crack profile can be represented by taking $\theta = \pm\pi$. It results in the following expressions for the extra weakly non linear contribution:

$$u_x(r) = \left(\frac{3K_I}{4E\sqrt{2\pi}} \right)^2 \left[-\frac{11}{9} \log(r) + \frac{61}{15} \right] \quad (5.43)$$

$$u_y(r) = \left(\frac{3K_I}{4E\sqrt{2\pi}} \right)^2 \left(\frac{2\pi}{9} \right) \quad (5.44)$$

Several important features can be noticed about these expressions. First, the WNL theory was derived with the implicit assumption that there exists a zone surrounding the nonlinear region where the K-singular fields dominate. Within this framework, the authors derives displacement fields that depend only on the value of K . This is what is called the principle of autonomy of the process (or nonlinear) zone, that had already been introduced by Irwin & Orowan: different systems with different loadings but still the same K will behave the same in their respective nonlinear zones. Second, the WNL correction includes a $\log(r)$ contribution in the displacement field, which induces a strong departure from the LEFM asymptotic crack tip.

Why WNL theory breaks down in the Exponential Hardening case? In Eq.(5.41) and Eq.(5.42), the prefactor of these WNL contributions is more or less ℓ_{nl} for which we have taken the first and second order elastic moduli equal ($\bar{\mu} = \mu$). We will show that this statement is correct for both NH and EH materials. We recall the expression of the nominal

stress derived in Sec.2.3.3.2 for a compression test on respectively NH and EH materials:

$$N_{11}^{NH} = \mu(\lambda - \frac{1}{\lambda^2}) \quad (5.45)$$

$$N_{11}^{EH} = \mu(\lambda - \frac{1}{\lambda^2})e^{\frac{I_1-3}{J_m}} \quad (5.46)$$

If we write the stretch ratio λ as $1 - \epsilon$, we can develop N_{11} to the third order in power of ϵ . We find:

$$N_{11}^{NH} = \mu(-3\epsilon - 3\epsilon^2 - 4\epsilon^3) \quad (5.47)$$

$$N_{11}^{EH} = \mu(-3\epsilon - 3\epsilon^2 - (4 + 9/J_m)\epsilon^3) \quad (5.48)$$

In these two expressions, the first and second order terms have the same prefactor and thus $\bar{\mu} = \mu$. Bouchbinder & al state that the weakly nonlinear theory applies for general strain energy fonctionnals. WNL theory should thus apply. We think the theory is not wrong in the case of exponential stiffening but that it has a very limited range of validity. We have indeed checked the predictions for the crack shape and crack displacement fields in the case of agar gels at moderate velocities, where d^* is large enough to be measured but small enough to be sure that the nonlinear zone is still embedded in a K -dominated region. It did not induce any improvement. As an illustration, we show a crack shape in an agar gel (Fig.5.21) and compare it with the WNL prediction:

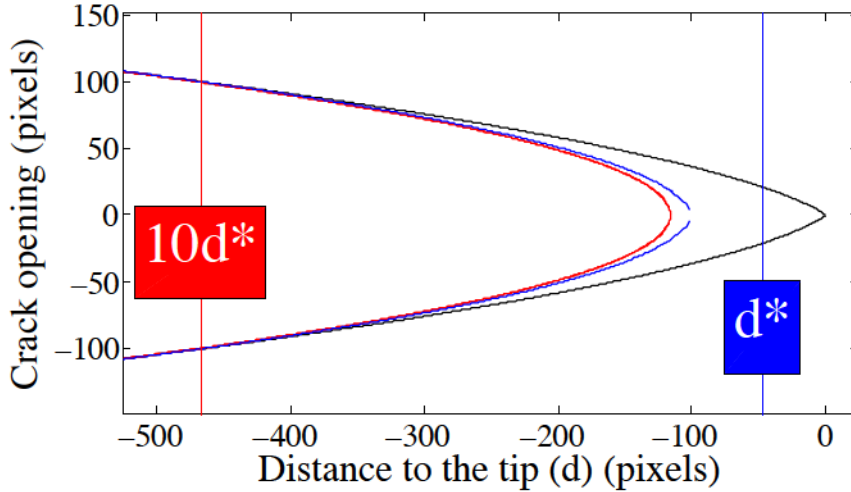


Figure 5.21: Experimental shape of a crack in a 1.5wt% agar gel (black). The LEFM parabola that best fits the experimental profile at $d > 10d^*$ is plotted in red. From the obtained K_I , we plot the WNL contributions (in blue). The improvement in the description of the crack shape is limited.

Experimental shape of a crack in a 1.5wt% agar gel is shown in black. The LEFM parabola that best fits the experimental profile at $d > 10d^*$ is plotted in red. From the obtained K_I , we plot the WNL contributions (in blue). The improvement in the description of the crack shape is limited. This suggests that the WNL theory, which is a second order theory is of limited validity in the case of EH materials. To get a better idea of the reason explaining this limitation, we plot each term of Eq.5.48 and compare their relative contribution for $J_m = 0.05$ see Fig.5.22. The result is surprising: for the NH material, whatever ϵ , the magnitude of the first order remains larger than the second, which is itself always larger than the third order. For the EH case, the third order term is doped by the exponential term and, for $J_m = 0.05$, $9/J_m = 180$. Consequently, above 2% strain, the third order contributes more than the second one, which reduces a lot the range of validity of the WNL theory.

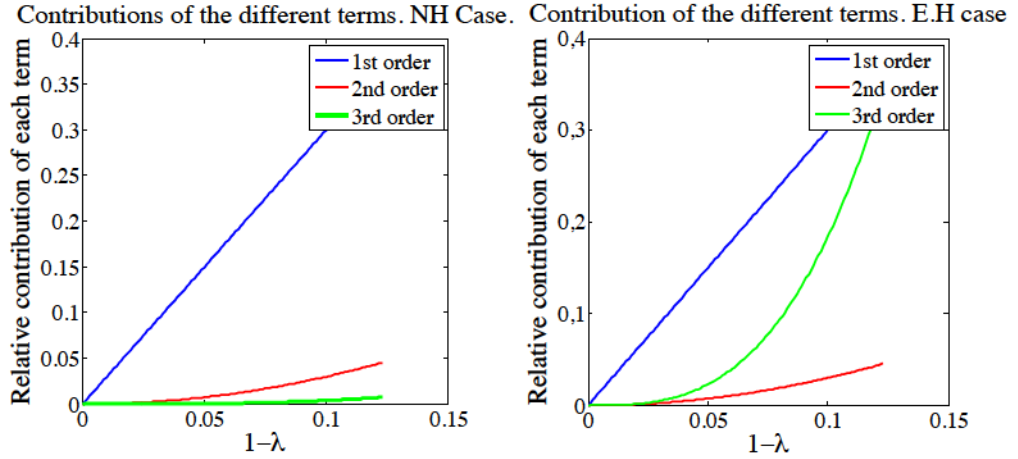


Figure 5.22: Relative contribution of each term of Eq.5.48 for $J_m = 0.05$.

Similarly, for the crack displacement field obtained with DIC at high velocities, for which we had reported large discrepancies with LEFM near the crack tip (see Fig.4.52), we tried to improve the quality map by adding the WNL corrections to the whole field after having found the best value for K_I but did not see any improvement either.

5.3.2.2 Strongly NL crack tips

As the weakly non linear theory has a very limited range in the case of concentrated agar gels, we focus on the strongly nonlinear theory developed by Long & al [73, 52]. Without entering into the details of the calculation, we review the main features of the predicted asymptotic displacement field and crack shape. To our knowledge, our experiments are the first that allow such high-magnification observation on such stiffening gels.

Krishnan & al performed both numerical simulations and theoretical computations to investigate the structure of the stress field in the vicinity of cracks embedded in stiffening materials. Figure 5.23 shows the reference undeformed configuration and deformed configuration :



Figure 5.23: Undeformed and deformed geometries of the strip specimen. We define the first Piola Kirchhoff stress (\mathbf{S}) and the true stress (\mathbf{T}). With \vec{df} , the force acting on a material surface of area $d\Gamma_0$ in the undeformed configuration with a unit normal vector \vec{n}_0 . After deformation, $d\Gamma_0$ becomes $d\Gamma$ with new unit normal vector \vec{n} . The first Piola Kirchhoff stress tensor \mathbf{S} is defined by $\vec{df} = \mathbf{S}\vec{n}_0 d\Gamma_0$. The true (Cauchy) stress tensor \mathbf{T} is defined by $\vec{df} = \mathbf{T}\vec{n} d\Gamma$.

There are major differences between the LEFM stress fields and the non linear true stresses. First, in LEFM, T_{11} , T_{22} , T_{12} share the same singularity in $1/\sqrt{r}$, where r is the distance to the undeformed tip. Ahead of the crack tip, there is thus a zone of pure hydrostatic tension. In the nonlinear theory, each component has its own singularity: for a neo-Hookean material, T_{11} is bounded while $T_{22} \propto 1/r$ and $T_{12} \propto 1/\sqrt{r}$. Sufficiently close to the crack tip, the material points are therefore in a state of uniaxial tension. Another major difference between linear and nonlinear theories is that, in nonlinear theory, each component can have a different singularity depending on the considered direction. It is consequently difficult to sum up the different results. Because it is easier to work in the deformed configuration, we focus on the true stress T_{22} , and especially on the opening strain field y_{22} ahead of the tip in the deformed configuration. We introduce R , the distance to the crack tip in the deformed configuration and write, for $\theta = 0$:

$$T_{22} \propto \frac{1}{R(-\log R)^{1.25}}$$

$$y_{22} \simeq \sqrt{-Jm \log(r/A_2)} \text{ where } r \propto R(-\log R)^{1/4}$$

We realize that the singularity for the strain is much weaker than the one for the stress. This is due to the strong stiffening of the material.

While, for neo-Hookean materials, Geubelle & Knauss [57] predict a "linear-like" parabolic crack tip which was observed [11], Long & al compute the nonlinear crack tip shape in an exponentially stiffening material [52].

The following displacements are found for the crack faces (see Figure 5.23 for significance of y_1 and y_2)

$$y_2 \simeq \pm \sqrt{-J_m \log r / A_2}$$

$$y_1 \simeq \pm r (-J_m \log r / A_2)^{-1/4} G(\pi)$$

In what follows, we plot four different crack profiles. The first one is an LEFM parabolic profile. The three other ones are plotted using the previous equations and using three different values of the hardening parameter $J_m = 0.05, 1, 5$. For all these profiles, we normalize y_1 and y_2 by their values at a point $250\mu\text{m}$ away from the crack tip on the crack surface (in the undeformed configuration). The LEFM profile does have an infinite slope at its tip. One can see that, as J_m increases, the crack opening profile shows a larger slope near the crack tip because the material tends toward a neo-Hookean material. For the case $J_m = 0.05$, where the strain hardening effect is the strongest, the crack opening profile is very close to a wedge shape, very similar to the one observed in our fracture experiments at high velocity.

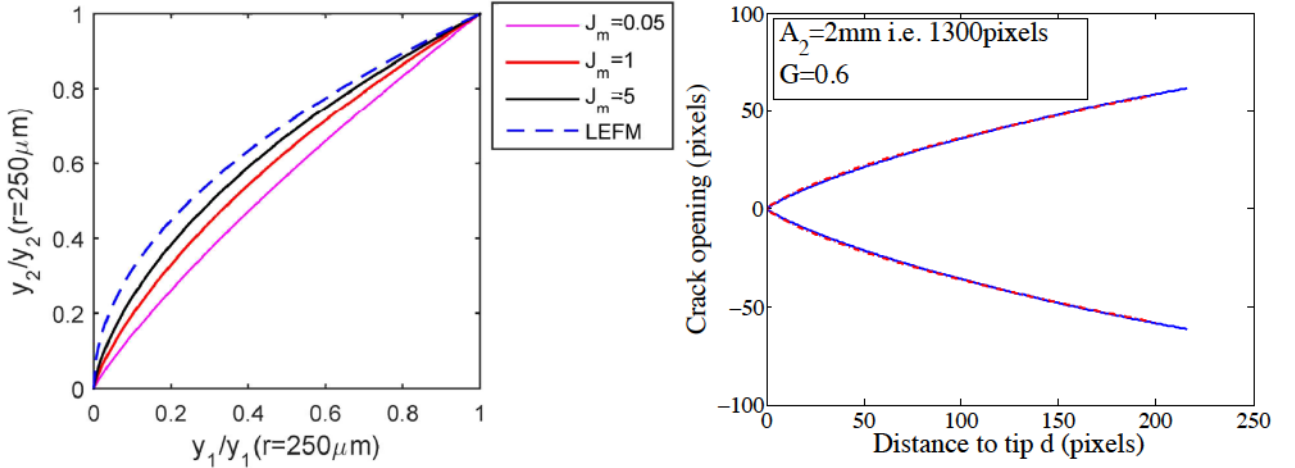


Figure 5.24: Left: Normalized crack opening displacement: LEFM versus Exponential Hardening crack with increasing J_m . Right: Experimental crack profile (blue line) versus analytical profile predicted for an exponentially hardening material. $J_m = 0.05$ is set by the nonlinear elastic characterization; A_2 and G are free parameters.

We thus try to investigate if our experimental profile can be described by the EH crack tip. On the right of Fig.5.24, we plot an experimental profile with $d^* = 70\text{pixels}$ and $A = 0.90$. We try to find, with J_m fixed to 0.05, a couple (A_2, G) that matches our experimental profile. We find $A_2 = 2\text{mm}$ and $G = 0.6$, which have good orders of magnitude if we compare to the

typical values found with numerical simulations [52]. Of course, for more robustness, we should then measure the crack displacement field and check, using the same parameters, if the measured displacement fields can be well described by the analytical or even by the numerical field obtained by Finite Element Modeling. It should be recalled indeed that the great advantage of using FE-DIC for measuring a displacement field is that it then directly allows for a comparison with FE simulations that have been performed using the same mesh.

5.4 Conclusion: disentangling dissipation and large deformations

Finally, we have realized that d^* was a dynamic nonlinear length scale, that it provided information on the distance from the crack tip below which reversible nonlinear elasticity became relevant while providing information on the amount of energy dissipated by the crack propagation. We have also shown that the rate dependency of the fracture properties is not due to bulk viscous or viscoelastic dissipation but is rather due to the rate dependent failure of the polymer chains in the cohesive zone.

Analyzing the velocity dependence of our crack energy release rate using a semi phenomenological approach (Bouchbinder's derivation of $\mathcal{G}(V)$) and comparing it with models predicting the crack dynamics in physical network, allowed us to understand two crucial features:

(1) Because failure occurs through the unreeling of the physical bonds rather than chain scission, describing the viscoplastic yielding of the material in the cohesive zone requires a good description of the behaviour of the weak physical junctions under stretch.

(2) Then a distinction should be made between two kinds of physical networks. A first type of networks is made of junctions with low spatial extension and little topological constraints. These can unreel and unzip without causing a great deal of dissipation, and the dynamics is thus controlled by the thermal or mechanical activation processes. We think these gels are well described by the models of Baumberger [63] or Hui & al [74]. A second kind of physical gels, to which we think agar belongs, holds thanks to extended junctions in which the degree of confinement of the chain is much higher. Unreeling of the chain thus requires sliding of the chains relative to each other and a much higher degree of cooperativity. We think the self-assembled triblock copolymer gels described in Ref. [62, 75] belong to the same category. Fig. 5.25 gives a good idea of the structure of this gel and of its behaviour. In water, the endblocks of the copolymer self-assemble into aggregates below some temperature (CMT). They form a network architecture of aggregates bound by soft elastic chains. At moderate temperature, the aggregates are liquid and the endgroups can reversibly go in and out of the aggregates. At low temperature (the one of interest), the aggregates are below their glass transition and behave as a strong elastic solid: the network is permanent and the pullout of an endgroup requires a lot of energy.

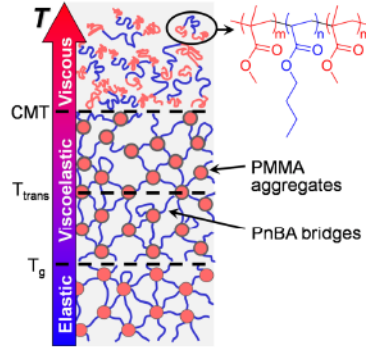


Figure 5.25: Organization of triblock copolymer in water with temperature. In water, the endblocks of the copolymer self-assemble into aggregates below some temperature (CMT). They form a network of aggregates bound by soft elastic chains. At moderate temperatures, the aggregates are liquid and the endgroups can reversibly go in and out of the aggregates. At low temperatures (the one of interest), the aggregates are below their glass transition and behave as a strong elastic solid: the network is permanent and the pullout of an endgroup requires lot of energy.

As we mentioned earlier, agar gels and copolymer gels share very similar features as for the rate dependence of their fracture properties. But, additionally, as described in Ref. [75], they also share dramatic strain stiffening at high strain. For copolymer gels, this is attributed to the high degree of connectivity and to the short length of the chains binding the aggregates. Failure of this gel presumably occurs in a similar way as it occurs for agar gels: the yield stress builds up very rapidly due to exponential stiffening and, as the chains are deeply confined in the glassy aggregate, this confinement results in measured effective viscosities that are orders of magnitude higher than the ones predicted for viscous pull out in the solvent swelling the gel. Such high effective viscosities would rather be found when considering entangled polymer melts. Stretched junctions would then have the same dynamics as entangled polymer chains.

Owing to this scenario, and as the cohesive zone (where microscopic damage occurs) is deeply embedded in the nonlinear elastic zone, understanding the material elastic nonlinearities is very important. A material that stiffens exponentially with a low J_m , strongly stiffens after a few percents of strain. Its mechanical response is very binary: either it is in its linear elastic regime at very low strain or it is strongly nonlinear. No weakly nonlinear regime can establish. Furthermore, J_m , which is a material property, sets a kind of upper bound for the deformation that the material can undergo.

When we try to understand the observed increase of d^* with V , two scenarii can be proposed (where we should remind that J_m is nearly independent of V):

(1) This increase can suggest an increase of the deformation to failure (but keeping J_m constant) for increasing crack velocity. This would be in agreement with the observed rate-dependency of the failure properties of agar networks measured by compression experiments (see for example Fig. 5, 6 and 7 in Ref.[20]).

(2) It can also be due to an increase of the yield stress in the cohesive zone, which, at constant J_m would result in a very little change in the strain to failure.

This will be analyzed more systematically by measuring the strains in the crack tip vicinity for different crack velocities.

An open possibility would be to build a rate dependent Maxwell-like cohesive model to take into account all of these observations. The chains of contour length Λ bridging the crack faces would have a characteristic relaxation time τ_{rep} due to reptation. If we write the pull out velocity as $\mathcal{V} = \alpha V$, there will be a low velocity regime ($\mathcal{V}\tau_{rep} < \Lambda$ *i.e.* $\alpha V\tau_{rep} < \Lambda$) where the reptation has time to occur. The Maxwell element behaves as a viscous dashpot of viscosity $\eta_{eff} = G\tau_{rep}$. Chains are pulled out at velocity $\mathcal{V} = \alpha V$ at low stresses, d_\star is small.

At high velocity ($\alpha V\tau_{rep} > \Lambda$), reptation has no time to occur, the yield stress builds up and so as the energy release rate, which causes the dynamic length scale d_\star to emerge and the crack to blunt. This "blunting" induces an increase of the wedge angle α until $\alpha V\tau_{rep}$ goes above Λ and allows the crack faces to detach.

One of the things that remains to be checked is that all the damage definitely occurs in the cohesive zone. Another possibility would be that the relatively high stress levels in the nonlinear zone are sufficient to damage the material and thus to provide an extra contribution to the energy dissipation. This question could be answered by computing the nonlinear J -integral (with exponential hardening constitutive law [11]) over contours of various size around the crack tip. If there is no irreversibility in the nonlinear zone, the value of the J -integral should not depend on the contour size until the scale of the cohesive zone is reached.

6

Conclusion & Perspectives

Contents

6.1 Conclusion.	229
6.2 Perspectives	230

6.1 Conclusion.

This doctoral thesis aimed at taking advantage of the high compliance and large structural lengthscales of soft materials to investigate experimentally the phenomenons occuring in the very vicinity of a crack tip.

This was done by developping a new "on a chip" experimental setup that allows the study of the propagation of mode I plane stress cracks growing at controlled rate. The designed experiment has the following novel specificities:

1. Performing fracture experiments on different classes of soft materials
2. Controlling the physical chemistry of the experimental conditions
3. Visualizing the material at mesoscopic/microscopic scales during crack propagation.
4. Building a mechanical test requiring low volumes of material

On top of that, one developped or adapted two complimentary techniques to perform measurements. First technique allows the high resolution detection of the shape of a crack while it is propagating. Second technique uses Digital Image Correlation to map the displacement fields around the crack tip. We showed how these two techniques allow us to extract macroscopic and microscopic quantities. Besides, the very simple crack configuration one works with has the great advantage to allow for direct comparison between our experimental observations and analytical or numerical predictions. For instance, the prediction for the asymptotic crack shape in a nonlinear elastic

exponentially hardening material could be validated. A full understanding of the displacement field of the crack at intermediate scales is still in progress, based on the work of Long & al [52].

In our experiments on agar gels, we were able to recover the energy release rate measured by other authors [38, 76, 77] from macroscopic experiments, by simply analyzing the morphology of the crack tip. Because fracturing our physical gels at high velocity V causes a great deal of dissipation, the stress intensity factor K_I must increase with V accordingly. This induces large strains in the crack tip vicinity, which translates into an earlier departure from LEFM. In this purely elastic solid with rate-independent mechanical properties, such a large rate-dependency of the fracture properties is surprising. Our first investigations to understand the origin of this V -dependent dissipation seems to lie in the rate-dependency of its nonlinear elastic properties. It comforts ones in the importance of taking nonlinear elasticity at the crack tip into account in our attempt to understand the mechanisms of dissipation at smaller scale: Because nonlinear elasticity occurs at scales intermediate between the LEFM scale where the energy comes from and the process zone scale where the energy is dissipated, nonlinear elasticity will influence a lot how the energy is transferred from large to microscopic scale.

One realised that, in this soft polymer gel, for crack velocities where the energy dissipation is large, there was a wide separation of scale between the macroscopic scale for which LEFM applies, the mesoscopic scale at which elastic nonlinearities show up and the microscopic scale at which dissipation occurs. Unfortunately, for now, one was not able to observe the microscopic dissipative processes occurring in this polymer physical gel. To circumvent this and to manage to access this scale, one developped, in collaboration with University of Amsterdam, an experimental setup specially dedicated to the study of the fracture properties of colloidal gels. For such materials, one expects dissipative processes 2 or 3 orders of magnitude larger than for the soft polymer gels one previously worked with. The preliminary experiments conducted recently indeed showed microcrack nucleation and non-affine displacements but the tools needed to make this study more quantitative remain to be developed.

6.2 Perspectives

The 3 years spent on this PhD project have been mainly used to show that novel experimental directions could be possible for a better understanding of material fracture properties. Fortunately, perspectives are numerous and they will hopefully not remain as perspectives for long.

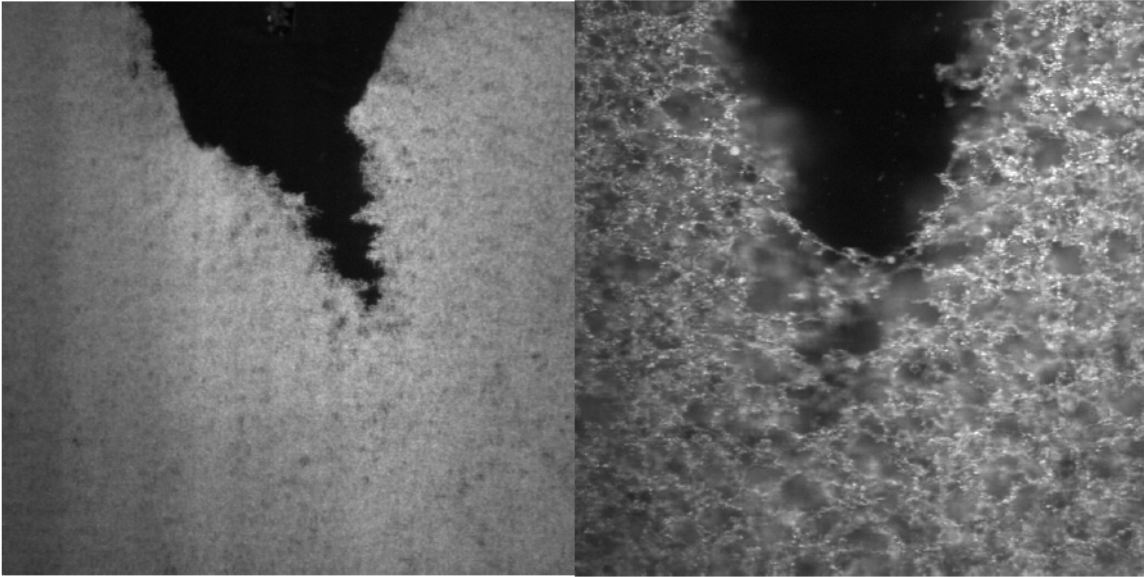


Figure 6.1

Fracture experiments on colloidal gels or, let us dream, on colloidal glasses are promising. The interest in using such materials is that, in principle, one is able to physico-chemically tune all the parameters governing interactions. It is thus possible to vary the attraction potential between the colloids and to explore a rich phase diagram while investigating the material fracture properties.

For these materials, confocal microscopy is a required tool to scan the material structure. It is, in theory, possible to track every colloid's position while the crack is propagating. But for now, confocal microscopy is too slow to get an "instantaneous" capture of the structure: investigated crack should be very slow to allow such an approach. For now he have only acquired 2D images of the growing crack. These first images will serve as test cases to develop new toolboxes to measure the relevant physical quantities. One of the last challenge is to find the proper colloidal system that would allow to brdige all the length scales and that would allow to measure both macroscopic dissipation while allowing visualization of the dissipative processes at "microscopic scale".

In polymer gels, the microstructure cannot be accessed and the dissipative zone iss too small. For the Casimir colloidal system, the problem is that the length scale at which LEFM applies is too large with respect to our specimen size. One is thus not able to measure the fracture energy of the crack one is looking at. One think smaller colloids, for example silica ones, of size 10 to 100 nm would allow to bridge all these length scales.

From a more applied point of view, an interesting project would consist in investigating the effect of the fracturing fluid on the fracture properties

of soft solid. For instance, it is known that clays are of fundamental importance in geology, especially in the field of oil extraction. It is a common technique to pump fluid at high pressure and high rates in the oil reservoir to induce cracks in the geological formation. The composition of the pumped fluid is known to be of tremendous importance but there was no systematic study to optimize the fluid composition. In our experiment, the physico-chemical environment is very well controlled and the fracturing fluid can be changed. It would thus be possible to study crack nucleation and crack propagation criteria for different compositions of fracturing fluids and adopt a more systematic approach in finding the best/less pollutant candidates.

Bibliography

- [1] C. L. Rountree, R. K. Kalia, E. Lidorikis, A. Nakano, L. Van Brutzel, and P. Vashishta. Atomistic aspects of crack propagation in brittle materials: Multimillion atom molecular dynamics simulations. *Annual Review of Materials Research*, 32(1):377–400, 2002.
- [2] M L Falk. Molecular-dynamics study of ductile and brittle fracture in model noncrystalline solids. *Physical Review B*, 60(10):7062–7070, 1999.
- [3] C. Maloney and A. Lemaitre. Subextensive scaling in the athermal, quasistatic limit of amorphous matter in plastic shear flow. *Phys. Rev. Lett.*, 93:016001, Jul 2004.
- [4] A. Tanguy, F. Leonforte, and J.-L. Barrat. Plastic response of a 2D Lennard-Jones amorphous solid: detailed analysis of the local rearrangements at very slow strain rate. *The European physical journal. E, Soft matter*, 20(3):355–64, July 2006.
- [5] F Célarié, S Prades, D Bonamy, L Ferrero, E Bouchaud, C Guillot, and C Marliere. Glass breaks like metal but at the nanoeterscale. *Physical Review Letters*, 90, 2003.
- [6] E. Bouchbinder, T. Goldman, and J. Fineberg. The Dynamics of Rapid Fracture: Instabilities, Nonlinearities and Length Scales. *Reports on progress in physics. Physical Society (Great Britain)*, 77, May 2014.
- [7] E. Bouchbinder, J. Mathiesen, and I. Procaccia. Branching instabilities in rapid fracture: dynamics and geometry. *Physical Review E - Statistical, Nonlinear and Soft Matter Physics*, 71(5 Pt 2):9, 2004.
- [8] P. Schall, D. A. Weitz, and F. Spaepen. Structural rearrangements that govern flow in colloidal glasses. *Science*, 318(5858):1895–1899, 2007.
- [9] P. Schall, I. Cohen, D. A. Weitz, and F. Spaepen. Visualizing dislocation nucleation by indenting colloidal crystals. *Nature*, 440(7082):319–23, March 2006.

- [10] A. Basu, Q. Wen, X. Mao, TC Lubensky, PA Janmey, and AG Yodh. Non-affine displacements in flexible polymer networks. *Macromolecules*, 44(6):37, 2010.
- [11] A. Livne, E. Bouchbinder, I. Svetlizky, and J. Fineberg. The near-tip fields of fast cracks. *Science (New York, N.Y.)*, 327(5971):1359–63, March 2010.
- [12] MJ. Buehler, FF. Abraham, and H. Gao. Hyperelasticity governs dynamic fracture at a critical length scale. *Nature*, 426(6963):141–6, November 2003.
- [13] K C Labropoulos, D E Niesz, S C Danforth, and P G Kevrekidis. Dynamic rheology of agar gels : theory and experiments . Part I . Development of a rheological model. *Carbohydrate Polymers*, 50:393–406, 2002.
- [14] J-Y. Xiong, J. Narayanan, X.-Y. Liu, T. K. Chong, S. B. Chen, and T.-S. Chung. Topology evolution and gelation mechanism of agarose gel. *The journal of physical chemistry. B*, 109(12):5638–43, March 2005.
- [15] S. Boral, A. Saxena, and HB Bohidar. Universal growth of microdomains and gelation transition in agar hydrogels. *The journal of physical chemistry. B*, 112(12):3625–32, March 2008.
- [16] K. C. Labropoulos, S. Rangarajan, D. E. Niesz, and S. C. Danforth. Dynamic Rheology of Agar Gel Based Aqueous Binders. *Journal of the American Ceramic Society*, 84(6):1217–1224, 2001.
- [17] D. Bulone, D. Giacomazza, V. Martorana, J. Newman, and P. San Biagio. Ordering of agarose near the macroscopic gelation point. *Physical Review E*, 69(4):041401, April 2004.
- [18] M. Manno, A. Emanuele, V. Martorana, D. Bulone, P. San Biagio, M. Palma-Vittorelli, and M. Palma. Multiple interactions between molecular and supramolecular ordering. *Physical Review E*, 59(2):2222–2230, February 1999.
- [19] P. Aymard, DR Martin, TJ Foster, AH Clark, and IT Norton. Influence of Thermal History on the Structural and Mechanical properties of agarose gels. 2001.
- [20] H McEvoy, S. B. Ross-Murphy, and A H Clark. Large deformation and ultimate properties of biopolymer gels : 1 . Single biopolymer component systems. *Polymer*, 26:1483–1492, 1985.
- [21] P. G. Higgs and R C Ball. Some Ideas Concerning the Elasticity of Biopolymer Networks. *Macromolecules*, 22:2432–2437, 1989.

- [22] M. Tokita and K. Hikichi. Mechanical studies of sol-gel transition: Universal behavior of elastic modulus. *Physical Review A*, 35(10):4329–4333, 1987.
- [23] M. Rubinstein and R. H. Colby. *Polymer Physics*. Oxford uni edition, 1993.
- [24] Y. Hu and Z. Suo. VISCOELASTICITY AND POROELASTICITY IN ELASTOMERIC GELS. *Acta Mechanica Solida Sinica*, 25(5), 2012.
- [25] M. Watase and K. Nishinari. Rheological properties of agarose-gelatin gels. *Rheologica Acta*, 19(2):220–225, March 1980.
- [26] C. Storm, J. J. Pastore, F. C. MacKintosh, T. C. Lubensky, and P. A. Janmey. Nonlinear elasticity in biological gels. *Nature*, 435(7039):191–194, May 2005.
- [27] T. Z. Pavan, E. L. Madsen, G. R. Franck, A. A. O. Carneiro, and T. J. Hall. Nonlinear elastic behavior of phantom materials for elastography. *Physics in Medicine and Biology*, 55:2679–2692, 2010.
- [28] T.J. Hall, M. Bilgen, M.F. Insana, and T.A. Krouskop. Phantom materials for elastography. *IEEE Transactions on Ultrasonics, Ferroelectrics and Frequency Control*, 44(6):1355–1365, November 1997.
- [29] J. P. Tordella. Fracture in the Extrusion of Amorphous Polymers through Capillaries. *Journal of Applied Physics*, 27(5):454, 1956.
- [30] P. J. Skrzyszewska, J. Sprakel, F. A. de Wolf, R. Fokink, M. A. Cohen Stuart, and J. van der Gucht. Fracture and Self-Healing in a Well-Defined Self-Assembled Polymer Network. *Macromolecules*, 43(7):3542–3548, April 2010.
- [31] T. Gallot, C. Perge, V. Grenard, M-A. Fardin, N. Taberlet, and S. Manneville. Ultrafast ultrasonic imaging coupled to rheometry: principle and illustration. *The Review of scientific instruments*, 84(4):045107, April 2013.
- [32] C. Ligoure and S. Mora. Fractures in Complex Fluids: the Case of Transient Networks. *Rheologica Acta*.
- [33] JF Berret and Y Séréro. Evidence of shear-induced fluid fracture in telechelic polymer networks. *Physical Review Letters*, 87(4):048303, 2001.
- [34] H Tabuteau, S Mora, G Porte, M Abkarian, and C Ligoure. Microscopic mechanisms of the brittleness of viscoelastic fluids. *Physical Review Letters*, 102(15):155501, 2009.

- [35] J. Nase, A. Lindner, and C. Creton. Pattern formation during deformation of a confined viscoelastic layer: From a viscous liquid to a soft elastic solid. *Physical review letters*, pages 1–4, 2008.
- [36] M. I. Smith, R. Besseling, M. E. Cates, and V. Bertola. Dilatancy in the flow and fracture of stretched colloidal suspensions. *Nature communications*, 1(8):114, 2010.
- [37] H. Tabuteau, S. Mora, M. Ciccotti, C.-Y. Hui, and C. Ligoure. Propagation of a brittle fracture in a viscoelastic fluid. *Soft Matter*, 7(19):9474, 2011.
- [38] T Baumberger, C Caroli, and D Martina. Fracture of a biopolymer gel as a viscoplastic disentanglement process. *Eur. Phys. J. E*, 21(1):81–9, September 2006.
- [39] E Lemaire, P Levitz, G Daccord, and H Van Damme. From viscous fingering to viscoelastic fracturing in colloidal fluids. *Physical Review Letters*, 67(15):2009, 1991.
- [40] G. Foyart, L. Ramos, S. Mora, and C. Ligoure. The fingering to fracturing transition in a transient gel. *Soft Matter*, 9(32):7775, 2013.
- [41] A. Piruska, I. Nikcevic, H. Lee, C. Ahn, W. R. Heineman, A. Limbach, and C. J. Seliskar. The autofluorescence of plastic materials and chips measured under laser irradiation. *Lab on a chip*, pages 1348–1354, 2005.
- [42] S. Mora, C. Maurini, T. Phou, J.-M. Fromental, B. Audoly, and Y. Pomeau. Solid Drops: Large Capillary Deformations of Immersed Elastic Rods. *Physical Review Letters*, 111(11):114301, September 2013.
- [43] D Bartolo, G. Degré, P. Nghe, and V. Studer. Microfluidic stickers. *Lab on a chip*, 8:274–279, 2008.
- [44] F. Hild and S. Roux. Digital Image Correlation: from Displacement Measurement to Identification of Elastic Properties - a Review. *Strain*, 42(2):69–80, May 2006.
- [45] B. Lawn. *Fracture of brittle Solids- 2nd Edition*. Cambridge s edition, 1993.
- [46] D. Maugis. *Contact, adhesion, and rupture of elastic solids*. Springer series in solid-state sciences edition, 1999.
- [47] C.-Y. Hui and A. Ruina. Why K ? High order singularities and small scale yielding. *International Journal of Fracture*, 72(1):97–120, 1995.
- [48] M. L. Williams. On the Stress Distribution at the Base of a Stationary Crack. *Journal of Applied Mechanics*, (3), 1956.

- [49] E.G. Coker and L.N.G. Filon. *A Treatise on Photo-Elasticity, by E.G. Coker and L.N.G. Filon*. University Press, 1957.
- [50] P G De Gennes. Soft Adhesives. *Langmuir*, 12(19):4497–4500, 1996.
- [51] F. Saulnier, T. Ondarcuhu, A. Aradian, and E. Raphael. Adhesion between a viscoelastic material and a solid surface. *Macromolecules*, 37(3):1067–1075, 2002.
- [52] R. Long, V. R Krishnan, and C.-Y. Hui. Finite strain analysis of crack tip fields in incompressible hyperelastic solids loaded in plane stress. *Journal of the Mechanics and Physics of Solids*, 59:672–695, 2011.
- [53] F. Hild and S. Roux. Comparison of local and global approaches to digital image correlation. *Experimental Mechanics*, 52:1503–1519, 2012.
- [54] F. Hild and S. Roux. Digital Image correlation. In *Optical Methods for Solid Mechanics*, pages 183–228. WILEY-VCH Verlag, 2012.
- [55] G. Besnard, F. Hild, and S. Roux. "Finite-element" displacement fields analysis from digital images : Application to Portevin-Le Châtelier bands. *Experimental Mechanics*, 2006.
- [56] E. Bouchbinder, A. Livne, and J. Fineberg. Weakly nonlinear fracture mechanics : experiments and theory. *Int. J. Fract.*, 162:3–20, 2010.
- [57] P. H. Geubelle and W. Knauss. Finite strains at the tip of a crack in a sheet of hyperelastic material: I. Homogeneous case. *Journal of Elasticity*, 35:61–98, 1993.
- [58] G.I Barenblatt. Equilibrium cracks formed during brittle fracture rectilinear cracks in plane plates. *Journal of Applied Mathematics and Mechanics*, 23(4):1009–1029, 1959.
- [59] C.-Y. Hui, D.-B. Xu, and E. J. Kramer. A fracture model for a weak interface in a viscoelastic material (small scale yielding analysis). *Journal of Applied Physics*, 72(8):3294, 1992.
- [60] JK Knowles and E Sternberg. Large deformations near a tip of an interface-crack between two N e o - H o o k e a n sheets *. *Journal of elasticity*, 13:257–293, 1983.
- [61] A. A. Griffith. The Phenomena of Rupture and Flow in Solids. *Philosophical transactions. Series A, Mathematical, physical, and engineering sciences*, 163(6), 1921.
- [62] M. E. Seitz, D. Martina, T. Baumberger, V. R. Krishnan, C.-Y. Hui, and K. R. Shull. Fracture and large strain behavior of self-assembled triblock copolymer gels. *Soft Matter*, 5(2):447, 2009.

- [63] T Baumberger and O Ronsin. From thermally activated to viscosity controlled fracture of biopolymer hydrogels. *The Journal of chemical physics*, 130(6):061102, March 2009.
- [64] A. N. Gent and J. Schultz. Effect of wetting liquids on the strength of adhesion of viscoelastic material. *The Journal of Adhesion*, 3(4):281–294, 1972.
- [65] D. Maugis. Review Subcritical crack growth, surface energy, fracture toughness, stick-slip and embrittlement. *Journal of materials science*, 20:3041–3073, 1985.
- [66] A N Gent. Adhesion and Strength of Viscoelastic Solids . Is There a Relationship between Adhesion and Bulk Properties ? †. *Langmuir*, 7463(10):4492–4496, 1996.
- [67] T. Baumberger, C. Caroli, and D. Martina. Solvent control of crack dynamics in a reversible hydrogel. *Nature materials*, 5(7):552–5, July 2006.
- [68] E. Bouchbinder and E. Brener. Viscoelastic fracture of biological composites. *Journal of the Mechanics and Physics of Solids*, 59(11):2279–2293, November 2011.
- [69] B N J Persson and E A Brener. Crack propagation in viscoelastic solids. *Physical Review E - Statistical, Nonlinear and Soft Matter Physics*, 71(036123), 2005.
- [70] T. Lake and A. G. Thomas. The strength of highly elastic materials. *Proceedings of the Royal Society A: Mathematical, Physical and Engineering Sciences*, 300(1460):108–119, 1967.
- [71] Costantino Creton, Jacob Hooker, and Kenneth R. Shull. Bulk and interfacial contributions to the debonding mechanisms of soft adhesives extension to large strains. *Langmuir*, 17(16):4948–4954, 2001.
- [72] E. Bouchbinder, A. Livne, and J. Fineberg. Journal of the Mechanics and Physics of Solids The $1 = r$ singularity in weakly nonlinear fracture mechanics. *Journal of the Mechanics and Physics of Solids*, 57(9):1568–1577, 2009.
- [73] V. R Krishnan, C.-Y. Hui, and R. Long. Finite Strain Crack Tip Fields in Soft Incompressible Elastic Solids. *Langmuir*, 24(11):14245–14253, 2008.
- [74] C.-Y. Hui, T. Tang, and Y.-Y Lin. Failure of Elastomeric Polymers Due to Rate Dependent. *Langmuir*, 20(11):6052–6064, 2004.

- [75] K. Erk. Strain-Stiffening in Synthetic and Biopolymer Networks Strain-Stiffening in Synthetic and Biopolymer Networks. *School of Materials Engineering*, 2010.
- [76] J. Zhang, C. Daubert, and E. A. Foegeding. Fracture Analysis of Alginate Gels. *journal of food science*, 70(7), 2000.
- [77] Y. Tanaka, K. Fukao, and Y. Miyamoto. Fracture energy of gels. *Eur. J. Phys. E*, 3:395–401, March 2000.